
**Like ice in the sunshine:
surface rearrangement and pre-melting
of the three most prominent surfaces
of hexagonal ice**

Dissertation
zur Erlangung des Grades eines
„Doctor rerum naturalium (Dr. rer. nat.)“

der Fachbereiche:

08 – Physik, Mathematik und Informatik,
09 – Chemie, Pharmazie und Geowissenschaften,
10 – Biologie,
Universitätsmedizin
der Johannes Gutenberg-Universität

vorlegt von
Tanja Kling
geboren in Wiesbaden

Max-Planck Graduate Center
mit der Johannes Gutenberg-Universität

angefertigt am MPI für Polymerforschung
Mainz, den 13.11.2017

D77 (Dissertation Johannes Gutenberg-Universität Mainz)

Dean of the Faculty Prof. Dr. Dirk Schneider

1st report Prof. Dr. Kurt Kremer
Max Planck Institute for Polymer Research

2nd report Prof. Dr. Marialore Sulpizi
Johannes Gutenberg University Mainz

Submitted: 13 November 2017

Oral examination:

Abstract

In this thesis, the low-index surfaces of hexagonal ice are examined in a temperature range from 200 K to 270 K, using classical molecular dynamics simulations employing the TIP4P/Ice rigid water model. With structural analysis we probed the transition from ordered to disordered arrangements at the top surface layers. Our structural analysis indicates that 2–3 layers are disordered, with a structure similar to that of liquid water at 270 K for the basal plane, 1–2 layers for the primary prismatic plane, and 2–4 layers for the secondary prismatic plane. A sudden increase of disorder is detected for the second layer of the basal plane between 260 K–270 K. Even though local order is lost within the top layer at the highest temperatures, the surfaces retain an ordered structure averaging over several snapshots as revealed by two-dimensional density maps. A different picture is obtained from dynamical analysis, where only the top layer displays normal diffusion and can be considered liquid-like for all surfaces at high temperatures. At lower temperatures, sub-diffusion is observed. The next few layers are only structurally similar to liquid water close to the melting point, but do not diffuse or display glass-like dynamics.

Zusammenfassung

In dieser Arbeit werden die Oberflächen mit niedrigem Index von hexagonalem Eis in einem Temperaturbereich von 200 K bis 270 K mit klassischen Molekulardynamiksimulationen, die das starre TIP4P/Ice-Wassermodell verwenden, untersucht. Mittels Strukturanalysen untersuchen wir den Übergang von einer geordneten zu einer ungeordneten Anordnung in den obersten Schichten der Oberfläche. Die Strukturanalyse ergibt, dass etwa 2–3 Schichten bei der Basalfläche, 1–2 Schichten bei der primären prismatischen Fläche und 2–4 Schichten bei der sekundären prismatischen Fläche eine ungeordnete, wasserähnliche Struktur aufweisen. Ein plötzlicher Anstieg der Unordnung wird bei der Basalfläche zwischen 260 K und 270 K gemessen. Obwohl die Ordnung innerhalb der ersten Schicht verloren geht, behält die Oberfläche im zeitlichen Mittel eine geordnete Struktur. Dies sieht man in zweidimensionalen Dichteprofilen. Ein anderes Bild ergibt sich aus der dynamischen Analyse, da dort nur die erste Schicht normale Diffusion zeigt und als einer Flüssigkeit ähnlich bei allen Oberflächen und hohen Temperaturen angesehen werden kann. Die nächsten Schichten sind nur strukturell wasserähnlich nahe am Schmelzpunkt, aber diffundieren kaum oder zeigen eine glasartige Dynamik.

Abstract

Ice is ubiquitous in nature and all around us. Of particular interest is the surface, where interactions with the environment take place. The surface of the most stable polymorph, hexagonal ice I_h , is known to pre-melt at temperatures close to the melting point.

In this thesis, the low-index surfaces of ice I_h —namely the basal (0001), the primary prismatic (10 $\bar{1}$ 0), and the secondary prismatic ($\bar{1}$ 2 $\bar{1}$ 0) plane—are examined in a temperature range from 200 K to 270 K, using classical molecular dynamics simulations employing the TIP4P/Ice rigid water model.

With structural analysis we probed the transition from ordered to disordered arrangements at the top surface layers. Our structural analysis, including radial distribution functions, hydrogen bond analysis, medium-range network topology, and order parameters, indicates that 2–3 layers ($\approx 8\text{ \AA}$ – 12 \AA) are disordered, with a structure similar to that of liquid water at 270 K for the basal plane, 1–2 layers ($\approx 4.5\text{ \AA}$ – 8.5 \AA) for the primary prismatic plane, and 2–4 layers ($\approx 5\text{ \AA}$ – 9.5 \AA) for the secondary prismatic plane. A sudden increase of disorder is detected for the second layer of the basal plane between 260 K–270 K explaining a peak shift observed in sum-frequency-generation spectroscopy measurements.^[1] Even though local order is lost within the top layer at the highest temperatures, the surfaces retain an ordered structure averaging over several snapshots as revealed by two-dimensional density maps explained by a templating effect induced by the underlying layer.

A different picture is obtained from dynamical analysis. According to the mean square displacement calculation only the top layer displays normal diffusion and can be considered liquid-like for all surfaces at high temperatures. Diffusion is isotropic. At lower temperatures, sub-diffusion is observed. The next few layers are only structurally similar to liquid water close to the melting point, but do not diffuse or display glass-like dynamics.

Zusammenfassung

Eis ist allgegenwärtig in der Natur und unserer Umgebung. Von besonderem Interesse ist die Eisoberfläche, auf der die Interaktion mit der Umgebung stattfindet. Für die Oberfläche der stabilsten Modifikation, Eis I_h , ist die Bildung einer quasi flüssigen Schicht an der Oberfläche schon vor dem Schmelzpunkt bekannt.

In dieser Arbeit werden die Oberflächen mit niedrigem Index, das heißt die Basalfläche (0001), die primäre prismatische Fläche (10 $\bar{1}$ 0) und die sekundäre prismatische Fläche ($\bar{1}$ 2 $\bar{1}$ 0), in einem Temperaturbereich von 200 K bis 270 K mit klassischen Molekulardynamiksimulationen, die das starre TIP4P/Ice-Wassermodell verwenden, untersucht.

Mittels Strukturanalysen untersuchen wir den Übergang von einer geordneten zu einer ungeordneten Anordnung in den obersten Schichten der Oberfläche. Die Strukturanalyse, die sowohl radiale Verteilungsfunktionen, Wasserstoffbrückenbindungsanalyse, mittelreichweitige Netzwerktopologie, als auch Ordnungsparameter verwendet, ergibt, dass etwa 2–3 Schichten ($\approx 8 \text{ \AA}$ – 12 \AA) bei der Basalfläche, 1–2 Schichten ($\approx 4.5 \text{ \AA}$ – 8.5 \AA) bei der primären prismatischen Fläche und 2–4 Schichten ($\approx 5 \text{ \AA}$ – 9.5 \AA) bei der sekundären prismatischen Fläche eine ungeordnete, wasserähnliche Struktur aufweisen. Ein plötzlicher Anstieg der Unordnung wird bei der Basalfläche zwischen 260 K und 270 K gemessen und erklärt eine Verschiebung des Maximums des experimentell bestimmten Summenfrequenzspektroskopiesignals. Obwohl die Ordnung innerhalb der ersten Schicht verloren geht, behält die Oberfläche im zeitlichen Mittel eine geordnete Struktur. Dies sieht man in zweidimensionalen Dichteprofilen und wird durch einen Templateffekt der darunterliegenden Schicht erklärt.

Ein anderes Bild ergibt sich aus der dynamischen Analyse. Aus der Berechnung der mittleren quadratischen Verschiebung ergibt sich, dass nur die erste Schicht normale Diffusion zeigt und als einer Flüssigkeit ähnlich bei allen Oberflächen und hohen Temperaturen angesehen werden kann. Die nächsten Schichten sind nur strukturell wasserähnlich nahe am Schmelzpunkt, aber diffundieren kaum oder zeigen eine glasartige Dynamik.

Statutory declaration

I hereby declare that I wrote the dissertation submitted without any unauthorized external assistance and used only sources acknowledged in the work. All textual passages which are appropriated verbatim or paraphrased from published and unpublished texts as well as all information obtained from oral sources are duly indicated and listed in accordance with bibliographical rules. In carrying out this research, I complied with the rules of standard scientific practice as formulated in the statutes of Johannes Gutenberg-University Mainz to insure standard scientific practice.

Mainz, den 13.11.2017

Tanja Kling

” *Wer nichts weiß, muß alles glauben.*

— **Marie von Ebner-Eschenbach**

Aphorismen, 1893

Dedicated to my husband Felix

Contents

1	Melting away—hexagonal ice and its surface	1
1.1	Why ice is slippery	1
1.2	Research on the ice surface	5
1.2.1	Experimental research	5
1.2.2	Theory and simulations	9
1.3	Outline of the thesis	14
2	Methods	15
2.1	Classical molecular dynamics	15
2.1.1	Canonical ensemble	17
2.1.2	Molecular interactions	17
2.1.3	Constraints	19
2.2	Selection of a force-field	20
2.2.1	How to choose a force-field for hexagonal ice	20
2.2.2	The TIP4P/Ice model	22
2.3	Simulation details and systems	23
3	Structural analysis	27
3.1	Low-index surfaces of hexagonal ice	27
3.2	Density profiles	29
3.3	Two-dimensional density maps	30
3.4	Radial distribution functions	34
3.5	Conclusion	37
4	Hydrogen bonding analysis	39
4.1	The importance of networking	39
4.1.1	Importance and general definition of an H-bond	39
4.2	Statical analysis	41
4.3	Dynamical analysis	46
4.4	Network analysis	48
4.4.1	Basal surface	49
4.4.2	Prismatic surfaces	51
4.5	Conclusion	52
5	Everything in order?	53
5.1	Introduction	53
5.2	Layer-resolved order parameter analysis of the ice surface	59

5.2.1	Basal plane	60
5.2.2	Primary and secondary prismatic plane	63
5.3	Conclusion	65
6	Self-diffusivity of the three most prominent ice surfaces	67
6.1	Diffusion and mean square displacement	67
6.2	Self-diffusion and mean square displacement at the hexagonal ice surfaces	69
6.3	Comparison to supercooled water and literature	73
6.4	Self-diffusion anisotropy	75
6.5	Conclusion	76
7	Conclusion	77
8	Appendix	81
8.1	Chapter 1: Melting away—hexagonal ice and its surface	81
8.2	Chapter 3: Structural analysis	82
8.2.1	Miller-Bravais indices	82
8.2.2	Two-dimensional density profiles	84
8.2.3	Rescaled RDFs for a slab with two sharp interfaces	85
8.3	Chapter 4: Hydrogen bonding analysis	86
8.3.1	Percentage of free OH on non-rearranged surfaces	86
8.3.2	Statical Analysis	88
8.3.3	Spheres	89
8.3.4	Orientation of the <i>OH</i> -vector	92
8.3.5	Dynamical analysis	95
8.3.6	Network analysis	95
8.4	Chapter 5: Everything in order?	102
8.4.1	Percentage of analysed molecules	102
8.4.2	Z- and layer-resolved distributions of the q_i , $i = 2, 3, 5, 6$ of the low-index surfaces of hexagonal ice	102
8.4.3	Temperature-dependent behaviour of the upper three layers of the low index-faces of ice	115
8.4.4	Temperature-dependent layer-resolved LSOP distributions of the upper six layers of the low-index surfaces of hexagonal ice	123
8.4.5	Comparison between the criterion used in this work and an alter- nate criterion to select neighbours based on H-bonds	129
8.5	Chapter 6: Self-diffusivity of the three most prominent ice surfaces	130
8.5.1	Out-of-plane diffusion	130
8.5.2	In-plane diffusion	131
8.5.3	Liquid water references	136
8.5.4	Self-diffusion anisotropy	138
8.6	Software list	140
	Bibliography	141

Melting away—hexagonal ice and its surface

1.1 Why ice is slippery

Water as a liquid is all around us and essential to life on earth. However, its solid form, ice, is equally well represented as it makes up the most common molecular solid in nature. Of particular interest is the ice surface, where all of the interactions with the environment take place, serving as a structural template to mediate interfacial chemical reactions and governing further ice nucleation.

Let us take a closer look at ice. Snow flakes, for example, have a six-fold symmetry (Figure 1.1), which indicates a hexagonal structure of ice. Indeed, the majority of ice consists of hexagonal ice, called ice I_h .^a

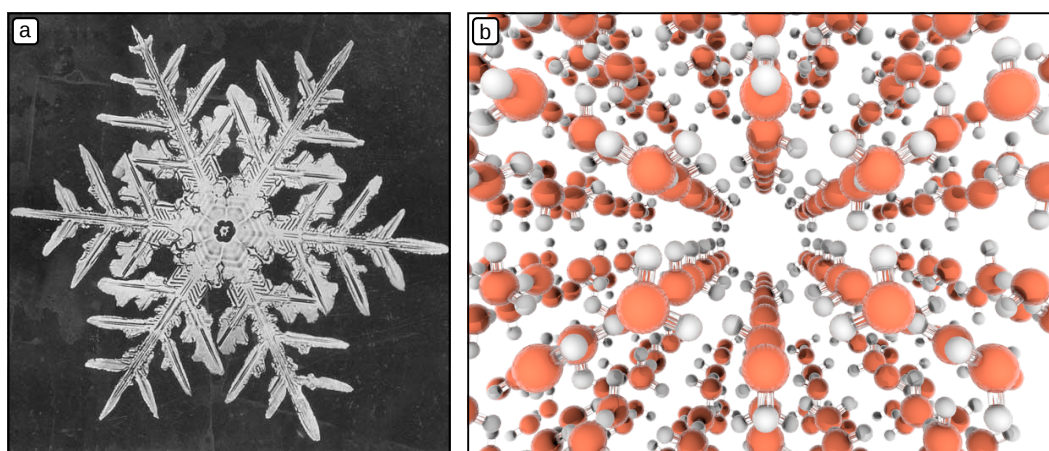


Fig. 1.1: (a) Snowflake displaying six-fold symmetry. Photograph by Wilson A. Bentley. (b) Molecular picture of hexagonal ice.

Ice I_h is not the only form of ice that exists in nature. In fact, the phase diagram of water is one of the most complex. There are roughly eighteen known crystalline phases of ice and three amorphous phases.^{b[3–8]} One reason for this complexity lies in the nature

^aThe Roman letter I stands for ice one and the subscript h indicates the hexagonal structure in the Bridgman nomenclature.^[2] There is also another form of ice I, I_c , which has a cubic structure.

^bThe high pressure phases beyond Ice VII are not hydrogen-bonded (except for ice XI).

of the hydrogen bonding in water, which allows for a very large number of crystalline structures and amorphous networks with different types of medium-range features.^[7,9] An example for the unique character of hydrogen bonding is its strong directionality. The abundance and diversity of hydrogen bonds is explained in particular by the difference between hexagonal ice I_h and ice XI. The only structural distinction between the two ice modifications is the proton arrangement. Ice I_h is proton-disordered, that is the arrangement does not follow any regular pattern, but obeys the ice rules.^{c[10]} Ice XI, on the other hand, is proton ordered. This difference has severe consequences on their respective properties. For instance, ice I_h is thermodynamically stable under ambient conditions, while ice XI is only metastable. Hence, not only the oxygen arrangement, but also the variety of hydrogen arrangements define the properties of the resulting crystal structure. The discovery of new forms of ice is still ongoing.^[11] Since hexagonal ice I_h is the crystal modification at ambient conditions, the focus of this thesis is on hexagonal ice.

The unit cell of ice I_h is depicted in Figure 1.2. In the hexagonal ice structure, the oxygen atoms are arranged in a wurtzite structure. Ice I_h is, as already mentioned, proton-disordered and Figure 1.2 (b) shows one of the possible hydrogen arrangements.^[10] By cutting the hexagonal unit cell as implicated in Figure 1.2 (c), three prominent low-index faces emerge, namely the basal faces $\{0001\}$, the primary prismatic faces $\{10\bar{1}0\}$ (1st prism) and the secondary prismatic faces $\{11\bar{2}0\}$ (2nd prism) are obtained.

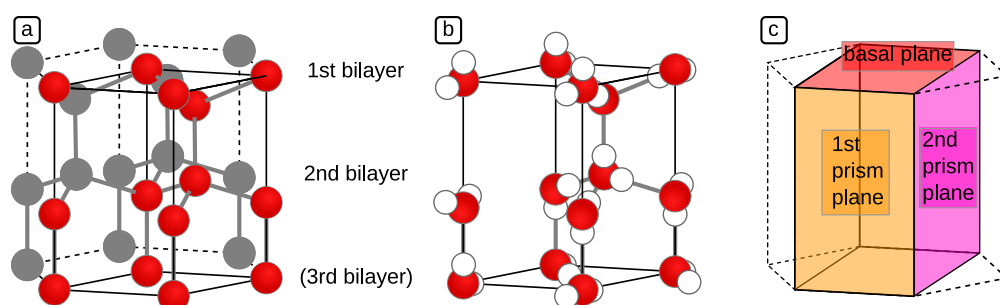


Fig. 1.2: In the hexagonal ice structure, the oxygen atoms are arranged in a so-called wurtzite structure. The hydrogen bonds are proton-disordered. (a) Schematic drawing of the I_h unit cell. The basal plane is organised in bilayers as marked by the labels. The hydrogen bonds are indicated by bold lines. The full hexagon is shown in grey. The red circles represent the oxygen atoms. (b) The unit cell with a proton-disordered hydrogen arrangement. (c) The three most prominent planes: the basal plane (0001), the primary prismatic plane (10 $\bar{1}$ 0) and the secondary prismatic plane (11 $\bar{2}$ 0).

However, the true surface structure is quite different from the ideal structure after cleaving, as was already discovered by no other than Michael Faraday in 1842. He conducted an experiment in which he put two ice^d cubes together at a temperature below the melting

^cThe ice rules basically state that one oxygen atom is covalently bonded to two hydrogen atoms and that the oxygen atom in each water molecules forms four hydrogen bonds with the other oxygen atoms, which results in an arrangement with exactly one hydrogen located between each pair of oxygen atoms.

^dFrom now on ice refers to ice I_h .

point and observed that both merge and freeze into one large ice cube.^[12] He explained this phenomenon with a liquid layer at the ice surface, a simple and logical idea, which proved to be correct. Nevertheless, the structural nature of this liquid layer has to this day not been fully resolved. It seems to be very similar, but not identical to that of liquid water and is therefore, often referred to as a 'quasi-liquid-layer' (QLL).

The general phenomenon of a molten layer at the surface of a solid in contact with a gas/vacuum below the melting point is known as pre-melting or surface melting.^e Pre-melting is, however, not unique to ice. It occurs at the surfaces of several solids, for instance the surface of Pb(110) exposed to vacuum.^[13]

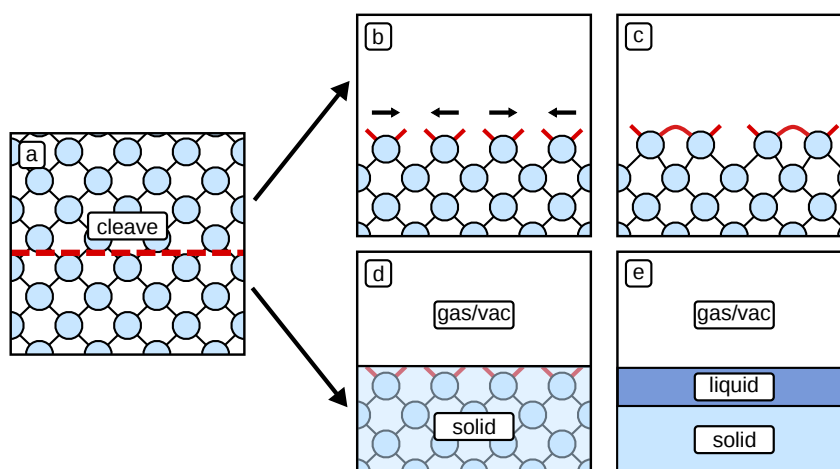


Fig. 1.3: (a) Two-dimensional schematic picture of a bulk crystal. The red line indicates the cleaving line. (b) Bulk after cleaving. The atoms at the surface possess dangling bonds. (c) The surface reconstructs in order to minimise the amount of dangling bonds and, thus, also the surface energy. (d) + (e) Alternative path for lowering the surface free energy. Surface melting creates two interfaces instead of one interface, which happens because the molecules at the surface are loosely bound and start to move below the melting temperature.

The reason for surface melting is the difference between the surface and the bulk crystals, as illustrated in Figure 1.3. In Figure 1.3 (a), the schematic bonding situation for atoms in bulk is shown in two dimensions, where all molecules possess four bonds to their neighbours. Upon cleavage, bonds break at the surface (see Figure 1.3 (b)). These bonds are called dangling bonds. As this situation is energetically unfavourable, the system will now try to reduce the surface energy. One possibility to do so is to rearrange as illustrated in Figure 1.3 (c).^f This is what the ice surface does at low temperatures. The water molecules at the surface rearrange, but do not form any regular structure.^[14–16] Accordingly, the ice surface is characterised by disorder at low temperatures.

^eThis discovery and the explanation of Faraday started a long debate about the existence of such a QLL. This debate lasted for more than a century.

^fIt should be mentioned that an additional possibility exists for reactive materials, namely the reaction of the surface's dangling bonds with gas molecules. Especially metals often form an oxide layer at their surfaces.

Another way to reduce the energy is to form two interfaces instead of one. By surface melting, an interface between air and liquid and an interface between liquid and bulk can be created. This idea is illustrated in Figure 1.3 (e). Due to the reduced number of dangling bonds, the molecules at the surface are mobile and able to form some kind of liquid, which happens for ice close to the melting point. Interestingly, the discovery of Faraday was one of the first observations of surface melting which also instigated the discovery of pre-melting for many other solids.^[17] A thorough overview of the physics of pre-melting can be found in the literature reviews [17] and [18].

The presence of a QLL on the ice surface readily explains the extraordinary properties of ice, such as its slipperiness. In contrast to common belief, this is not pressure induced.⁸ For ice skating or skiing, there is additional friction induced melting.^[19] Yet, the presence of a QLL is still essential, as was experienced by a south pole expedition in 1910 lead by Robert Falcon Scott. While skiing was easy at -30°C , the snow became sand-like at -46°C .^[19] In fact, it was one of the reasons for the failure of the expedition, since their luggage had to be dragged along on skis at temperatures of around -46°C for larger parts of the journey. Their observation suggests that the thickness of the QLL is temperature-dependent, a phenomenon which was supported by several experiments performed afterwards.

As already mentioned, pre-melting itself is not unique to ice. However, the importance and pervasiveness of the environmental consequences of the pre-melting of ice are unique:

“Working as a pathway for flowing water, as a carrier of electrical charge and as a catalytic surface for the ozone depletion, the QLL is able to force boulders from the ground, blast lightning bolts from the sky and govern the ozone depletion.”^[20]

Hence, the QLL not only makes ice a good ground for winter sports, it also influences a number of key processes observed in nature.

Cirrus and mixed-phased clouds consist of ice and, accordingly, the weather is influenced by the microphysics of ice. On the QLL at the ice crystals in thunderclouds, transfer of mass and charge during collisions takes place, leading to the electrification of thunderclouds and in turn to lightning.^[18]

The size of the ozone hole at the Antarctica is related to the presence of special ice clouds

⁸The idea of pressure induced melting originates from the regelation of ice. The regelation is evident, since ice floats on water, which is only possible if the density of the solid is lower than the one of the liquid. By applying pressure, a phase transition can be induced due to regelation. However, the regelation leads to a decrease in melting point by far less than a Kelvin, which does not suffice to explain why ice is slippery far below the melting point.^[19]

called polar stratospheric clouds type II. The general ozone destruction in the stratosphere due to trace gases is strongly enhanced in the presence of such clouds, since the QLL on the ice surface catalyses the formation of ozone depleting species.^[17,18]

Additionally, the present global warming and the resulting climate change are influenced by processes involving ice surfaces. This is because the QLL plays an important part in glacier sliding and the melting of sea ice.^[18,21,22]

Finally, the surface of ice also regulates its freezing properties. Hence, the food industry is interested in its research for cryo-preservation, the conversation of food, and the production of ice cream.^[21,23–25]

In summary, the numerous unusual properties of the ice surface—especially the formation of a QLL—are important for a vast amount of applications. A detailed overview of the processes in which the QLL is involved can be found in [18].

1.2 Research on the ice surface

1.2.1 Experimental research

An intense debate about the existence of the QLL started after its discovery by Michael Faraday in 1842, which lasted over a century. Nowadays it is widely accepted that a QLL is present on ice, even far below the melting point. Yet, the precise onset temperature for the transition of a disordered interface to a QLL and its temperature-dependent thickness remain unknown.

With the emergence of surface-sensitive experimental methods, it became possible to study properties of the disordered surface and the QLL. A variety of experimental methods have been employed to investigate the onset temperature of the surface rearrangement, the thickness of the disordered layer, the onset temperature of the QLL formation and its temperature-dependent thickness. However, results vary by several orders of magnitude (Figure 1.4) even for the same method.^h For instance, the onset temperature ranges from -2°C in optical ellipsometry experiments^[27], -13.5°C in grazing angle-X-ray scattering^[28], -20°C in electrical conductivity^[29], -60°C in proton channelling^[30,31], -73°C in He-scattering^[32], -93°C in sum-frequency-generation spectroscopy^[33], -100°C in nuclear magnetic resonance^[34] to -160°C in photoemission^[35] experiments.

^hIn Figure 1.4, some values for the thickness lower than 0.3 nm are depicted. This is roughly the diameter of a water molecule and, hence, the lower physically meaningful limit of a thickness.^[26] The reason for these values is that the thickness itself is not a direct observable in the experiment. Measurement values represent average values over the entire probing area. In addition to averaging, the calculation of the thickness from the observed quantity leads to further uncertainties.

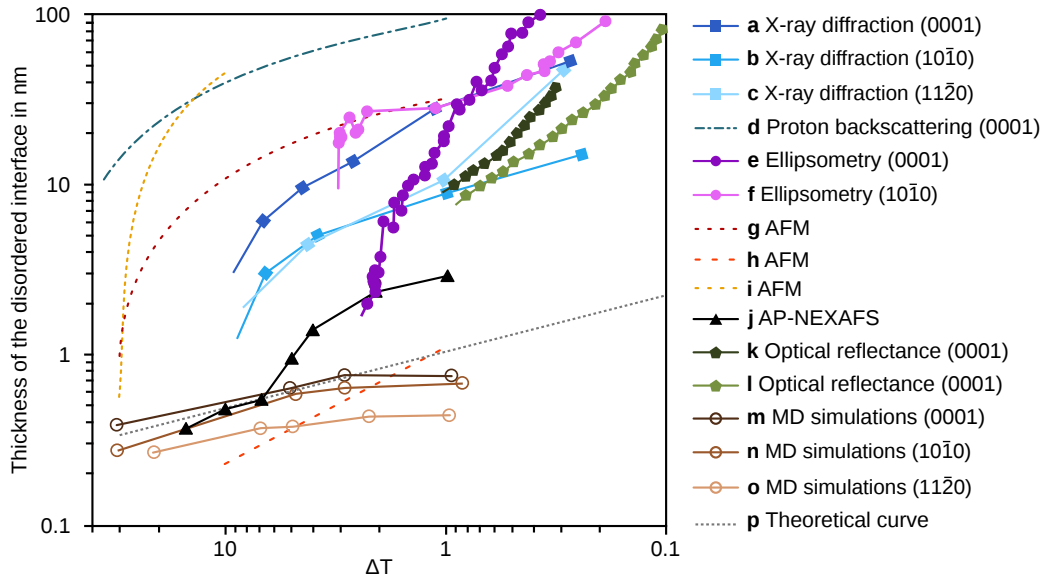


Fig. 1.4: Comparison of different methods to derive the thickness of the disordered interface (DI) at the ice/vapour interface versus the degree of supercooling $\Delta T = T_m - T$. Solid symbols represent measured data, while dashed lines are functions fitted to experimental data. Molecular dynamics (MD) simulations are represented by open circles. Grazing angle-X-ray diffraction^[28] on (a) basal and (b) primary prismatic, (c) secondary prismatic surfaces; (d) proton backscattering^[30] on basal ice; ellipsometry^[36] on (e) basal and (f) prismatic crystal surfaces; (g) atomic force microscopy (AFM)^[37] on a 100 ml frozen droplet and vapour deposited on mica; (h) AFM^[38] for vapour-deposited ice on metal; (i) AFM^[39] for ice frozen on a metal substrate; (j) ambient pressure near-edge X-ray absorption fine structure^[40] for vapour-deposited ice on metal; HeNe laser optical reflectance^[41] on basal crystals in the presence of (k) water vapour and (l) 30 Torr air; TIP4P/Ice MD simulations^[42] for (m) basal, (n) primary prismatic, (o) secondary prismatic surface; (p) simple thermodynamic model^[18]. Adapted with permission from [26], CC-BY 3.0 License^[43]. A more detailed list of experiments can be found in the Appendix (Table 8.1).

Nonetheless, experiments agree that different surfaces of ice have differing onset temperatures for disorder or pre-melting and respective thicknesses (Figure 1.4). Grazing angle-X-ray diffraction found an onset temperature of -13.5°C for the basal plane, while a temperature of -12.5°C was obtained for the prismatic surfaces.^[28] Accordingly, different thicknesses are obtained as well (Figure 1.4 (a), (b) and (c)). The highest thickness was measured for the basal plane (0001) (Figure 1.4 (a)). Ellipsometry measurements found a higher thickness of disorder at low temperatures for the primary prismatic plane than for the basal plane (Figure 1.4 (e) and (f)). The trend is reversed at higher temperatures.^[27,36] To conclude, these examples agree on a difference between the three surfaces, but are inconclusive about trends or absolute values.

By performing X-ray diffraction measurements of the ice surface, it was found that the QLL does not have a long-range ordered structure.^[44] Grazing angle-X-ray diffraction allows for a variation of the probing depth from 5 nm to 100 nm, while recording the disorder of the oxygen atoms and disruptions in the hydrogen bonding network separately.^[28,45] However, because the height of one bilayer is only about 0.4 nm, the technique is only interesting close to the melting point, where several bilayers are molten.

One reason for the observed discrepancies is the fairly complicated nature of the ice surface. It is known to rearrange at low temperatures, while it pre-melts close to the melting point.^[46] Consequently, disorder and degree of liquidity are two different properties and should not be mixed up. Furthermore, the QLL is characterised only by liquidity and it is difficult to map the degree of disorder to the degree of liquidity. Thus, two different onset temperatures exist: the onset temperature of the formation of a disordered interface and the onset temperature for the emergence of the QLL. Likewise, two different thicknesses exist. Hence, it is difficult to map the change in a measured quantity to the thickness of the QLL when, for instance, statical parameters such as disorder are measured. This is a general problem, even if the values for the liquid and the solid reference are known. A threshold needs to be set to decide when the disorder is high enough to count a surface as liquid for each of the measured properties. For dynamical parameters such as diffusion coefficients, this is easier than for statical parameters. Therefore, the thickness of the disordered interface and not of the thickness of the QLL is plotted against the degree of supercooling ΔT in Figure 1.4.

Other reasons for the discrepancies are problems that arise due to experimental limitations and sample preparation issues. Ellipsometry measurements are a good example for the experimental limitations, because the ice/glass interface is probed instead of the ice/vapour interface, since a glass plate needs to be brought in contact with the sample for measurement. Parameters such as the roughness of the glass plate influence the results significantly and it is difficult to map these back to the ice/vapour interface. Similarly, atomic force microscopy (AFM) measurements bring along their own set of issues, because they are invasive. When force-distance curves are obtained, the interaction of a tip with the QLL is studied. Hence, the studied system is the one between the tip and the QLL, allowing for interfacialⁱ pre-melting.^[47] In fact, the interaction of the tip with the QLL can even destroy the sample surface.

In addition, it is known that the thickness of the QLL is strongly increased by any impurities.^[26,40,41,48–50] Impurities can originate from the water itself, the surrounding air, or from the measuring probe itself, for example an AFM tip. Another problem can be the water condensing on the ice surface, which can lead to the observation of two different types of coexisting QLLs.^[51–59]

Therefore, the ideal ice sample should be pure with a defined surface. To prepare the sample, it can be grown on a substrate from vapour or from a melt. On a substrate, it can nucleate either by using a supplied substrate or by particulate matter in the air.^[60]

ⁱIn this case, interfacial pre-melting describes the pre-melting between the interfaces of two solids, namely the ice and the AFM tip. Surface pre-melting is, in contrast, the pre-melting of the ice/vapour interface.

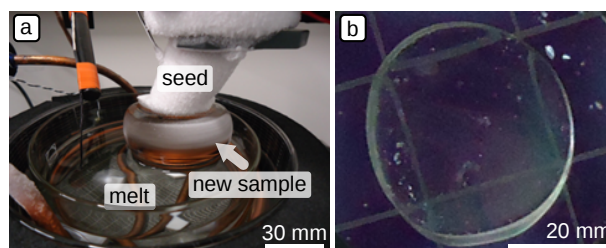


Fig. 1.5: Single-crystalline ice. (a) Picture of the experimental ice-growing machine showing the seed and supercooled melt. (b) Ice between two crossed polarisers: only one big domain is observed in the single-crystalline sample.^[1]

This approach has the disadvantage of resulting in changes in the ice structure due to the templating effect of the substrate.^j If the ice sample is grown from the melt instead, the macroscopic sample has a random crystal orientation.^[60,63] Apart from that, the stable ice/water interface is not the basal face of hexagonal type ice in case of, for example, the case of the ice/air interface. Instead, it consists of pyramidal or prismatic faces.^[60,64] These difficulties can be overcome by a series of elaborate procedures (Figures 1.5 and 1.6).^{k[65]} Nevertheless, the sample surface remains fairly rough and is far from atomically flat, independent of the preparation method.^[47]

In addition, the nature of the QLL has not yet been resolved. Some reports suggest that it is not identical to liquid water, since its density is significantly higher than that of bulk water.^[66] Others claim that the QLL is just like ordinary water^[67] or a combination of liquid water and solid ice^[39]. It becomes apparent that the task to find criteria for the differentiation between the two states is challenging. A major difference between liquid and solid water is the structure of the hydrogen bonding network. One approach for probing the hydrogen bonding network at the surface is surface-sensitive optical spectroscopy, such as vibrational sum-frequency-generation spectroscopy (SFG) spectroscopy.

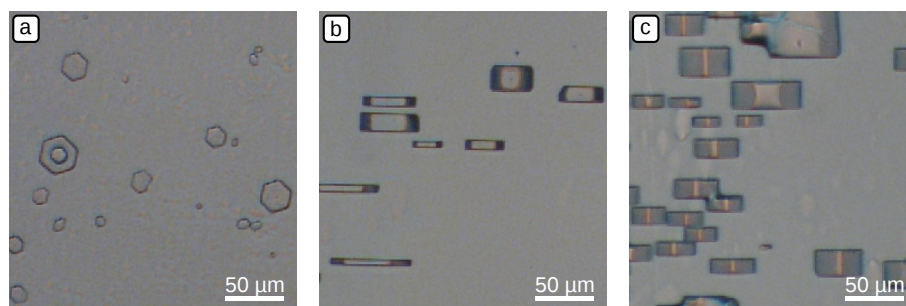


Fig. 1.6: Images of the (a) basal, (b) primary prismatic, and (c) secondary prismatic plane after Formvar etching to determine the orientation of the grown crystal.^[1]

^jBaF₂ for instance is templating an oxygen lattice that is matching the ice one, but the hydrogen one is different. Due to the negatively charged fluoride ion the whole proton configuration is changed resulting in a hydrophobic surface.^[60–62]

^kMore details about the experimental growing process can be found in [1, 65].

It measures the vibrational response of those parts of a system, where the centrosymmetric geometry is broken, for example at the ice/vapour and at the ice/QLL interfaces. SFG spectroscopy can even be used to investigate properties of a system on a molecular level, such as the average orientation of water molecules at the surface. However, the interpretation of the spectra is fairly complicated and the exact thickness of the probed layer still remains unknown.^[69]

Furthermore, the interface between the QLL and the solid ice might not be as sharp as depicted in Figure 1.3 (e). Surface-sensitive vibrational SFG spectroscopy experiments^[70], proton channelling^[30], and grazing angle-X-ray studies^[71] all detect an inhomogeneous behaviour of the QLL perpendicular to the air/ice interface, which points towards a gradual change of the QLL perpendicular to the surface.^[26]

All of the above mentioned reasons readily explain the diversity of onset temperatures for the existence of a QLL found in literature.

Facing severe problems with sample preparation and the interpretation of experimental data, it almost seems like a natural alternative to perform computer simulations of the ice/vapour interface. In such simulations, a well-defined system can be set up, monitored, and studied at a defined temperature. Apart from that, experimental results such as optical spectra can be simulated and molecular contributions identified. Furthermore, the probing depth can be easily varied in simulations and its influence on the measured quantities such as spectra investigated. In this way, it is also possible to systematically quantify the influence of defects, step-edges and solutes to name a few.

1.2.2 Theory and simulations

Simulations start with a slab of proton-disordered hexagonal ice possessing a well-defined surface exposed to vacuum. With time, the system starts to melt at the surface. Therefore, a method allowing the system to evolve in time is necessary and, thus, the ice surface is usually computed using molecular dynamics (MD) simulations. MD simulations calculate the time-dependent behaviour of a molecular system by integrating Newton's equations of motion and propagating the system in time and space.

Three main flavours of MD exist for different levels of detail (Figure 1.7). For longer time scales and larger system sizes, the level of detail needs to be reduced. The major difference between all of these methods is the calculation of the force. Ab-initio MD (AIMD) simulations calculate the force using quantum mechanics by taking the electrons explicitly into account.^[72] Classical MD simulations, on the other hand, use an empirical force-field to describe interactions between the atoms instead of solving the electronical Schrödinger equation.^[73]

¹In addition, the system can be influenced by laser heating and surface roughening.^[68,69]

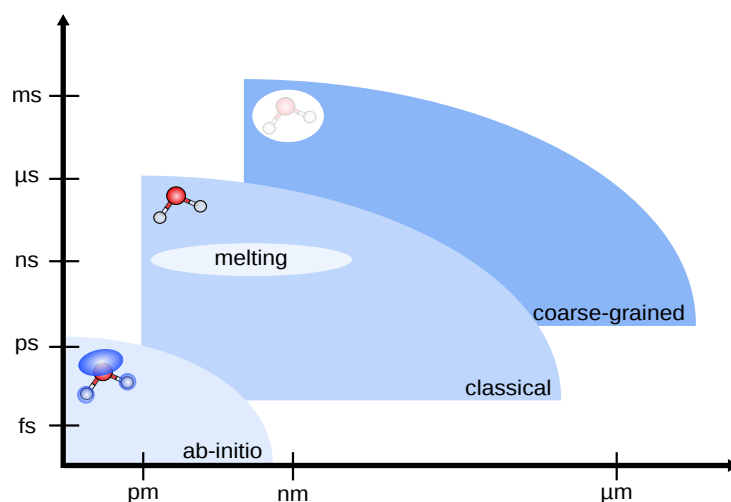


Fig. 1.7: Time and spatial resolution of the main molecular dynamics (MD) simulation methods. Ab-initio MD simulates up to several picoseconds (ps) and few nanometers (nm), classical MD up to few microseconds (μ s) and hundreds of nanometers (nm) and coarse-grained MD up to a few milliseconds (ms) and over one micrometer (μ m).

In a coarse-grained MD approach, atoms are no longer explicitly represented and beads are used instead to represent a group of atoms.^[74] In case of water, one unit could be used to represent a whole water molecule.

To cut a long story short, the difference among the three different MD simulations are the degrees of freedom included explicitly. AIMD includes atoms and electrons, classical MD only atoms and coarse-grained MD coarse-grained molecules. Since the QLL forms in simulations of several nanoseconds (ns), the method of choice is classical MD simulations. In other words, the melting process is too slow to be simulated by purely AIMD simulations. For simulations close to the melting point, the formation of the QLL takes far more time due its increased thickness. Thus, only coarse-grained MD simulations can be employed in this case. These, however, show larger fluctuations in thickness of the disordered interface, which increases its thickness by about 2 nm within 50 ns.^[75,76] In case a higher resolution is needed, a so-called top-down multi-scale approach can be chosen. In this approach, the ice sample is, for instance, first equilibrated with classical MD simulations and the molten sample is then used as input for AIMD simulations.

For classical MD simulations, the crucial parameters are the choice of the force-field, the simulation time and the sample size.^m

The selected force-field has to reproduce the physics of the system and account for any quantum effects.^[78] To evaluate a force-field for ice, the melting point needs to be known and the phase diagram needs to match accordingly.ⁿ This last point is of great

^mIn addition, the proper ice needs to be selected. Notably, some early simulations used proton-ordered ice (ice *XI*) instead of ice *I_h*.^[77]

ⁿThe estimated uncertainties of the melting temperatures of the models are roughly ± 2 K.

importance, because a high-pressure rhombohedral ice polymorph, ice II, is found to be more stable than ice I_h for many popular force-fields, although their melting point agrees well with the experimental one.^{o[79]} No water model is perfect or universally accepted. Still, the results can be mapped back to those of real ice if the water model is evaluated properly.^[80,81]

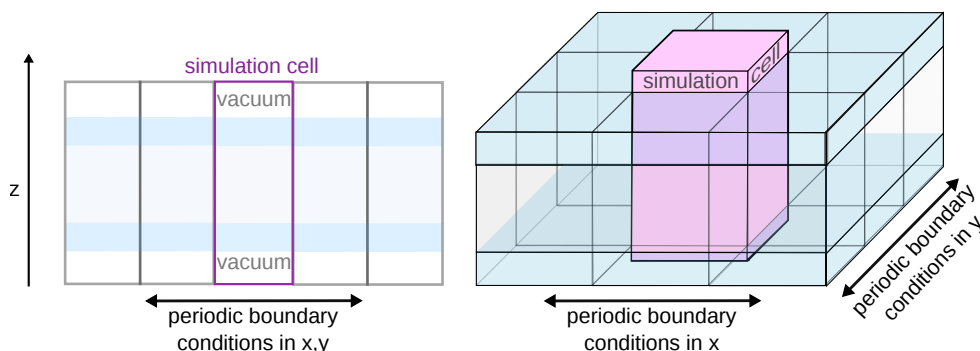


Fig. 1.8: Periodic boundary conditions in lateral directions.

Since the number of molecules which can be simulated is limited for practical reasons, the size of the simulation cell is limited, too. A sample thickness of approximately 10 nm is possible with classical MD simulations, corresponding to thousands of water molecules. Similar size restrictions limit the sample size in the lateral direction. Periodic boundary conditions are applied to circumvent such lateral limitations (Figure 1.8). Yet, local melting and rough surfaces are difficult to simulate due to the periodicities. Coarse-grained MD simulations can, however, simulate larger cells. Recently, coarse-grained MD simulations with thicknesses up to 16 nm have been performed.^[76,82]

The third limitation is the simulation time. It needs to allow for the formation of the QLL as well as further equilibration of the system. The time scale is also important for monitoring processes such as that of diffusion. The system is usually simulated for tens of nanoseconds with classical MD. The upper limit is a few microseconds.

The output of a classical MD simulation is a trajectory containing all kinds of information, such as the positions and the velocities of each atom. Hence, a good post-processing is as important as the simulation itself. It is difficult to extract a property, such as the degree of liquidity, from a trajectory. A variety of structural and dynamical parameters have been applied to analyse the ice surface, such as density profiles, manifold order parameters, radial distribution functions, and diffusion coefficients. From the assumption of ergodicity one can assume that the trajectory, if long enough, samples sufficiently well the phase space of the corresponding thermodynamic ensemble. Thus, one can get

^oThis is the case for the TIP3P, SPC, SPC/E and TIP5P models to name a few. More details can be found in Chapter 2.

meaningful thermodynamic averages from a well converged MD simulation and, using the fluctuation-dissipation theorem, also response functions.

The full bilayer-terminated ice bulk was found to be more stable than a half bilayer-terminated upper bilayer.^{p[83,84]} All simulations demonstrate that a disordered layer develops spontaneously at the free surface of ice at temperatures far below the melting point. This has been observed for a variety of water models and surfaces.^[16,26,76,85–88] The onset temperature for disorder depends on the simulated surface. For the basal plane, the first signs of disorder occur earlier than for the primary prismatic plane.^[42] Consequently, the thickness of the QLL at a certain temperature varies for the different surfaces. The QLL on the basal plane is found to be slightly thicker than on the prismatic surfaces, as it can also be observed in some experiments.^[26,42,88]

At low temperatures prior to pre-melting, disorder is characterised by the formation of a mixture of mainly five-, six- and seven-membered rings of water molecules at the surface.^{q[14–16]} Apart from that, the preferred arrangement of the water molecules at the outer layer has been found to be with the oxygen atoms pointing outwards and the hydrogen atoms pointing inwards, which is the opposite of what has been found for the water/vapour interface.^[14,89] Consequently, the underlying ice surface might cause a templating effect for the above QLL. In simulations based on the TIP4P/Ice model, the highest thickness has been obtained for the basal plane (Figure 1.4 (m)), while for the secondary prismatic plane (Figure 1.4 (o)) the lowest thickness of the disordered interface has been found.^[42] The thickness of the primary prismatic plane (Figure 1.4 (n)) has been assigned to be intermediate.^{r[42]} In addition, it is known that the surface curvature has a strong effect on the QLL. A recent MD study applying the TIP5P-E Model^{s[91]} found the melting temperature to decrease with increasing curvature.^{t[92]} Interestingly, this study reveals that the secondary prismatic/vapour interface converts spontaneously to the primary prismatic/vapour interface in few hundred of picoseconds.^[92]

In general, classical MD simulations provide a far thinner thickness than most experi-

^pIf a bulk is cleaved as indicated in Figure 1.3 (a), a cleaving plane has to be chosen. In case of the basal plane of hexagonal ice, there are two possibilities. Either the cleaving plane is between two bilayers or within one bilayer, which results in a half bilayer-terminated slab. For the simulation, it is important to know which cleaving plane is more stable and, hence, more likely.

^qBoth cited simulations use the TIP4P-model with a melting point of 230 K and short simulation times. Nonetheless, the low temperatures may still be valuable if being calibrated using the melting point of the model. A detailed ring analysis studying the surface rearrangement is presented in Section 4.4.

^rHowever, their results depend on a debatable criterion for distinguishing between QLL and crystal. In fact the choice of the order parameter is critical^[90] (Chapter 5).

^sThe TIP5P-E model is based on the TIP5P model and includes proper long-range electrostatic interactions. It reproduces the experimental melting point well, but its phase diagram is, to the best knowledge of the author, not fully known. It is only known that simply adding long-range interactions does not overcome the general problems of a model. Since TIP5P predicts ice II as the most thermodynamic stable phase and ice I_h is found to be metastable at ambient conditions, it should be taken with care.

^tAlso known as the Gibbs-Thomson effect.

ments (Figure 1.4). The thicker QLL in experiments is readily explained by the presence of impurities in the ice samples, interfacial-melting between grain boundaries in polycrystalline samples, and the presence of defects.

Apart from that, the dynamics of water molecules located in the top two to three bilayers of the basal surface differ from those deeper in the bulk. A rapid exchange between the bilayers occurs, which is far larger than deeper in the bulk. Activation energies of in-plane diffusion have been determined which are equivalent to the amount of energy needed to break a hydrogen bond.^[16] An in-plane diffusion mechanism has been identified^[16] as displayed in Figure 1.9. Molecules first need to jump in a vertical diffusion to the above bilayer before they can continue to diffuse in a lateral direction. In contrast to the rapid exchange, the bilayers statically still appear to be like 'normal' ice.

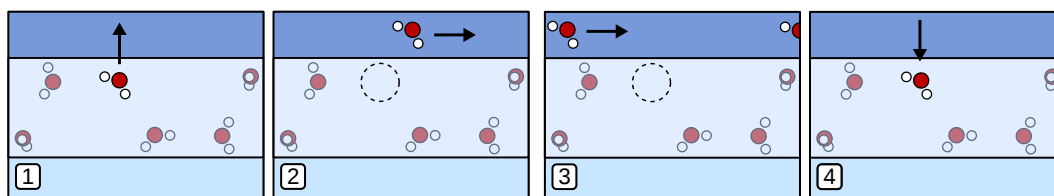


Fig. 1.9: Parking lot mechanism of the in-plane diffusion. Molecules need to jump in a vertical direction to the next bilayer where they can continue to diffuse in a lateral direction.

Various order parameters have been used to characterise the amount of disorder in a surface. A good set of order parameters already exists to distinguish between hexagonal ice and liquid water.^[90] However, those order parameters are not transferable to the ice/vapour interface. Merely superimposing the order parameters for the liquid and solid references to obtain information about the amount of liquid molecules in the ice/vapour interface turned out to be difficult. The same holds true for assigning molecules as liquid or solid based on a cut-off.^u Yet, roughness analysis based on such an assignment has been performed yielding a fairly rough interface between the QLL and bulk ice.^[82,93] Nonetheless, while this approach works well for nucleation analysis, we think that it overestimates the roughness. So far, it is not clear which order parameter is ideal for analysing the ice surface.

Classical MD simulations, which often use rigid models, prohibit intra-molecular vibrations, which contribute to the dynamics of the hydrogen bonding network. Hence, for simulating optical spectra, either flexible force-fields or a top-down approach should be chosen. In general, ab-initio MD simulations reproduced optical spectra very well and provided a valuable, and sometimes indispensable, molecular-scale interpretation of the

^uMore details will follow in Chapter 5.

experimental results. For liquid water, a detailed interpretation of the complex shape and features of the IR stretching band is available which singles out the contribution from intermolecular and intramolecular interactions and the effects of the local hydrogen bonding structure.^[94–96] For the water/air interface, a detailed analysis mapping the dipole orientation of the interfacial water molecules to the assignment in vibrational SFG spectra exists.^[97] In addition, it has been revealed that the intermolecular vibrational couplings induced a red shift in the OH stretch response, while the intramolecular coupling generated a double-peak feature in the OH stretching mode in the SFG spectra.^[98]

In summary, the onset temperature of pre-melting and the temperature-dependent thickness of the disordered layer or QLL are controversial, even for the simplest case of defect-free single-crystalline ice. The reasons for this controversy are experimental limitations and difficulties to distinguish between disorder and the degree of liquidity. These issues need to be clarified and thoroughly understood before moving on to study more complex systems, such as systems including defects, step-edges, solutes, and polycrystalline samples.

1.3 Outline of the thesis

In this work, the surface of hexagonal ice is investigated by applying classical molecular dynamics simulations employing the force-field TIP4P/Ice. In post-processing, we differentiate between static disorder analysis describing surface rearrangements and loss of structure on the one hand and dynamical analysis, such as the calculation of diffusion coefficients, on the other hand.

A methodological introduction and computational details are given in Chapter 2. In Chapter 3, we take a look at static structure in terms of density profiles, two-dimensional density maps and radial distribution functions to investigate how far disorder propagates into the bulk and to monitor temperature-dependent changes. The density profiles allow for a layer-resolved analysis in the forthcoming chapters.

A key feature in water/ice systems is hydrogen bonding and Chapter 4 analyses the hydrogen bonding situation at the ice surface both statically and dynamically. In addition, a topological network analysis of the hydrogen-bonded rings is presented. Another approach for quantifying order is to evaluate the first coordination shell with order parameters. In Chapter 5, several order parameters are compared and all surfaces are analysed using local Steinhardt order parameters. The results are especially interesting in combination with diffusion analysis, since a liquid-like structure does not necessarily imply true liquid-like behaviour. In Chapter 6, self-diffusion coefficients and diffusion barriers are determined and compared to liquid water references.

Methods

In this chapter, the basic principles of classical molecular dynamics simulations are discussed. Computational details and the simulated systems are provided as well.

2.1 Classical molecular dynamics

In classical molecular dynamics (MD) simulations, electrons are not explicitly taken into account. Instead, atoms are treated as point charges and any interactions between them are modelled by empirical force-fields. A crucial factor in each classical MD simulation is the choice of the force-field, which is usually adapted according to experimental data or based on ab-initio molecular dynamics. The force-field is meant to reproduce special features such as the melting temperature.

In classical MD, the system starts from an initial set of positions and momenta and evolves by integrating Newton's equations of motion (EOMs). The trajectory, if sufficiently long, samples the phase space of the corresponding thermodynamic ensemble according to the assumption of ergodicity. In other words, the long time averages are equal to the statical ensemble averages in a well converged MD simulation.

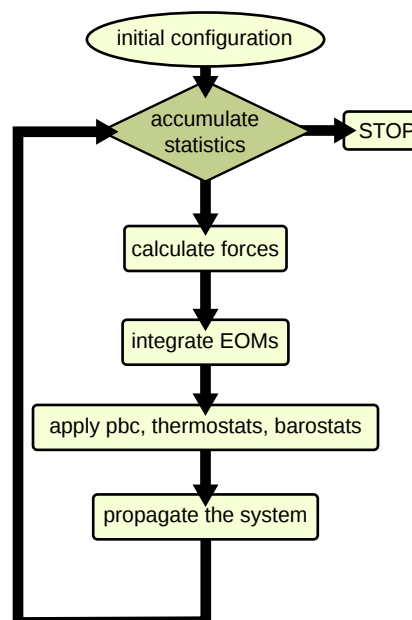


Fig. 2.1: Flowchart of a classical MD simulation.

An overview of the basic steps in a classical MD simulation are depicted in Figure 2.1. Several aspects of these are discussed in the following.^a

^aA detailed explanation can be found elsewhere.^[73,99,100]

An N -particle system with an initial set of $3N$ -dimensional vectors of position \mathbf{q} and momenta \mathbf{p} can be described by the Hamiltonian:

$$H(\mathbf{p}^N, \mathbf{q}^N) = K(\mathbf{p}^N) + V(\mathbf{q}^N) = \sum_{i=1}^N \frac{\mathbf{p}_i^2}{2m_i} + V(\mathbf{q}^N), \quad (2.1)$$

where m_i refers to the mass of particle i and the Hamiltonian equals to the sum of the kinetic energy $K(\mathbf{p}^N)$ and the potential energy $V(\mathbf{q}^N)$.

The system can be evolved through a $6N$ -dimensional phase space by solving the EOMs associated with each coordinate:

$$\frac{d\mathbf{q}_i}{dt} = \frac{\partial H}{\partial \mathbf{p}_i} = \frac{\mathbf{p}_i}{m}, \quad (2.2)$$

$$\frac{d\mathbf{p}_i}{dt} = -\frac{\partial H}{\partial \mathbf{q}_i} = -\nabla_{\mathbf{q}_i} V(\mathbf{q}^N). \quad (2.3)$$

Equations (2.2) and (2.3) are a system of coupled finite differences integration equations. There are many methods available for numerically integrating these step-by-step. The most commonly used integrators are from the Verlet family.^[100–102] In this work, the velocity verlet algorithm is chosen, since it is time reversible, conserves the phase space volume (symplectic), contains only low order time-derivatives^b, is easy to implement,^c and, last but not least, requires only one computationally expensive force evaluation per step in comparison to other integrators.^[100,101,104]

For the velocity verlet algorithm, positions (\mathbf{q}), velocities $\mathbf{v} = \dot{\mathbf{q}}(t)$, and forces \mathbf{f} are known at each full time step. The velocity verlet algorithm can be divided into four steps.^[100]

Step 1: Calculation of the half step velocity

$$\mathbf{v}_i(t + \frac{1}{2}\Delta t) = \mathbf{v}_i(t) + \frac{1}{2}\Delta t \frac{\mathbf{f}_i(t)}{m}. \quad (2.4)$$

Step 2: Calculation of the full time step position

$$\mathbf{q}_i(t + \Delta t) = \mathbf{q}_i(t) + \Delta t \cdot \mathbf{v}_i(t + \frac{1}{2}\Delta t). \quad (2.5)$$

Step 3: Update of the force $\mathbf{f}_i(t + \Delta t)$ using the full time step position

$$\mathbf{f}_i(t + \Delta t) = -\nabla_{\mathbf{q}_i} V(\mathbf{q}^N(t + \Delta t)). \quad (2.6)$$

^bIt only relies on velocities and positions at time t and, thus, allows for larger time steps.

^cIt is usually implemented via the RATTLE algorithm.^[103]

Step 4: Calculation of the full time step velocity

$$\mathbf{v}_i(t + \Delta t) = \mathbf{v}_i(t + \frac{1}{2}\Delta t) + \frac{1}{2}\Delta t \frac{\mathbf{f}_i(t + \Delta t)}{m}. \quad (2.7)$$

A microcanonical ensemble (NVE) is generated by integrating Newton's EOMs.

2.1.1 Canonical ensemble

Often MD simulations need to be performed at a specific target temperature to compare them to experiments which are conducted at a certain temperature or in order to investigate temperature-dependent properties. Therefore, the temperature of the simulated system needs to be controlled by a thermostat.^d Numerous algorithms exist to introduce thermostats in a simulation. It is interesting to note that not all thermostats give correct canonical fluctuations of the kinetic energy and volume and, thus, do not sample the canonical ensemble.^[105] In this thesis, however, a stochastic velocity-rescaling approach has been chosen, which preserves the kinetic energy and, hence, generates a well-defined ensemble.^[105] To rescale the velocities, the target kinetic energy \bar{K} is replaced by K_t , where K_t is generated by a stochastic procedure based on the canonical equilibrium distribution of the kinetic energy.^[105]

$$\bar{K}(K_t) dK_t \propto K_t^{(N_f/2-1)} \exp(-\beta K_t) dK_t. \quad (2.8)$$

The velocities are obtained after integrating the EOMs and then rescaled according to:^[105]

$$v_{\text{new}} = \alpha v_{\text{old}}, \quad \alpha = \sqrt{\frac{K_t}{K}}. \quad (2.9)$$

To overcome limitations imposed by small sample sizes, circumvent finite size effects, and avoid artefacts which arise from the boundaries of the simulation cell, periodic boundary conditions are usually applied. The simulation box is virtually replicated in all directions and particles at the boundary of the simulation cell only interact with the closest image of the cell also known as the minimum image convention. If a particle leaves the original simulation cell during a simulation, the original simulation cell can be switched to the next replica.^[73,100]

2.1.2 Molecular interactions

For the integration of the EOMs, calculations of the forces need to be performed. They are derived from a potential energy $V(\mathbf{q}^N(t))$ according to:

$$\mathbf{f}_i(t) = -\nabla_{\mathbf{q}_i} V(\mathbf{q}^N(t)). \quad (2.10)$$

^dThe temperature itself is not kept constant, but the thermodynamic average of the kinetic energy is.

Therefore, a functional of the potential energy is required. In general, the potential energy in an atomic description can be split into two contributions:

$$V(\mathbf{q}^N(t)) = V_{\text{non-bonded}}(\mathbf{q}^N(t)) + V_{\text{bonded}}(\mathbf{q}^N(t)). \quad (2.11)$$

The non-bonded part of the potential energy $V_{\text{non-bonded}}$ originates mainly from inter-molecular interactions and is usually split into n -body terms, $n = 1, 2, 3, \dots$:

$$V_{\text{non-bonded}}(\mathbf{q}^N) = \sum_i V(\mathbf{q}_i) + \sum_i \sum_{j>i} V(\mathbf{q}_i, \mathbf{q}_j) + \dots \quad (2.12)$$

The first term $\sum_i V(\mathbf{q}_i)$ arises from an external potential field, which is usually neglected for fully periodic bulk system simulations.^e In addition, any contributions higher than two-body interactions are also neglected. Therefore, the remaining non-bonded interactions $V_{\text{non-bonded}}(\mathbf{q}_i)$ are equivalent to the pairwise potential $V(\mathbf{q}_{ij})$, which is the sum of V_{LJ} (accounting for repulsion and van der Waals forces) and V_{Coulomb} (accounting for all electrostatic interactions in the system):^[100]

$$V_{\text{non-bonded}}(\mathbf{q}^N) = \sum_i \sum_{j>i} V(\mathbf{q}_i, \mathbf{q}_j) = \sum_i \sum_{j>i} V(\mathbf{q}_{ij}) = V_{\text{LJ}} + V_{\text{Coulomb}}, \quad (2.13)$$

with $r_{ij} = |\mathbf{q}_i - \mathbf{q}_j|$. The individual contributions are equal to

$$V_{\text{LJ}}(r) = 4\epsilon \left[\left(\frac{\sigma}{r} \right)^{12} - \left(\frac{\sigma}{r} \right)^6 \right], \quad (2.14)$$

where σ refers to the diameter and ϵ to the well depth and

$$V_{\text{Coulomb}}(r) = \frac{Q_1 Q_2}{4\pi\epsilon_0 r}, \quad (2.15)$$

where Q_1, Q_2 are the charges and ϵ_0 is the permittivity of free space.

While the Lennard-Jones term can be truncated due to its relatively short-range nature, the evaluation of the long-range Coulomb term is rather time-consuming and its truncation would lead to large errors in the description of the electrostatics of the simulation. Therefore, the so-called Ewald summation and variants thereof should be used.^[73,106] To demonstrate this, the $\frac{1}{r}$ term in Equation 2.15 can be divided into two parts,

$$\frac{1}{r} = \frac{\text{erfc}(ar)}{r} + \frac{\text{erf}(ar)}{r}, \quad (2.16)$$

where

$$\text{erf}(r) = \frac{2}{\pi} \int_0^r \exp(-t^2) dt \quad (2.17)$$

^eThis term is neglected in this work.

and

$$\text{erfc}(r) = 1 - \text{erf}(r) = \frac{2}{\pi} \int_r^\infty \exp(-t^2) dt. \quad (2.18)$$

Thus, a division of the Coulomb interaction into a short- and a long-range interaction is possible. The long-range interaction can easily be evaluated in reciprocal space, since large r values in real space correspond to small values in Fourier space and vice versa. In this way, any interactions of the respective charge with all of its periodic images may be included. The calculation of the long-range part in the Fourier space can further be improved by assigning all charges to a grid and performing a spline interpolation (particle-mesh Ewald (PME)).^[107,108]

The second contribution of the interactions in Equation 2.11 V_{bonded} originates from the intramolecular interactions of the atom groups which are connected through covalent bonds. They consist of linear bond-stretching (2-body), angular bending (3-body) and dihedral torsional (4-body) interactions. In principle, any functional capturing the physics of the interaction would be a possible choice. The simplest bonded potential is the harmonic potential. Another choice could be, for example, the Morse potential. For the harmonic potential, the bonded interactions can be written as:^[100]

$$\begin{aligned} V_{\text{bonded}}(\mathbf{q}^N) = & \frac{1}{2} \sum_{\text{bonds}} k_{ij}^r (r_{ij} - r_{eq})^2 + \frac{1}{2} \sum_{\text{angles}} k_{ijk}^\theta (\theta_{ijk} - \theta_{eq})^2 \\ & + \frac{1}{2} \sum_{\text{torsions}} k_{ijkl}^\phi (1 + \cos(m\phi_{ijkl} - \gamma_m)), \end{aligned} \quad (2.19)$$

where $r_{ij} = |\mathbf{q}_i - \mathbf{q}_j|$ equals to the distance between the atoms i and j , r_{eq} refers to the equilibrium density, θ_{ijk} , and ϕ_{ijkl} denote the respective angles and torsions, k_{ij}^r , k_{ijk}^θ and k_{ijkl}^ϕ are the corresponding strength parameters described by the respective force-field, m is an integer describing periodicity, and γ_m refers to the phase shift angle.^[109]

2.1.3 Constraints

In classical MD simulations, intramolecular bonds are often not explicitly included in the potential energy functions.^f Bonds could be included in a constrained way, for example by fixing the bond length. A general scheme to include constraints is based on Lagrange multipliers.^[73]

In this thesis, a rigid water model is chosen and the motion can be divided into two parts

^fThis choice might originate from the high vibration frequency of those bonds.^[73]

originating from the translational centre-of-mass motion and the rotational centre-of-mass motion.^[110] The rotational equations of motion can be written as:

$$\dot{\omega}_i = \frac{\tau_i}{I_i}, \quad (2.20)$$

where $\dot{\omega}$ refers to the angular acceleration and τ to the torque, which originates from a force acting on the molecules and I the moment of inertia.^[110] The translational and rotational sets of equations can be solved simultaneously if both force and torque on its centre-of-mass are known.^g

2.2 Selection of a force-field

2.2.1 How to choose a force-field for hexagonal ice

Given the global significance of water, a huge variety of force-fields has been applied to study water systems. To provide a number, a review article from 2002 compared almost fifty different models.^[111] This is a clear indication that none of these has performed satisfactorily over a wide range of thermodynamic conditions and that, overall, no water model is perfect or universally accepted. Therefore, the choice of a force-field is strongly dependent on the type of properties that need to be reproduced by the model.

Water models can be mostly sorted into three groups. The first group are types of rigid models, where all atom positions are fixed. Those models include only non-bonded interactions explicitly.^h The second group are flexible non-polarisable water models, which include bond stretching and angle bending. The third group consists of polarisable water models with explicit polarisation terms.

The most common group of rigid models has positive charges, which can be located at the hydrogen atoms and a second negative Lennard-Jones (LJ) interaction site. The family of models with three interaction sites such as TIP3P, SPC, and SPC/E, locate the negative charge on the oxygen atom. If the negative charge is located on the HOH-bisector, the model contains four interactions sites as for the TIP4P-family models. Models with five interaction sites, such as TIP5P, locate the the negative charge on the lone-pair-electrons of the oxygen atoms.^[112]

In this work, the surface of hexagonal ice is simulated with the goal to monitor the transition from a disordered interface to a quasi-liquid-layer at temperatures below the melting point. The selected force-field has to reproduce the physics of the system as well as to

^gImplementation details can be found in [110]. A simulation of a system with rigid bodies is not equivalent to one without any constraints, which can lead to difficulties.^[73]

^hA review about this group of water models can be found in [80].

account for any quantum effects.^[78] Thus, a good force-field needs a known melting point that resembles the experimental one and it must also match the phase diagram. In Figure 2.2, the phase diagrams and the respective melting points of common water models are depicted.

The metastable ice II is found to be more stable than ice I_h at normal pressure for the TIP5P model (Figure 2.2 (e)), the TIP3P model (Figure 2.2 (f)), and the SPC/E model (Figure 2.2 (g)).ⁱ Thus, the phase diagram is incorrect and the force-fields are inappropriate to simulate the pre-melting of the ice surface. Interestingly, TIP5P reproduces the melting point reasonable well, which illustrates the importance of a known phase diagram (instead of a melting point only). The TIP4P model seems to differ mainly in the melting point by about 40 K. The model TIP4P/2005, which was fitted to reproduce the temperature of maximum density, and the model TIP4P/Ice, which was fitted to reproduce the experimental melting point, were obtained from the TIP4P model by modifying the parameters only slightly.^j

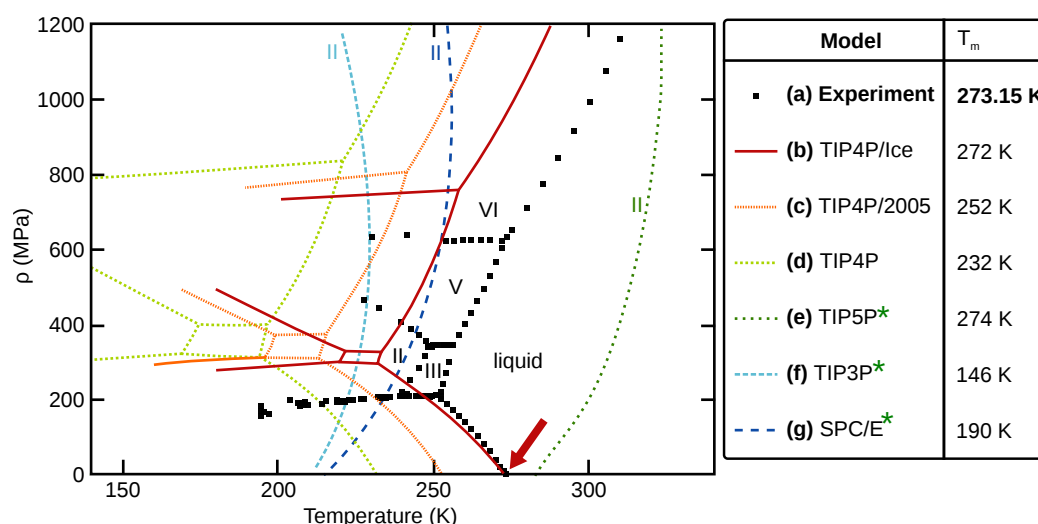


Fig. 2.2: The phase diagrams and the melting points of prominent water models in comparison to the experimental values. (a) Experiment^[113], (b) TIP4P/Ice^[114], (c) TIP4P/2005^[114], (d) TIP4P^[114], (e) TIP5P^[81], (f) TIP3P^[81], (g) SPC/E^[114]. The red arrow marks the pressure region of up to 0.1 MPa, which is of interest for the simulations. The green stars mark all models that prefer the metastable form ice II over ice I_h at ambient pressure.

It has been discovered that the ability of models to predict the phase diagram of water correctly is determined by their dipole-quadrupole force ratios.^[114] Interestingly, this ratio varies significantly between different water models.^[112,114] The ability to predict a good phase diagram depends on two properties. On the one hand, a good description

ⁱThe normal pressure region is marked with a red arrow.

^jIn addition to predicting the phase diagram reasonably well, both models are known to reproduce the densities of different ice polymorphs well.^[112]

of the solid-solid-coexistence curves in the phase diagram is needed and, on the other hand, the relative stabilities of the ice polymorphs with respect to the liquid needs to match. Both requirements are fulfilled for the TIP4P/Ice and the TIP4P/2005 model.^[112] The ability to predict the proper melting point depends strongly on the quadrupole of the water models.^[115] Interestingly, the melting temperature and the temperature of maximum density are two interdependent properties and can, thus, not be fitted separately.^[116] On top of that, the melting temperature and the enthalpy of vaporisation cannot be separated as well.^[113] Therefore, we chose the rigid TIP4P/Ice model that reproduces the experimental melting point of ice and has a phase diagram that matches the experimental one in the studied region sufficiently well.^[113]

2.2.2 The TIP4P/Ice model

Models from the family of TIPnP models are rigid planar non-polarisable n -site interaction potentials for water. The abbreviation TIPnP refers to Transferable Intermolecular Potential with n points, which rely only on non-bonded interactions.

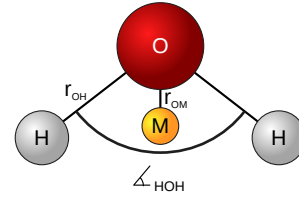


Fig. 2.3: Geometry of the TIP4P and TIP4P/Ice models.

For the TIP4P/Ice model used in this work, four interaction sites exist (Figure 2.3). Three of them are located on the oxygen and the two hydrogen atoms positions respectively and the fourth is placed on a dummy atom M . For TIP4P/Ice, r_{OH} and \angle_{HOH} are fixed to the experimental values.

The two contributions of the intermolecular pair potential are the Lennard-Jones term

$$V_{LJ} = 4\epsilon \left[\left(\frac{\sigma}{r_{OO}} \right)^{12} - \left(\frac{\sigma}{r_{OO}} \right)^6 \right] \quad (2.21)$$

and the Coulomb-Term

$$V_{\text{Coulomb}} = \frac{e^2}{4\pi\epsilon_0} \sum_{a,b} \frac{q_a q_b}{r_{ab}}, \quad (2.22)$$

where e refers to the proton charge, ϵ_0 equals to the permittivity of the vacuum, and a and b are the charged sides of molecules i and j respectively.^[113] The remaining parameters differ for TIP4P, TIP4P/2005 and TIP4P/Ice (Table 2.1). Interestingly, the oxygen sites carry no charge, but contribute to the Lennard-Jones term.^[113]

Tab. 2.1: Comparison of parameters for the TIP4P, the TIP4P/2005 and the TIP4P/Ice model.^[113,114]

Model	ϵ/κ in K	σ in Å	q_H in e	d_{OM} in Å	μ in D	Q_T in DÅ	$\frac{\mu}{Q_T}$ in Å ⁻¹
TIP4P	78.0	3.1540	0.5200	0.1500	2.177	2.147	1.014
TIP4P/2005	93.2	3.1589	0.5564	0.1546	2.305	2.297	1.004
TIP4P/Ice	106.1	3.1668	0.5897	0.1577	2.425	2.434	0.996

2.3 Simulation details and systems

Although hexagonal ice has a hexagonal crystal lattice, it is possible to use an orthorhombic unit cell.^[118] The initial slab of proton-disordered ice is created by employing a Monte-Carlo technique.^{k[119]}

The initial sizes of the periodic simulation box were $36 \text{ \AA} \times 31.18 \text{ \AA} \times 43.92 \text{ \AA}$ for the basal plane, $36 \text{ \AA} \times 46.77 \text{ \AA} \times 29.28 \text{ \AA}$ for the primary prismatic plane, and $54 \text{ \AA} \times 31.18 \text{ \AA} \times 29.28 \text{ \AA}$ for the secondary prismatic plane. Although interface properties may be strongly influenced by finite size effects, the obtained areas for the ice/vacuum interfaces were considered to be large enough. Since a buffer of about ten molecular diameters already provide reliable estimates for the surface tension for the water vapour/liquid interface, it is assumed that the same is true for the ice/vacuum interface.^[42,120,121]

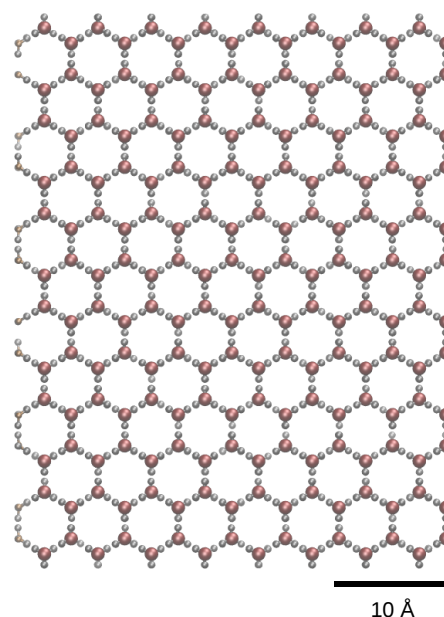


Fig. 2.4: Side view of the simulation cell for the primary prismatic plane. The picture was produced with the software VMD.^[117]

To take thermal expansion into account, we performed simulations of bulk ice in the NpT ensemble at each target temperature, which were in a range from 200 K to 270 K, at a pressure of 0 bar.^l In Table 2.2, the respective obtained slabs and their surface areas and densities are depicted for all temperatures and surfaces. We then generated a slab for each sample previously equilibrated in the NpT ensemble by introducing a vacuum layer of about 20 Å and applied a 10 ns equilibration in the NVT ensemble, in which the temperature was controlled by stochastic velocity rescaling^[105] with a coupling constant of 2 ps. Thereafter, we performed 40 ns-long production runs also in the NVT ensemble for all temperatures and surfaces but for the highest simulated temperature of the basal surface. Since the melting process propagates the furthest into the bulk for the basal surface (Chapter 6), the highest temperature was simulated for 190 ns (instead of only 40 ns). In addition to the longer simulation time, the vacuum was also extended to 100 Å. As mentioned before, the TIP4P/Ice force-field was chosen and periodic boundary conditions were applied in all three (x,y,z) directions. The equations of motion were integrated

^kSince the full bilayer-terminated ice bulk is more stable than a half bilayer-terminated upper bilayer, the former is chosen.^[83,84]

^lThe angles were kept orthogonal during this NpT simulation, such that they were not modified with respect to the original configuration. The NpT equilibration was applied for 600 ps.

with a time step of $dt = 1$ fs using the velocity verlet integrator. Ewald sums were employed to treat electrostatics in the system. The real part of the Coulombic potential was truncated at 9 \AA . Long-range electrostatic interactions were calculated using a smooth PME summation. All simulations have been conducted with the DL POLY software.^[122]

Tab. 2.2: Sizes of the simulation cells for the basal, primary prismatic, and secondary prismatic slabs obtained after the NpT simulation, its respective surface areas and its (estimated) densities without the applied vacuum. Thereupon, a vacuum of 20 \AA was added and NVT production runs were performed for 40 ns.

Basal T in K	x in \AA	y in \AA	z (+vac) in \AA	A_{surface} in \AA^2	ρ_{est} in g/cm^3
200 K	36.13	31.29	64.08	1130.33	0.92
210 K	36.14	31.29	64.09	1130.84	0.92
220 K	36.20	31.35	64.16	1134.91	0.92
230 K	36.22	31.36	64.18	1135.91	0.92
240 K	36.16	31.32	64.12	1132.41	0.92
250 K	36.25	31.39	64.23	1138.03	0.91
260 K	36.19	31.35	64.16	1134.53	0.92
270 K	36.39	31.52	144.00	1147.00	0.91
1st prism T in K	x in \AA	y (+vac) in \AA	z in \AA	A_{surface} in \AA^2	ρ_{est} in g/cm^3
200 K	36.15	66.96	29.40	1062.71	0.92
210 K	36.21	67.03	29.45	1066.15	0.92
220 K	36.14	66.94	29.39	1062.03	0.92
230 K	36.23	67.06	29.46	1067.32	0.91
240 K	36.24	67.08	29.48	1068.45	0.91
250 K	36.21	67.04	29.45	1066.59	0.92
260 K	36.19	67.01	29.43	1065.19	0.92
270 K	36.30	67.15	29.52	1071.43	0.91
2nd prism T in K	x (+vac) in \AA	y in \AA	z in \AA	A_{surface} in \AA^2	ρ_{est} in g/cm^3
200	74.27	31.33	29.43	922.08	0.92
210	74.24	31.31	29.41	920.96	0.92
220	74.29	31.35	29.44	922.74	0.92
230	74.31	31.36	29.45	923.37	0.92
240	74.28	31.34	29.43	922.49	0.92
250	74.40	31.41	29.50	926.39	0.91
260	74.43	31.42	29.51	927.39	0.91
270	74.49	31.46	29.54	929.37	0.91

A similar approach was taken for the simulation of the reference systems of bulk ice and liquid water. For the solid reference, the first step is the same as that for the simulated slabs with the only difference that no vacuum was added for the NVT simulation. For the liquid water system, a smaller system with only 480 water molecules and an initial cell

size of $22.5 \text{ \AA} \times 31.18 \text{ \AA} \times 21.96 \text{ \AA}$ was used. An NVT simulation was performed at 400 K for 400 ps to melt the initial ice sample. In a second step, the thermal relaxation (NpT) at the respective target temperatures was performed for 600 ps. All resulting cell sizes can be found in Table 2.3. In addition, a third simulation in an NVT ensemble was performed for 50 ns including 10 ns of equilibration time.

Tab. 2.3: Dimensions of the simulation cells of the solid and liquid reference samples and their respective densities obtained after the NpT simulation. Thereafter, NVT production runs were performed for 40 ns.

Solid ice	x in \AA	y in \AA	z in \AA	ρ in g/cm^3
200	36.12	46.92	29.38	0.92
210	36.19	47.01	29.43	0.92
220	36.17	46.99	29.42	0.92
230	36.19	47.01	29.44	0.92
240	36.21	47.04	29.45	0.92
250	36.16	46.98	29.41	0.92
260	36.21	47.04	29.45	0.92
270	36.27	47.12	29.50	0.91
272	36.24	47.08	29.48	0.91
Liquid water	x in \AA	y in \AA	z in \AA	ρ in g/cm^3
200	22.27	30.85	21.73	0.96
210	22.41	31.05	21.87	0.94
220	22.37	31.00	21.83	0.95
230	22.28	30.87	21.75	0.96
240	22.39	31.03	21.85	0.95
250	22.29	30.89	21.75	0.96
260	22.07	30.58	21.54	0.99
270	22.19	30.75	21.66	0.97
272	22.11	30.64	21.58	0.98
275	22.19	30.75	21.66	0.97
300	22.05	30.55	21.52	0.99

Structural analysis

Molecular simulations provide an unparalleled microscopic insight into the surface structure. On the one side, averaged structural properties, such as the radial distribution function, allow for obtaining a fingerprint of complex structures and for a direct comparison to bulk phases. On the other side, MD simulations help with the interpretation of quantities measured with, for example, scanning probe microscopy techniques or neutron scattering. This last point is crucial, because data from liquid surfaces is especially difficult to interpret.

3.1 Low-index surfaces of hexagonal ice

The three most prominent surfaces of hexagonal ice are the basal plane $\{0001\}$, the primary prismatic plane $\{10\bar{1}0\}$, and the secondary prismatic plane $\{\bar{1}2\bar{1}0\}$.^a The question of which of these is the most stable surface is, however, surprisingly difficult to answer. It has been observed in several crystal growth experiments that the secondary prismatic plane is the most predominant face at the solid/liquid interface, while the basal and primary prismatic surface dominate at the solid/vapour interface.^[123,124] This has been explained by the observation that growth at the solid/liquid interface is thermodynamically controlled, while at the solid/vapour interface it is kinetically controlled.^[123,124] The different growth characteristics of the various faces also lead to the familiar hexagonal shape of snowflakes.^[125,126] Therefore, all three surfaces are of interest, although most studies have focussed on the basal plane so far.

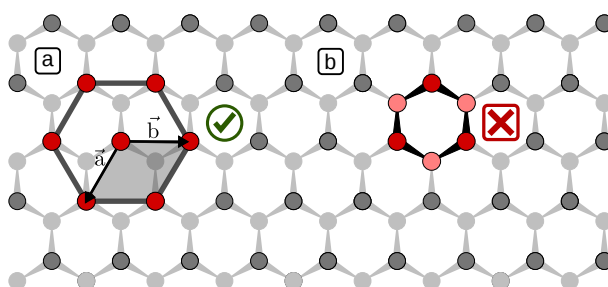


Fig. 3.1: Top view of the basal plane. The darker grey dots represent the oxygen atoms of the upper part, while the lighter grey dots represent the oxygen atoms of the lower part of the bilayer. The unit cell is illustrated in (a). If the unit cell is assigned incorrectly to the hexagon in (b), the primary and the secondary prismatic planes will be mixed up.

^aThis four index notation is called Miller-Bravais indices (Appendix 8.2).

This means that the basal and the primary prismatic planes are arranged in a bilayer structure. In contrast, the secondary prismatic plane consists of chain-like equally spaced single-layers (Figure 3.3 (c)). The different structures of the ideal surfaces lead to different melting behaviour, as we will see in the following sections.

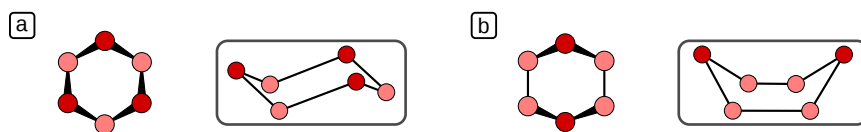


Fig. 3.4: Hexagonal arrangement of oxygen atoms for the (a) basal {0001} and (b) primary prismatic surfaces {10 $\bar{1}$ 0} of hexagonal ice. The darker circles represent the oxygen atoms of the upper part of the bilayer, while the lighter ones belong to the lower part. The two hexagons correspond to the (a) chair and (b) boat conformations similar to those created by the well-known cyclohexane ring.

3.2 Density profiles

Density profiles (Figure 3.5) are of great importance, because they show the fingerprint of the layer structure of the surface planes discussed above.^c Profiles have already been published for similar systems, but only for a narrow temperature range.^[42]

As already mentioned in the previous section, the basal and primary prismatic planes are arranged in bilayers and the secondary prismatic plane in equally spaced single-layers. The double peak in the density profiles of the basal plane slab and the primary prismatic slab is a fingerprint of the existing crystalline ice bilayers. A smearing of the double peak indicates that a bilayer is disordered and possibly molten. The outermost bilayers of the basal plane never exhibit a double peak. At the second outermost bilayers

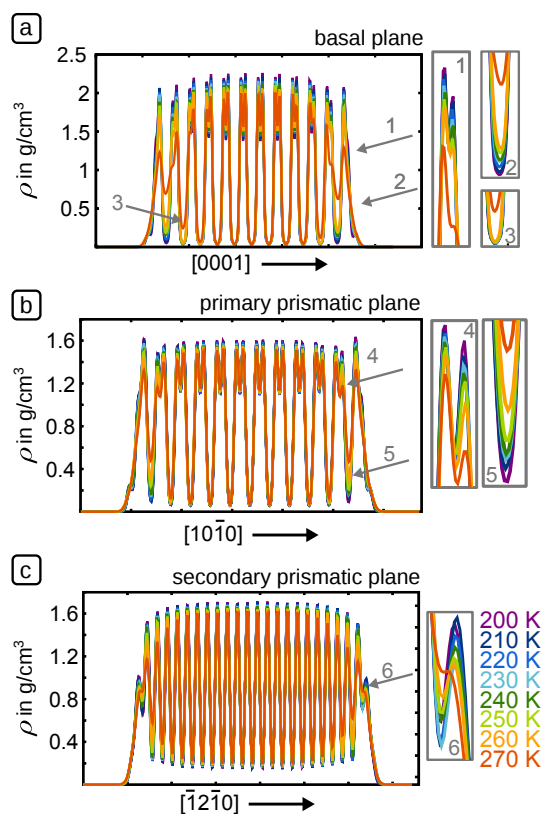


Fig. 3.5: Density profiles obtained with the TIP4P/ice model for the (a) basal, (b) primary prismatic plane, and (c) secondary prismatic plane of hexagonal ice, illustrating the bilayer and monolayer structures, respectively.

^cThe profiles in this work were computed by averaging over a 40 ns trajectory. In the case of the basal plane at 270 K, a trajectory of 190 ns was used. Each point of the profile was obtained by convoluting the instantaneous atomic positions with a normalised triangular weighting function, for snapshots taken every 10 ps of the trajectory. A triangle width of 0.105 nm was chosen for all.

of the basal plane, the double peak vanishes only at 270 K (Figure 3.5 (a) in (1)). At the same time, the minimum which separates the first and the second bilayer rises significantly, indicating intermixing among molecules in the two bilayers (Figure 3.5 (a) in (2)). This transition occurs sharply between 260 K and 270 K. For the primary prismatic plane, the bilayer feature persists even at 270 K (Figure 3.5 (b) (3)), while there is a significant difference in the minimum depth at 270 K. For the secondary prismatic slab (Figure 3.5 (c)), the ice disorder transitions seems to be less sharp. The envelope of the density profiles evolves smoothly from a rectangular shape to an ellipsoidal one with a gradual decrease of the distance between peaks and valleys from the outer layers inward (Figure 3.5 (c) (5)), which is in agreement with [42].^[1]

In general, the layer structure is well preserved throughout all simulated temperatures. Due to the symmetry of the slabs, it is reasonable to average over the left and right sides of the slabs for better statistics.

3.3 Two-dimensional density maps

In contrast to single snapshots, two-dimensional density maps visualise the time-averaged atom positions in a layer. They may be useful for a future comparison to experiments, because most imaging techniques probe time-averaged surface structures.

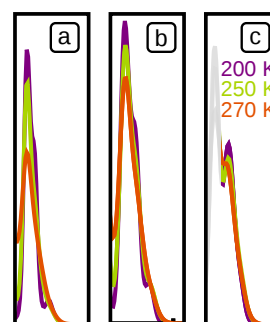


Fig. 3.6: Z-intervals for the two-dimensional density maps.

(a) First bilayer of the basal plane, (b) first bilayer of the primary prismatic plane, and (c) first single-layer of the secondary prismatic plane.

The calculation of the two-dimensional density maps is similar to the one of the density profiles in the previous section and uses a conical weighting function instead of a triangular one.^d The minima obtained from the density profiles were used to select the z-interval for the density maps (Figure 3.6). Instead of using all atoms, only the oxygen atoms belonging to one layer were analysed.

^dThe two-dimensional density maps were computed by averaging over a 40 ns trajectory of systems for snapshots taken every 10 ps. Roughly 128 oxygen atoms were analysed per bilayer for the basal and primary prismatic plane, while only 64 atoms per single-layer were analysed for the secondary prismatic plane. The colour scale in the diagrams is a measure of the probability of finding a molecule at that pixel-position (on a scale of 10^{-5} per pixel).

Two-dimensional density maps at three selected temperatures are depicted in Figure 3.7.^e They are time-averaged and, thus, not equivalent to individual snapshots.^f Nevertheless, the diffusion and movement of the surface oxygen atoms at 200 K is negligible, and, therefore, the two-dimensional density maps at 200 K are similar to single snapshots.^g Five- and seven-membered rings form at all surfaces for that temperature (Figures 3.7 (a), (d), and (g)).^h

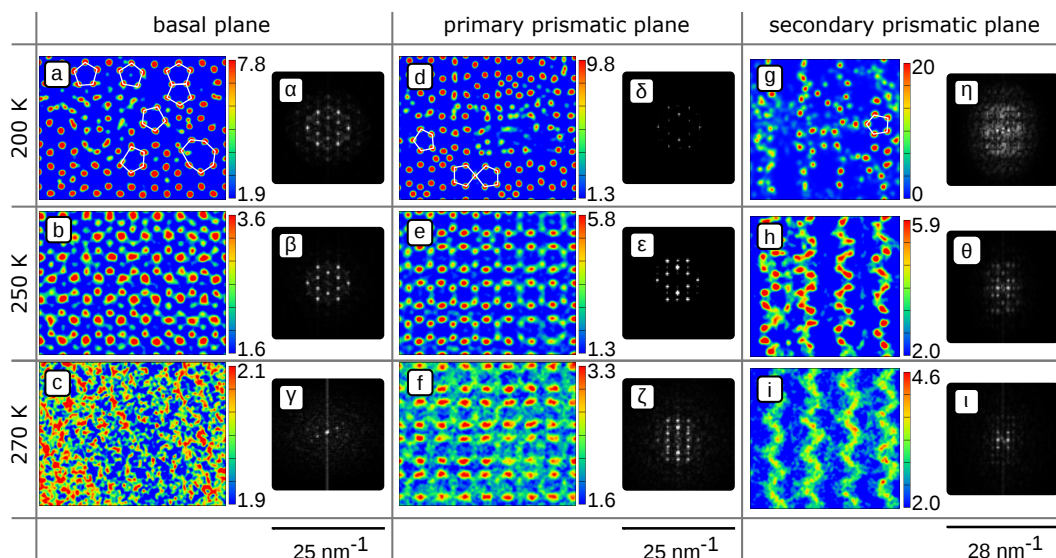


Fig. 3.7: Two-dimensional density maps of the oxygen atoms belonging to the first layer of the (a)–(c) basal, (d)–(f) primary prismatic, and (g)–(i) secondary prismatic plane at three selected temperatures. The colour scale represents the probability (in 10^{-5} per pixel) to find a single atom at a pixel. In addition, the respective FFTs of the density maps illustrate the periodicities and were obtained with the program Gwyddion.^[128]

The density maps of the basal plane in Figures 3.7 (a) and (b) display the hexagons shown in Figure 3.8 (a). It is apparent that the order at the surface is still preserved. The upper part of the bilayer (darker atoms in Figure 3.8 (a)) contains dangling bonds and is, thus, more weakly bound (see Chapter 4). Consequently, these molecules have a higher surface mobility and are less restricted to their positions.

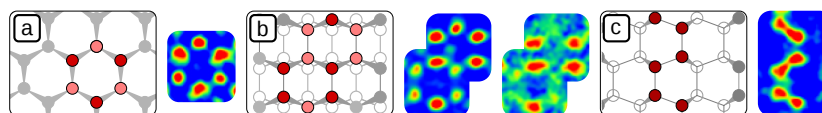


Fig. 3.8: (a) The chair conformation of oxygen atoms at the basal plane in a schematic drawing and a corresponding detail of the two-dimensional density map (Figure 3.7 (a)–(c)). (b) The boat conformation of the primary prismatic plane and details of density maps of the primary prismatic plane (Figure 3.7 (d)–(f)). The lighter dots represent the oxygen atoms belonging to the upper part of the bilayer, which are more mobile than these in the lower part. (c) Atom chains at the first single-layer of the secondary prismatic plane and the two-dimensional density maps.

^eSee Appendix Section 8.2 Figure 8.7 for all studied temperatures.

^fSimilar types of snapshots were already presented in a different context in [14] and [127].

^gThis assumption is verified in the diffusion analysis of the surface atoms in Chapter 6.

^hA detailed ring analysis can be found in Section 4.4.

When comparing the images of the primary prismatic plane to the ones of the basal plane, it seems that the regular pattern is more pronounced at the primary prismatic plane at 270 K. Furthermore, the oxygen atoms of the lower half of the bilayer in the primary prismatic plane (Figure 3.7 (f)) appear to be less mobile than the corresponding atoms of the basal plane (Figure 3.7 (c)) at the same temperature (Figures 3.8 (a) and (b)). After all, the primary prismatic surface turns out to be less disordered than the basal one.

The secondary prismatic plane (Figure 3.7 (g)–(i)) seems to be the most disordered surface at 250 K, but the order seems to increase with temperature. At first glance, this seems unexpected. However, surface layers are kinetically trapped in single disordered configurations at low temperatures, whereas at higher temperatures, when diffusion kicks in, the two-dimensional density maps reveal a pattern governed by the underlying ice structure.

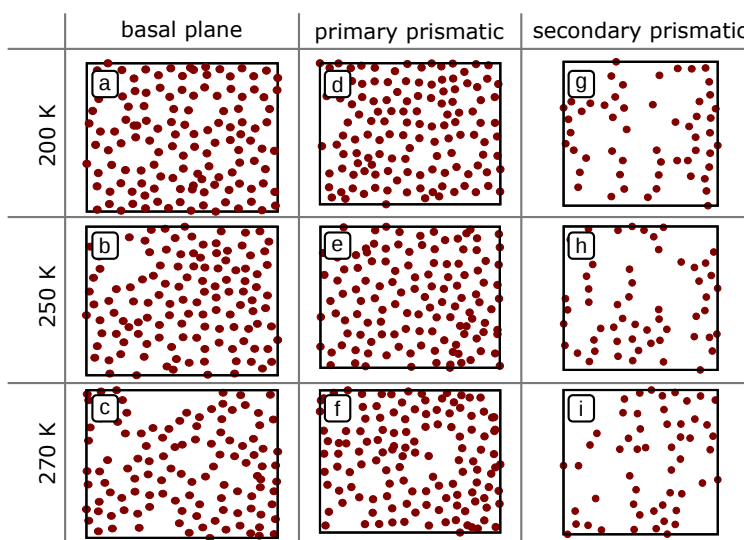


Fig. 3.9: Snapshots of the oxygen atoms of the first layers of the (a)–(c) basal plane, (d)–(f) the primary prismatic plane, and (g)–(i) the secondary prismatic plane taken at 50 ns (200 ns for 270 K at the basal plane) at three selected temperatures (200 K, 250 K, and 270 K).

Nonetheless, single snapshots are even more disordered (Figure 3.9), which is quantified, for instance, by the RDFs in the next section. This finding implies that measurement techniques averaging over several nanoseconds may detect higher order than measurements with femtosecond-resolution.

In addition, two-dimensional (fast-)Fourier transformations (FFT) of the two-dimensional density maps were computed using the program Gwyddion^[128] in order to identify periodicities even in seemingly disordered images. They yield patterns that could be compared to diffraction experiments.

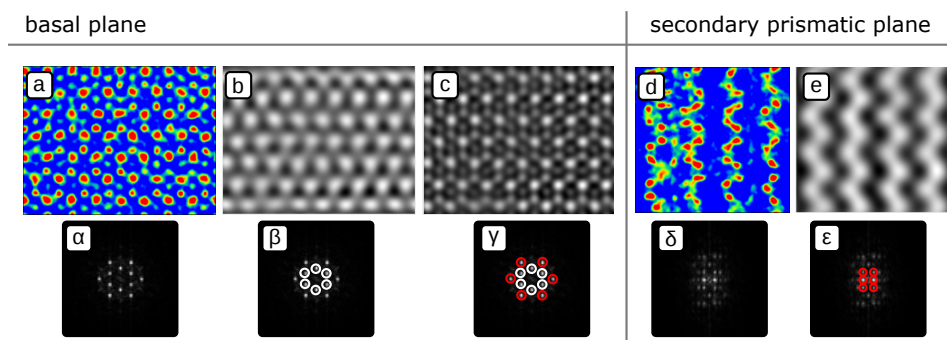


Fig. 3.10: Two-dimensional density map of the basal surface (a) and the corresponding 2D-FFT (α). The real space representations of the spots marked in (β) and (γ) are displayed in (b) and (c) (2D-FFTs of the 2D-FFTs). Likewise, a two-dimensional density map of the secondary prismatic plane and the corresponding 2D-FFT are displayed in (d) and (δ), while (e) and (ϵ) depict the structure resulting from the maxima marked with circles.

In Figure 3.10 (a), the maxima in the FFT of the basal surface are analysed separately to help with the interpretation of the two-dimensional FFTs. In 2D-FFTs a structure is basically transformed to reciprocal space using sinusoidal functions. Maxima indicate periodicities with a frequency proportional to the distance from the centre of the FFT. Therefore, maxima with larger distances from the centre of the FFT correspond to smaller periodicities in real space and vice versa. By transforming a part of the image only containing the inner maxima (white circles in Figure 3.10 (b)) back to real space (with another FFT), the hexagonal pattern formed by molecules of half of the bilayer is obtained (Figure 3.10 (b)). In combination with the outer maxima (red circles in Figure 3.10 (γ)) the complete structure is reproduced (Figure 3.10 (c)).

The same can be done for the secondary prismatic plane (Figure 3.10 (d)) to identify the structural pattern corresponding to the maxima in the FFT (Figure 3.10 (e)). The red circles in the FFT of the original image (Figure 3.10 (ϵ)) display two kinds of periodicities: the circles left and right represent the longer periodicity along the $[\bar{1}010]$ direction, while the circles at the top and bottom correspond to the zig-zag pattern along the $[0001]$ direction.ⁱ

Although little order can be observed at first glance in Figure 3.7 (c), the corresponding 2D-FFT (Figure 3.7 (γ)) reveals a hexagonal symmetry.^j Therefore, a templating effect of the underlying layer is present for all surfaces even at 270 K.

ⁱSee Appendix Section 8.2 Figure 8.8 for more details.

^jThe underlying bilayer of the basal plane at 270 K is considered to be severely disordered based on statical analysis, as will be seen in the forthcoming chapters.

3.4 Radial distribution functions

The structural properties of disordered and diffusive systems, such as glasses and liquids, can be characterised by measuring the structure factor $S(q)$ with X-ray or neutron diffraction. The same information is estimated in computer simulations by calculating radial distribution functions (RDFs), because if the structure factor is mapped back to real space by a Fourier transformation, the radial distribution function is obtained.^[113] The process to extract a radial distribution function from diffraction data is, however, not straightforward and details for experimentally determined temperature- and pressure-dependent radial distributions for liquid water and ice have been discussed in literature.^[129]

The RDF is the probability of finding another particle B at a distance r from the particle A, normalised by the overall particle density of the system ρ , such that it tends to 1 at large distance:

$$g_{AB}(r) = \frac{\langle N_{\text{shell}}(r) \rangle}{\rho_{\text{av}} V_{\text{shell}}(r)}. \quad (3.1)$$

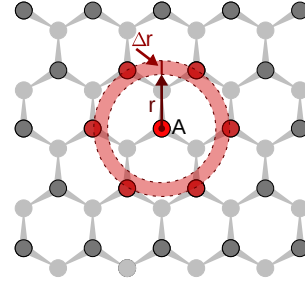


Fig. 3.11: A radial distribution function (RDF) is calculated by counting all particles B in part of a sphere shell defined by the interval $[r - \frac{\Delta r}{2}, r + \frac{\Delta r}{2}]$. The RDF is then calculated by Equation 3.1.

The RDF for a homogeneous system is calculated as a histogram of molecules per volume within a certain distance relative to the average density. The name ‘radial distribution’ function can be attributed to the fact that the studied volume depends only on the distance r and the bin-width Δr .^k The RDF calculated for liquid water with TIP4P/Ice has been known to agree reasonably well with experimental data.^[113]

The calculation of the RDFs for the pre-melting surfaces is more difficult. A method averaging over the whole system suppresses any effects from a minority of molecules at the surface. Hence, a layer-resolved analysis is performed for all surfaces. To calculate layer-resolved radial distribution functions, the spheres need to be sliced in the direction perpendicular to the surfaces of interest. Technically, this leads to a more complicated normalisation:^{l[130]}

$$g_{\text{scaled}}(r) = g_{\text{slab}}(r) / \kappa(r) \quad (3.2)$$

with

$$\kappa(r) = \frac{l_s}{\Delta z} \cdot \begin{cases} 1 - \frac{1}{2} \frac{r}{\Delta z} & \text{for } r \leq \Delta z, \\ \frac{1}{2} \frac{\Delta z}{r} & \text{for } r > \Delta z. \end{cases} \quad (3.3)$$

^kSometimes the RDF is also called a pair distribution function.

^lFor details see Appendix 8.2.3.

Here, Δz is the thickness of the layer, while l_z is the full length of the simulation box in the z -direction as determined according to Figure 3.5.^m Effectively, the layer-resolved RDFs are two-dimensional, since only the molecules within one layer are probed.ⁿ

In Figure 3.12 (a), the calculated RDFs for the bulk hexagonal ice and supercooled liquid water references are displayed for comparison. The biggest differences between those are the long-range order, the depth of the first minimum, and the number of extrema (Figure 3.12 (a)).

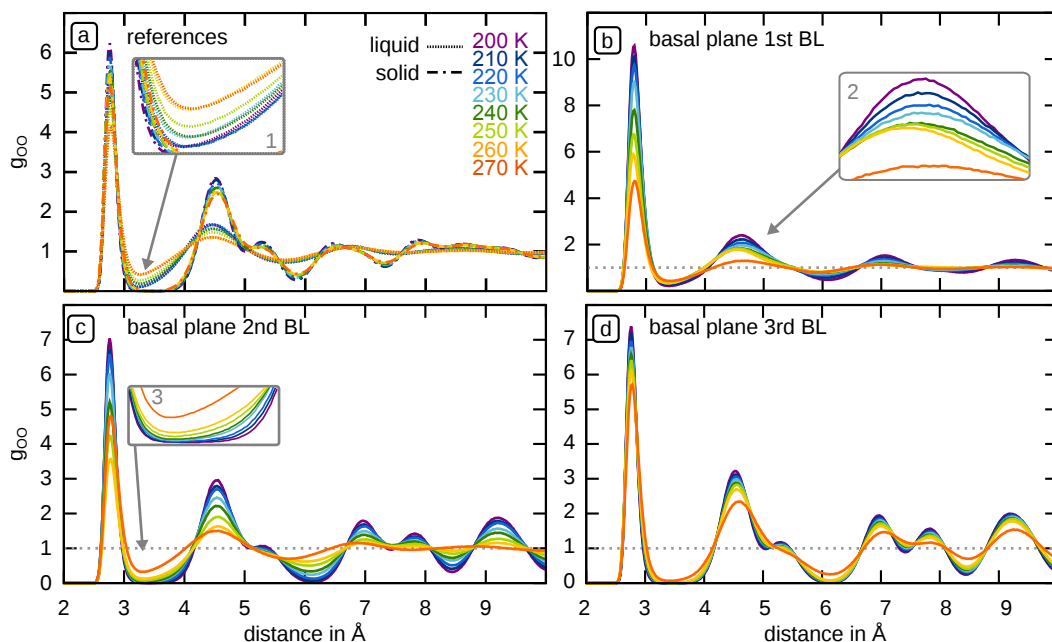


Fig. 3.12: (a) Temperature-dependent RDFs of solid ice I_h systems and liquid water. Temperature-dependent RDFs for the (b) first, (c) second, and (d) third bilayer of the basal plane of hexagonal ice.

At the first bilayer of the basal plane (Figure 3.12 (b)), the shoulder above 5 Å has already vanished at lower temperatures and the RDFs resemble rather the bulk water reference. A jump is visible between 260 K and 270 K (Figure 3.12 (b) and (c)) and this is at last the temperature where all long-range order is lost. At the second bilayer, the situation is different (Figure 3.12 (c)). While the RDFs at low temperatures resemble the solid references, they start to smear out with increasing temperature and between 260 K and 270 K the RDF becomes abruptly liquid-like. This is in agreement with X-ray diffraction measurements, where the Bragg reflection was lost in the layer close to the surface at temperatures above 271 K.^{o[44]} The third bilayer (Figure 3.12 (d)) is solid-like throughout the whole temperature range.

^mFor details see Appendix 8.2 Figure 8.9.

ⁿThe displayed RDFs were averaged over the left and right surface for each respective temperature.

^oStill, some care should be taken when comparing to the results obtained in [44], since thin ice films on a substrate were measured.

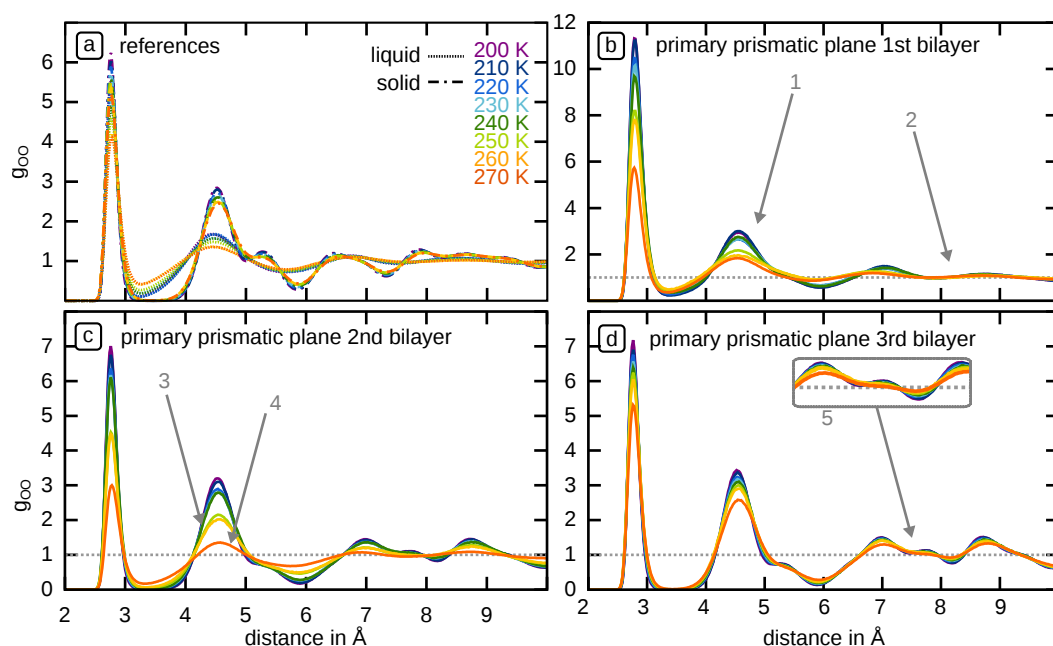


Fig. 3.13: (a) Temperature-dependent RDFs of reference ice I_h systems and liquid water. Temperature-dependent RDFs for the (b) first, (c) second, and (d) third bilayer of the primary prismatic plane of hexagonal ice.

At the primary prismatic plane, the disorder spreads less into the bulk (Figure 3.13). Yet, the first bilayer resembles the liquid reference even at low temperatures. In the second bilayer, two significant changes in peak height at the second maximum are observed: one between 240 K and 250 K (Figure 3.13 (3)) and one between 260 K and 270 K (Figure 3.13 (4)).

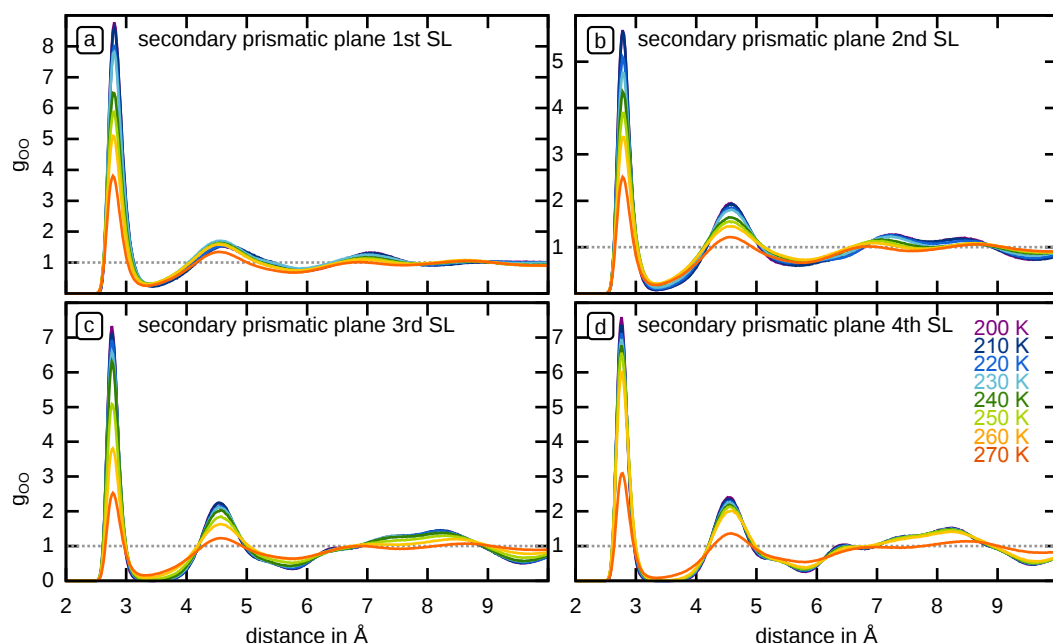


Fig. 3.14: Temperature-dependent RDFs for the (a) first, (b) second, (c) third, and (d) fourth single-layer of the secondary prismatic plane of hexagonal ice.

After the last change, no long-range order can be observed. The third bilayer is close to the ice reference throughout the entire temperature range, although it evolves to a slightly flattened function at higher temperatures.

The secondary prismatic plane is completely different due to the single-layer structure. The first layer displays little long-range order even at the lowest temperatures. The second layer appears to be slightly more ordered than the first layer and becomes very similar to the first layer at 270 K. The same holds true for the third single-layer. Only the fourth layer displays long-range order for all temperatures except for 270 K, where it approaches the liquid reference.

3.5 Conclusion

In summary, the layer structure is preserved throughout the whole temperature range and for all surfaces, as apparent in the density profiles. The profiles of the basal and primary prismatic plane change stepwise, while they evolve gradually to an ellipsoidal envelope in case of the secondary prismatic plane. This points to a layer-by-layer increase of disorder for the basal and primary prismatic plane in agreement with sum-frequency-generation spectroscopy measurements.^[1]

The outer layers rearrange and form, for instance, five-membered rings as revealed by the two-dimensional density maps. Nevertheless, a regular pattern is maintained on average even at the highest temperatures for all surfaces originating from a templating effect of the underlying layer. This templating effect is only observed on average, while single snapshots are fairly disordered. Accordingly, experiments averaging over several nanoseconds could detect more order than measurements with higher time-precision. The radial distribution functions display a significant increase in disorder between 260 K and 270 K for all surfaces. While the first bilayer is liquid-like for all temperatures, the second bilayer becomes similar to the liquid reference only at high temperatures for the basal and primary prismatic plane, where the third bilayer is always ice-like. In case of the secondary prismatic plane, the outer three single-layers are rather close to the liquid reference and only the fourth single-layer is ice-like except for 270 K. However, a dynamical analysis as performed in the next chapters is necessary to decide whether a layer is truly liquid.

Hydrogen bonding analysis

In this chapter, a layer-resolved hydrogen bonding (H-bonding) analysis of the three most prominent ice surfaces is presented. The first section of this chapter focusses on the importance of H-bonding for water/ice systems. Furthermore, the different hydrogen bond (H-bond) definitions are discussed. In Section 4.2, the geometrical descriptors and properties of H-bonding are analysed in a layer-resolved manner and a comparison between the H-bonding situation of a pre-melted ice surface versus pure ice and water is made. Eventually, the dynamical properties of H-bonding such as the rate of H-bond breaking are analysed. In Section 4.4, a ring analysis is performed to characterise the medium-range order of the H-bonding network. The influence of temperature on those topological networks are evaluated both in the bulk and at the surface.

4.1 The importance of networking

4.1.1 Importance and general definition of an H-bond

H-bonding is responsible for the high boiling point of water and, hence, H-bonds are the reason why water is a liquid at ambient conditions.^[131,132] Several H-bonds need to break for the evaporation of a single water molecule, resulting in a high heat of vaporisation, a phenomenon that enables animals to cool themselves down by the process of perspiration. Another prominent, every-day example to highlight the importance of



Fig. 4.1: Floating ice in the Weddell Sea (Antarctic). Photograph by Ursula Burgard-Kling

H-bonds is the floating of ice on water caused by the directionality of the H-bonding. This directionality presupposes a certain coordination of water molecules which results in the familiar hexagonal arrangement of hexagonal ice. In liquid water, however, the mobility of molecules is higher and the directionality of H-bonds is reduced. This last point leads to a higher density and makes the floating of ice on water possible. Along that

line, the polymorphism of ice differs from the behaviour of many other solids. When a typical crystal is exposed to a very high pressure, the coordination number increases. In the case of ice, the majority of ice polymorphs still obey the ice-rules and the tetrahedral-coordinated network is preserved.^a In general, the presence of H-bonding in water is largely responsible for the diverse variety of anomalies it can display.^[131,132] Therefore, an H-bond analysis is a good approach for the characterisation of the ice surface.

It is difficult to find a universal definition of an H-bond. The IUPAC definition states:^[134]

“The hydrogen bond is an attractive interaction between a hydrogen atom from a molecule or a molecular fragment X–H in which X is more electronegative than H, and an atom or a group of atoms in the same or a different molecule, in which there is evidence of bond formation.”^[134]

Quantum chemical calculations yield an energy of about 0.2 eV for the H-bond, which is between van der Waals interactions and covalent bonds.^[135] In contrast to van der Waals interactions, H-bonds are strongly directional. Specifically, it is known that a single individual H-bond is stronger the shorter the distance r_{HO_A} between the accepting oxygen atom and the hydrogen atom is and the closer the bonding angle is to 180° (Figure 4.2 (a)).^[134] This directionality enables H-bonds to form large networks. Interestingly, the overall strength of H-bonds does not only originate from the strength of a single H-bond, but also out of a cooperative effect, which emphasises the importance of networking for H-bonds.^[136]

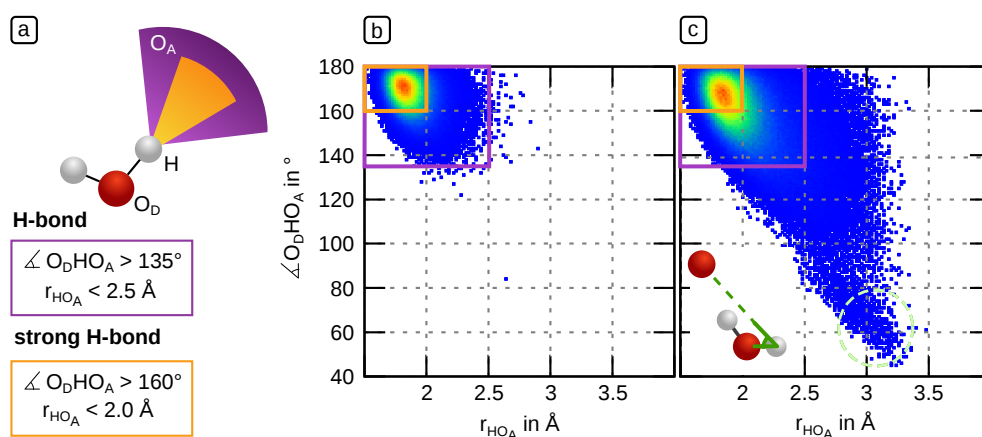


Fig. 4.2: (a) Visualisation of the selected H-bond criteria used in this work.

Distribution of angles $\angle O_D H O_A$ and distances between the hydrogen and the accepting oxygen atom for (b) the solid ice reference at 250 K and (c) the liquid water reference at 300 K. (b) and (c) display the distribution of angles $\angle O_D H O_A$ and the distances between the hydrogen atom and the next oxygen atom. Many $O_D H O_A$ -configurations of the liquid reference display an angle of 60° , which corresponds to the angle between the oxygen acceptor atoms and the neighbouring hydrogen bond, as depicted on the bottom left in Figure 4.2 (c).

^aAt very high pressures and temperatures superionic ice structures are predicted, where oxygen and hydrogen atoms separate and only oxygen atoms form a lattice.^[133]

Throughout the literature, plenty of other H-bond definitions have been suggested. These criteria can generally be categorised into two groups. The first group mainly uses geometrical criteria, while the second group uses energetic ones. It was found that the geometrical criteria are not only simpler, but also perform better.^{b[137]} In this work, an H-bond is assigned as long as the distance between the hydrogen atom and the oxygen acceptor is less than 2.5 Å and the bonding angle above 135°.^c As it is known that H-bonds are stronger the shorter the distance and the closer the angle is to 180°, a strong H-bond is defined when the angle is above 160° and the distance is less than 2 Å in order to better quantify the average bond strength. This definition is visualised in Figure 4.2 (a).

The analysis of the solid reference reveals that most of the H-bonds have an angle between 135° and 180°, while the bond length typically is less than 2.5 Å.^d This way, more than 99.9 % of all bonds are counted as H-bonds and more than 80 % of them are considered to be strong H-bonds. The liquid water reference, on the other hand, has more bonds with larger bond lengths and smaller angles and, hence, more of these bonds do not actually count as H-bonds.

4.2 Statical analysis

The amount of H-bonds is not the only property that changes during the transition from solid ice to liquid water. The average length between a hydrogen and a possible accepting oxygen atom is larger for the liquid reference, while the average angle, $\angle O_D H O_A$, is smaller (Table 4.1).

Tab. 4.1: H-bonding analysis for the solid ice reference at 250 K and the liquid water reference at 300 K.

	r_{HO_A}	$r_{O_A O_D}$	$\angle O_D H O_A$	strong H-bonds (%)	free OH (%)
Solid ice	1.86	2.79	167.9	80.66	0.03
Liquid water	1.94	2.85	161.8	49.96	5.78

Another quantity that changes during the transition is the percentage of free OH. The situation is, however, more complicated for the simulated systems with the surface exposed to vacuum. In the following, the evolution of the aforementioned parameters with temperature is analysed for the simulated ice slabs.

^bIn this work, a definition of Reference [137] was chosen. It is depicted in Figure 4.2 (a).

^cNote that all the studied H-bond definitions rely only on assumptions. In literature, some definitions exist that do not rely on any assumptions and are machine-learning based.^[138] However, for the present work and its scope the chosen definition was considered to be sufficient.

^dDetails on the solid ice and liquid water reference systems used in this work can be found in Chapter 2.

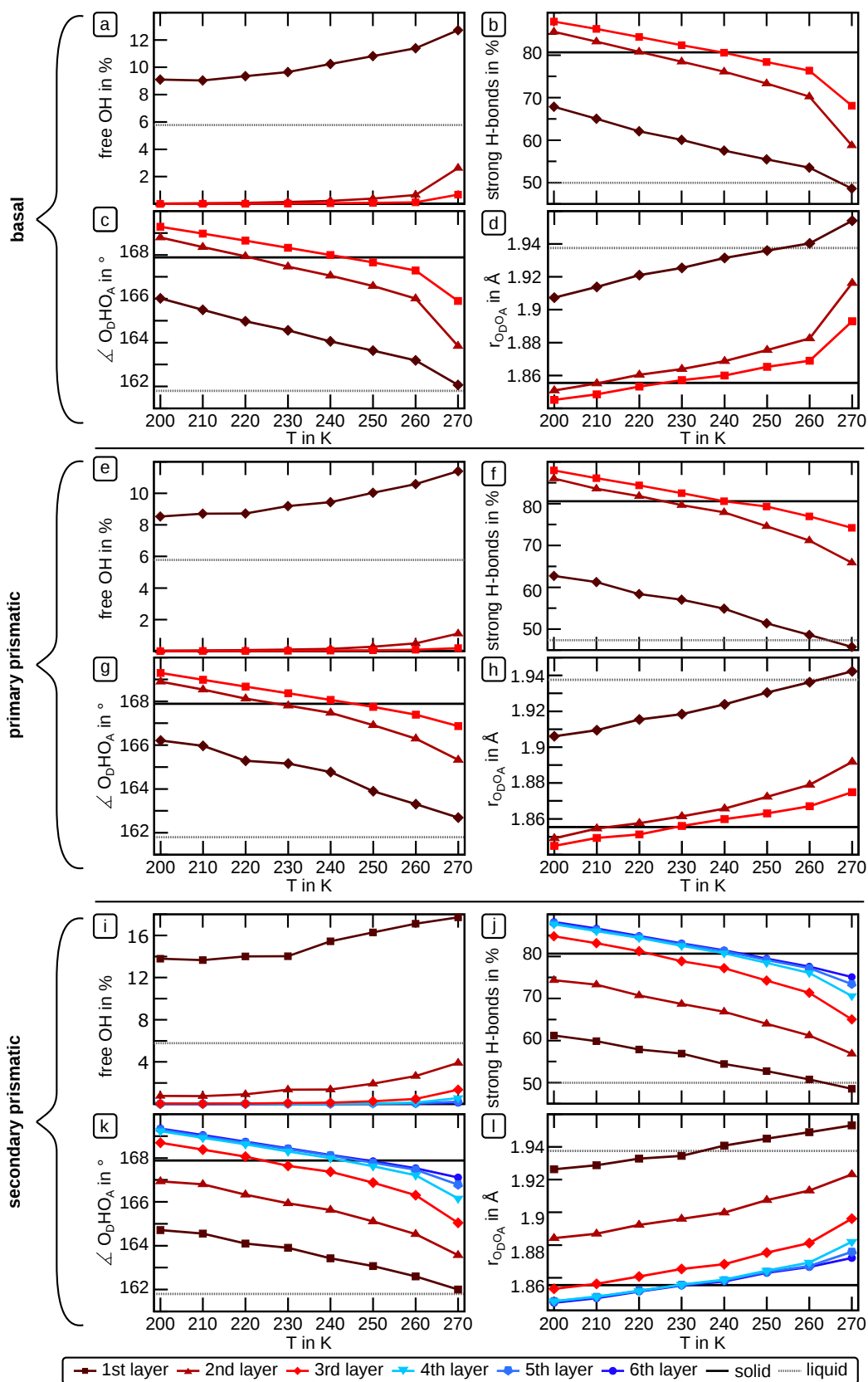


Fig. 4.3: Temperature-dependent percentage of free OH at the surface, percentage of strong H-bonds, average $\angle O_D H O_A$ -angles, and the average $r_{O_D O_A}$ of the pre-melting slabs of hexagonal ice with the three low-index surfaces exposed to vacuum for the upper three to six layers. A liquid water reference at 300 K and a bulk ice reference at 250 K are displayed.

The theoretical percentage of free OH at a perfect, non-rearranged surface in the first layer equals 12.5% for the basal plane (≈ 1.4 free OH per nm^2), 12.5 % for the primary prismatic plane (≈ 1.5 free OH per nm^2), and 25 % for the secondary prismatic plane (≈ 1.7 free OH per nm^2).^e If the molecules are allowed to move, they will change their energetically unfavourable situation and reduce the amount of free OH significantly. It is interesting to quantify the effect of surface rearrangement on the total amount of dangling bonds by comparing the theoretical percentage to the percentage of the simulated system. The amount of free OH, the amount of strong H-bonds, the average angle $\angle O_D H O_A$, and the average $r_{O_D O_A}$ for ice slabs were calculated in a layer-resolved manner for different surfaces and temperatures (Figure 4.3).^{f,g} The amount of free OH was seen to be significantly lower than the aforementioned percentages for all three surfaces at low temperatures (Figures 4.3 (a), (e) and (i)). At the secondary prismatic surface, the amount of free OH is reduced even by a factor of almost two (Figure 4.3 (i)). Accordingly, the effect of surface rearrangement is strongest for the secondary prismatic plane. The amount of free OH steadily grows with increasing temperature, which is readily explained by the rising thermal fluctuations and the related gain in free OH. However, while it increases almost linearly for the primary prismatic plane, a steeper increase can be observed for the basal plane between 260 K and 270 K (Figure 4.3 (a)). Interestingly, the amount of free OH in the first single-layer of the secondary prismatic plane starts to rise only above 230 K (Figure 4.3 (i)). The other quantities, namely strong H-bonds, average $\angle O_D H O_A$ -angles, and the average $r_{O_D O_A}$ are more similar when comparing all three surfaces.

While the amount of strong H-bonds and the average $\angle O_D H O_A$ -angle decrease with temperature, the average $r_{O_D O_A}$ increases. This trend has been observed before.^[139] All of them approach the value of the liquid reference linearly.

The only exception is a jump between 260 K and 270 K observed for the basal plane especially in the second layer. Such an abrupt change may indicate the melting of the second bilayer.^h

While almost all parameters are very close to the liquid reference at 270 K, the $r_{O_D O_A}$ of the secondary prismatic plane exceeds the value already at 240 K. Interestingly, this is the temperature, where the amount of free OH also starts to increase (Figures 4.3 (l) and (i)).

^eSee Appendix 8.3.1 for more details.

^fWe display no error bars, since all the depicted quantities depend strongly on the H-bond definition. Also, the inclusion of small statistical error bars would give the impression of a certainty, which is too high.

^gA trajectory of 40 ns (for all temperatures and surfaces except for the temperature 270 K of the basal plane, where 190 ns are evaluated) with a time step of 10 ps between the evaluated snapshots is analysed, which yields 4000 snapshots for all surfaces and temperatures (for the basal plane at 270 K 11700 snapshots were analysed).

^hSee Chapter 6 for more details.

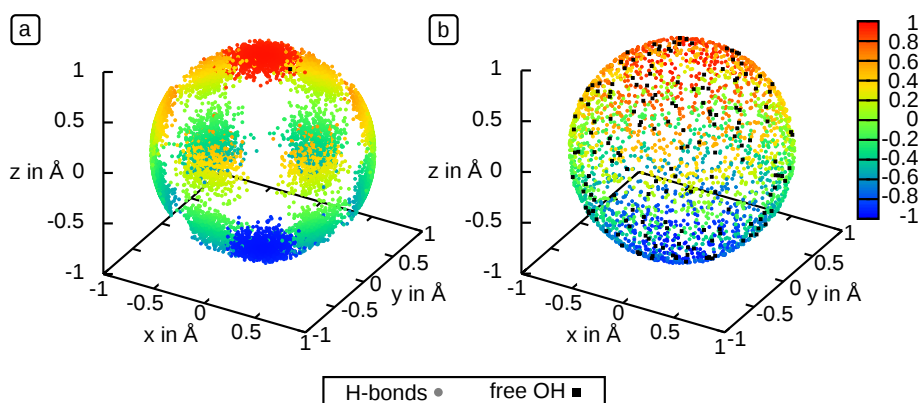


Fig. 4.4: Spherical orientation of the *OH*-vectors for (a) the bulk ice reference at 250 K and (b) the liquid reference at 300 K. The spheres were obtained by plotting *OH*-vectors of ten snapshots of a total analysed simulation time of 40 ns (one snapshot per 4 ns). The colour represents the *z*-component of the vectors, resembling the cosine of the angle since the vector length is close to one.

A powerful visualisation which allows for the distinction between an ordered arrangement (solid ice) and a more disordered one (liquid water) is the orientation of the *OH*-vector (Figure 4.4).ⁱ

The liquid reference shows some free OH with arbitrary orientation. For the solid reference, a high-symmetry arrangement can be identified when looking along the direction [0001] in the bulk, which originates from the mirrored arrangements of the bilayers. The liquid reference, however, does not show any order.

When comparing the *OH*-vectors to these of the references, it is evident that the free *OH*-vectors of the first layer point to the direction perpendicular to the surface (see Figure 4.5).^j The disorder increases gradually in the first bilayer for the basal and primary prismatic plane with temperature. While the first layer looks like a mixture of the solid and liquid reference at low temperatures, it becomes more and more similar to that of the liquid reference around the melting point.

Noteworthy is the behaviour of the second bilayer of the basal plane. At 200 K, it is similar to the ice reference and becomes more and more disordered until 260 K (Figure 4.5 (e)). While some order is still preserved at 260 K, it vanishes completely at 270 K (Figure 4.5 (h)). On the contrary, the third bilayer remains ordered throughout the entire temperature range, while the disorder increases only slightly.

ⁱIn Chapter 5, a quantitative analysis based on order is presented.

^jFor all temperatures see Appendix 8.3, Figures 8.14, 8.15 and 8.16. Ten snapshots within 40 ns of simulation time were analysed. The number of molecules in one layer is 128 for the systems with bilayer structure and 64 for the single-layers in the secondary prismatic plane.

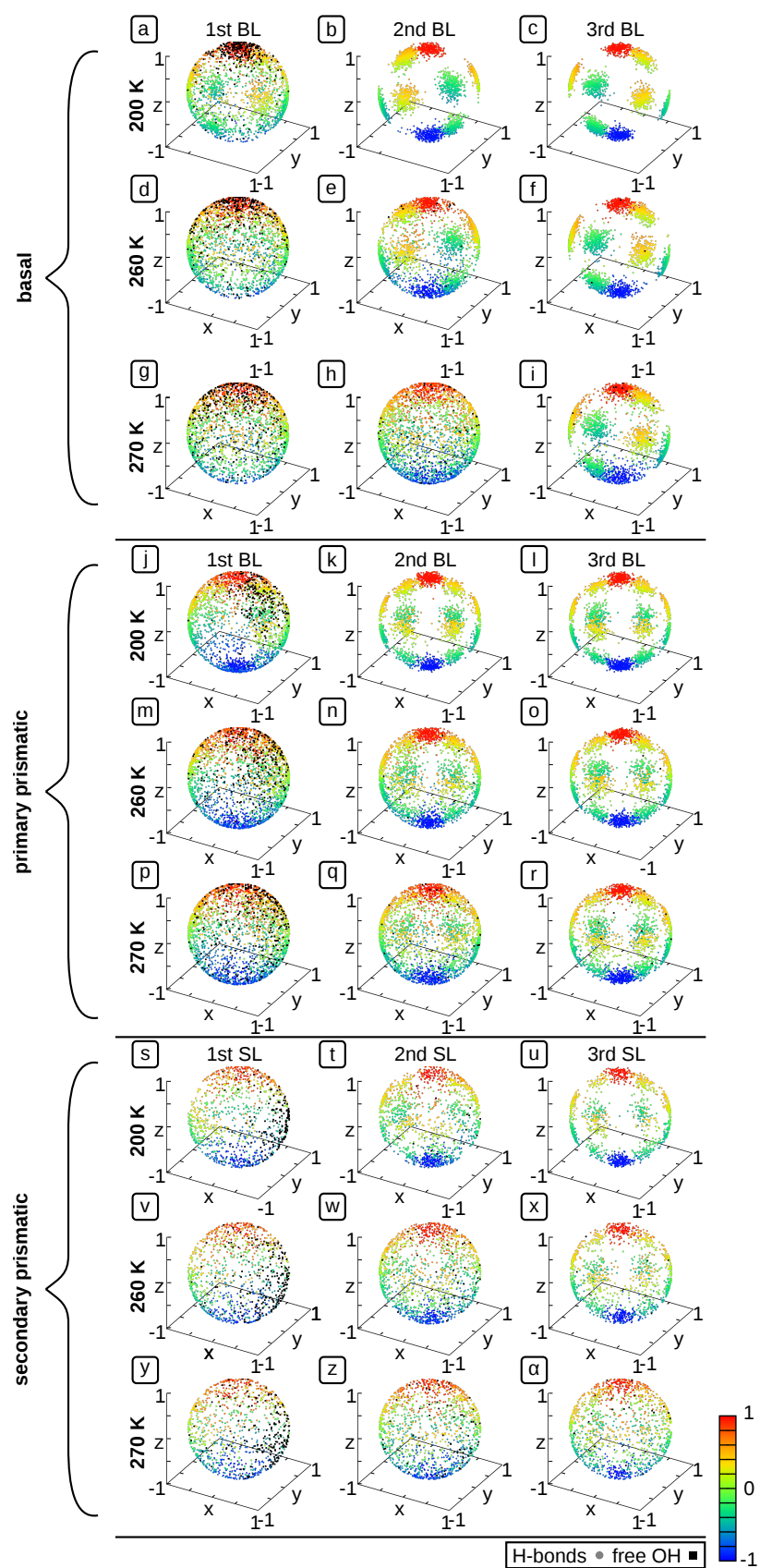


Fig. 4.5: Spherical orientation of the *OH*-vectors for the upper three layers of the three most prominent ice surfaces at three selected temperatures.

However, there is an asymmetry for the third bilayer at 270 K and one side can be observed to be more disordered than the other (Figure 4.6).^k

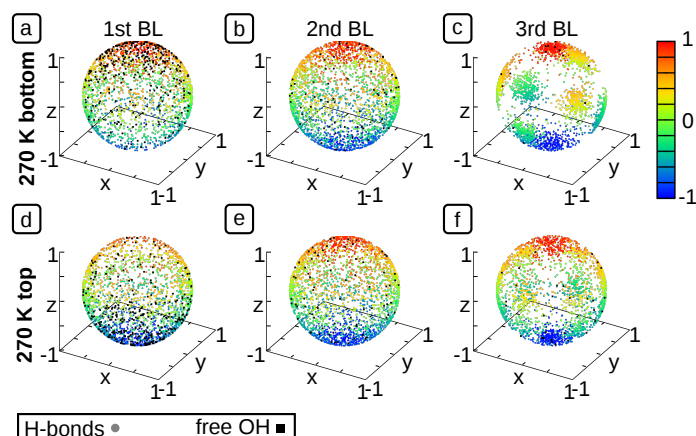


Fig. 4.6: Spherical orientation of the *OH*-vectors for the upper three bilayers of the basal plane for 270 K, comparing the top and the bottom surfaces.

One may also notice the mirrored arrangement of molecules in subsequent bilayers visible in this analysis (compare Figure 4.5 (b) and (c)). Interestingly, the second bilayer of the primary prismatic plane (Figure 4.5 (q)) looks far more ordered than the second bilayer of the basal plane at that respective temperature (Figure 4.5 (h)). The third bilayer remains ordered even at 270 K.

The situation is different for the secondary prismatic plane. While the first single-layer is completely disordered already at 200 K, the disorder in the second and third layer only rises gradually. The second single-layer is completely disordered at 270 K and the pattern of the ice structure is barely visible for the third.

4.3 Dynamical analysis

In this section, we analyse dynamical properties, such as bond breaking rates, and hence, start to examine time-dependent properties for the first time in this thesis.

An H-bond is considered broken if the bonding situation of a hydrogen atom between two consecutive snapshots of a simulation changes from an H-bond to a free OH according to the definition of the previous section. If, on the other hand, the H-bond of one atom has simply solely swapped its partner between two images, it is considered as swapped.

^kAll studied systems have been symmetrical except for the highest simulated temperature of the basal plane.

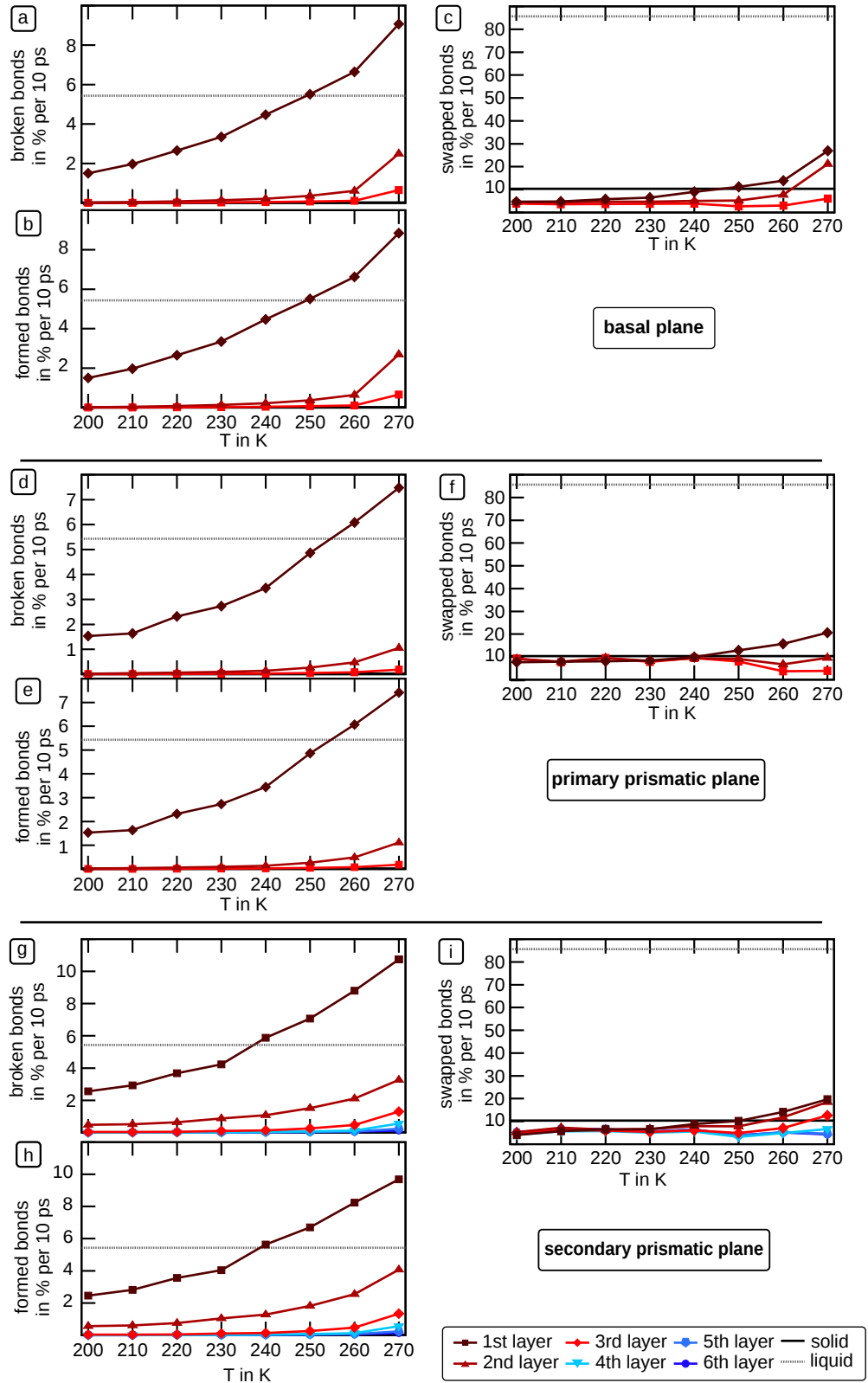


Fig. 4.7: Dynamical properties of the H-Bonding at the three most prominent surfaces of hexagonal ice. Amount of broken H-bonds ((a),(d) and (g)) formed H-bonds ((b), (e) and (h)) swapped H-bonds ((c), (f) and (i)) in % per 10 ps.

Formed bonds are incremented once a free OH forms an H-bond in the second image.^l With this definition of broken and formed bonds, the total percentage of broken bonds should equal the one of the formed bonds. Otherwise, the total amount of H-bonds would not be constant and this would indicate a non-equilibrated simulation.

In case of the basal plane (Figures 4.7 (a)–(c)), the first bilayer shows a rapid increase for the percentage of broken and formed bonds per 10 ps. For all three bilayers, a sudden alteration between the temperatures 260 K and 270 K is visible. The amount of swapped bonds ascends stepwise and linearly between 210 K–230 K and 240 K–260 K.

Comparing the basal plane to the primary prismatic plane (Figure 4.7 (d)–(f)), one major difference is that no jump can be observed between 260 K and 270 K for the first bilayer of the primary prismatic plane. Apart from that, the second and third bilayer break and form far less bonds than the basal ones. Only above 250 K, a measurable rate can be detected (Figure 4.7 (f)). These layers behave similarly to the third bilayer of the basal plane.^m

Interestingly, the amounts of broken and formed bonds for the secondary prismatic plane differ slightly. More bonds are broken than formed in the first single-layer and vice versa for the second single-layer. The reason seems to be the bonds at the layer boundary: if molecules need to move away from the second single-layer in order to break the bond, the H-bonds split more frequently in the first layer, because both the donor and acceptor molecule move upwards. On the contrary, a molecule may move towards the second layer more often for the formation. The total rates for the first six single-layers are equal, which supports this interpretation. In general, more bonds are broken and formed at the secondary prismatic plane than at the basal and the primary prismatic surface.

A remarkable feature of all three surfaces is the rapid breaking and swapping of H-bonds within the outermost layer at higher temperatures, which is even faster than for the liquid reference. This might be an effect caused by the dangling bonds at the surface, that always try to find a new partner.

4.4 Network analysis

One key feature of an H-bond network is the ability to form rings, that is a closed path via H-bonded molecules.ⁿ In ice, the vast majority of rings is six-membered (according to the definition in [140]), while several ring types can be found in liquid water. The concept of using a ring analysis to characterise order in ice simulations has been introduced by [141].

^lTrajectories of 40 ns (for all temperatures and surfaces except for 270 K for the basal plane, where 190 ns were evaluated) with a time step of 10 ps between the evaluated snapshots were analysed, i.e. 4000 snapshots for all surfaces and temperatures (for the basal plane at 270 K, 11700 snapshots were analysed).

^mAll rates are shown in one plot in Figure 8.20 in the Appendix.

ⁿThe H-bond definition presented in Section 4.1 is utilised for the determination of the rings in combination with the ring definition from [140].

To quantify the difference between ice and water, the average number of participations in n -membered rings per molecule of the ice and water references have been calculated (Table 4.2).

Tab. 4.2: Amount of n -membered rings ($n = 3$ –10) per molecule for a solid ice reference system at 250 K and a liquid water reference system at 300 K.

Ring size	3	4	5	6	7	8	9	10	$\sum n$
Ice 250 K	0	0	0	11.98	0	0.01	0	0.02	12.01
Water 300 K	0.01	0.34	1.51	2.40	2.65	2.02	1.63	0.95	11.51

In liquid water, the distribution of n -membered rings is far more diverse. Here, seven-membered rings are slightly more abundant than six-membered rings. Interestingly, the total amount of rings formed per molecule is roughly equal to twelve for both systems.

4.4.1 Basal surface

In Figure 4.8, the amount of n -membered rings ($n = 3$ –10) formed per molecule of the first, second, and third bilayer of the basal plane is visualised in a stacked bar diagram.^o

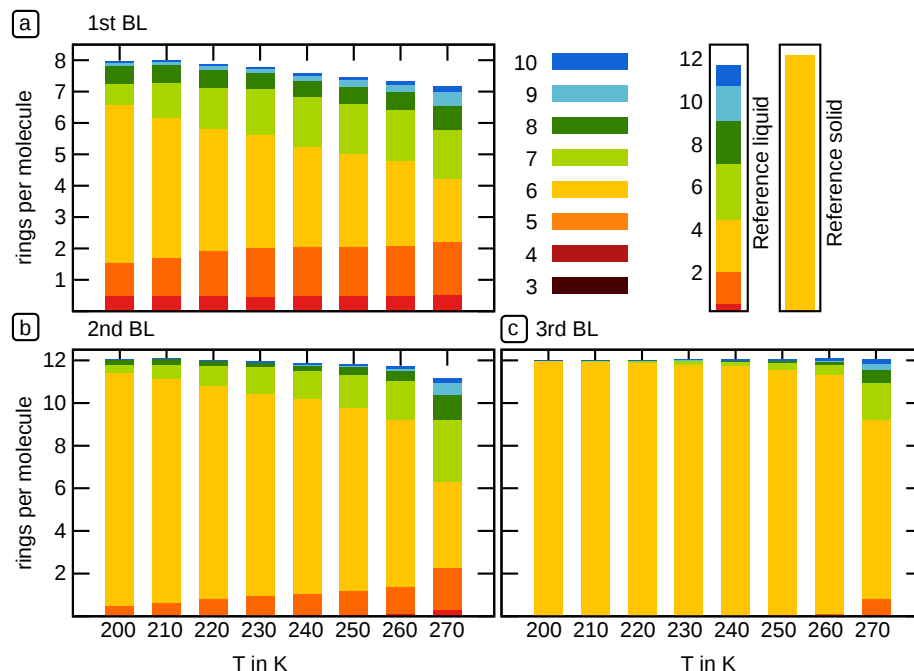


Fig. 4.8: Stacked bar diagram of the amount of rings per molecule of the first three bilayers of the basal plane. The total height of the bar equals to the total amount of n -membered rings per molecule, while the individual contributions of the n -membered rings ($n = 3$ –10) are coloured.

^oThe layers are determined utilising the density profiles from Chapter 3.2.

This analysis counts the number of rings a molecule of the respective layer participates in, even if a part of the ring is located in another layer.

The individual bars represent the amount of n -membered rings each and the total bar size the the sum of all rings per molecule. The depicted stacked bars of the liquid and solid reference are a visualisation of Table 4.2. The distribution of n -membered rings for the first bilayer is far more diverse than the one of bulk ice even at low temperatures. This is readily explained by the presence of dangling bonds at the surface and the resulting surface rearrangement. Comparing the first, second, and third bilayer, the amount of six-membered rings per molecule increases steadily with ascending distance from the surface. The total number of rings is somewhat bigger than for a non-rearranged surface at low temperatures, which would be 7.5 rings per molecule. At higher temperatures, the value is slightly lower. The total amount of n -membered rings, corresponding to the total height of the bar, increases with ascending distance from the surface.

The amount of six-membered rings per molecule within one bilayer decreases with ascending temperature, while the amount of five- and seven-membered rings increases. This is in agreement with literature, since it is already known that five- and seven-membered rings are formed at the surface.^{p[14–16]} The amount of six-membered rings within the first bilayer decreases linearly.^q In contrast, a jump between 260 K and 270 K can be observed for the second and third bilayer (see Figure 4.8 (b)). In addition, the total amount of rings decreases considerably at 270 K in the second bilayer, while only at the highest temperature of 270 K a significant amount of non-six-membered rings is observed in the third bilayer. Notably, the obtained distribution of n -membered rings at the highest simulated temperature differs from the liquid reference, although the bilayer can be considered molten as the diffusion analysis clearly shows. One reason for this is the spatially limited formation of rings along the direction perpendicular to the surface. Another aspect is the templating effect of the ordered second and third bilayers, which causes a more ordered structure of the layer above. Furthermore, some rings are formed perpendicular to the surface and, thus, include some molecules of the other bilayers.

To conclude, the disorder in the ring network increases linearly at the first bilayer. The second and third bilayer show a significant discontinuity between 260 K and 270 K, which is assigned to an abrupt onset of disorder occurring between the two temperatures. This is in agreement with other analysis methods which quantify disorder such as, for instance, the order parameter analysis in Chapter 5.

^pSimilar observations are made in Chapter 3.

^qThe trends are plotted as line diagrams in the Appendix in Figure 8.21.

4.4.2 Prismatic surfaces

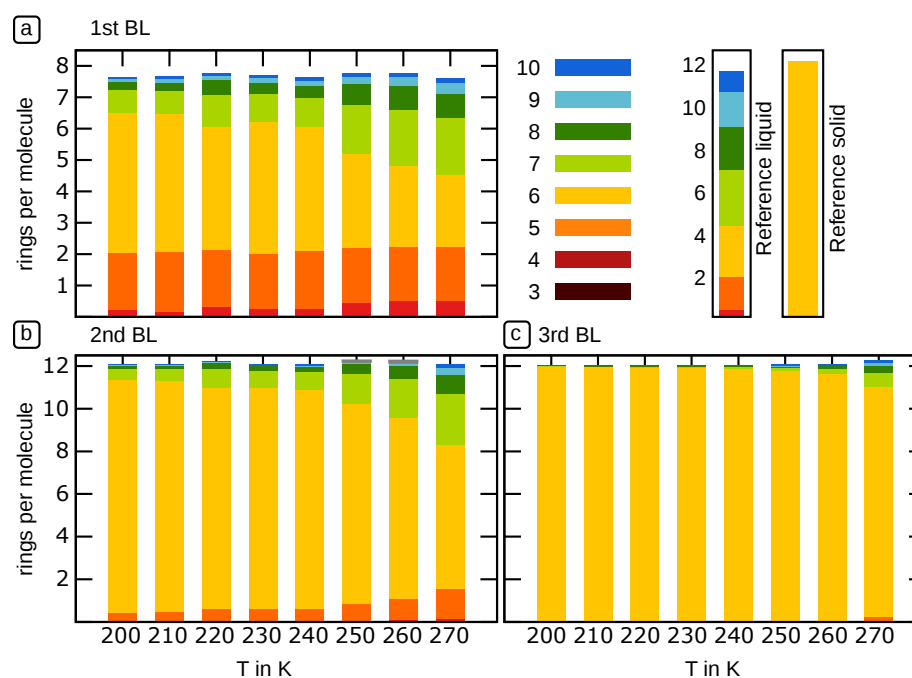


Fig. 4.9: Stacked bar diagram of the amount of rings per molecule of the first three bilayers of the primary prismatic plane.

Comparing the stacked bar diagrams for the primary prismatic plane (Figure 4.9) with the one for the basal plane (Figure 4.8), the trends in the first bilayer are less clear for the primary prismatic surface.

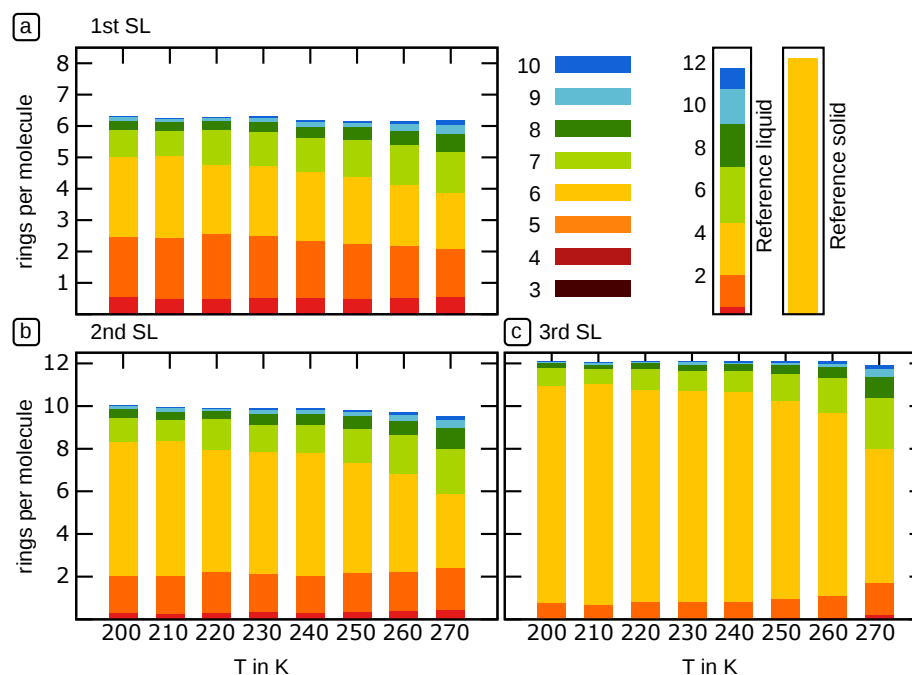


Fig. 4.10: Stacked bar diagram of the amount of rings per molecule of the first three single-layers of the secondary prismatic plane.

The amount of seven-membered rings decreases between 220 K and 230 K instead of the expected increase. Nevertheless, the overall trend remains the same. Between 240 K and 250 K, the amount of hexagons seems to decrease remarkably. In general, the primary prismatic plane seems to be slightly less disordered than the basal plane at 270 K. A jump as observed between 260 K and 270 K for the basal plane cannot be observed for this surface.^r

The situation is different for the secondary prismatic plane, where the first and second single-layers together resemble the first bilayer of the basal plane (Figure 4.10).^s

4.5 Conclusion

In conclusion, all analysis methods presented in this chapter detect an abrupt onset of disorder for the first bilayer of the basal plane between 260 K and 270 K, which may indicate the onset of melting. The basal plane is, in general, more disordered than the primary prismatic plane. Disorder spreads to the third bilayer for the basal plane, while for the primary prismatic plane only the upper two bilayers are affected at the highest temperature. Just the first bilayer is completely disordered for both systems at temperatures below 270 K. The first two single-layers of the secondary prismatic plane combined resemble the first bilayer of the basal plane.

Noticeably, the amount of free OH is lower for the primary prismatic plane than for the basal plane, indicating a more efficient rearrangement at the primary prismatic plane. Disorder seems to propagate stepwise into the bulk for the basal plane, while for the other two surfaces a rather gradual behaviour is observed. Interestingly, no onset of disorder can be detected, as the first layers are already disordered at 200 K. The number of formed and broken bonds is even higher than in the liquid reference for all systems, probably due to the instability of the surface compared to that of bulk water.

The network analysis of the upper three layers reveals a significant increase of non-six-membered rings, which is in agreement with the formation of five- and seven-membered rings at the surface that has been reported.^[14–16] Still, the composition is quite different from that of liquid water. The disorder seems to be higher at the basal surface than at the primary prismatic plane, although all surfaces are fairly similar.

^rAll trends for the first, second, and third layer of the three most prominent surfaces are visualised in a single plot respectively in Appendix Figure 8.24.

^sIt should be kept in mind that single-layers contain only half of the molecules of a bilayer.

Everything in order?

In this chapter, the amount of disorder at the surface of ice as a function of temperature is quantified using suitable order parameters. In addition, it is determined whether the disorder decreases gradually or stepwise with increasing distance from the surface at a fixed temperature. This analysis answers the question whether there is a sharp order/disorder boundary. We also examine how disorder changes with temperature.

5.1 Introduction

The process of surface melting can be interpreted as a transition from an ordered to a less ordered arrangement. To monitor such transitions, several structural order parameters (OP) can be employed. Here, a distinction must be made between global OPs, which provide a single value for the whole system, and local OPs, which are calculated for each molecule. In this chapter, several commonly used OPs are compared for the analysis of the ice surface. Due to the local rearrangement that occurs at the surface, a global OP will not suffice and a local OP is applied instead. In general, global OP are not suitable for studying first order phase transitions like melting/nucleation.^[142] The local order of ice is characterised by the tetrahedral bonding arrangement as depicted in Figure 5.1.

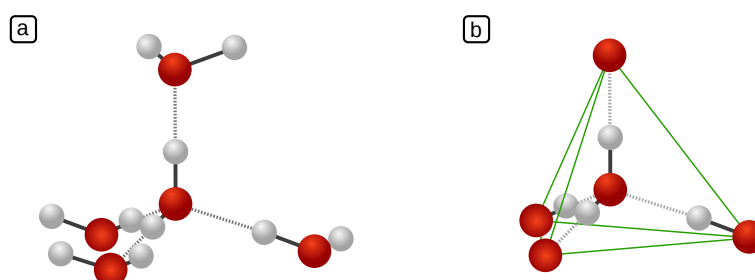


Fig. 5.1: Tetrahedral bonding arrangement of the neighbouring oxygen atoms of a central oxygen atom in the hexagonal ice lattice. **(a)** The dashed lines indicate the hydrogen bonds pointing towards the neighbouring oxygen atoms. **(b)** A tetrahedron formed by the four neighbouring oxygen atoms sometimes also referred to as a 'Walrafen'-pentamer.^[143]

In water, most molecules still bind to four neighbouring oxygen atoms, but the structure is far less close to a perfect tetrahedron than in the case of ice. More importantly, even if water exhibits a certain degree of local tetrahedral order, it forms a dynamic disordered network beyond the first coordination shell. Thus, the tetrahedrality and medium-range

order of the neighbouring oxygen atoms provide a good criterion to describe the ordering/disordering at water/ice interfaces. The task is to find an order parameter (OP) that can transform ‘tetrahedrality’ into a single number. Furthermore, resulting OPs need to be rotationally invariant, as they should not depend on the coordinate system or the numbering of neighbours.

One approach is the so-called ‘tetrahedral’ OP:

$$q_{\text{tetrahedral}}(\tau) = 1 - \frac{3}{8} \sum_{\alpha > \beta} \left(\cos(\tau_{\alpha\beta}) + \frac{1}{3} \right)^2, \quad (5.1)$$

with the angle $\tau = \angle \alpha X \beta$ formed between the central atom X and its two neighbours α and β . The number of angles corresponds to the six edges of a tetrahedron. This OP equals to one for a tetrahedral arrangement, since $\cos(\tau_{\alpha\beta})$ equals to $-1/3$ for a perfect tetrahedron. A factor $3/8$ is included to yield $q_{\text{tetrahedral}} = 0$ for a random arrangement on average.^[144]

A more sophisticated approach is the use of a so-called local Steinhardt order parameter (LSOP) which encompasses spherical harmonics, $Y_{l,m}$, and is rotationally invariant as well:^[145,146]

$$q_l(i) = \sqrt{\frac{4\pi}{2l+1} \sum_{m=-l}^{+l} |q_{l,m}(i)|^2}, \quad (5.2)$$

with

$$q_{l,m}(i) = \frac{1}{N_{\text{neigh}}(i)} \sum_{j=1}^{N_{\text{neigh}}(i)} Y_{l,m}(\theta_{ij}, \varphi_{ij}). \quad (5.3)$$

In Equation 5.3, the spherical harmonics $Y_{l,m}$ are calculated for all nearest neighbours N_{neigh} .^a To illustrate these equations, the real linear combinations of the spherical harmonics for $l = 1$ are depicted in Figure 5.2.^b

In addition, the bond configuration with two neighbours is plotted on a straight line. According to Equation 5.3, all $Y_{\text{real } 1, m}$ must be calculated separately for each bond to a neighbouring atom. Due to the linear arrangement, $Y_{\text{real } 1, \pm 1}$ equal to zero and do not contribute, while $Y_{\text{real } 1, 0}$ becomes $\pm \sqrt{3/4\pi}$, and, thus, also vanishes. Since every component of Equation 5.3 is equal to zero, $q_{1,m}$ equals to zero as well.

^aThe spherical harmonics and, thus, the LSOPs have no radial component (apart from the chosen neighbours). They depend only on the inserted spherical angles θ and ϕ of the neighbours relative to the central atom.

^bThe real linear combinations are equivalent to the complex spherical harmonics for the calculation of the LSOPs.^[147] The real spherical harmonics $Y_{\text{real } l, m}$ are constructed from the complex spherical harmonics $Y_{l,m}$:

$$Y_{\text{real } l, m} = \begin{cases} \frac{i}{\sqrt{2}} (Y_{l,m} - (-1)^m Y_{l,-m}) & \text{if } m < 0 \\ Y_{l,m} & \text{if } m = 0 \\ \frac{1}{\sqrt{2}} (Y_{l,-m} + (-1)^m Y_{l,m}) & \text{if } m \geq 0. \end{cases}$$

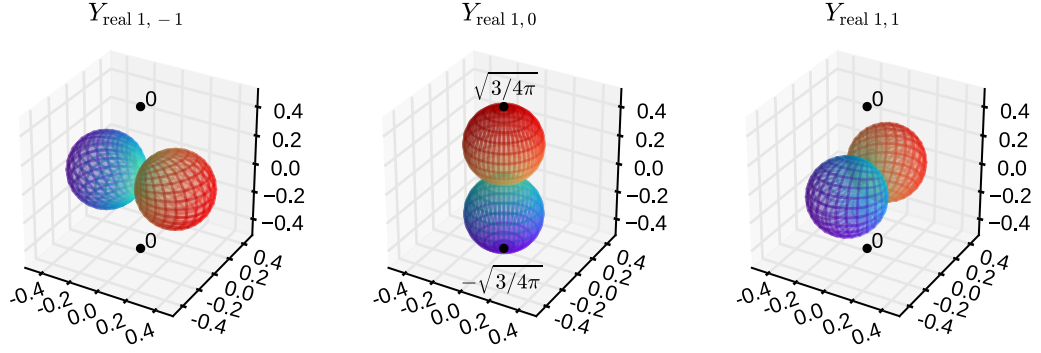


Fig. 5.2: Contributions to q_1 for a linear arrangement. The absolute value of $Y_{\text{real } l, m}$ for any direction corresponds to the respective distance between the origin and the surface of the plot. This is obtained by distorting a unit sphere and scaling each point radially by the absolute value of $Y_{\text{real } l, m}$. The sign is indicated by the colour of the plot (positive: red, negative: blue).

As a second example, a tetrahedral arrangement is depicted in Figure 5.3. The value of any $q_{1, m}$ is equal to zero, since the contributions of all individual bonds cancel one another. Hence, q_1 is equal to zero for a perfect tetrahedral arrangement.

Bond orientation analysis with LSOPs is a common approach for identifying different crystalline phases and clusters. For water/ice interfaces, q_6 is commonly used to identify nucleating ice crystals in water.^[148] In order to distinguish hexagonal from cubic ice, a modified version of LSOPs, \bar{q}_l , can be applied. This order parameter takes the second neighbour shell explicitly into account:

$$\bar{q}_l(i) = \sqrt{\frac{4\pi}{2l+1} \sum_{m=-l}^{+l} |\bar{q}_{l, m}(i)|^2}, \quad (5.4)$$

with

$$\bar{q}_{l, m}(i) = \frac{1}{N_{\text{neigh}}(i) + 1} \sum_{j=0}^{N_{\text{neigh}}(i)} q_{l, m}(j). \quad (5.5)$$

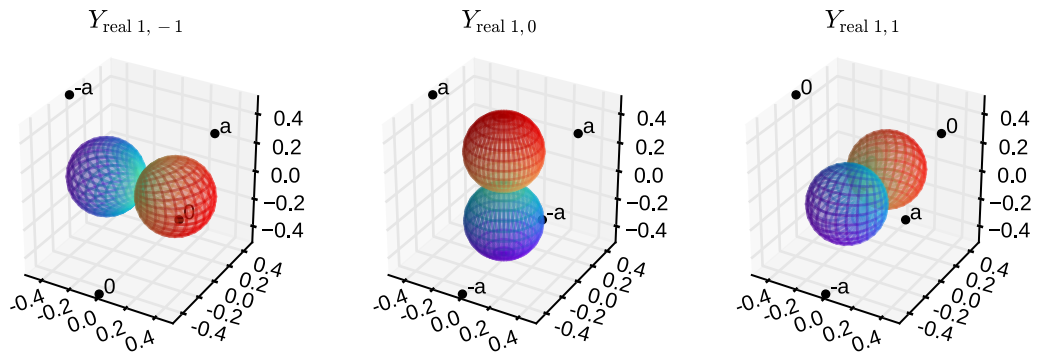


Fig. 5.3: Contributions to q_1 for a tetrahedral arrangement similar to Figure 5.2, with $a = \sqrt{3/8\pi}$.

In Equation 5.5, twenty bond vectors can now be calculated, as $\vec{q}_{l,m}$ not only takes the bonds of the central molecule to its neighbours into account, but also the bonds of these neighbouring atoms to their respective neighbours. For a differentiation between hexagonal ice I_h , cubic ice I_c , and liquid water, plots of for instance the (\vec{q}_4, \vec{q}_6) plane can be employed.^[90,149,150] Cubic and hexagonal ice differ in their molecular arrangement around the nearest neighbours and can thus be distinguished.^c A different approach uses the dot product

$$d_l(i, j) = \vec{q}_l(i) \cdot \vec{q}_l^*(j), \quad (5.6)$$

where $\vec{q}_l(i)$ has $(2l + 1)$ components $q_{l,m}(i)$ with $m \in [-l, +l]$.^[150] It is also possible to use

$$\text{the averaged } \bar{d}_l(i) = \frac{1}{N_{\text{neigh}}(i)} \sum_{j=1}^{N_{\text{neigh}}(i)} d_l(i, j).^{[151]}$$

However, as we are interested in a layer-resolved analysis, this approach cannot be used since the order parameter takes too many molecules from other layers into account and simply cannot be calculated at the surface due to the low N_{neigh} .

In general, the interpretation of $q_{\text{tetrahedral}}$ and the LSOPs is non-trivial. One may argue that q_3 is a good choice, as $Y_{3,2}$ and $Y_{3,-2}$ are of tetrahedral symmetry. Notwithstanding, things are not that easy, since, for a given l , the sum over all $Y_{l,m}$ is calculated (Equation 5.2) resulting in a different overall symmetry.

To help with the interpretation of the LSOPs, the order parameters for four neighbours randomly arranged on a sphere, a single tetrahedral, and a single squared arrangement of four neighbouring atoms are displayed in Figure 5.4. The tetrahedron and square were chosen to compare the random arrangements with those of high symmetry.

In Figure 5.4 (d), the q_3 value for a square is lower than that of the mean random distribution, while the value for the tetrahedron is higher. Generally, there is no direct relationship between the degree of symmetry and the value of an order parameter. In the case of q_4 (Figure 5.4 (b)), the value for the tetrahedron even corresponds to the maximum of the random distribution. Hence, q_4 is a poor descriptor when trying to separate tetrahedral from random arrangements. An interesting observation is the clean separation between a tetrahedron and a random distribution based on q_5 . Hence, q_5 is a promising OP candidate for the pre-melting of ice.

It is also interesting to see how such general considerations can directly be translated into distributions obtained for real systems.

^cFor cubic ice, the arrangement of molecules around four neighbouring atoms is inverted with respect to the arrangement around the central molecule, while for hexagonal ice it is inverted for only three neighbours and mirrored for one.

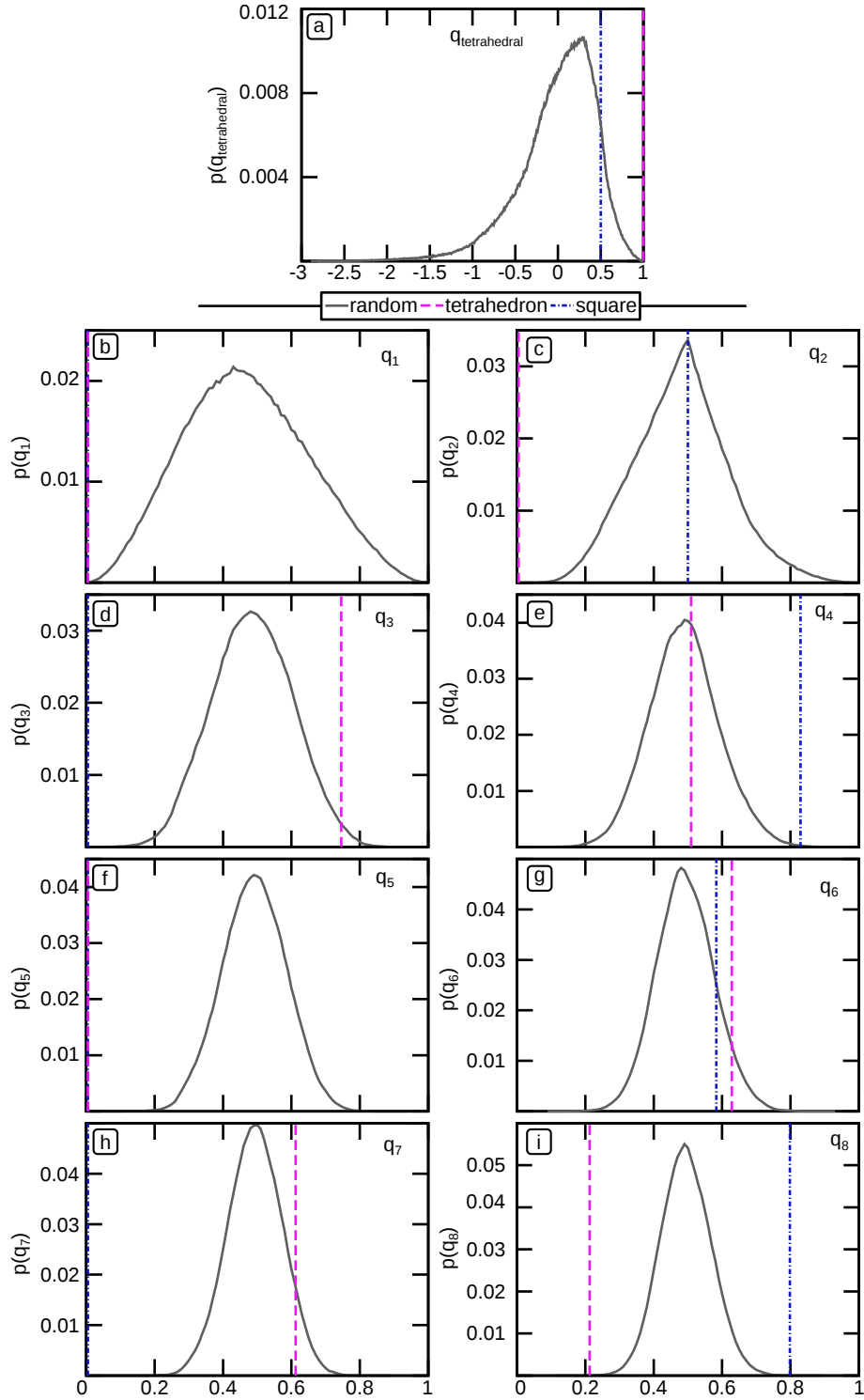


Fig. 5.4: $q_{\text{tetrahedral}}$ and the LSOPs for $l = 1, 8$ for a pseudo-random distribution (grey line), a square (blue dash-dotted line), and a tetrahedron (magenta dashed line). The pseudo-random distribution is obtained by calculating the OPs for four random points on a sphere one million times. It turns out that q_4 , for which the maximum of the random distribution is equal to the value of the tetrahedron, is the worst order parameter for the characterisation of disorder at the surface. q_5 seems to be the most promising OP since it has a narrow distribution for the random configurations and the random distribution is separated by a large gap from the value for the tetrahedron.

In Figure 5.5, the OPs are depicted for a liquid reference with 480 water molecules at 300 K, a solid reference with 1536 water molecules at 250 K, and an ice slab at 250 K, where the basal plane is exposed to vacuum.^d As we will see in the next section, the distribution for the ice slab is not just a superposition of a solid and a liquid distribution. Thus, it is difficult, if not impossible, to extract the exact number of liquid-like molecules. Still, several attempts have been made to estimate the number of liquid-like molecules, which tends to result in too large thicknesses of the QLL.

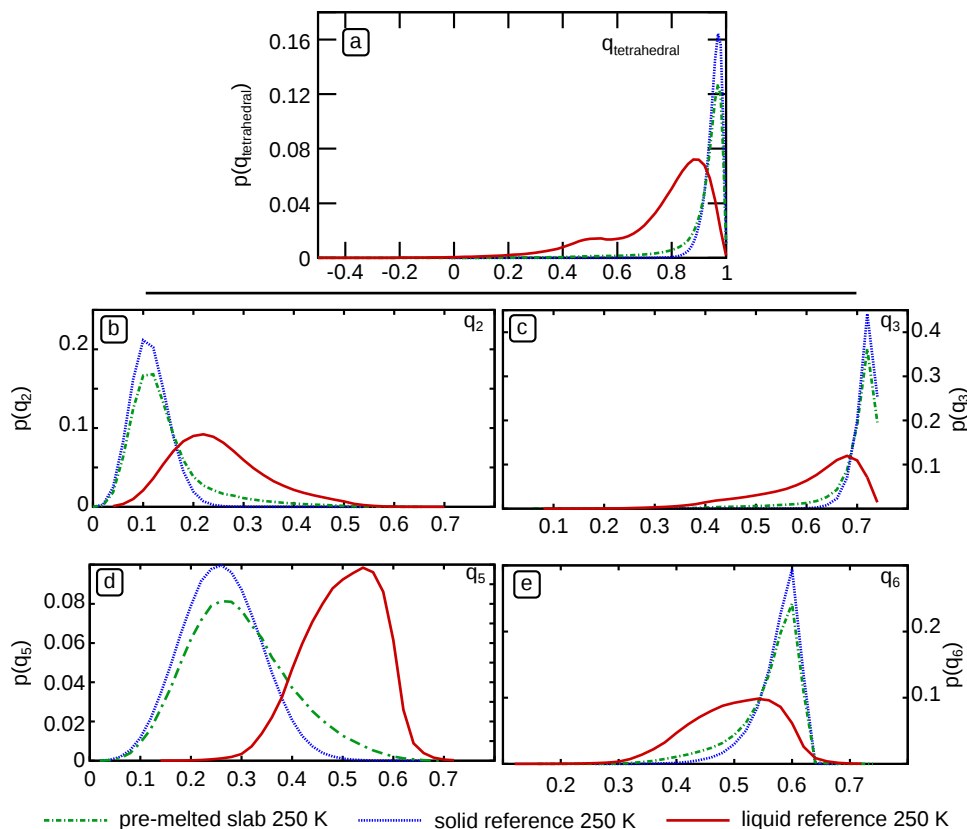


Fig. 5.5: Selected LSOPs for $l = 2, 3, 5, 6$ for a bulk solid reference at $T = 250$ K, a bulk liquid reference at $T = 300$ K, and an ice slab with the basal plane exposed to vacuum at $T = 250$ K. All five OPs allow for a differentiation between the solid and the liquid reference and it is possible to make a qualitative comparison of the slab to the references. In this case, the slab is more similar to the solid reference and the more pronounced tail indicates an increased disorder for some molecules. The peak position and amplitude of distributions change noticeably from the solid to the liquid reference for all OPs but q_5 , where only the peak position changes. Note that the distributions for the liquid reference differ from those of the random configurations due to the hydrogen bonding and the resulting remaining order in liquid water.

One attempt is to fit the distribution of an ice slab with a linear combination of the solid and liquid reference distributions and determine the fraction of liquid molecules via the obtained fit coefficients.^[152–154] Another approach is based on cut-off parameters, where

^dFor simulation details see Chapter 2.

everything is considered to be liquid below a certain cut-off.^[42,82,93,148,155] The cut-off q_t is usually determined via the following relation^[42,155]

$$\int_{q_t}^1 p_{\text{liquid}}(q) dq = \int_0^{q_t} p_{I_h}(q) dq, \quad (5.7)$$

where $p_i(q)$ are the probability densities originating out of the distributions. This definition corresponds to q_t being the crossover of the distributions, i.e. that the likelihood to find molecules of the solid reference below the cut-off equals to the chance to find molecules of the liquid reference above.^[42,155] The problem with this approach is that the distribution is non-zero (i) below the cut-off for a pure solid and (ii) above the cut-off for a pure liquid. In other words, some molecules would count as liquid for a pure solid sample and vice versa. This flaw cannot be corrected by adding or subtracting offsets. In fact, the fraction of molecules belonging to the QLL should rather be defined by dynamic properties such as the diffusivity.

In summary, different local order parameters can be used to measure tetrahedrality and q_5 seems to be the best candidate due to the gap between the values for a tetrahedron and a random distribution. In the past, mostly q_3 and q_6 have been applied to characterise water/ice systems, failing to consider q_5 . In addition, we utilise a layer-resolved approach to study the local effects at the surface. This will be demonstrated in the next section.

5.2 Layer-resolved order parameter analysis of the ice surface

As already mentioned, the evaluation of the ice slab in Figure 5.5 does not provide valuable insight into the structure of the ice surface. Since it is known that the low-index surfaces of hexagonal ice are arranged in a layer structure, LSOPs can be calculated in a layer-resolved manner. Of special interest is the change in order with increasing depth. Some experiments suggest that the order decreases gradually as one moves away from the surface towards deeper parts of the slab, while other report it to change in a more distinct, stepwise manner.^[26,30,70,71]

In order to calculate the LSOPs for a real system, the first step is to identify the nearest neighbours of each molecule. Several strategies for finding these have been applied. Here, it is important to note that the number of neighbours needs to be constant for a meaningful analysis using LSOPs. This is apparent in Figure 5.2, where the value of q_1 changes from 0 to 1 after having removed one of the neighbours. In the case of

a tetrahedron the effect is similar. To illustrate this, the values of several LSOPs are calculated for a tetrahedral arrangement, removing the neighbours of the central atom one by one (Table 5.1).

Tab. 5.1: Local Steinhardt order parameters as calculated for a tetrahedral arrangement of neighbours while reducing the number of neighbours sequentially.

N_{neigh}	q_1	q_2	q_3	q_4	q_5	q_6	q_7	q_8
4	0	0	0.75	0.51	0	0.63	0.61	0.21
3	0.33	0.33	0.78	0.58	0.33	0.68	0.67	0.39
2	0.58	0.58	0.84	0.71	0.58	0.77	0.76	0.60
1	1	1	1	1	1	1	1	1

Although many sophisticated H-bond definitions exist, a simple definition of the nearest neighbours is usually good enough. However, taking all molecules within a given cut-off distance into account leads to a varying number of neighbours and, hence, to results, which are difficult to interpret. A better approach is to use the four closest molecules. This approach has the drawback that for molecules with three next neighbours, like those present at the surface, some molecule far away, which does not bind to the central molecule, will be counted as fourth neighbour.^[156,157]

Therefore, a combined approach is utilised in this work. The four nearest neighbours are identified, but the LSOP is only computed if they are within a cut-off distance of 3.4 Å, which corresponds to the first minimum of the radial distribution function. Otherwise, no LSOP is calculated.^e

5.2.1 Basal plane

For each molecule of the bilayer, the LSOPs are calculated separately for each time step.^f Here, various LSOPs are chosen according to the aforementioned criteria to determine the best one. In this case, they are calculated bilayer-resolved for an ice slab at a temperature of 250 K with the basal plane exposed to the vacuum (Figure 5.6).

All displayed LSOPs show similar trends: the inner bilayers have distributions similar to the solid reference, while the outermost bilayers resemble the liquid reference. The second outermost bilayers have an intermediate distribution.

^e The above described definition was compared to a more sophisticated one utilising H-bond criteria like in Chapter 4. No big difference is observed (Figure 8.72 in Appendix 8.4.5).

^f At the top-most bilayer, roughly 70 % of the molecules are evaluated, while for other bilayers over 95 % of the molecules are used to calculate an order parameter. Note that the assignment of molecules to a certain bilayer is performed for every step due to the already mentioned parking lot mechanism.

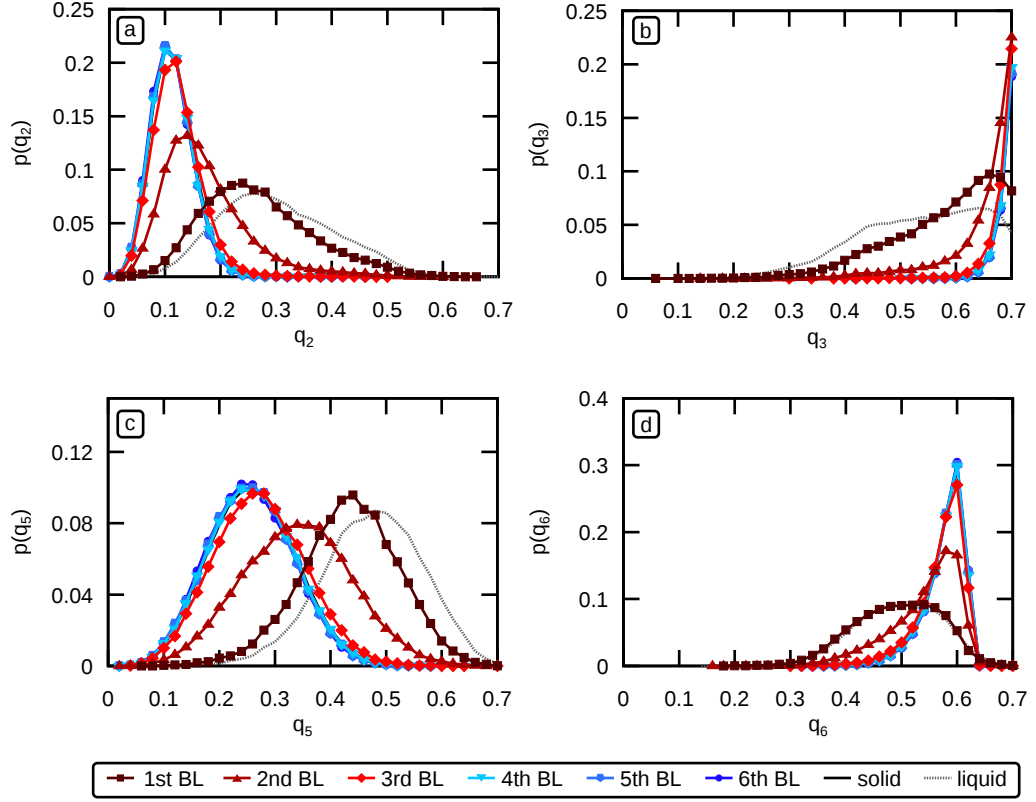


Fig. 5.6: Bilayer-resolved LSOPs, for $l = 2, 3, 5, 6$, for an ice slab at 250 K with the basal plane exposed to the vacuum. Liquid reference at $T = 300$ K, solid reference at $T = 250$ K. The inner bilayers resemble the solid reference. Only the first and the second bilayer differ and are shifted towards the liquid reference.

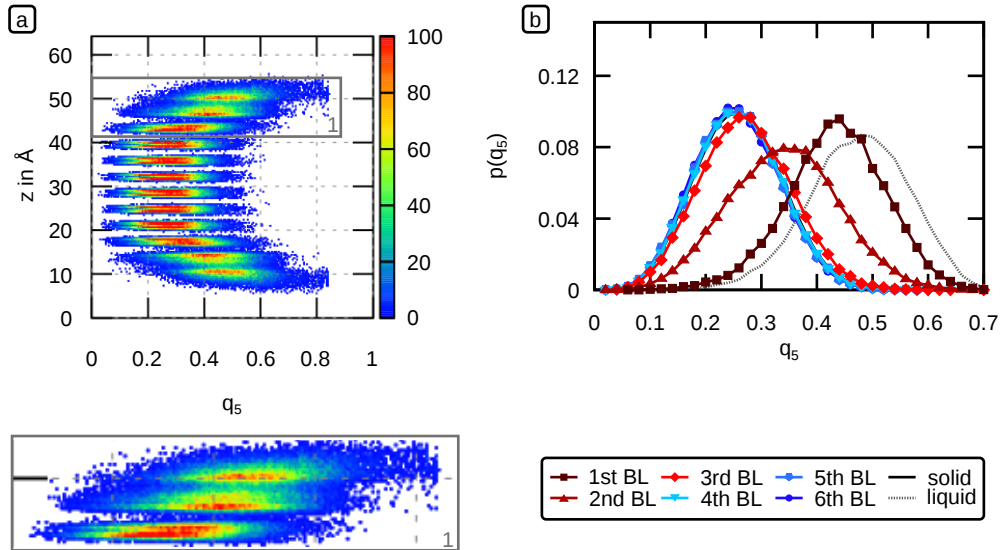


Fig. 5.7: Verification of the bilayer approach. (a) The z -resolved q_5 calculation displays a bilayer structure. (b) Respective bilayer-resolved representation.

By comparing the distributions of the individual bilayers with those of the references, information about the degree of disorder can be obtained. Regarding the choice of the

LSOPs, all the depicted LSOPs make for valid choices. While for q_3 only the peak amplitude decreases significantly for layers closer to the surface, q_2 and q_6 show an additional shift of the peak position. In contrast, the amplitude remains rather constant for q_5 , whereas the peak position changes noticeably.

Apart from that, the distribution of q_5 is approximately uniform within the bilayers and the underlying bilayer arrangement is clearly visible in Figure 5.7 (a).

For all further analysis, q_5 is used due to the good separation of the probability distributions between liquid and solid. Another advantage is the rather constant height of the distribution. Hence, only the peak position needs to be monitored in the analysis.

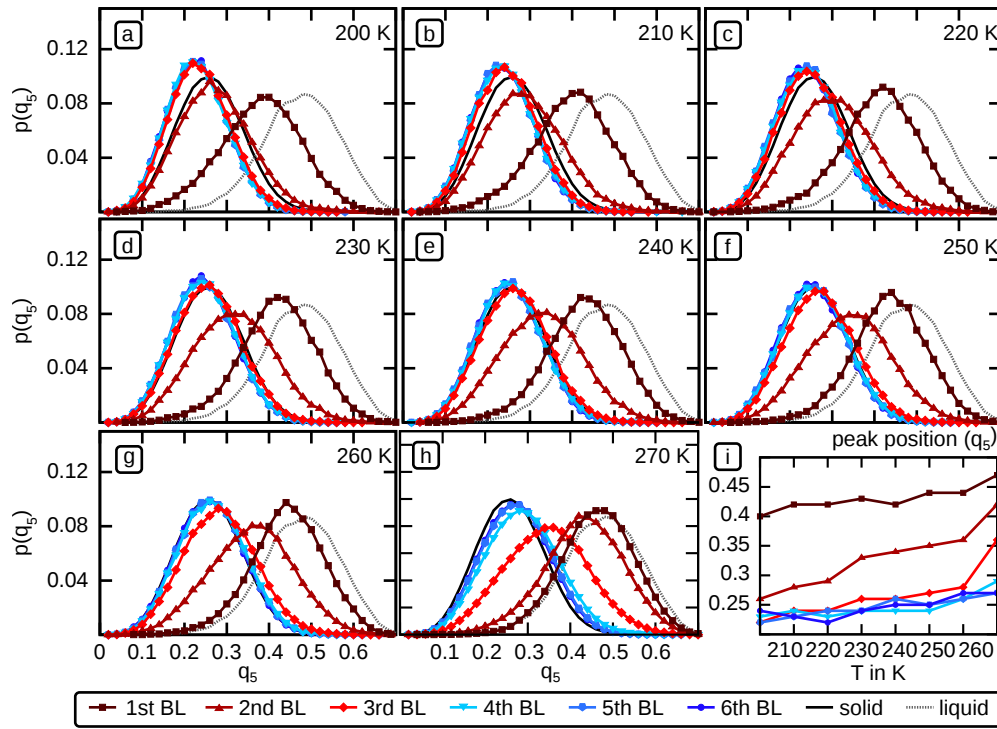


Fig. 5.8: Distributions of q_5 for the upper six bilayers for an ice slab with the basal plane exposed to the vacuum. Liquid reference at $T = 300$ K, solid reference at $T = 250$ K.

In Figure 5.8, the layer-resolved q_5 distributions are shown for different temperatures. Only the upper three bilayers undergo a notable change with temperature. At $T = 270$ K, the inner bilayers still resemble the solid reference. Hence, only the upper three bilayers are discussed in the following. Even at very low temperatures, the first bilayer is strongly disordered and the distribution becomes more similar to that of the liquid reference with increasing temperature. Since the QLL forms well above 200 K, this underlines the difference between disorder and pre-melting, as we will see in Chapter 6.

As shown in Figure 5.8, the order of the second bilayer is lower than that of the inner bilayers, even at 200 K. Interestingly, the distribution for the second bilayer is only close to that of the liquid reference at 270 K. Going from 230 K to 260 K, the second bilayer distribution resembles neither the solid nor the liquid reference distribution and looks more like an intermediate distribution. This may indicate the existence of an intermediate layer between the QLL and bulk ice. It is important to note that the nature of this distribution does not originate from the contact to the adjacent solid or liquid-like layers, since the order parameter distributions of the lower and upper part of the bilayer are similar (Figure 5.7 inset (1)). At 270 K, when the second bilayer becomes liquid-like ordered, the third bilayer is the intermediate layer. This analysis suggests that the disorder propagates stepwise into the bulk and that only the top layers are disordered.

5.2.2 Primary and secondary prismatic plane

A similar analysis was performed for the primary prismatic and the secondary prismatic surface.

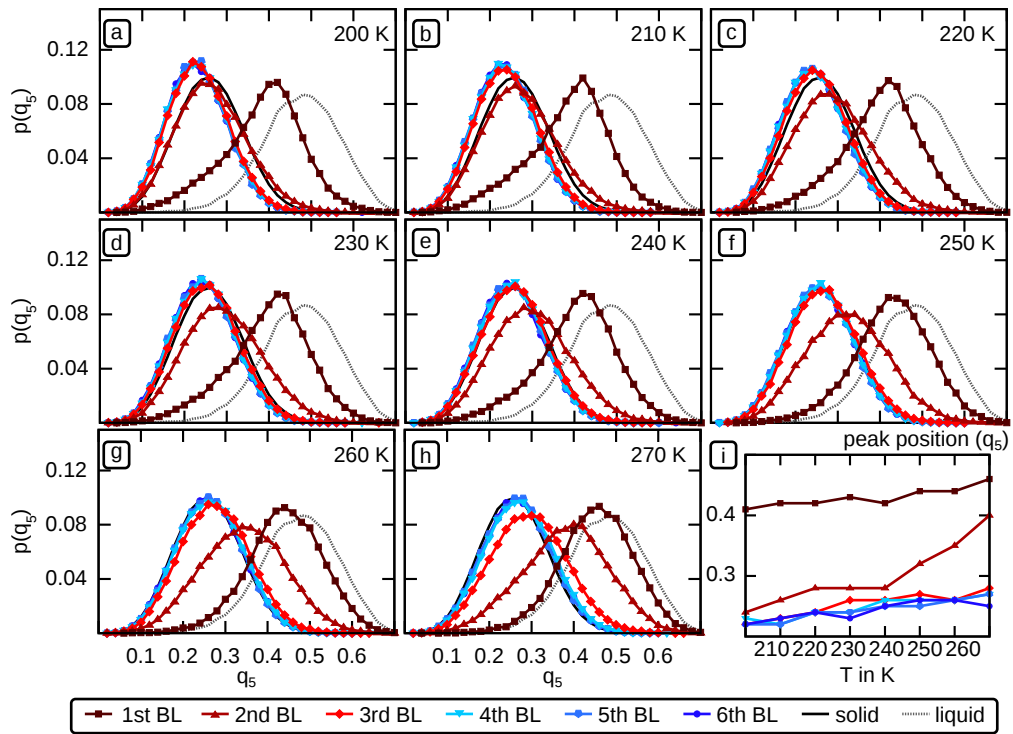


Fig. 5.9: Distributions of q_5 for the upper six bilayers for an ice slab with the primary prismatic plane exposed to the vacuum. Liquid reference at $T = 300$ K, solid reference at $T = 250$ K.

For the primary prismatic plane (Figure 5.9), the trends are similar to those of the basal plane, although the second bilayer looks like an intermediate layer only between 250 K and 270 K.

Therefore, it can be concluded that the second bilayer of the primary prismatic plane is less disordered than the second bilayer of the basal plane at the same temperature. This is in agreement with the dynamic analysis (Chapter 6), where only one bilayer is molten for the primary prismatic plane at 270 K.

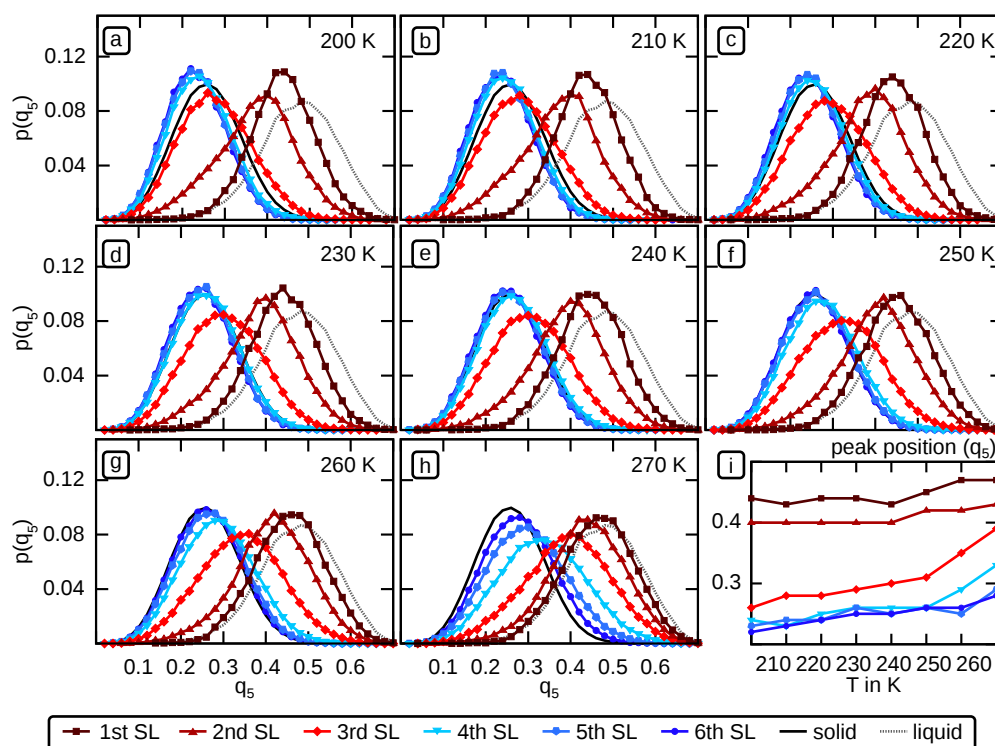


Fig. 5.10: Distributions of q_5 for the upper six single-layers for ice slabs with the secondary prismatic plane exposed to the vacuum. Only six layers are depicted since the distributions of the inner layers remain solid.

For the secondary prismatic plane, the upper six single-layers are studied. Due to the lower molecule density in a single-layer, disorder affects more layers. Notably, the changes in disorder seem to be stepwise first, while at 270 K the degree of disorder changes more gradually from layer to layer. The third layer could be interpreted as an intermediate layer between 250 K and 260 K.

5.3 Conclusion

In a nutshell, a layer-resolved analysis is presented using local Steinhardt Order parameters q_l (Equations 5.2 and 5.3). It turned out that q_5 , although rarely used elsewhere, is an excellent choice for the studied systems, especially since disorder can be mapped to the peak position. Clearly, an order parameter analysis cannot be utilised to measure the thickness of the QLL, so the terms disorder and degree of liquidity should not be used interchangeably. Moreover, only a layer-resolved approach is capable of monitoring the propagation of disorder into the bulk. Interestingly enough, only the first few layers are noticeably disordered at 270 K for perfect, defect-free ice in contrast to experiments which employ actual samples. For the primary prismatic and basal surface, only three bilayers are more disordered than the bulk at 270 K, while for the secondary prismatic plane surface about four single-layers are affected. In general, the basal surface is slightly more disordered than the primary prismatic surface. Our analysis suggests that disorder propagates stepwise into the bulk and that a gradual change is observed only for the secondary prismatic plane at 270 K. The distributions cannot be divided purely into liquid-like and solid-like orders, a remarkable finding pointing to the existence of an intermediate layer between QLL and bulk ice.

Self-diffusivity of the three most prominent ice surfaces

The most obvious difference between a liquid and a solid is the mobility of the molecules. While molecules oscillate around their equilibrium position in solids, they diffuse in liquids. In this chapter we study the dynamics of the surface layers to understand whether they behave as a liquid, a solid, or something in between.

6.1 Diffusion and mean square displacement

On a macroscopic scale, diffusion can be nicely visualised by a coloured tea bag in a hot water cup, where the diffusion of the coloured molecules can be observed. Diffusion in liquids is described at the molecular scale in terms of Brownian motion^a or, in other words, as a random walk of particles. Due to the non-zero kinetic energy, molecules move and change their moving directions due to collisions with other molecules. This picture is sufficient for our systems, because turbulences and other complex behaviour does not play a role. Early observations of Brownian motion were already made by Lucretius around 60 BC.^[159] Albert Einstein provided a description of Brownian motion in terms of diffusion processes.^{b[161,162]} According to Einstein, the relation between particle displacement and diffusion coefficient is:^[73]

$$\langle (x(t) - x(t_0))^2 \rangle = 2Dt, \quad (6.1)$$

where $\langle (x(t) - x(t_0))^2 \rangle$ is the mean square displacement (MSD) in one direction x , which can be easily obtained from molecular dynamics trajectories.^c This relation enables the determination of the one-dimensional diffusion coefficient D . For n dimensions this relation reads:^d

$$\langle (r(t) - r(t_0))^2 \rangle = 2 \cdot nDt. \quad (6.2)$$

^aBrownian motion was named after Robert Brown, who studied particles inside pollen grains in water.^[158]

^bThe Einstein-Smoluchowski relation has been published independently by Sutherland^[160], Einstein^[161,162], and Smoluchowski^[163]. A different approach for a theoretical description was provided by Langevin.^[164,165]

^cAnother possibility would be to obtain the diffusion coefficients over the velocity-velocity autocorrelation functions, which is an example for a so-called Green-Kubo relation, that relates transport coefficients to autocorrelation functions of a dynamical variable.^[166,167]

^dFor a three-dimensional system, the single components can also be obtained separately by Equation 6.1 by averaging over the three single diffusion coefficients.

In these equations the MSD increases linearly with time. One way to derive this linear relation is to describe diffusion as a random walk. It is easy to prove that the expectation value of the MSD in one dimension increases by l^2 with every step of length l :

$$\langle x(N+1)^2 \rangle = \frac{1}{2}(x(N) + l)^2 + \frac{1}{2}(x(N) - l)^2 = x(N)^2 + l^2, \quad (6.3)$$

where $x(N)$ is the distance from the origin after N steps. Since $x(N=0)^2 = 0$ it follows that $\langle x(N)^2 \rangle = Nl^2$.

The diffusion described by Equation 6.1 is called normal (or Fickian) diffusion, where the MSD is $\propto t^1$. If the MSD scales with t^η ($\eta \neq 1$), it is called anomalous diffusion.^[168,169]

One example for anomalous diffusion is the motion of free particles without collision, which is called ballistic motion and scales with an exponent of $\eta = 2$, because the distance from the origin grows linearly.^[161,162,170] Molecules always diffuse freely on very short time scales (less than a picosecond) until they collide with other molecules. Accordingly, the MSD scales with $\eta = 2$ first before normal diffusion starts. However, the time resolution of our analysis is too coarse to observe ballistic motion.

Another example for anomalous diffusion is confined motion, for example in glassy systems, where molecules are trapped in a kind of cage and cannot diffuse freely.^[171] In this case, the MSD scales with an exponent of $\eta < 1$.

In a solid, molecules oscillate around an equilibrium position. Thus, they return periodically to their starting position and the MSD displays a small oscillation.

The main quantity to describe diffusion is the already mentioned diffusion coefficient D . Most notably, a diffusion coefficient can only be determined with a linear fit of the MSD, if the molecules perform a random walk and, thus, the exponent η equals to one. Therefore, the first step in a diffusion analysis is to identify the exponent η of a process.

We study the diffusion of water molecules in water, which is called self-diffusion. Self-diffusion coefficients are temperature-dependent. Normal diffusion displays an Arrhenius behaviour and the temperature dependence can be expressed as^[172]

$$\ln(D) = \ln(D_0) - \frac{E_{A,\text{mol}}}{R \cdot T} = \ln(D_0) - \frac{E_A}{k_B \cdot T}, \quad (6.4)$$

where D is the diffusion coefficient and $E_{A,\text{mol}}$ is the molar activation energy (diffusion barrier) of the diffusion process, while E_A refers to the activation energy. D_0 is a temperature-independent constant, often referred to as the pre-exponential factor. R is the gas constant, k_B the Boltzmann constant, and T is the thermodynamic temperature.^[172]

6.2 Self-diffusion and mean square displacement at the hexagonal ice surfaces

Molecules diffuse not only within the layers of ice surfaces, but also between them (Figure 6.1).^{e[88]} However, diffusion events between the layers are rather seldom but for the top layers.

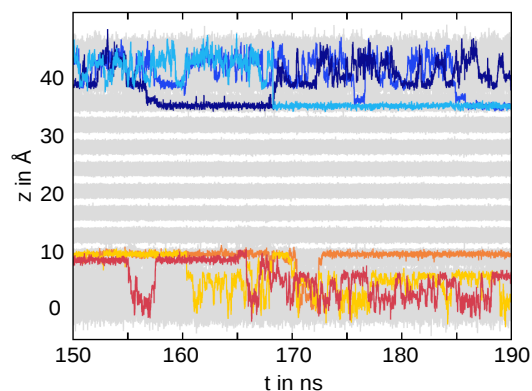


Fig. 6.1: Z-components of all oxygen atom trajectories for the last forty nanoseconds of the simulation of the basal plane at 270 K. Six selected trajectories are highlighted.

In order to quantify the exchange between the layers, rates were calculated by counting the molecules that intrude another layer by more than an arbitrary threshold of 0.8 \AA , which is about half the empty space between two inner layers in Figure

6.1. Molecules only touching the layer boundary would alter the rates without this threshold. Looking at the rates of the first layer of the basal plane, one could assume an Arrhenius behaviour between 200 K and 260 K (Figure 6.2). Nonetheless, the other rates do not display such a behaviour and a linear fit would, therefore, not be justified.

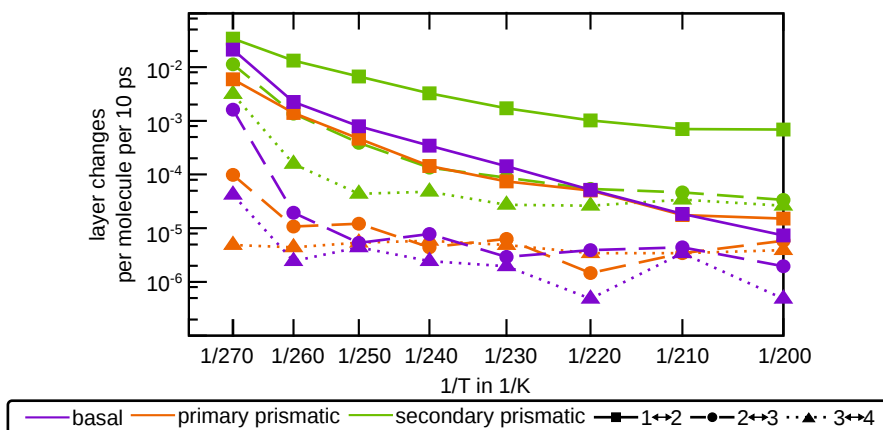


Fig. 6.2: Arrhenius plot of the exchange rates between the layers for all systems.

Due to the single-layer structure, the rates are largest for the secondary prismatic plane. The rates for the basal and the primary prismatic plane are similar besides a steep increase between 260 K and 270 K at the basal plane.

^eFor the visualisation of the paths of the primary and secondary prismatic plane see Appendix 8.5 Figure 8.73.

Only one evaporation event was observed for both the primary and the secondary prismatic plane within the last forty nanoseconds of the simulations at 270 K.^f

Of most interest is the in-plane self-diffusion, because it is larger than the out-of-plane self-diffusion. For a layer-resolved calculation of the mean square displacement, only parts of trajectories located in the analysed layer were evaluated.^g The obtained in-plane temperature-dependent MSDs of the surfaces are depicted in Figure 6.3.

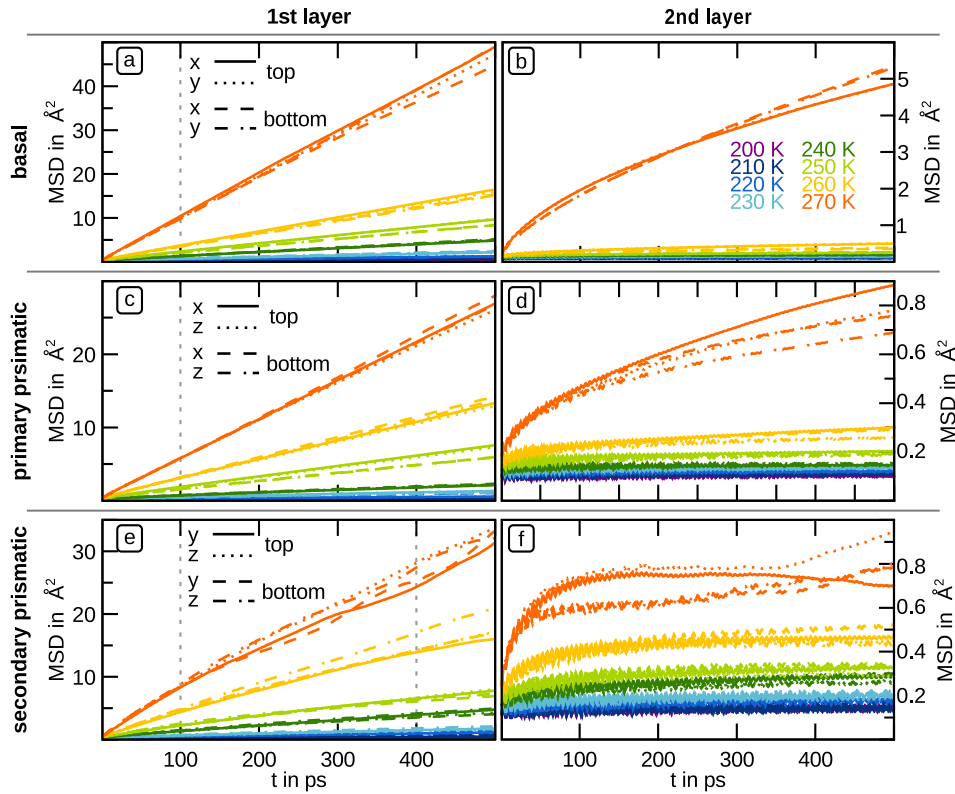


Fig. 6.3: Temperature-dependent mean square displacements for the first two layers of the basal plane, the primary prismatic plane, and the secondary prismatic plane. The time interval between 100 ps and 500 ps (400 ps for 270 K of the secondary prismatic plane) is indicated by grey dotted lines, because both linearity and statistics are considered sufficient within that range for a self-diffusion analysis. The corresponding contributions for the top and bottom surfaces and respectively the in-plane directions are displayed separately. See Appendix Figure 8.74 for log-log plots.

The MSDs of the first layer display the steepest increase at the basal plane (Figure 6.3 (a)), the second highest at the secondary prismatic plane (Figure 6.3 (e)), and the lowest at the primary prismatic plane (Figure 6.3 (c)). At low temperatures, the oscillations typical for solids are observed.

Evidently, the MSDs of all inner layers are far smaller than the ones of the first layers and below 1 Å^2 at 500 ps (Figures 6.3 (b), (d), and (f)). The only exception is the second layer of the basal plane at 270 K displaying anomalous diffusion.

^fFor details, see Appendix Figure 8.73.

^gThe top and bottom surfaces of the simulated slabs and their respective in-plane contributions were evaluated separately.

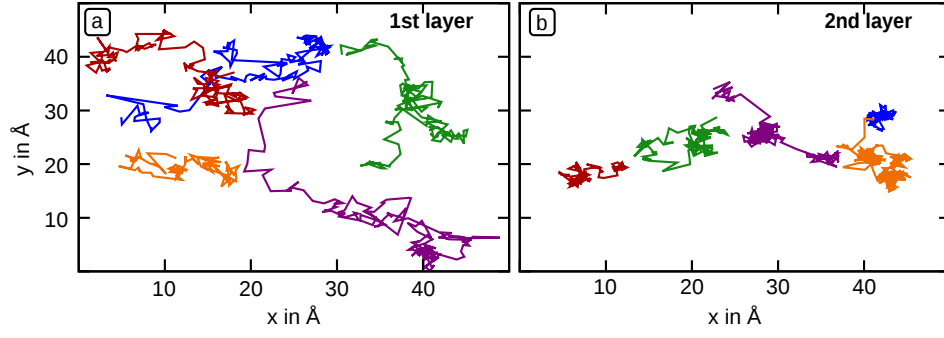


Fig. 6.4: Selected single-molecule trajectories of (a) the first bilayer and (b) the second bilayer of the basal plane at 270 K. The first bilayer displays normal diffusion resembling a random walk, while the trajectories in the second layer form clusters connected by narrow paths typical for diffusion in glassy systems.

While the molecules in the first layer can diffuse freely and perform random walks at 270 K (Figure 6.4 (a)), the molecules in the second layer cannot (Figure 6.4 (b)). In the second layer, the molecules are trapped in molecular cages and escape these cages infrequently until they become trapped again. This cage-effect is known from diffusion in glassy systems.^[173] On short time scales, diffusion is governed by movement inside the cages, while on long time scales, it is governed by diffusion between them.

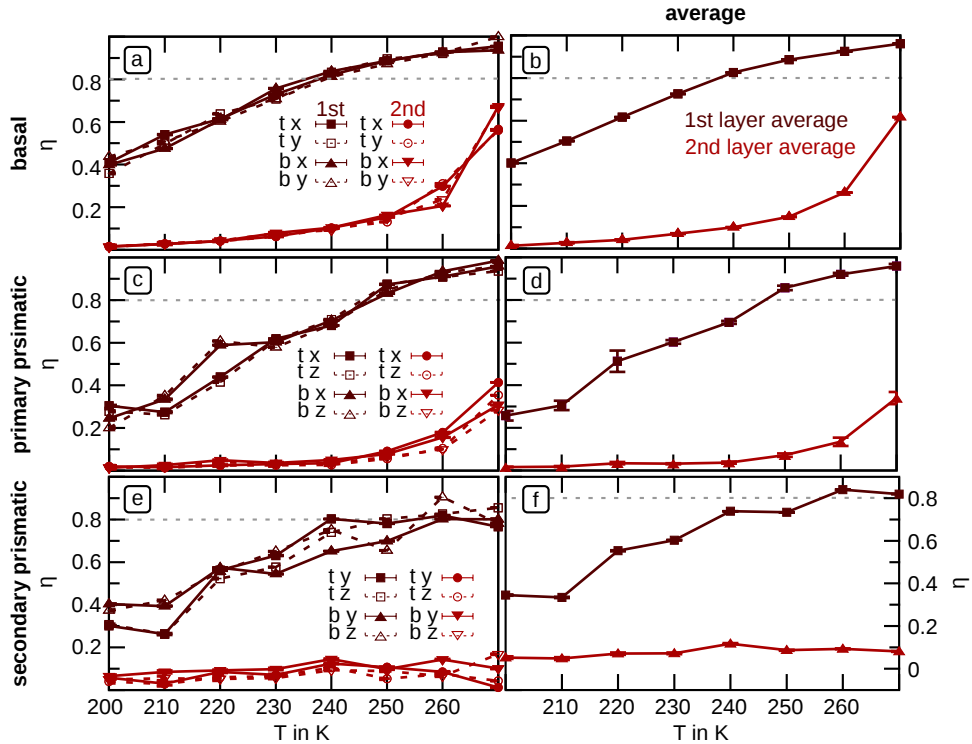


Fig. 6.5: Fitted exponents for the first two layers of the three ice surfaces. On the left side, the separate values for the in-plane directions at the top (t) and bottom (b) of the slabs are depicted. The average is plotted on the right hand side. The threshold of $\eta > 0.8$ is indicated by a grey dotted horizontal line.

In order to differentiate between normal (Figure 6.4 (a)) and glass-like (Figure 6.4 (b)) diffusion, the exponent of the $MSD \propto t^\eta$ was determined by a fit with Gnuplot^[174] using Equation 6.4 (Figure 6.5).^h[174] An arbitrary threshold of $\eta > 0.8$ was used to select the temperatures for which self-diffusion can be considered ‘normal’ and a meaningful self-diffusion coefficient can be calculated. This results in a temperature range from 240 K–270 K for the top bilayer of the basal plane, 250 K–270 K for the top bilayer of the primary prismatic plane and 260 K–270 K for the top single-layer of the secondary prismatic plane. Below these temperatures, diffusion can be considered glass-like.

The self-diffusion coefficients were then determined employing the relation $MSD(i) = 2D_i t$ for each in-plane direction i separately.ⁱ Thereafter, an Arrhenius analysis was performed using the calculated self-diffusion coefficients utilising Equation 6.4 (Figure 6.6). The fit parameters are displayed in Table 6.1.^j

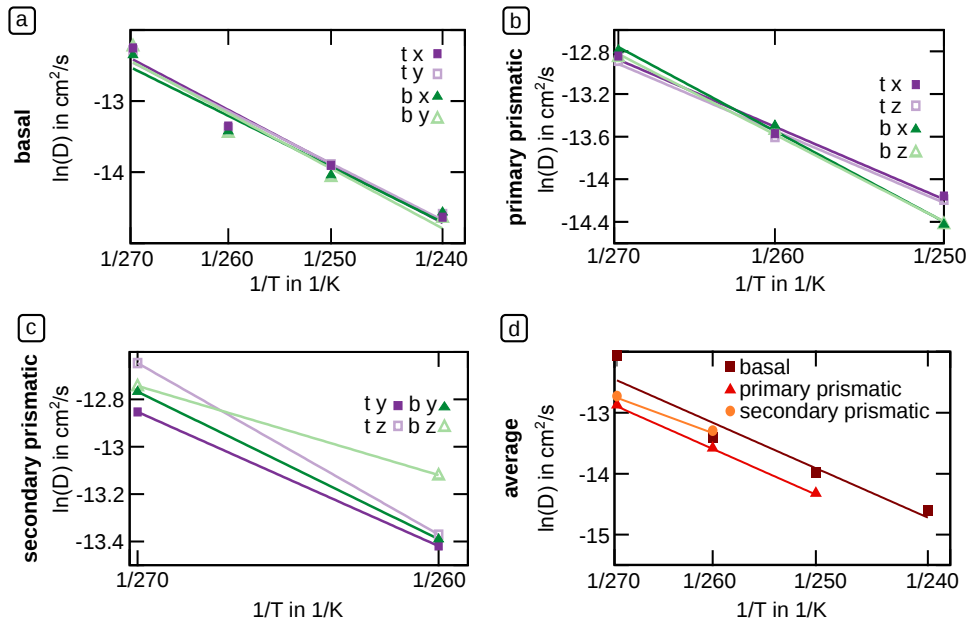


Fig. 6.6: (a)–(c) Arrhenius fits of the top (t) and bottom (b) surfaces and their respective in-plane directions separately. (d) Averaged fits.

Tab. 6.1: Fit parameters of the Arrhenius plots of Figure 6.6.

	D_0 in $\text{cm}^2 \text{s}^{-1}$	$E_{A,\text{mol}}$ in kJ mol^{-1}	E_A in eV
basal	0.031 ± 0.009	40.47 ± 0.71	0.42 ± 0.01
primary prismatic	0.080 ± 0.052	40.84 ± 2.44	0.42 ± 0.03
secondary prismatic	0.013 ± 0.012	33.42 ± 4.26	0.35 ± 0.04

^hThe respective values can be found in Appendix 8.5 in Tables 8.3 and 8.4.

ⁱThe obtained self-diffusion coefficients are displayed in the Appendix 8.5 in Table 8.5.

^jThe errors correspond to the standard errors of the separate values, which can be found in the Appendix 8.5 in Table 8.6.

The self-diffusion barriers for the basal plane and the primary prismatic plane are similar and slightly higher than the one for the secondary prismatic plane, although statistics are rather poor, especially for the secondary prismatic plane.

6.3 Comparison to supercooled water and literature

One question in the debate about the nature of the QLL is whether it behaves like supercooled water or not. Therefore, we compare the self-diffusion at the ice surface to supercooled water.

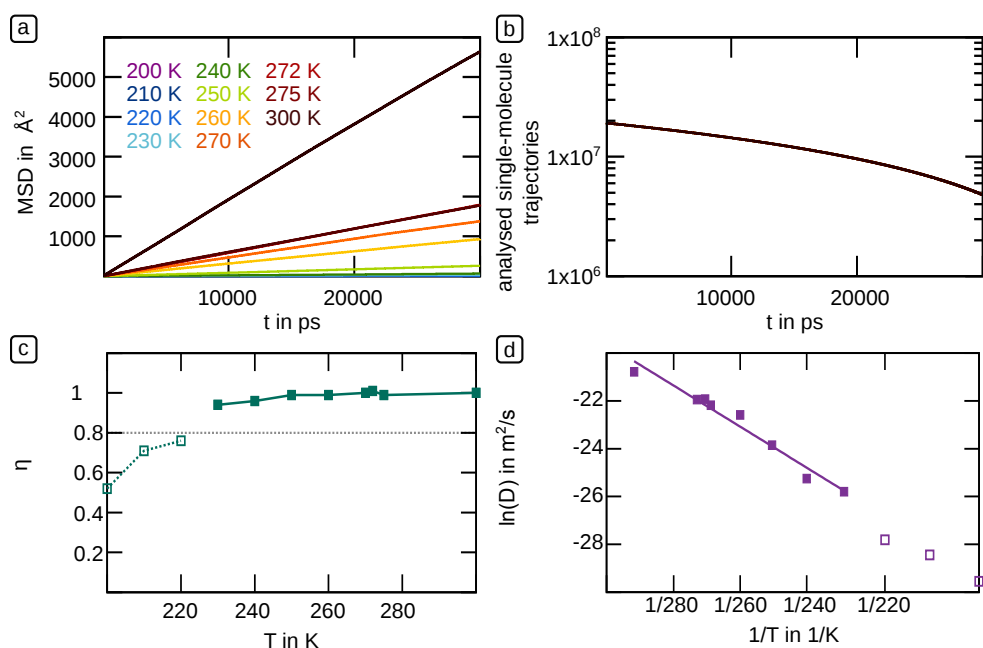


Fig. 6.7: (a) Mean square displacement (x-y-z-average). (b) Number of evaluated single-molecule trajectories. (c) Fitted exponents. Everything above a threshold of $\eta > 0.8$ is considered to be linear enough for fitting. (d) Fitted self-diffusion coefficients and their respective Arrhenius fits.

It is important to note that surface self-diffusion and bulk self-diffusion are different and, thus, a direct comparison is difficult.

In Figure 6.7 the temperature-dependent mean square displacements and the obtained Arrhenius fits are displayed.^k A self-diffusion barrier of 0.46 eV ($44.42 \text{ kJ mol}^{-1}$) was determined with an Arrhenius fit in agreement with literature.^[148] The self-diffusion barriers of the ice surfaces are only slightly smaller than the one of supercooled water.

^kThe program Gnuplot was used for the fits.^[174] All obtained values for the exponents can be found in the Appendix 8.5, Table 8.7. The self-diffusion coefficients are listed in Appendix 8.5 in Table 8.8.

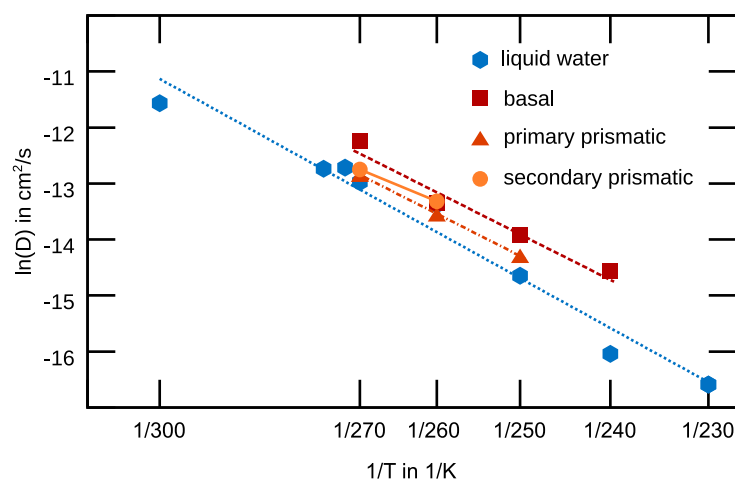


Fig. 6.8: Fitted self-diffusion coefficients for the reference liquid water, the basal, the primary prismatic, and the secondary prismatic ice surfaces and their respective Arrhenius fits.

In Figure 6.8, the self-diffusion coefficients of the ice surfaces and liquid supercooled water references are plotted together. It is evident that the self-diffusion coefficients are close to the ones of water for all surfaces and temperatures. They are only slightly higher—especially for the basal plane—probably due to the dangling bonds, resulting in an increased mobility of the surface molecules. This suggests that the nature of the QLL is similar to the one of liquid water with respect to self-diffusion.

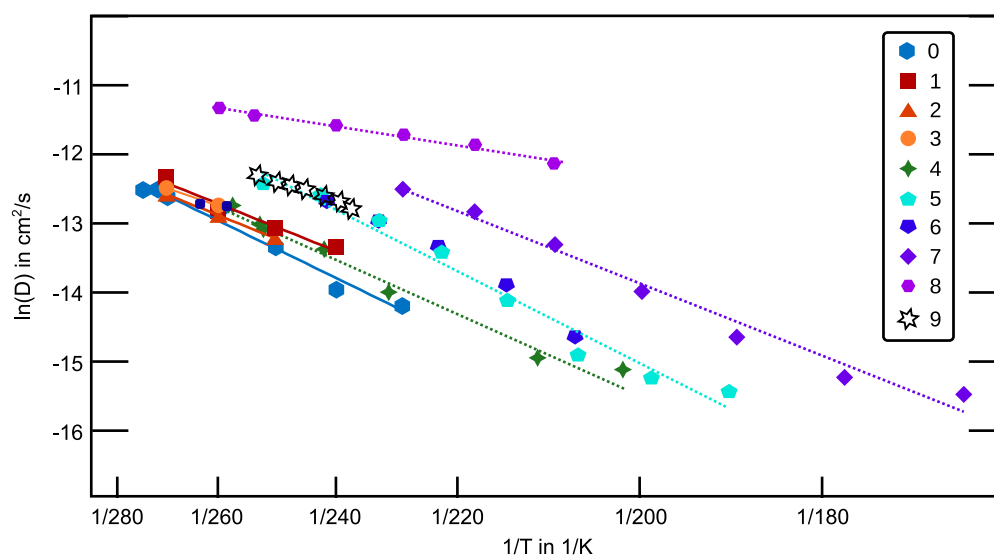


Fig. 6.9: Our simulations: (0) Supercooled water reference, (1) basal plane, (2) primary prismatic plane, (3) secondary prismatic plane. Literature values for diffusion coefficients of supercooled water as calculated from attachment rates in nucleation simulations using the force-fields: (4) TIP4P/Ice^[148], (6) TIP4P/2005^[148], (7) TIP4P^[148], (8) mW^[148]. (5) TIP4P/2005 for supercooled water up to 210 K.^[175] (9) Experimental values for supercooled water.^[176]

Last but not least, the self-diffusion analysis is compared to literature in Figure 6.9. The obtained values agree well with the values from simulations utilising the same force-field.^[148] The self-diffusion coefficient of liquid water is underestimated by the TIP4P/Ice force-field as already reported by literature.^[177]

6.4 Self-diffusion anisotropy

A self-diffusion anisotropy has been reported for the primary prismatic plane between the in-plane directions, while no anisotropy was found for the basal plane.^[155] On the contrary, our simulated systems display no significant differences between the in-plane directions and the differences between the top and bottom surfaces caused by statistical sampling are larger in agreement with [16]. Interestingly, the study mentioned previously^[155] rescaled their self-diffusion coefficients based on an order parameter based approach, which selects ‘liquid’ molecules. The drawbacks of such an approach were discussed in Chapter 5.

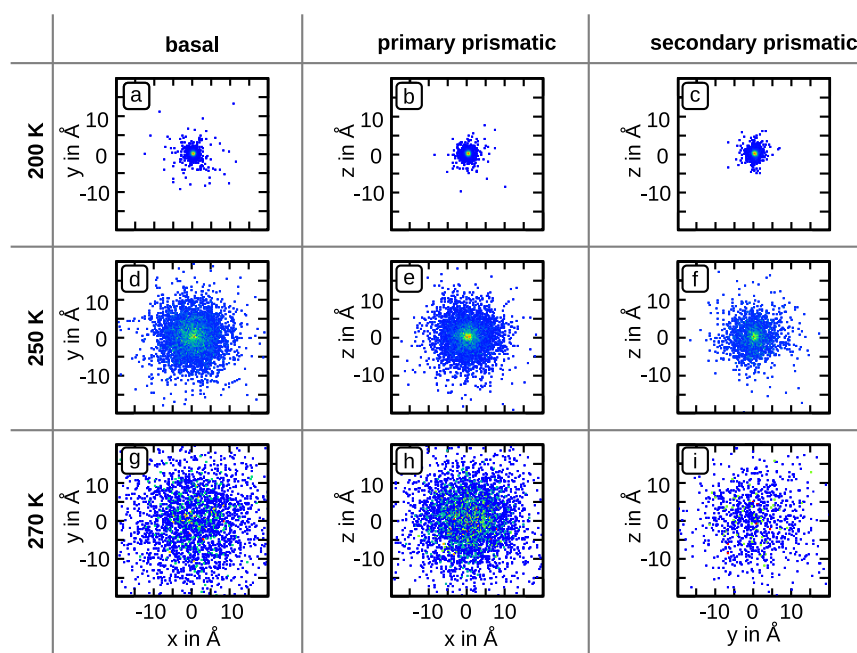


Fig. 6.10: Two-dimensional histograms of the oxygen atom motion vectors in the top layer of all three surfaces at 200 K, 250 K, and 270 K. Forty snapshots in an interval of 1 ns were analysed each.

Furthermore, the in-plane self-diffusion directions were analysed by plotting a two-dimensional histogram of the molecular translation vectors at the top layer between snapshots (Figure 6.10).¹ In general, no regular pattern can be observed for all surfaces and no preferred self-diffusion direction can be identified.

¹The pictures depend on the time between the snapshots, but no pattern was observed for different intervals (Appendix Figure 8.79).

6.5 Conclusion

In summary, three types of dynamical behaviour, namely solid-like, liquid-like, and glass-like, are observed at the ice surface. Only the first layer displays normal self-diffusion for all studied surfaces, in contrast to disorder, which propagates further into the bulk. At the first layer self-diffusion changes rather gradually from glass-like to normal diffusion with increasing temperature.

The second layer of the basal plane, where order parameter analysis (Chapter 5) already suggests a liquid-like structure, behaves like a glass in terms of diffusion at 270 K.

Surprisingly, little diffusion is observed in the second layer of the secondary prismatic plane, though it is more strongly disordered than the second layer of the basal plane. All other inner layers of all surfaces do not display large mean square displacements, even if order parameter analysis suggests a liquid-like structure in some cases.

This emphasises the importance of making a distinction between disorder and true liquid-like behaviour characterised by diffusion.

In contrast to [155] and in agreement with [16], no anisotropy was observed for the in-plane self-diffusion directions.

The highest self-diffusion coefficients were determined for the basal plane, followed by the secondary prismatic and the primary prismatic plane. The self-diffusion barriers for the basal and the primary prismatic plane are similar, while the barrier is lower for the secondary prismatic plane, even though the number of data points is limited. The self-diffusion coefficients of all surfaces at all temperatures are close to that of water. Therefore, the QLL can be considered liquid-like at high temperatures from a diffusion perspective.

Conclusion

In this thesis, the low-index surfaces of hexagonal ice I_h —namely the basal plane $\{0001\}$, the primary prismatic plane $\{10\bar{1}0\}$, and the secondary prismatic plane $\{\bar{1}2\bar{1}0\}$ —are examined in a temperature range from 200 K to 270 K using classical molecular dynamics simulations. The TIP4P/Ice rigid water model is employed, as it provides the closest resemblance to the thermodynamics of the solid-liquid phase transition of water.

The surface of ice has been a popular research topic throughout the last decades and has been studied extensively both experimentally and theoretically.^[18,26,123] The main purpose of this work is not only to quantify the changes the surface undergoes with increasing temperature, but to provide a careful analysis of these changes from different points of view. These perspectives can be divided into two main categories, namely dynamical analysis (such as the calculation of diffusion coefficients) and short-range and medium-range structural analysis (e.g. order parameter analysis).

With structural analysis we probed the transition from ordered to disordered arrangements of surface layers for all the surfaces considered.

We found the layer structure to persist throughout the whole temperature range. Our structural analysis, including radial distribution functions (Chapter 3), H-bond analysis (Chapter 4), medium-range network topology (Chapter 4.4), and order parameters (Chapter 5) indicates that 2–3 layers ($\approx 8 \text{ \AA}$ – 12 \AA) are disordered with a structure similar to that of liquid water at 270 K for the basal plane, 1–2 layers ($\approx 4.5 \text{ \AA}$ – 8.5 \AA) for the primary prismatic plane, and 2–4 layers ($\approx 5 \text{ \AA}$ – 9.5 \AA) for the secondary prismatic plane. We state ranges, because some parameters are just between the values of the liquid and solid references indicating some intermediate order. The observed trend that the thickness of the disordered interface at the basal plane is largest and the thickness at the primary and secondary prismatic plane is similar is in agreement with X-ray diffraction measurements.^[28]

Interestingly, a sudden increase of disorder is detected for the second layer of the basal plane between 260 K–270 K. This explains an abrupt peak shift observed in sum-frequency-generation spectroscopy measurements at about 260 K.^[1] The same measurements detect a gradual change in disorder at the secondary prismatic plane, where we do not see such a sudden change as well.^[1]

The surface of the primary prismatic plane is less disordered than the surface of the basal plane and the rearrangement of molecules at the top layer seems to be more efficient, because of the lower amount of dangling bonds (Chapter 4). While the disorder at 270 K changes smoothly from the surface into the bulk at the secondary prismatic plane, a step-wise decrease of disorder is observed for the basal plane and the primary prismatic plane and the difference in disorder among the layers is larger as revealed by order parameter analysis (Chapter 5).

The results of the topological network analysis are especially interesting (Chapter 4.4).^[14] The total number of rings (independent of the ring size) one molecule participates in is similar for both liquid water and ice. However, while ice consists almost exclusively of six-membered-rings, liquid water forms a variety of ring types (mainly six-, seven-, eight-, and nine-membered rings). The molecules of the top layers at all surfaces form mostly five-, six-, and seven-membered rings and, thus, differ significantly from both solid and liquid references. The formation of non-six-membered rings has already been reported in literature, but we are the first to provide a quantitative topological analysis.^[14–16]

Even though local order is lost within the top layer at the highest temperatures, the surfaces retain an ordered structure averaging over several snapshots as revealed by two-dimensional density maps (Chapter 3.3). This is caused by a templating effect induced by the underlying layer. Accordingly, measurements with a low time resolution, such as electron and X-ray diffraction, averaging over a time period in which molecules can diffuse may detect less disorder than techniques with a high time resolution, such as X-ray absorption and sum-frequency-generation spectroscopy, corresponding to single snapshots. This may explain some of the discrepancies in experimental literature.

A very different picture is obtained from dynamical analysis. According to the mean square displacement calculation, only the top layer displays normal diffusion and can be considered liquid-like for all surfaces at high temperatures (Chapter 6). Diffusion taking place only at the top layer of the basal plane has been reported before.^[16] At lower temperatures, diffusion is more similar to that of a glassy system, where molecules are trapped in molecular cages and infrequently escape them. To the best of our knowledge, glass-like diffusion has not been reported at the ice/vacuum interface before. In our work, we observe isotropic diffusion at the surface in agreement with [16].

The only second layer that displays a large increase of the mean square displacement is the one of the basal plane at 270 K. However, its dynamic is sub-diffusive and glass-like. All other layers display little diffusion. Although the first layer is liquid-like in terms of diffusion at temperatures close to the melting point, the self-diffusion coefficients are slightly higher than for supercooled water at the same temperature. This is explained by dangling bonds at the surface and the resulting increased mobility of the molecules. These findings are supported by the dynamical H-bond analysis, which quantifies the amounts of bonds breaking or changing the partner (Chapter 4.3). Finally, we found that diffusive layers are separated from the bulk by an interfacial layer that retains a crystalline arrangement, but exchanges molecules with the diffusive layer.

In summary, we show that different analysis techniques yield substantially different results for the very same system. The first layer of each surface is both dynamically and structurally similar to liquid water at temperatures close to the melting point. At low temperatures, sub-diffusion is observed when structural parameters already suggest a liquid-like structure. The next few layers are only structurally similar to liquid water close to the melting point, but do not diffuse or display glass-like dynamics. All the deeper layers behave just like bulk ice. Therefore, an assignment of liquid-like molecules solely based on a structural order parameter analysis overestimates the volume of the quasi-liquid-layer. Accordingly, measurement techniques probing the structure of a system measure the thickness of the disordered interface, which is higher than the thickness of the liquid layer from diffusional point of view.

Outlook

Ice is not perfect in nature. Thus, a next logical step would be to add defects and contaminants like molecules present in the atmosphere to the simulations. Apart from that, simulations closer to the melting point would be desirable to study the melting process, requiring longer trajectories of hundreds of nanoseconds. Also, the closer to the melting temperature, the larger the systems needed, since not only the period, but also the wavelength of the fluctuations diverges near a first-order phase transition.

In addition, classical MD simulations employing suitable polarisable force-fields like MB-pol would be interesting to simulate spectra for a comparison to spectroscopy experiments.^[178–182]

Appendix

8.1 Chapter 1: Melting away—hexagonal ice and its surface

Tab. 8.1: Measurement techniques probing the hexagonal ice surface.

Technique	References
Ellipsometry	[27, 41, 183, 184]
Nuclear magnetic resonance (NMR) spectroscopy	[34, 185–187]
Scanning probe microscopy (SPM)	[37–39, 47, 64, 188–190]
Sum-frequency-generation (SFG) spectroscopy	[68, 70, 191–193]
Laser confocal microscopy combined with differential interference contrast microscopy (LCM-DIM)	[51–59]
Optical microscopy/optical reflectometry	[41]
Proton channelling	[30, 31]
Neutron scattering	[194, 195]
He scattering	[32, 196]
X-ray diffraction	[28, 44, 45, 66, 71, 197]
Rutherford backscattering	[198]
Infrared laser resonant desorption (IR-LRD)	[199, 200]
Attenuated total reflection infrared spectroscopy (ATR-IR)	[201, 202]
Quartz crystal microbalance (QCM)	[203]
Thermal expansion	[204]
Volta effect	[89]
Electrical conductivity	[29, 205–207]
Photoemission spectroscopy (PES)	[35, 40]
Calorimetry	[208]
Wire regelation and freezing experiments	[209, 210]
Adsorption	[211]
Grazing angle laser spectroscopy	[212, 213]
Differential interference contrast microscopy	[214]
Low energy electron diffraction (LEED)	[84]
Growing of ice crystals and measuring the stability	[60]
Optical interference	[215]

8.2 Chapter 3: Structural analysis

8.2.1 Miller-Bravais indices

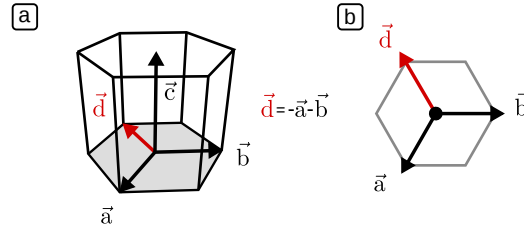


Fig. 8.1: Miller-Bravais indices and its vectors: introduction of an auxiliary vector \vec{d} .

Miller-Bravais-indices have four indices ($HKIL$), where $I = -H - K$, since an additional auxiliary vector \vec{d} is added as shown in Figure 8.1. A plane is defined as ($HKIL$), which cuts the unit vector \vec{a} at $1/H$, the unit vector \vec{b} at $1/K$, the auxiliary vector $\vec{d} = -\vec{a} - \vec{b}$ at $1/I$, and the unit cell vector \vec{c} at $1/L$. We use the four index Miller-Bravais indices since the planes ($HKIL$) are perpendicular to the directions $[HKIL]$, which is in general not the case for the Miller indices. In addition, it is easy to identify symmetrically equivalent planes, since the notation $\{HKIL\}$ corresponds to the set of planes obtained by permutation and sign changes of the first three Miller-Bravais indices.

For example, the symmetry equivalent set of the primary prismatic planes $\{10\bar{1}0\}$ corresponds to the set $\{10\bar{1}0\} = \{(10\bar{1}0), (\bar{1}100), (0\bar{1}10), (\bar{1}010), (1\bar{1}00), (01\bar{1}0)\}$. Along that line are the symmetry equivalent planes for the secondary prismatic face:

$\{\bar{1}2\bar{1}0\} = \{(\bar{1}2\bar{1}0); (\bar{1}\bar{1}20); (2\bar{1}\bar{1}0); (\bar{1}210); (11\bar{2}0); (2110)\}$.

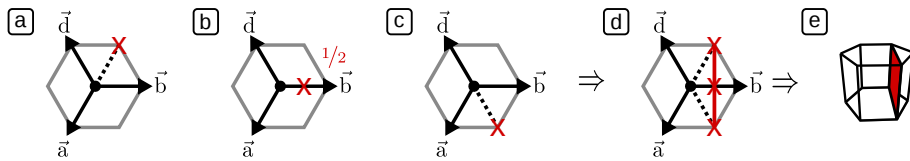


Fig. 8.2: Determination of one secondary prismatic plane based on the Miller-Bravais indices ($\bar{1}2\bar{1}0$).

This can be explained by the example of the secondary prismatic plane notation ($\bar{1}2\bar{1}0$) shown in Figure 8.2. Starting from the symbol of the plane ($\bar{1}2\bar{1}0$), it can be deduced that the vector \vec{a} is cut at $1/-1$ (Figure 8.2 (a)), while the vector \vec{b} is cut at $1/2$ (Figure 8.2 (b)). The vector \vec{c} is cut at $1/-1$ and the fourth index determines a cut at $1/0$, which leads to a parallel plane to \vec{c} . Similarly, the other two surfaces can be determined (Figure 8.3).

In a nutshell, the primary prismatic surfaces are the planes which are tangential to the hexagon (Figures 8.3 (b) and 8.5), while the secondary prismatic planes cut the edges of the hexagon (Figures 8.3 (c) and 8.6).

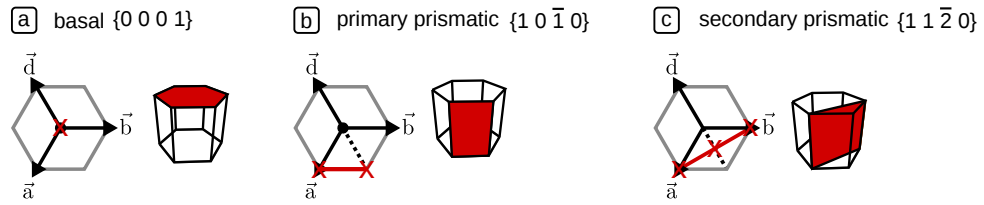


Fig. 8.3: Examples of the symmetry-equivalent planes for the three low-index surfaces of hexagonal ice.

More details about all members of the groups are shown in Figures 8.4, 8.5, and 8.6.

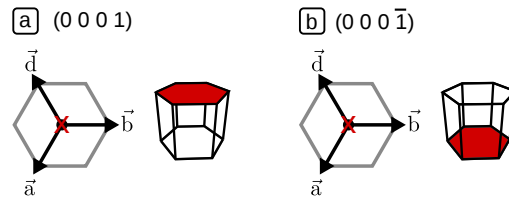


Fig. 8.4: Full set of symmetry equivalent planes for the basal plane $\{0001\} = \{(0001); (000\bar{1})\}$.

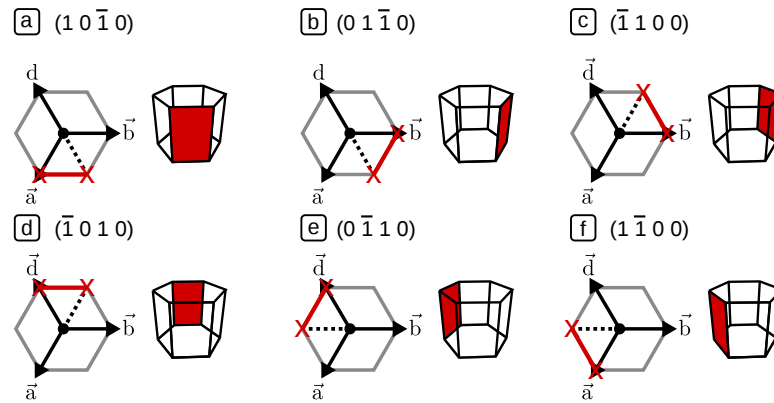


Fig. 8.5: Full set of symmetry equivalent planes for the primary prismatic plane $\{10\bar{1}0\} = \{(10\bar{1}0), (\bar{1}100), (0\bar{1}10), (\bar{1}\bar{1}00), (1\bar{1}00), (01\bar{1}0)\}$.

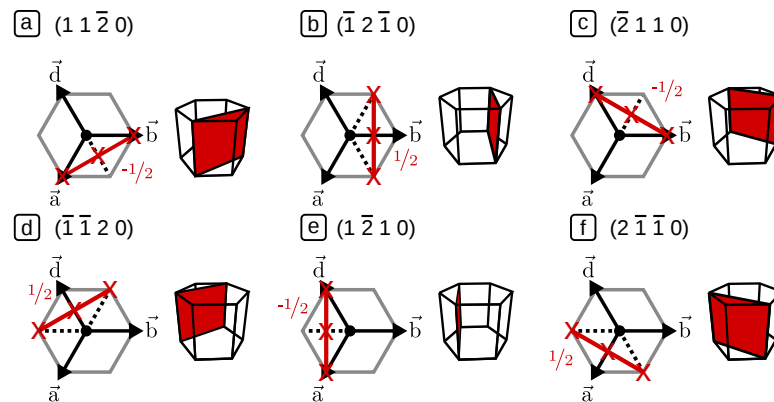


Fig. 8.6: Full set of symmetry equivalent planes for the secondary prismatic plane $\{\bar{1}2\bar{1}0\} = \{(\bar{1}2\bar{1}0), (\bar{1}\bar{1}20), (2\bar{1}\bar{1}0), (1\bar{2}10), (1\bar{1}20), (2\bar{1}10)\}$.

8.2.2 Two-dimensional density profiles

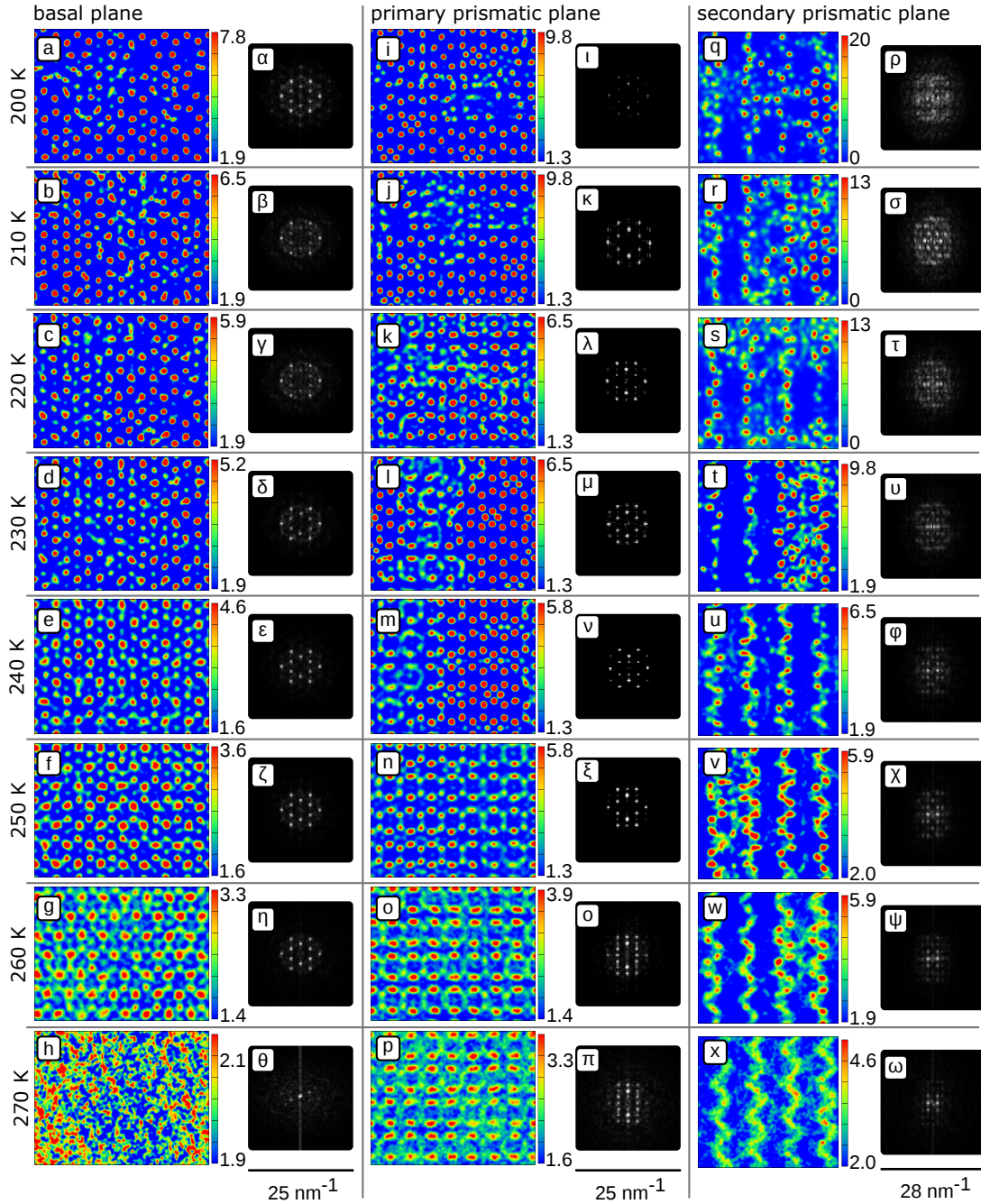


Fig. 8.7: Two-dimensional density maps of the oxygen atoms belonging to the first layer of the basal, primary prismatic, and secondary prismatic plane for all simulated temperatures.

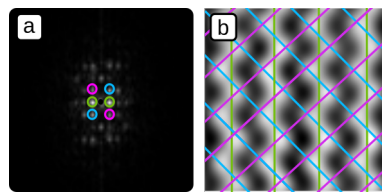


Fig. 8.8: (a) 2D-FFT of the original 2D density map of the secondary prismatic plane at 250 K. (b) 2D-FFT of (a). The coloured circles in (a) refer to the respective coloured periodicities in (b).

8.2.3 Rescaled RDFs for a slab with two sharp interfaces

A radial distribution function (RDF) is defined as the average atom density relative to the overall density at a distance r from the centre of the atom:

$$g(r) = \frac{\langle N(r) \rangle}{\frac{dV(r)}{dr}} \cdot \frac{1}{\rho_{\text{tot}}}, \quad (8.1)$$

where $\langle N(r) \rangle$ is the average number of particles at the distance r , $\frac{dV(r)}{dr}$ is the infinitesimal small volume at that distance, and ρ_{tot} the total density of the system.

This may be rewritten as:

$$g(r) = \frac{\sum_{i=1}^N \sum_{j \neq i} \delta(r_{ij} - r)}{N \cdot A_{\text{sphere}}(r)} \cdot \frac{V_{\text{tot}}}{N}. \quad (8.2)$$

Here, r_{ij} is the distance between the two particles i, j and V_{tot} defines the volume of the entire system. The surface of the sphere A_{sphere} corresponds to the volume element $\frac{dV(r)}{dr}$ of an infinitesimal thin spherical shell of the surface area A . The delta function ensures that only the particles at a distance r are counted when calculating the average. Hence, the double sum is divided by the number of particles N .

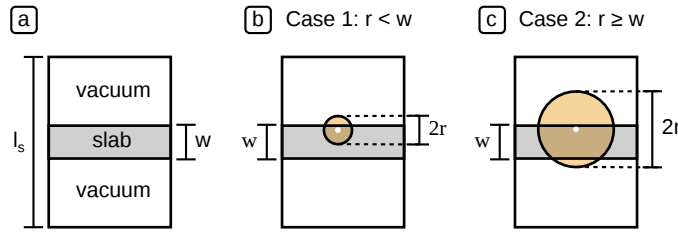


Fig. 8.9: Illustrations for the rescaling of the RDF for a slab with two sharp interfaces.

It is often desirable to compare the RDFs of a slab with two sharp interfaces to that of a bulk system. Therefore, a scaled RDF, g_{scaled} , is calculated by rescaling the slab RDF g_{slab} thereby removing the effects of the empty volume (Figure 8.9 (a)). Here, two cases need to be distinguished:

- CASE 1: $r < w$ (Figure 8.9 (b))

Only atoms in the vicinity of the slab boundary are affected by the empty volume around the slab. In other words, only atoms in a distance smaller than r to the surface are influenced. Since a slab has two boundaries, $2 \cdot \frac{r}{w}$ is the fraction of molecules which fulfil these requirements. Assuming that all atoms are distributed evenly, a quarter of the spheres (based on their volumes) are outside of the slab on average as a maximum of 0.5 and a minimum of 0 of the shells may be outside of the slab. The surface area of a segment, A_{seg} , is proportional to the height h of a spherical segment according to $A_{\text{seg}} = A_{\text{sphere}} \cdot \frac{h}{2r}$, where A_{sphere} corresponds to

the surface area of a sphere with radius r and a total height of $2r$ (Figure 8.9 (b)). This relation is based on a discovery by Archimedes, which states that a sphere of radius r has the same surface area as the curved surface area of a cylinder with radius and height r . In other words, the surface of a sphere segment equals to the corresponding cylinder segment.

Accordingly, the infinitesimal small volume inside of the slab corresponds to $A_{\text{sphere}} \cdot (1 - \frac{2r}{w} \cdot \frac{1}{4})$.

Note that the change in volume of the slab needs to be considered for the density, too. The properly rescaled volume is $V_{\text{slab}} = V_{\text{tot}} \cdot \frac{w}{l_s}$, where l_s corresponds to the total height of the simulation box (Figure 8.9 (a)).

In a nutshell, the rescaled RDF for CASE 1 is:

$$g_{\text{slab}}(r) = \frac{\sum_{i=1}^N \sum_{i \neq j} \delta(r_{ij} - r)}{N \cdot A_{\text{sphere}} \cdot (1 - \frac{2r}{w} \cdot \frac{1}{4})} \cdot \frac{V_{\text{tot}} \cdot \frac{w}{l_s}}{N} = g(r) \cdot \frac{w}{l_s} \cdot \frac{1}{1 - \frac{r}{2w}}. \quad (8.3)$$

- CASE 2: $r \leq w$ (Figure 8.9 (c))

All atoms are affected by the empty volume outside of the slab. The fraction of the spheres inside the slab equals to $\frac{w}{2r}$, since the height of a sphere corresponds to $2r$, which leads to the formula

$$g_{\text{slab}}(r) = \frac{\sum_{i=1}^N \sum_{i \neq j} \delta(r_{ij} - r)}{N \cdot A_{\text{sphere}} \cdot \frac{w}{2r}} \cdot \frac{V_{\text{tot}} \cdot \frac{w}{l_s}}{N} = g(r) \cdot \frac{2r}{l}. \quad (8.4)$$

8.3 Chapter 4: Hydrogen bonding analysis

8.3.1 Percentage of free OH on non-rearranged surfaces

In Figure 8.10 (a), the oxygen atoms of the first bilayer of a basal surface are depicted. The darker red atoms belong to the upper half of the bilayer. Only the upper part of the bilayer has the possibility of having a free OH (Figure 8.10 (b)). By looking at only 50 % of the oxygen atoms (upper molecules), only 50 % of those have an H-bond that points upwards, while the other 50 % have H-bonds which point downwards. Since each depicted oxygen atom has two H-bonds instead of one, a total percentage of $50 \% \cdot 50 \% \cdot 50 \% = 12.5 \%$ of free OH are obtained in the case of a non-rearranged basal plane.

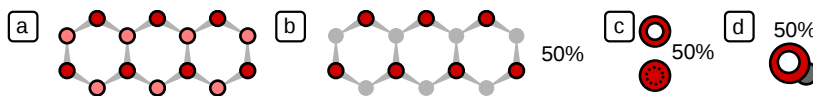


Fig. 8.10: Percentage of free OH present on a non-rearranged basal plane {0001}.

For the primary prismatic plane, 50 % of the molecules of the first bilayer belong to the upper half (Figure 8.11 (b)). The probability that an H-bond of those molecules points upwards is the same as that for an H-bond pointing downwards, namely 50 % (Figure 8.11 (c)). Each water molecule has two hydrogen atoms that can form H-bonds. In total, a percentage of free OH of $50 \% \cdot 50 \% \cdot 50 \% = 12.5 \%$ is obtained. Thus, the theoretical prediction of the amount of dangling bonds is the same for the basal and the primary prismatic plane.

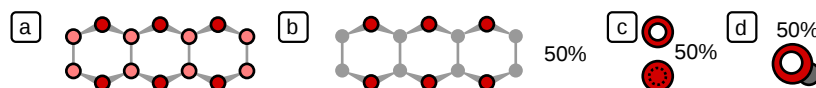


Fig. 8.11: Percentage of free OH present on a non-rearranged primary prismatic plane $\{10\bar{1}0\}$.

The secondary prismatic plane consists of equally spaced single-layers instead of bilayers, as we already discussed for the other two. In this case, all of the molecules are obviously in the ‘upper’ part of the layer. Each molecule has a 50 % chance that one H-bond points upwards. Since each of them has two H-bonds, this adds up to a percentage of $100 \% \cdot 50 \% \cdot 50 \% = 25 \%$ of theoretical free OH (Figure 8.12).

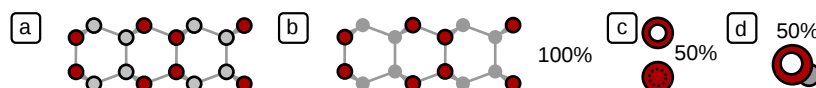


Fig. 8.12: Percentage of free OH present on a non-rearranged secondary prismatic plane $\{1\bar{2}10\}$.

8.3.2 Statical Analysis

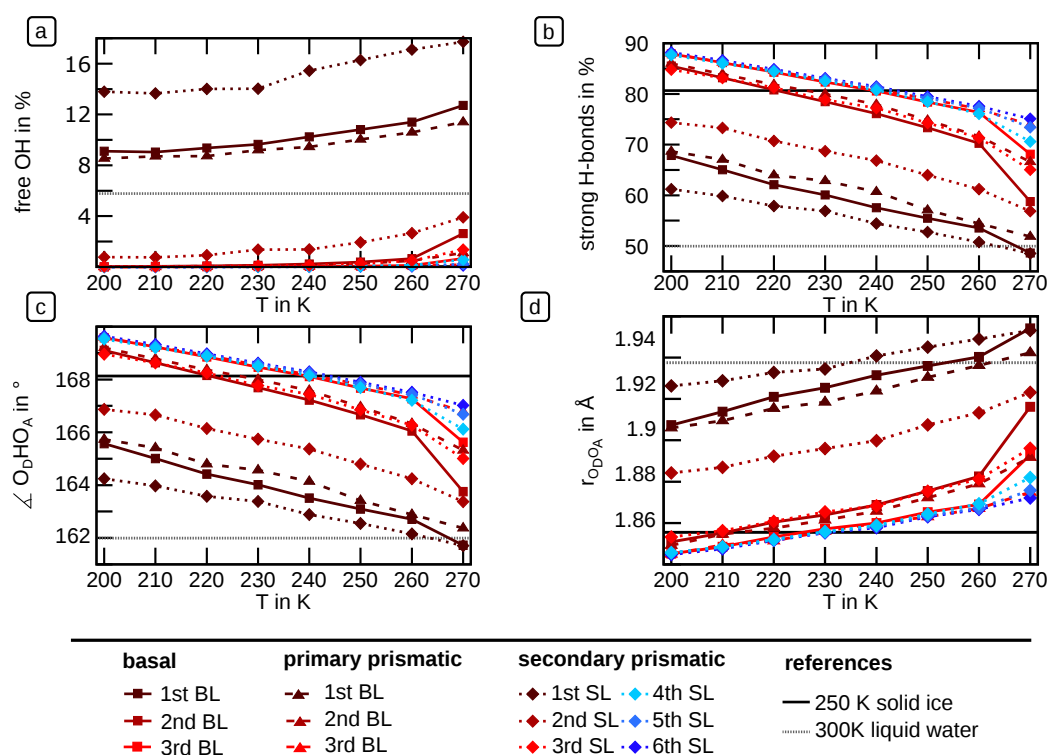


Fig. 8.13: Temperature-dependent (a) percentage of free OH at the surface, (b) percentage of strong H-bonds, (c) average $\angle O_D H O_A$ -angle, (d) average $r_{O_D O_A}$ of ice slabs for up to the upper six layers.

8.3.3 Spheres

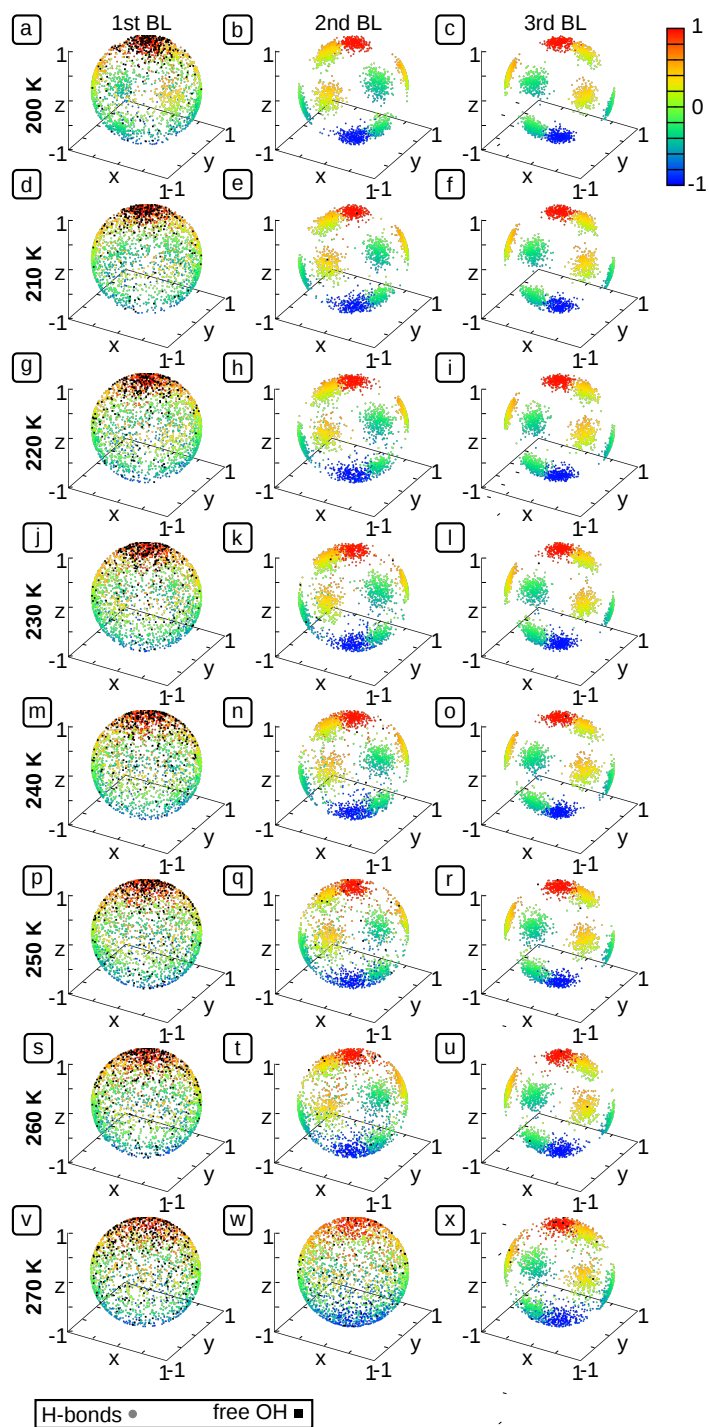


Fig. 8.14: Spherical orientation of the *OH*-vectors for the upper three bilayers of the basal plane at temperatures from 200 K–270 K.

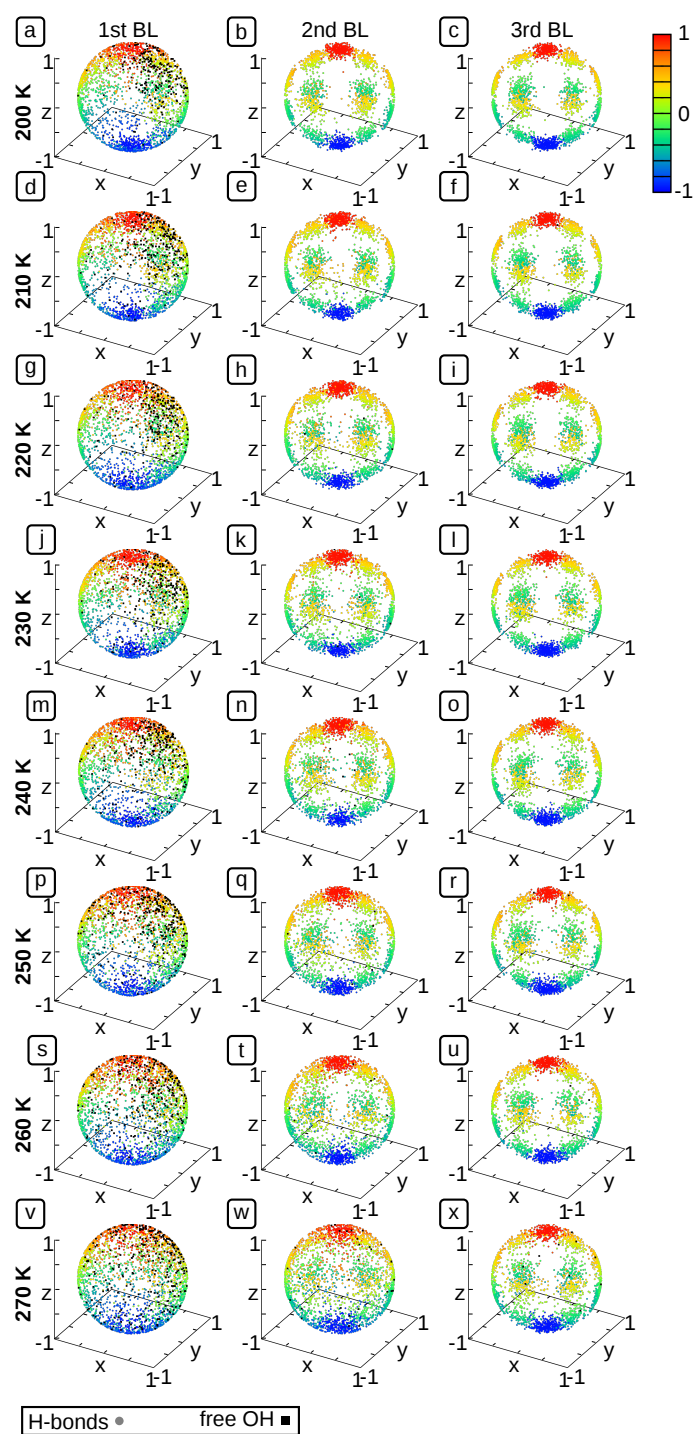


Fig. 8.15: Spherical orientation of the *OH*-vectors for the upper three bilayers of the primary prismatic plane at temperatures from 200 K–270 K.

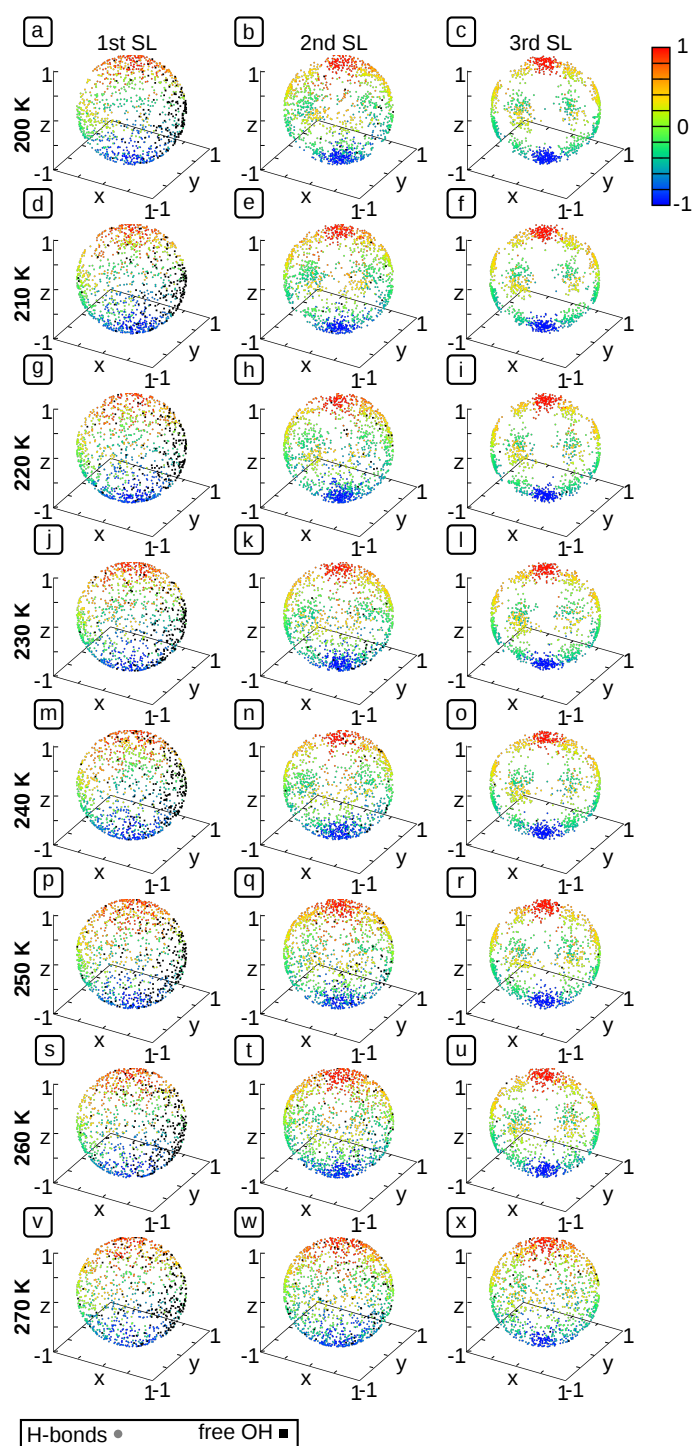


Fig. 8.16: Spherical orientation of the *OH*-vectors for the upper three single-layers of the secondary prismatic plane at temperatures from 200 K–270 K.

8.3.4 Orientation of the OH -vector

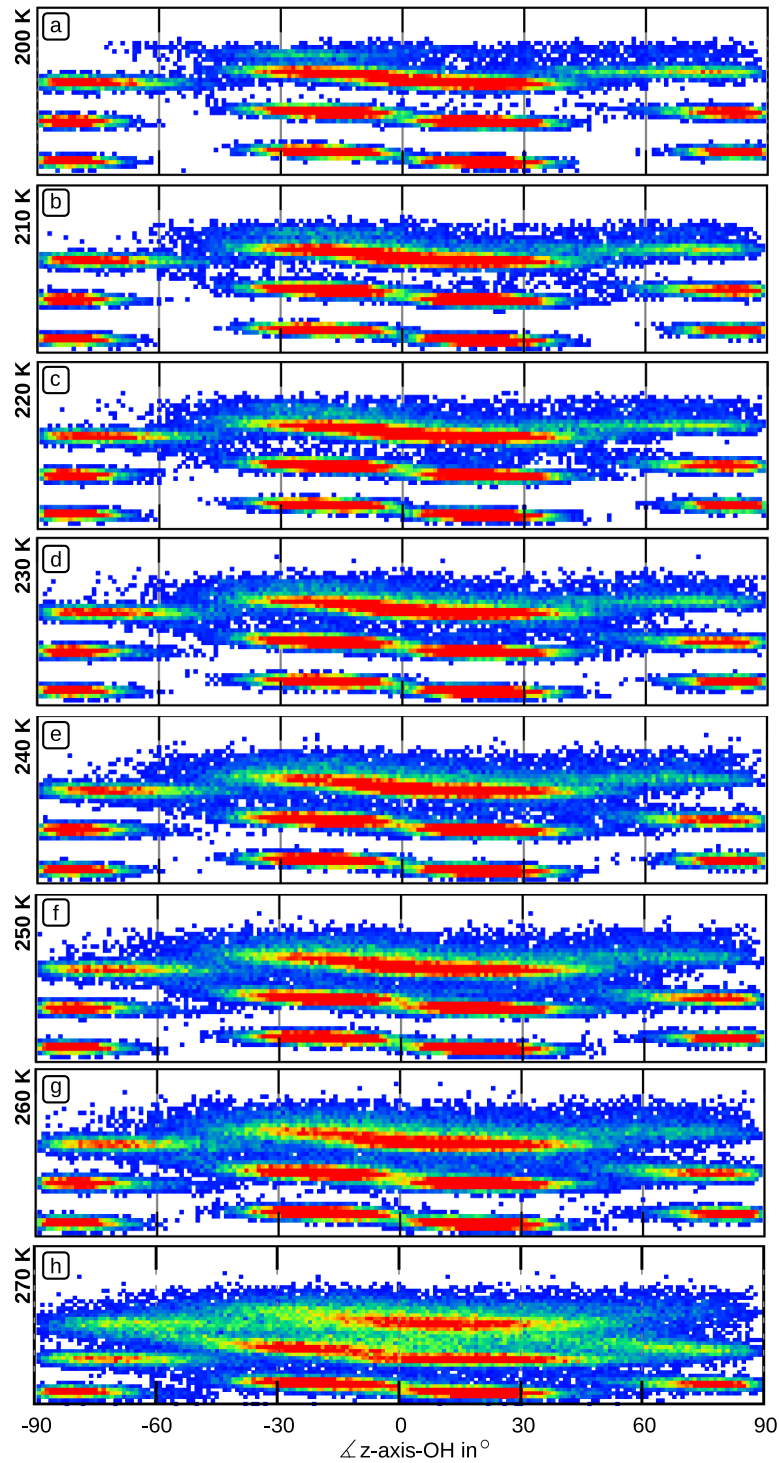


Fig. 8.17: Z-resolved two-dimensional histogram of the distributions of the OH -vector with respect to the $[0001]$ -direction for the basal plane exposed to vacuum.

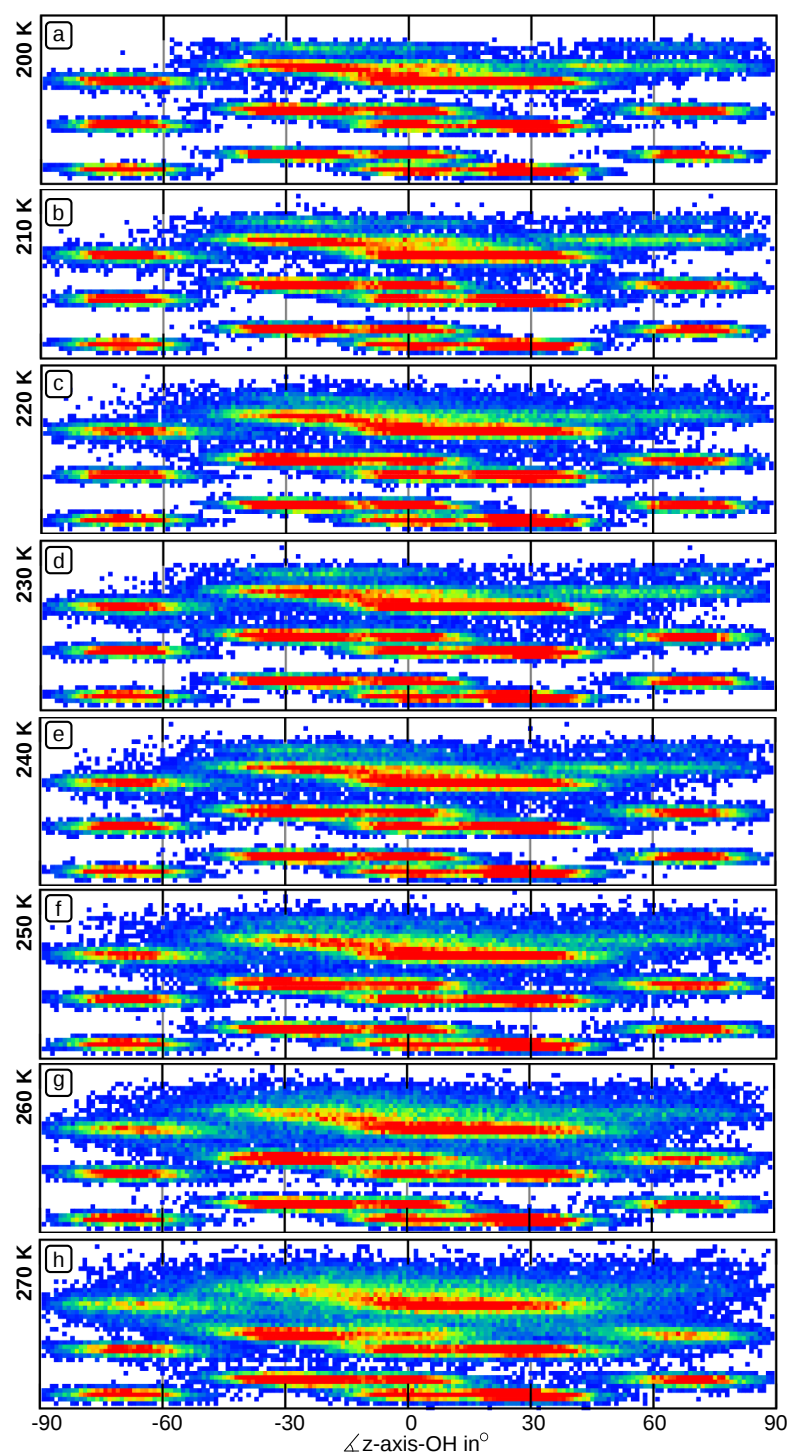


Fig. 8.18: Z-resolved two-dimensional histogram of the distributions of the *OH*-vector with respect to the $[10\bar{1}0]$ -direction for the primary prismatic plane exposed to vacuum.

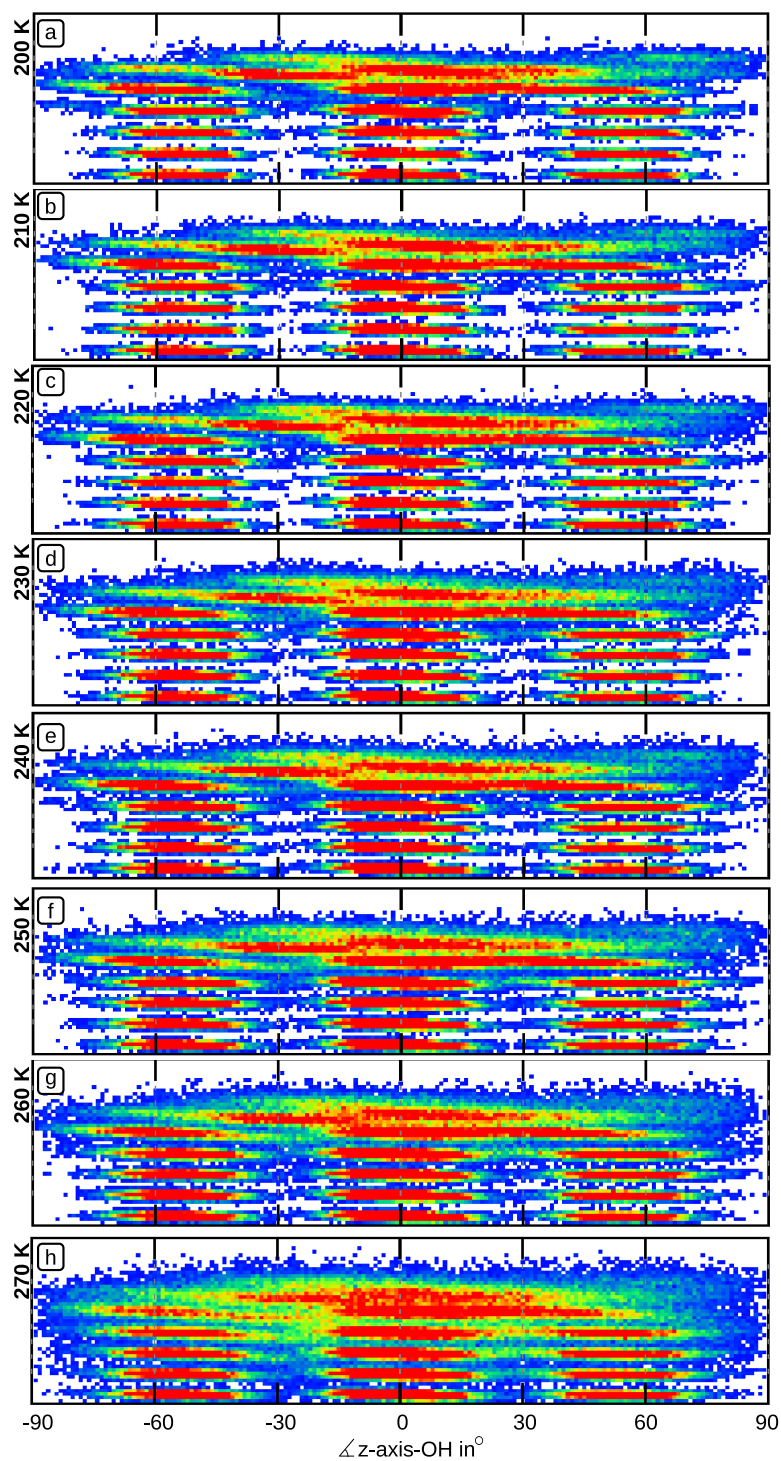


Fig. 8.19: Z-resolved two-dimensional histogram of the distributions of the *OH*-vector with respect to the $[\bar{1}2\bar{1}0]$ -direction for the secondary prismatic plane exposed to vacuum.

8.3.5 Dynamical analysis

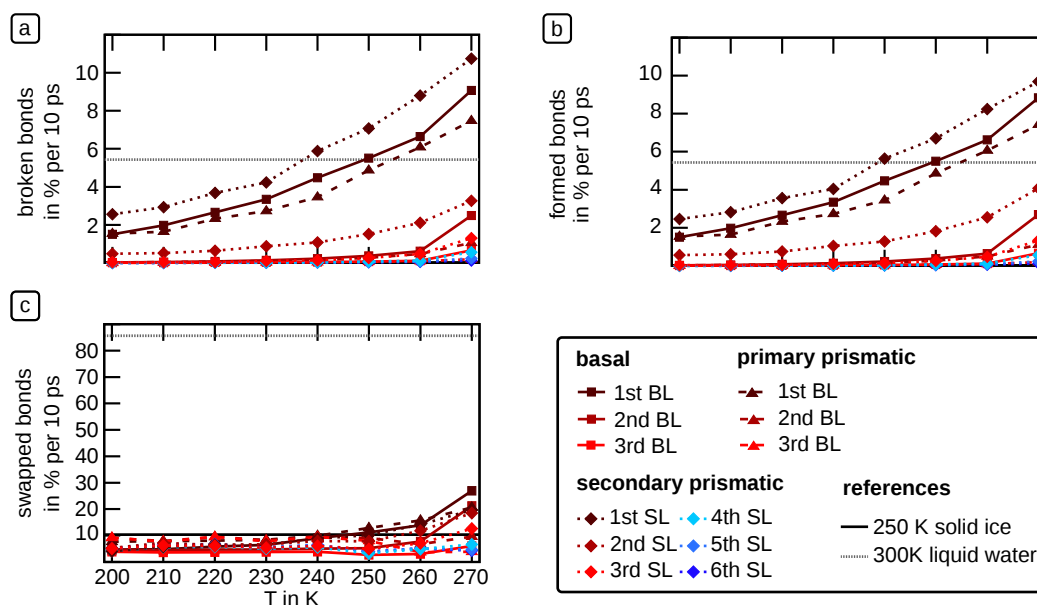


Fig. 8.20: Dynamic properties of H-bonding at all surfaces of hexagonal ice. Amount of (a) broken H-bonds (b) formed H-bonds (c) swapped H-bonds in units of % per 10 ps.

8.3.6 Network analysis

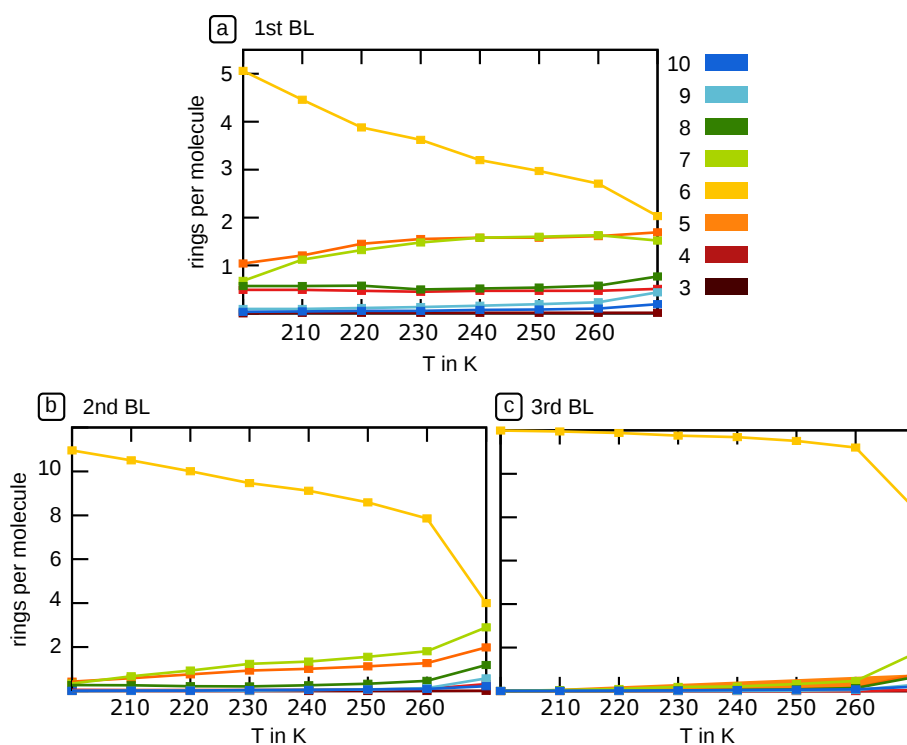


Fig. 8.21: Number of rings per molecule of the first three layers of the basal plane (see Figure 4.8).

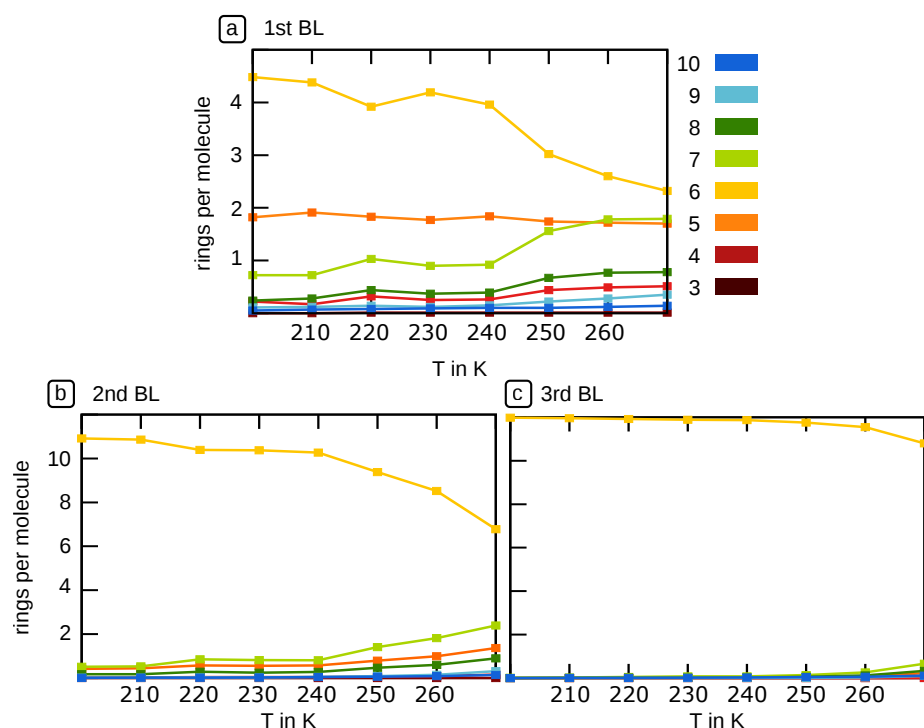


Fig. 8.22: Number of rings per molecule of the first three bilayers of the primary prismatic plane (see Figure 4.9).

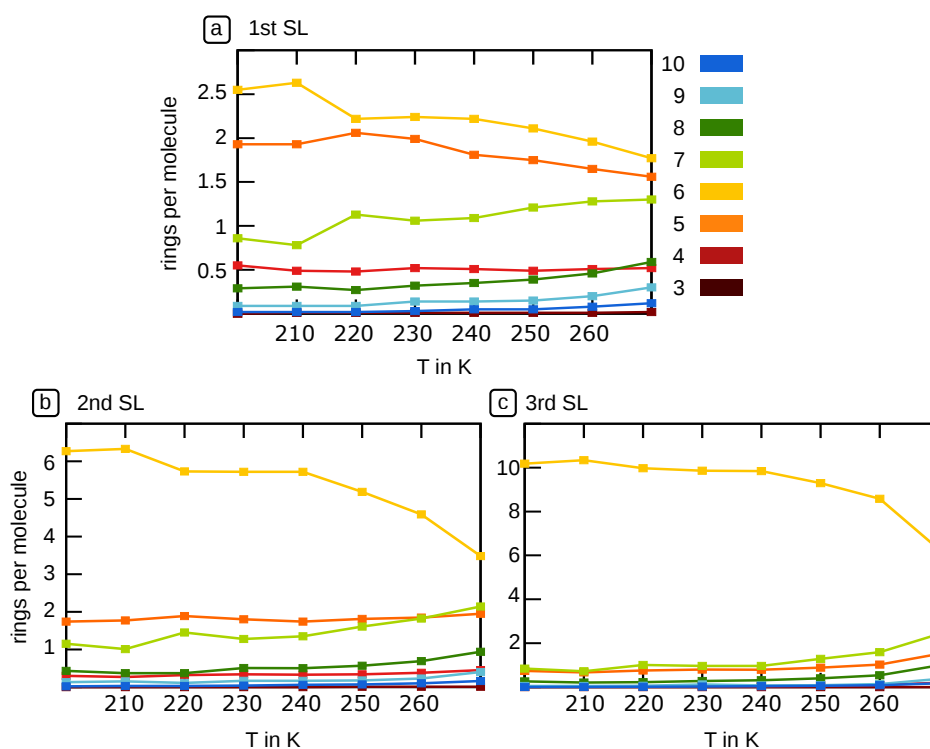


Fig. 8.23: Number of rings per molecule of the first three single-layers of the secondary prismatic plane (see Figure 4.10).

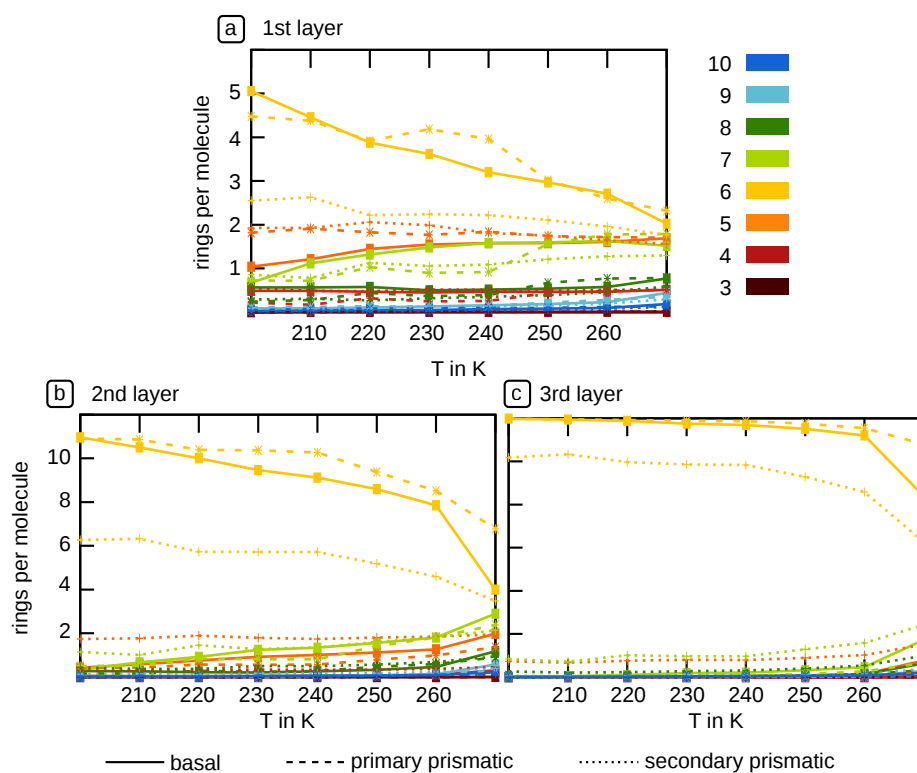


Fig. 8.24: Number of rings per molecule of the first three layers of the three most prominent ice surfaces in a single diagram.

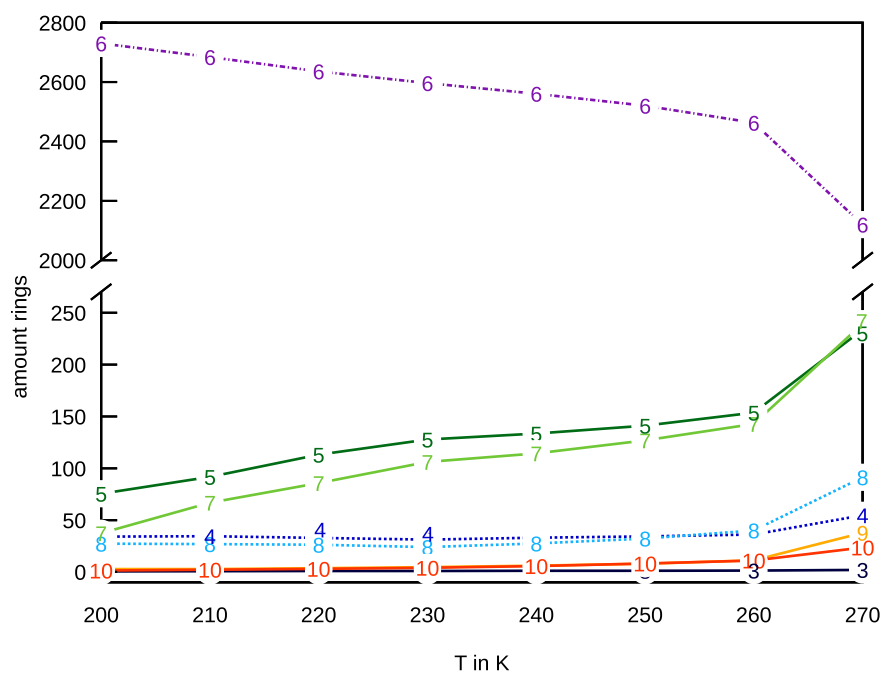


Fig. 8.25: Temperature-dependent total amount of n -membered rings for $n = 3-10$ for systems with the basal plane exposed to vacuum.

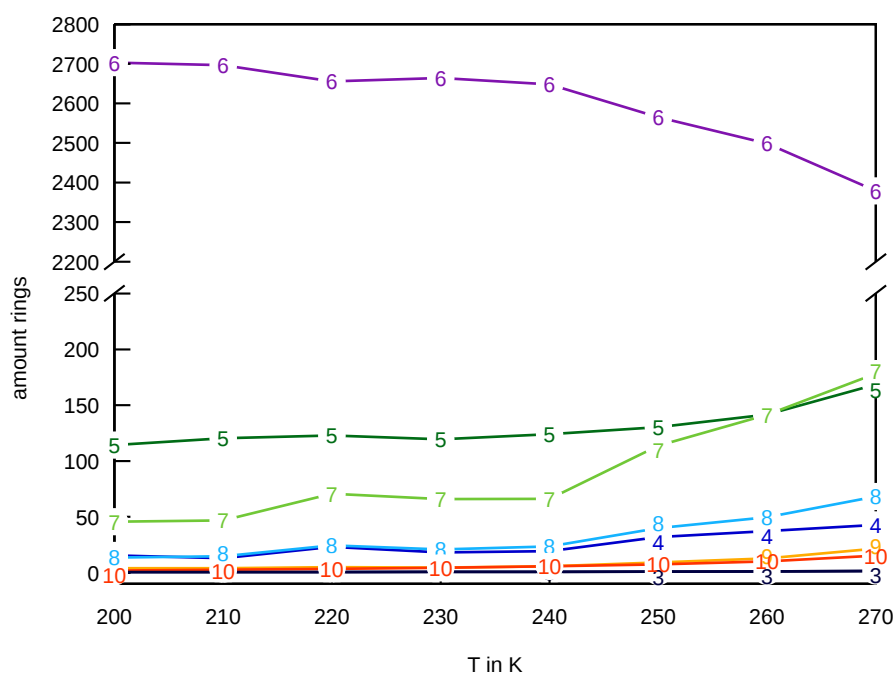


Fig. 8.26: Temperature-dependent total amount of n -membered rings for $n = 3$ – 10 for systems with the primary prismatic plane exposed to vacuum.

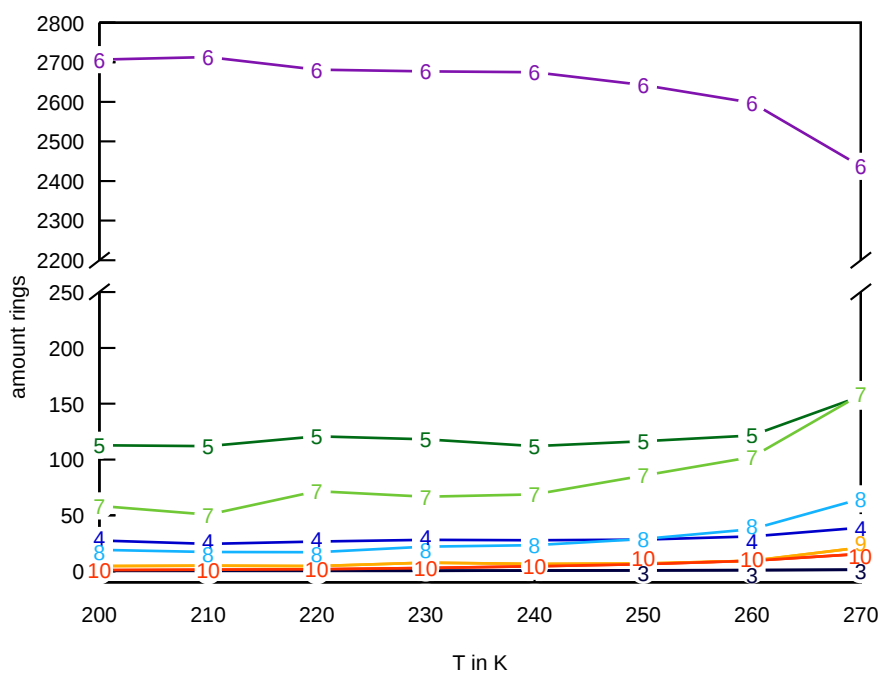


Fig. 8.27: Temperature-dependent total amount of n -membered rings for $n = 3$ – 10 for systems with the secondary prismatic plane exposed to vacuum.

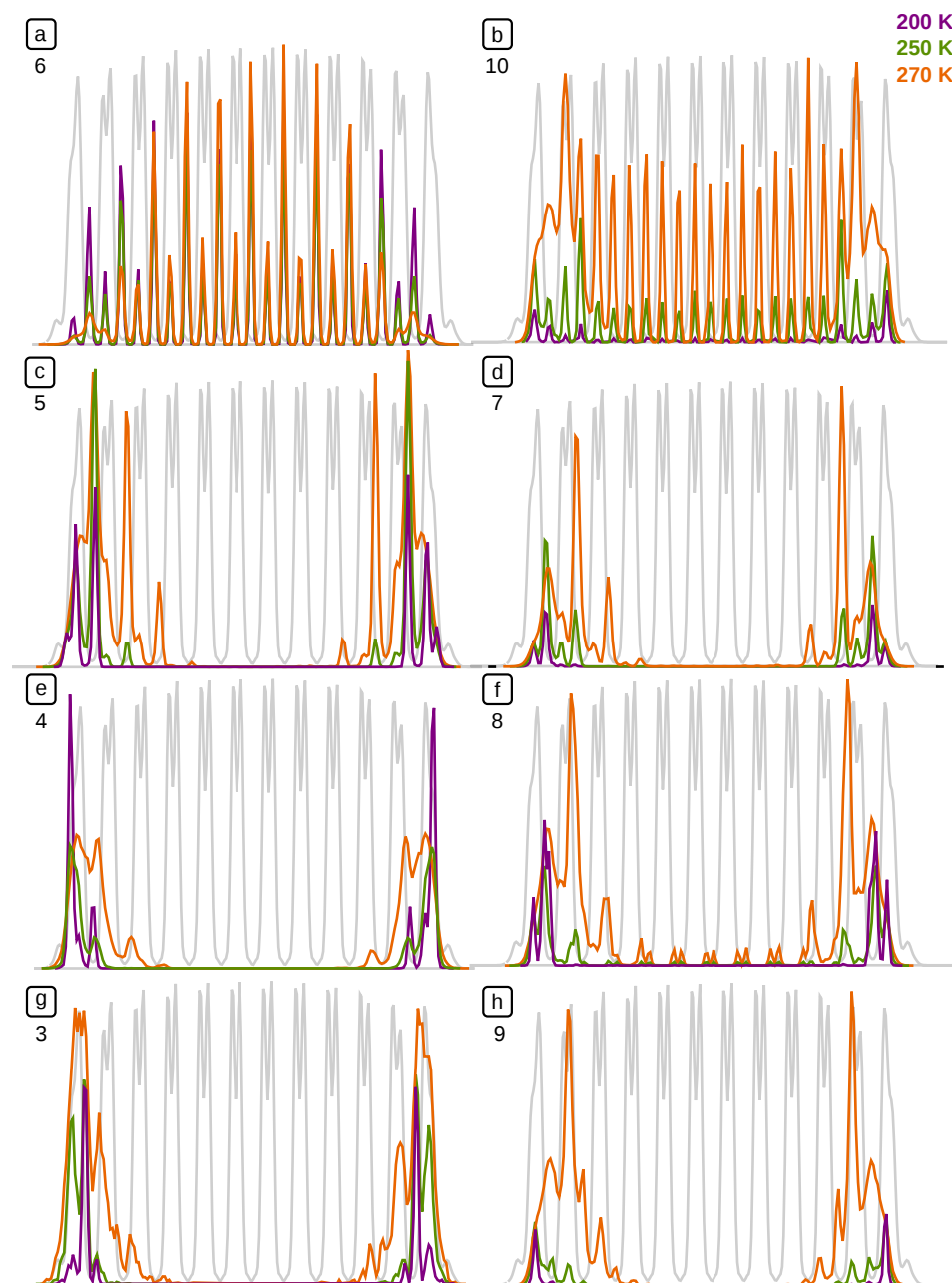


Fig. 8.28: Z-position of the centre-of-mass of the rings for three selected temperatures (200 K, 250 K, and 270 K) for slabs with the basal plane exposed to the vacuum. The density profile, which is shown in grey in the background, indicates the position of the respective bilayers. The surfaces are on the left (top) and right (bottom) side of the density profiles. All n -membered rings with $n \neq 6, 10$ form predominantly at the surface, while the other n -membered rings form both in the bulk and at the surface.

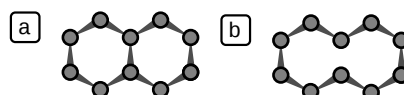


Fig. 8.29: Explanation for the formation of the ten-membered rings and its connection to the position of the original six-membered rings. The ten-membered rings form when one bond breaks in the ice structure, spread all over the bulk and, in contrast to all other n -membered rings ($n \neq 6, 10$) are not only present at the surface.

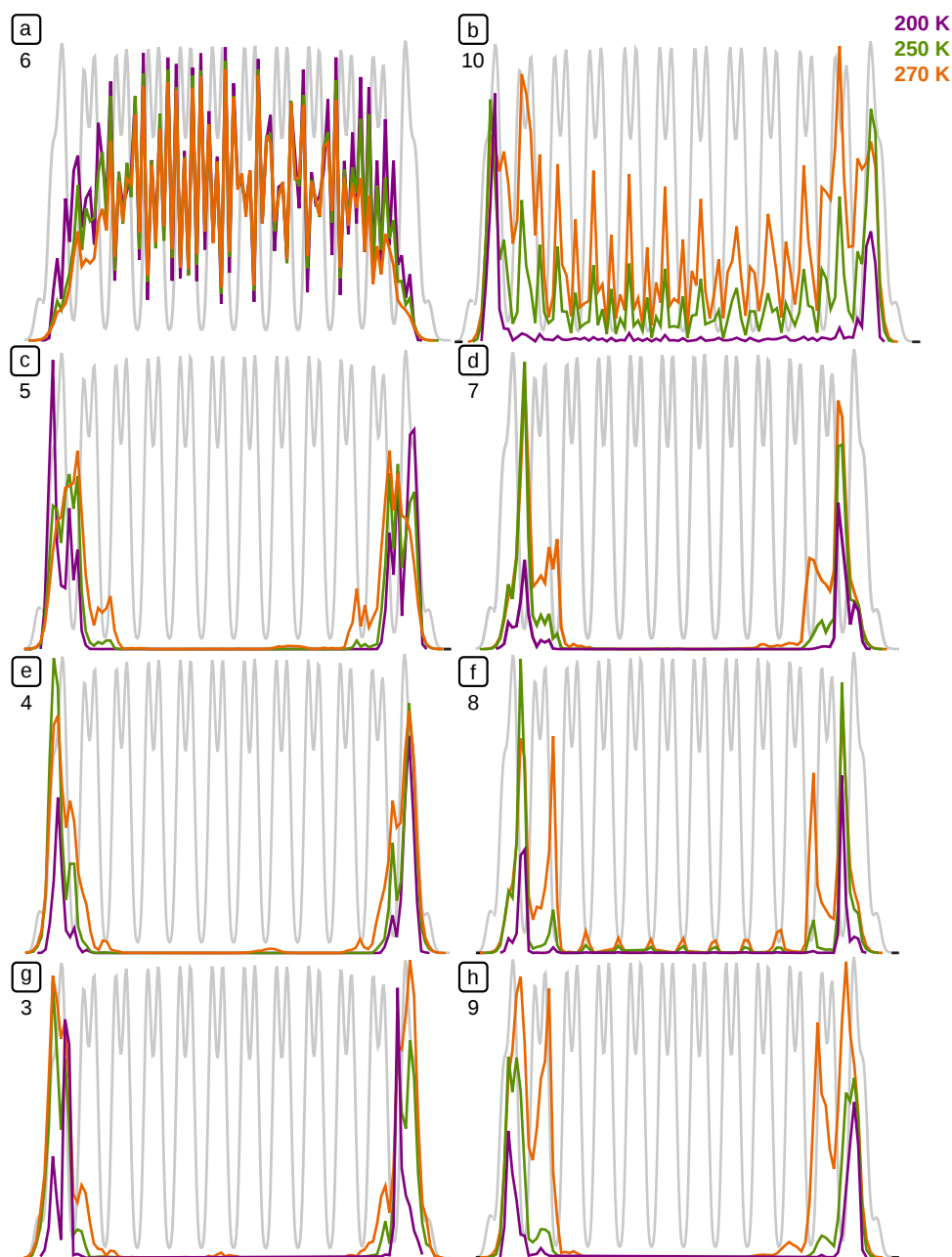


Fig. 8.30: Z-position of the centre-of-mass of the rings for three selected temperatures (200 K, 250 K, and 270 K) for slabs with the primary prismatic plane exposed to the vacuum. The density profile, which is shown in grey in the background, indicates the position of the respective bilayers. The surfaces are on the left (top) and right (bottom) side of the density profiles. All n -membered rings with $n \neq 6, 10$ form at the surface, while the other n -membered rings evolve further from the surface into the bulk with rising temperature.

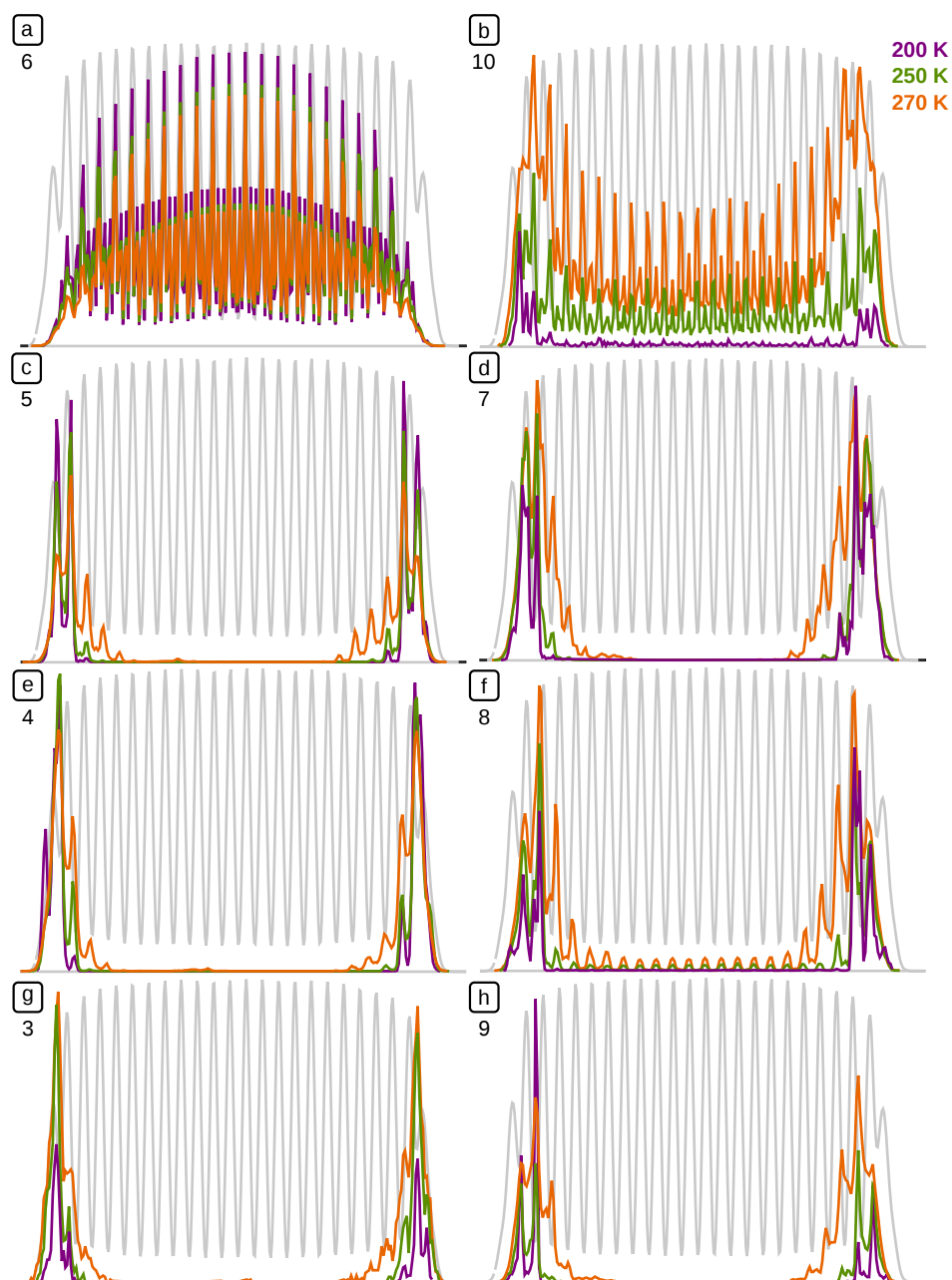


Fig. 8.31: Z-position of the centre-of-mass of the rings for three selected temperatures of 200 K, 250 K, and 270 K for slabs with the secondary prismatic plane exposed to the vacuum. The density profile, which is shown in grey in the background, indicates the position of the respective bilayers. The surfaces are on the left (top) and right (bottom) side of the density profiles. All n -membered rings with $n \neq 6, 10$ form at the surface, while the other n -membered rings evolve further from the surface into the bulk with rising temperature.

8.4 Chapter 5: Everything in order?

Tab. 8.2: Amount of analysed molecules in %

	Liquid reference	solid reference	pre-melted basal slab 250 K
# analysed molecules in %	94.77	99.89	89.43

8.4.1 Percentage of analysed molecules

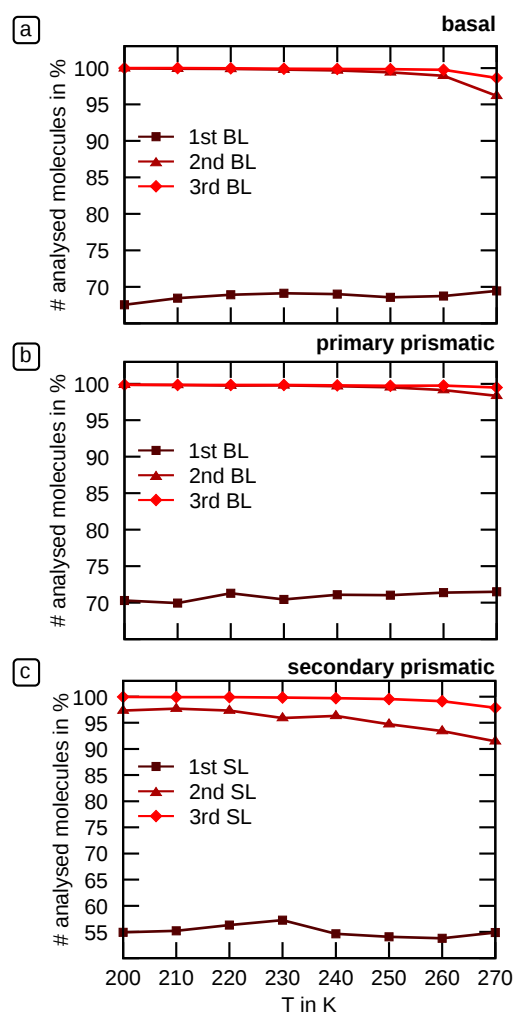


Fig. 8.32: Percentage of molecules analysed per layer for the low-index surfaces of ice.

8.4.2 Z- and layer-resolved distributions of the q_i , $i = 2, 3, 5, 6$ of the low-index surfaces of hexagonal ice

q₂

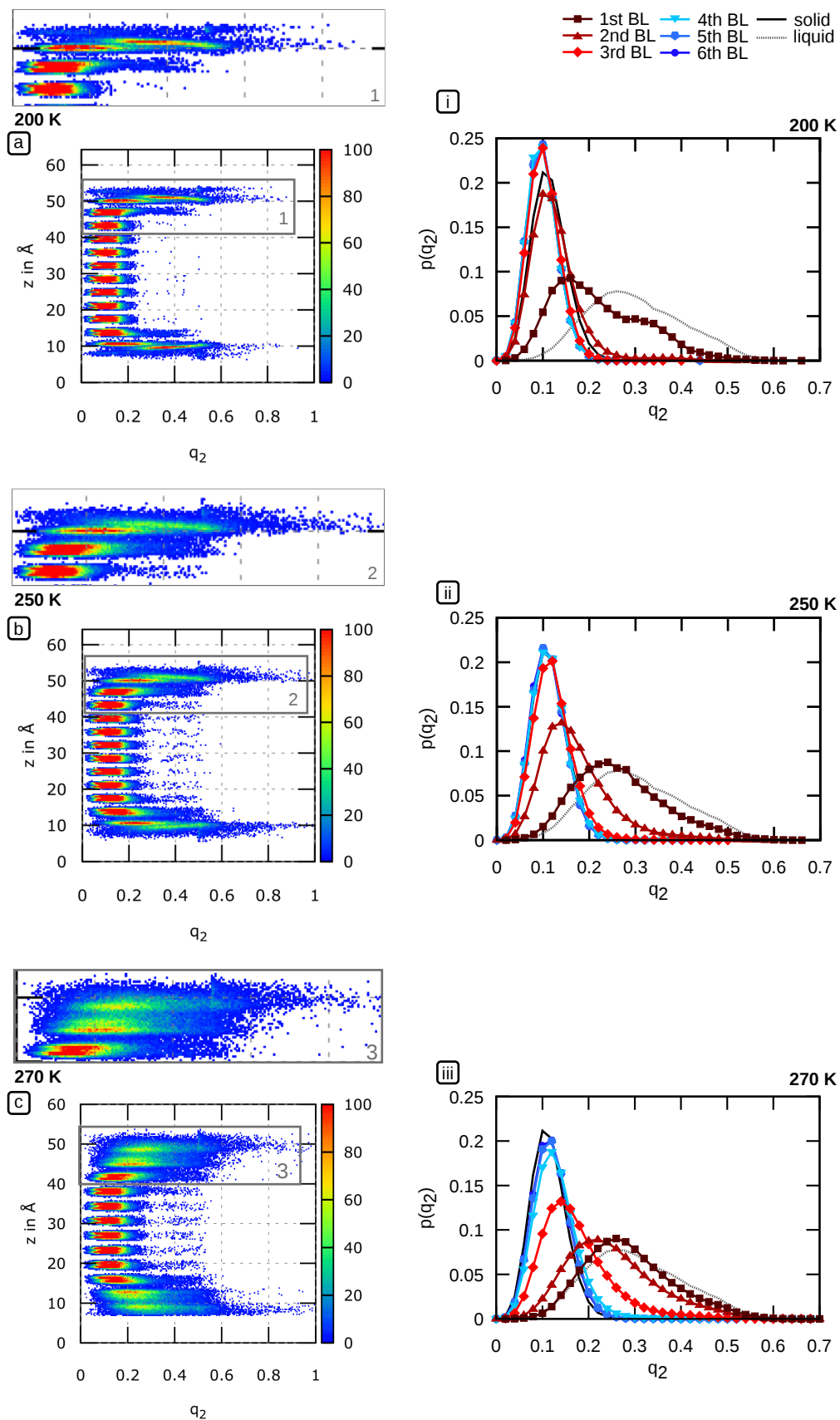


Fig. 8.33: Distributions of q_2 for the basal plane (a–c) z-resolved (i–iii) layer-resolved.

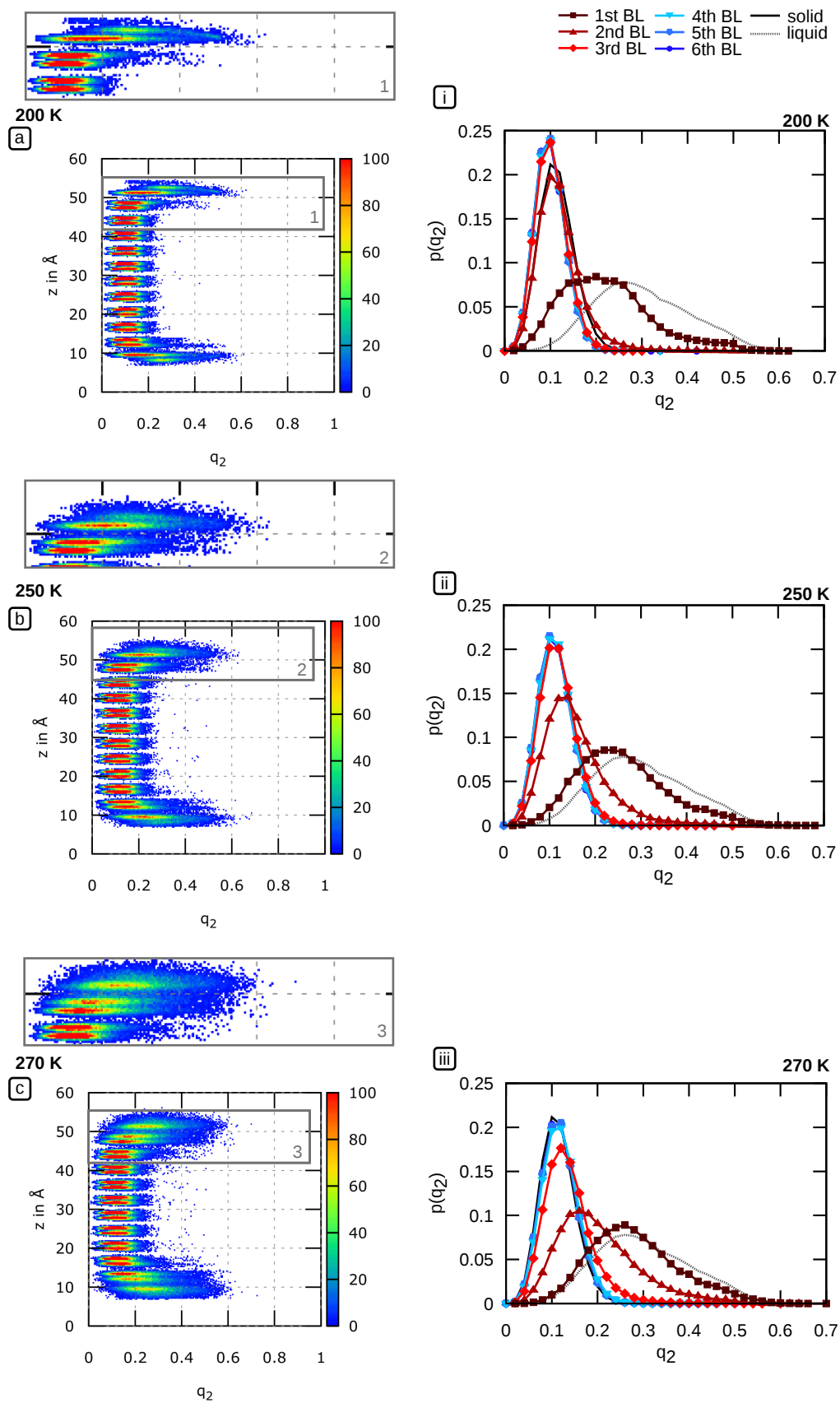


Fig. 8.34: Distributions of q_2 for the primary prismatic plane (a–c) z-resolved (i–iii) layer-resolved.

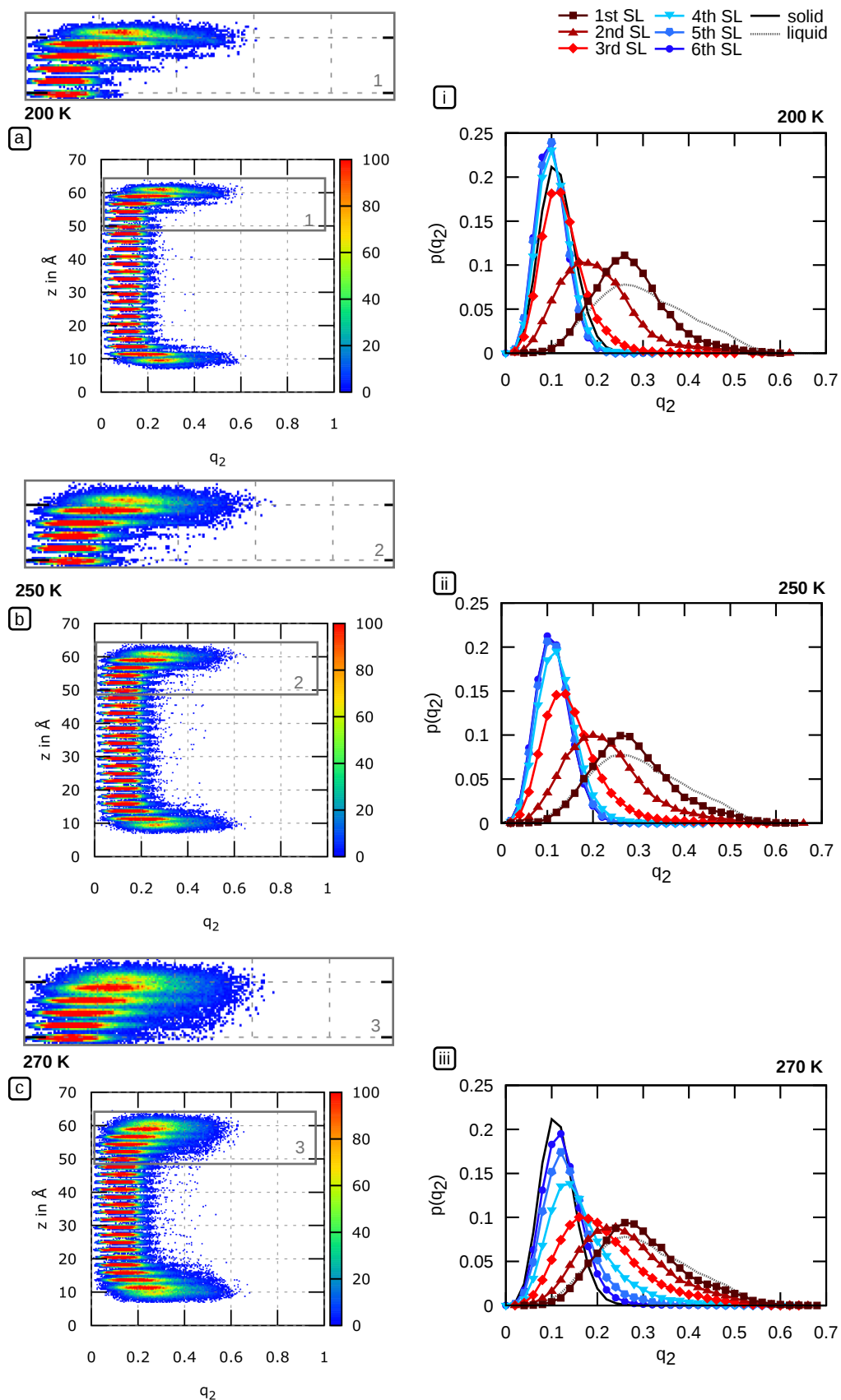


Fig. 8.35: Distributions of q_2 for the secondary prismatic plane (a–c) z-resolved (i–iii) layer-resolved.

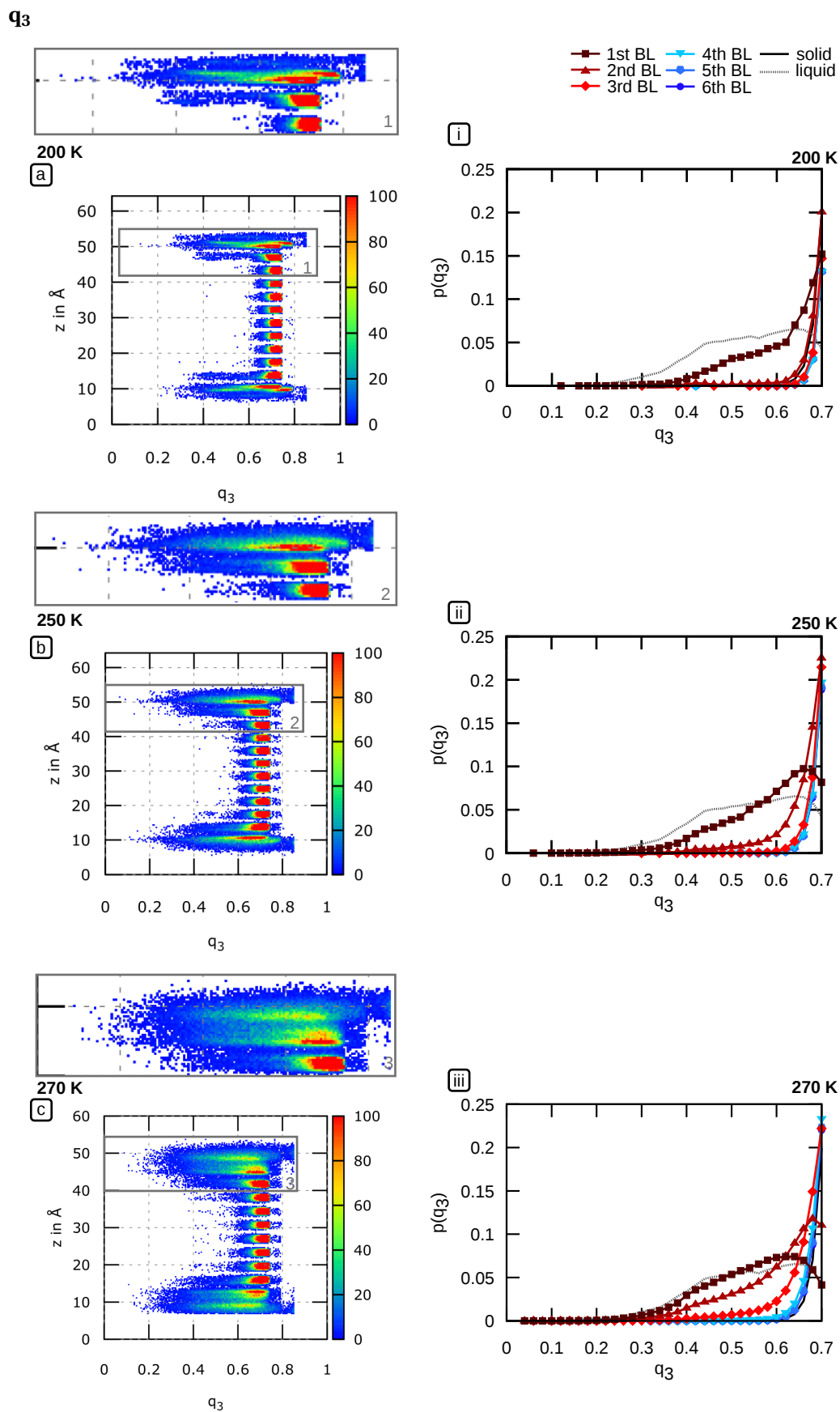


Fig. 8.36: Distributions of q_3 for the basal plane (a–c) z-resolved (i–iii) layer-resolved.

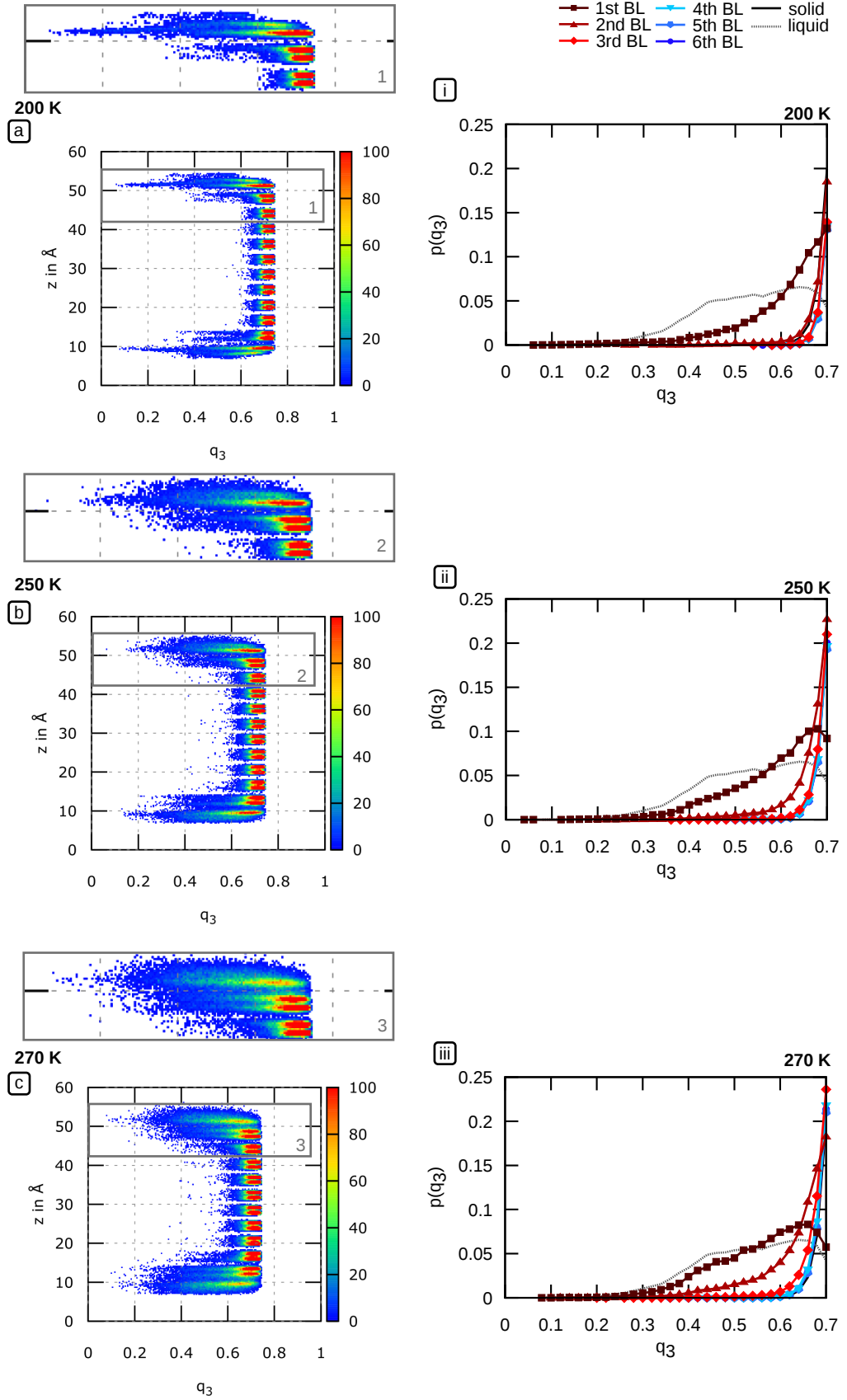


Fig. 8.37: Distributions of q_3 for the primary prismatic plane (a–c) z-resolved (i–iii) layer-resolved.

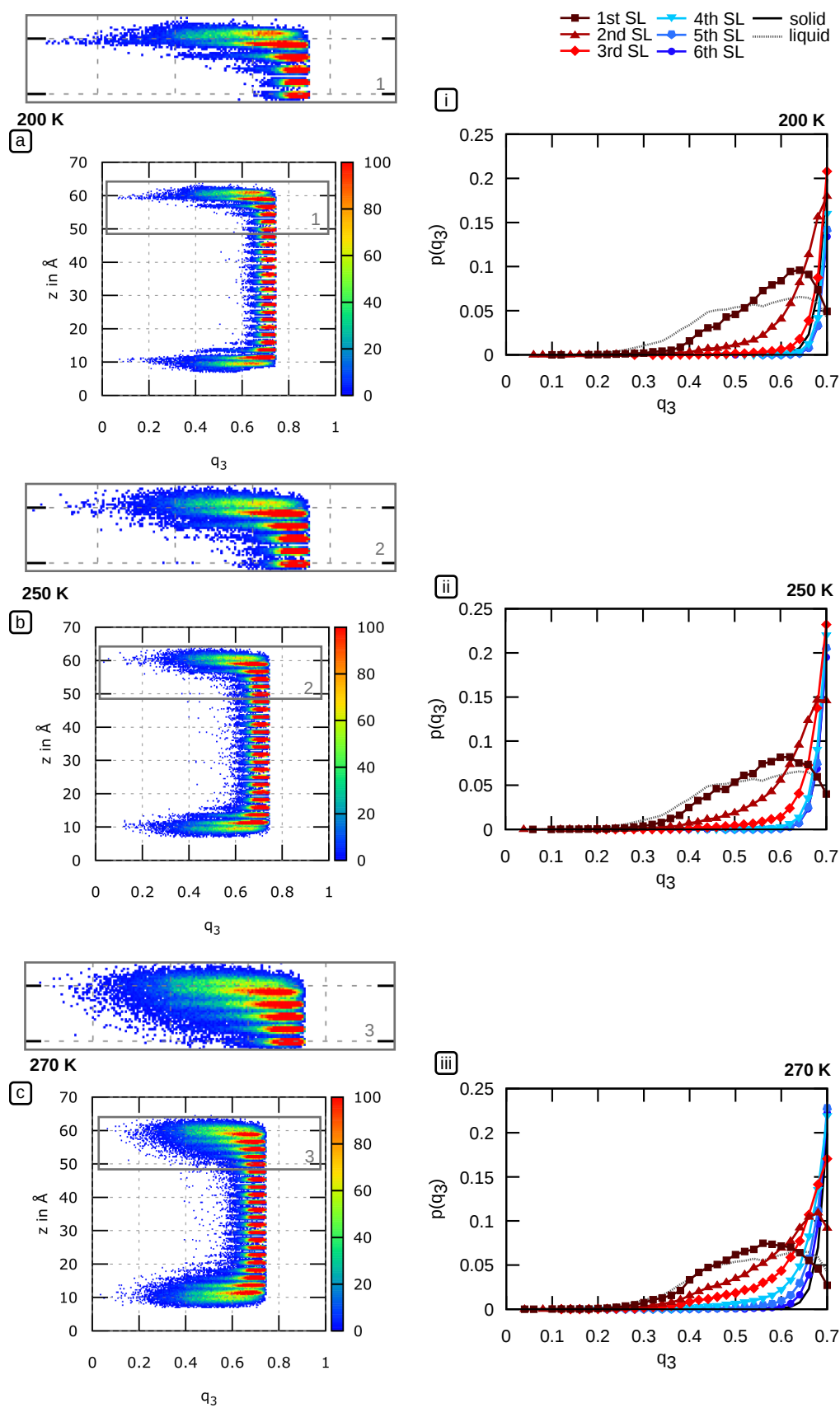


Fig. 8.38: Distributions of q_3 for the secondary prismatic plane (a-c) z-resolved (i-iii) layer-resolved.

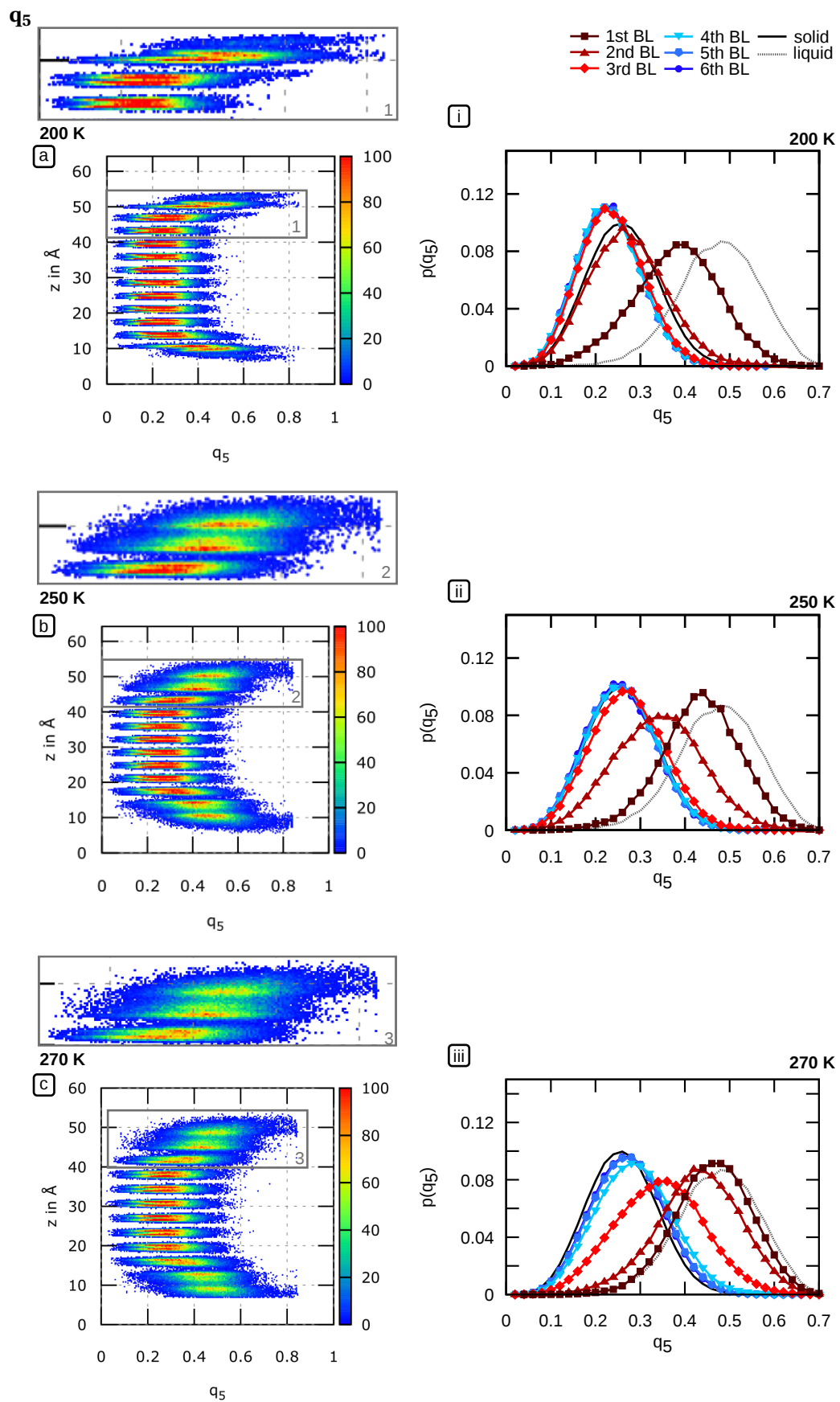


Fig. 8.39: Distributions of q_5 for the basal plane (a-c) z-resolved (i-iii) layer-resolved.

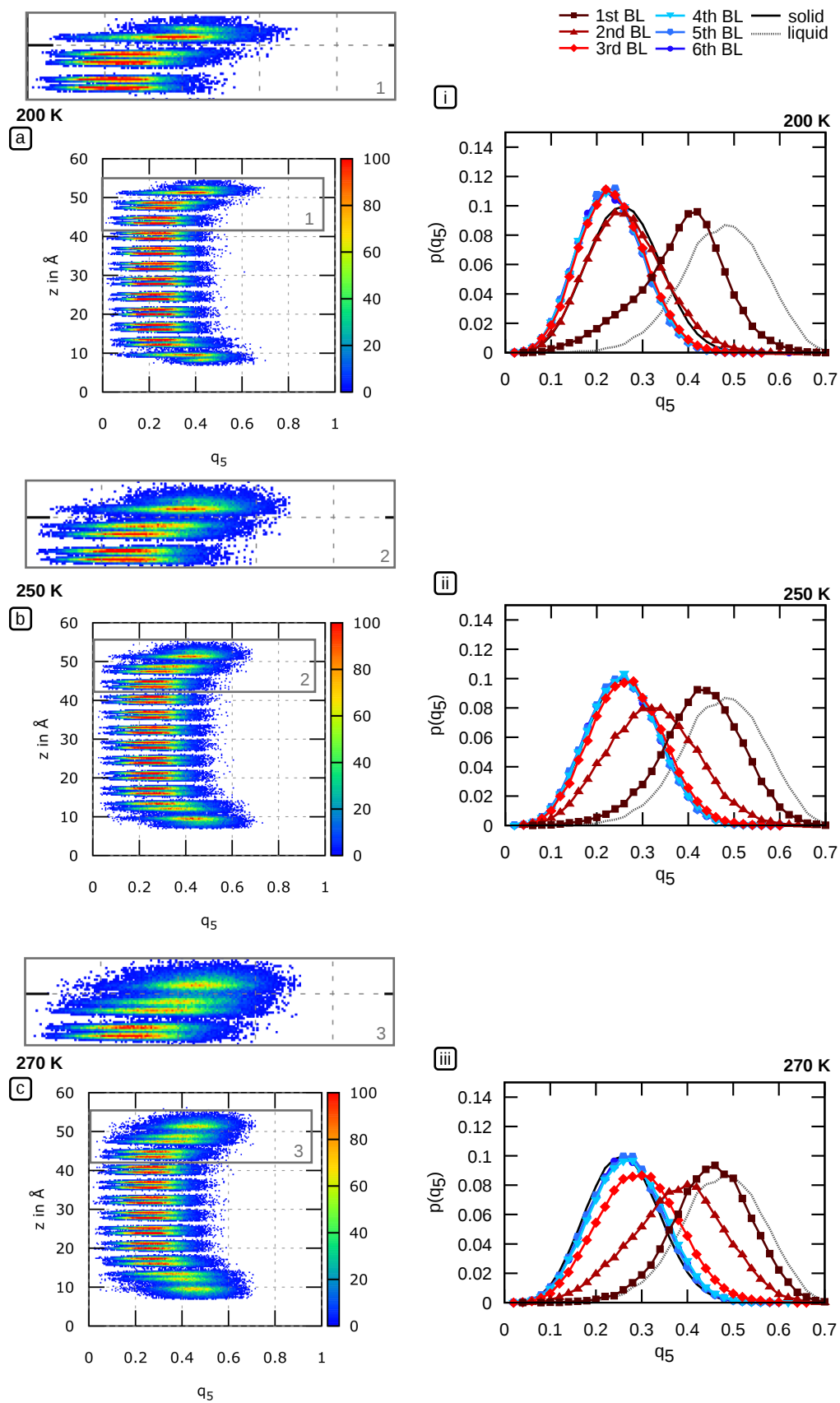


Fig. 8.40: Distributions of q_5 for the primary prismatic plane (a-c) z-resolved (i-iii) layer-resolved.

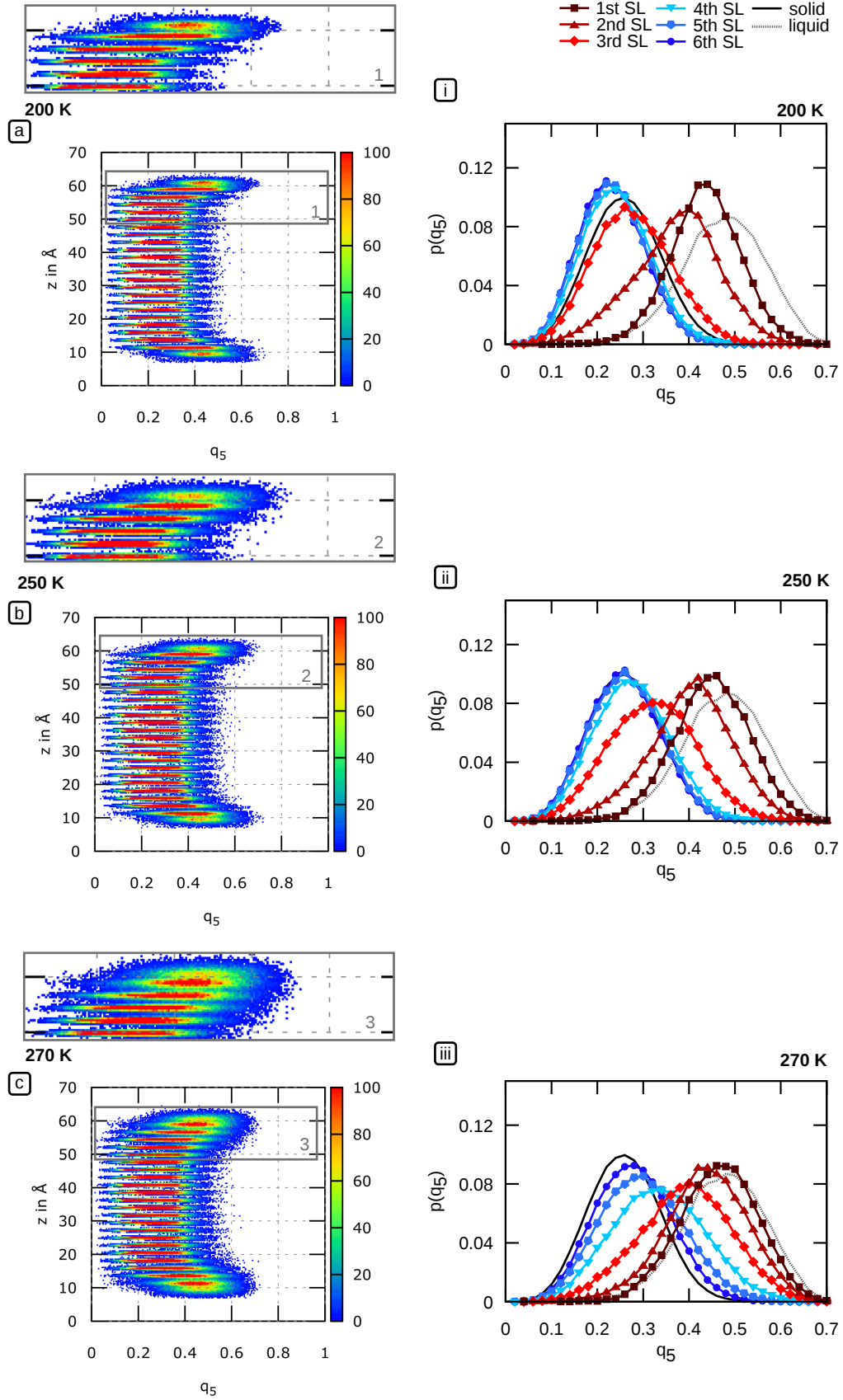


Fig. 8.41: Distributions of q_5 for the secondary prismatic plane (a-c) z-resolved (i-iii) layer-resolved.

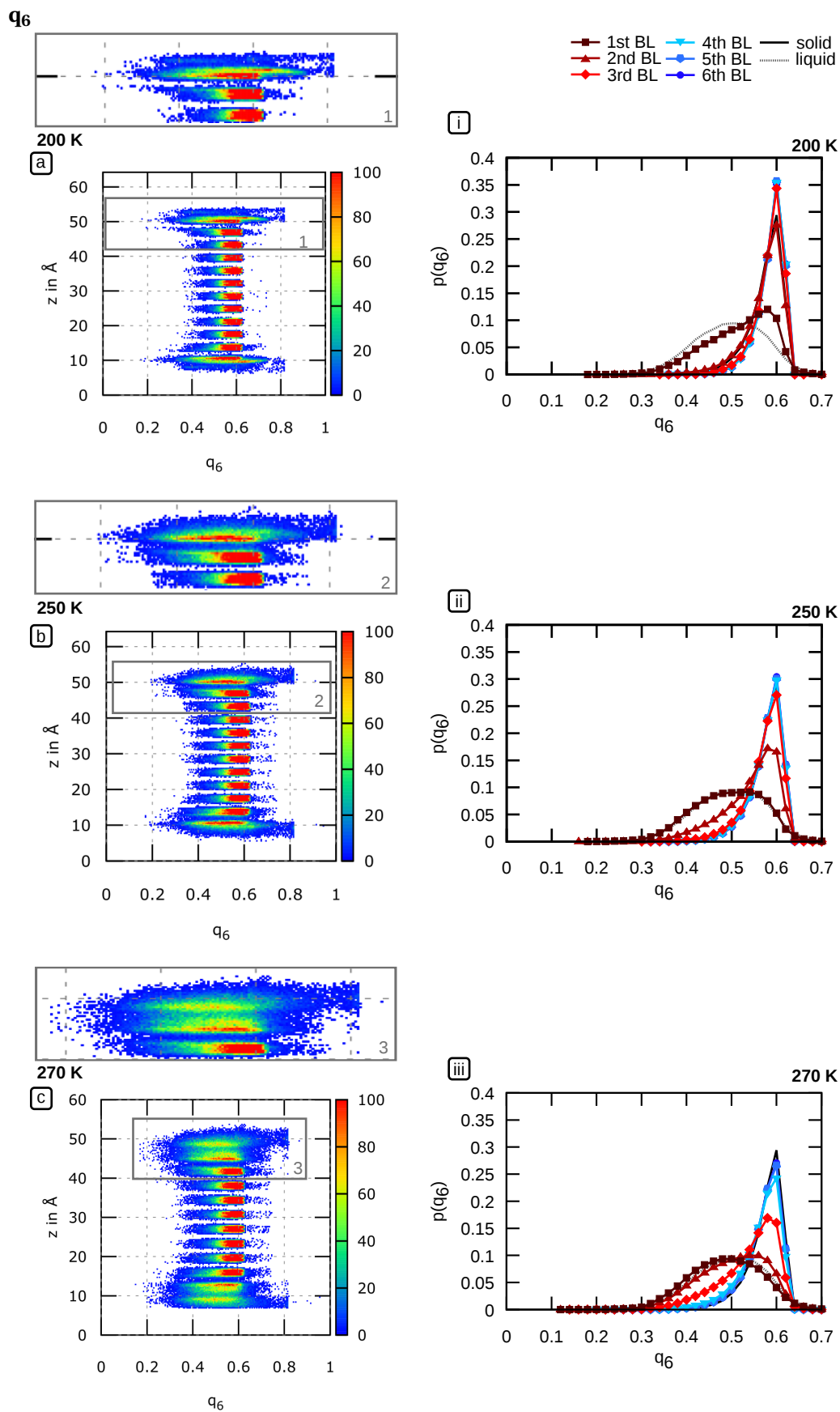


Fig. 8.42: Distributions of q_6 for the basal plane (a-c) z-resolved (i-iii) layer-resolved.

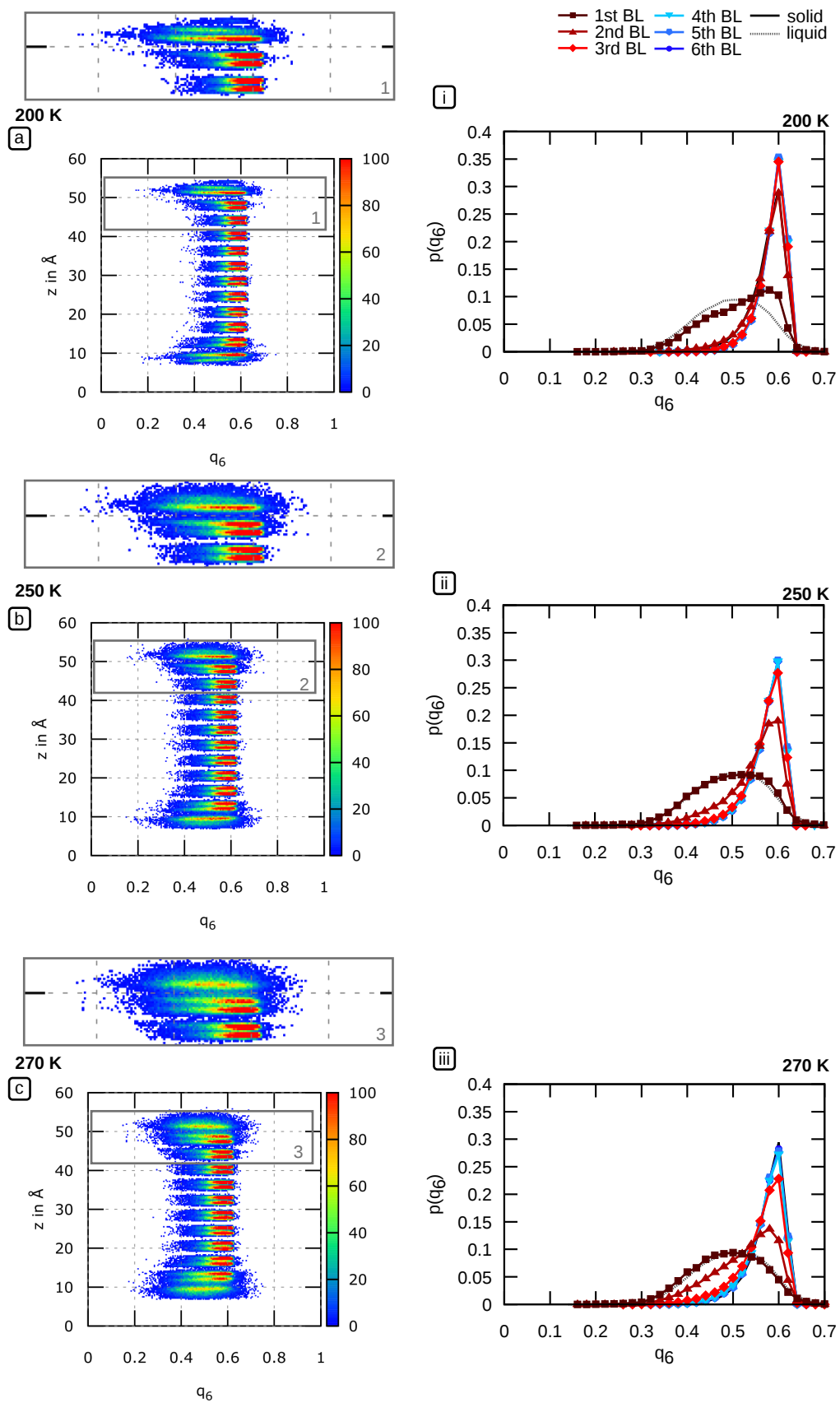


Fig. 8.43: Distributions of q_6 for the primary prismatic plane (a-c) z-resolved (i-iii) layer-resolved.

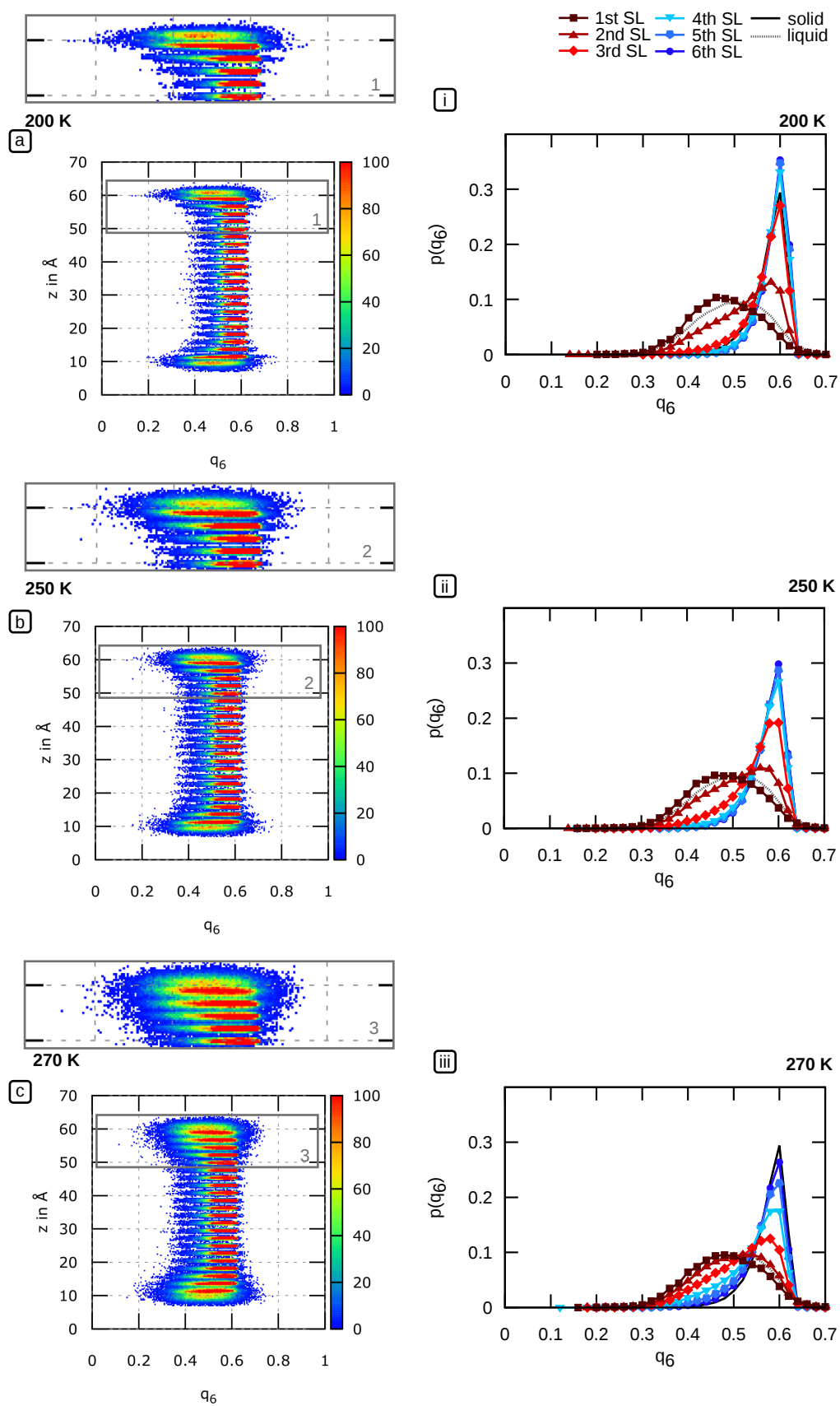


Fig. 8.44: Distributions of q_6 for the secondary prismatic plane (a-c) z-resolved (i-iii) layer-resolved.

8.4.3 Temperature-dependent behaviour of the upper three layers of the low index-faces of ice

q_2

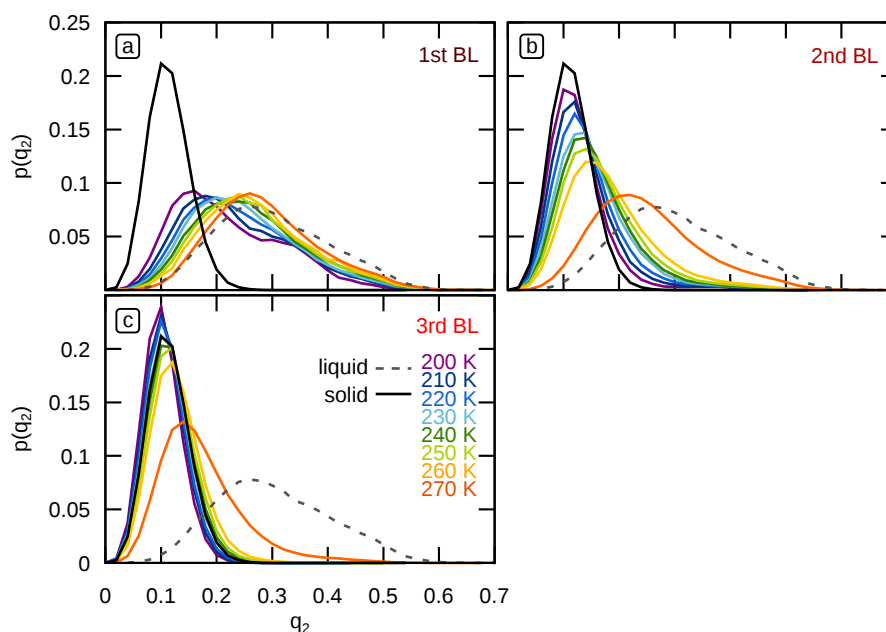


Fig. 8.45: Temperature-dependent behaviour of the distributions for q_2 for the upper three bilayers of the basal plane.

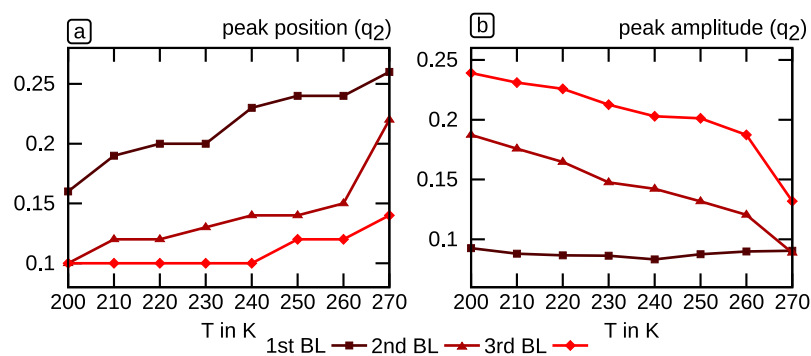


Fig. 8.46: Trends of the distributions from Figure 8.45.

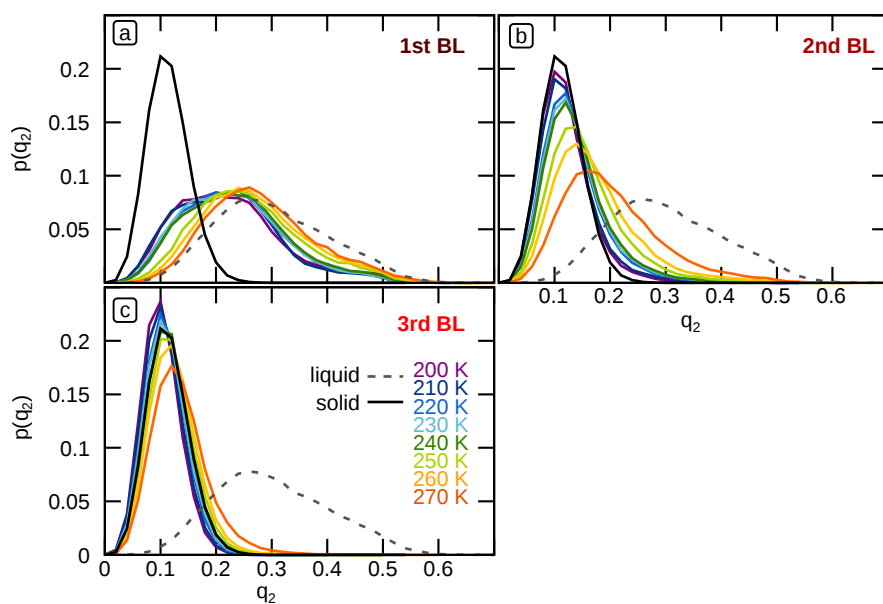


Fig. 8.47: Temperature-dependent behaviour of the distributions for q_2 for the upper three bilayers of the primary prismatic plane.

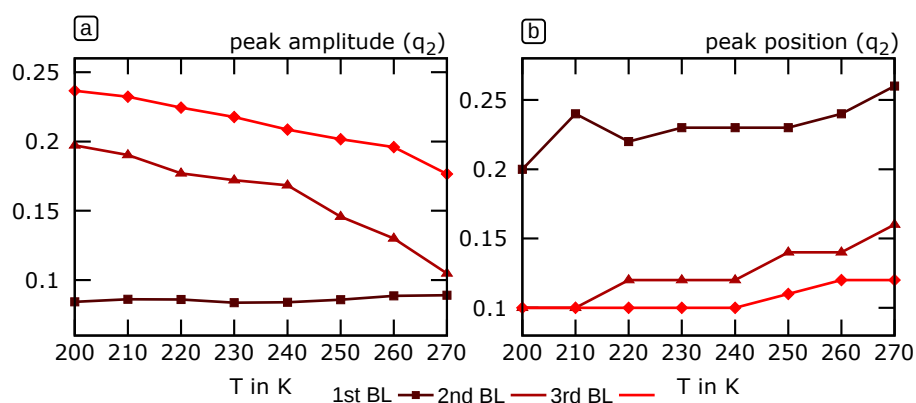


Fig. 8.48: Trends of the distributions from Figure 8.47.

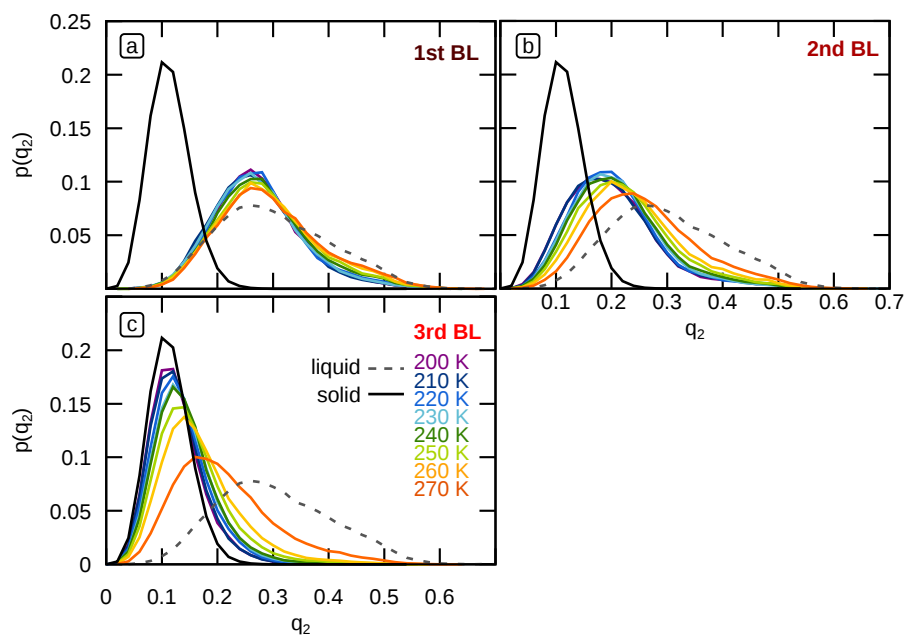


Fig. 8.49: Temperature-dependent behaviour of the distributions for q_2 for the upper three single-layers of the secondary prismatic plane.

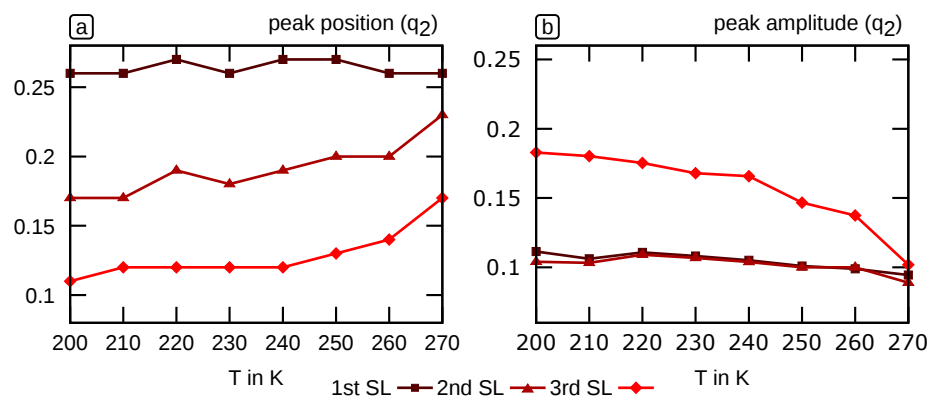


Fig. 8.50: Trends of the distributions from Figure 8.49.

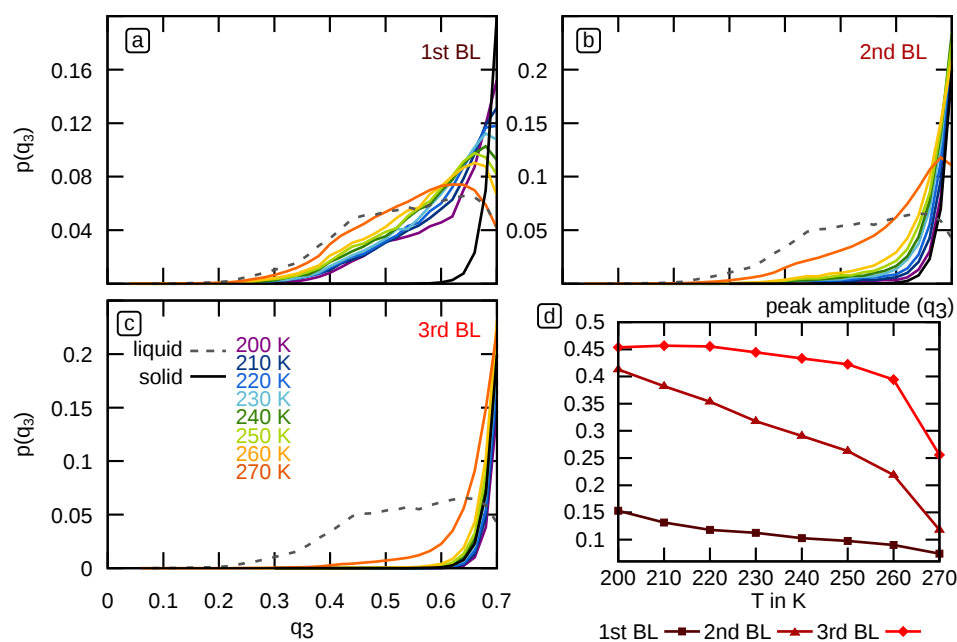


Fig. 8.51: Temperature-dependent behaviour of the distributions for q_3 for the upper three bilayers of the basal plane.

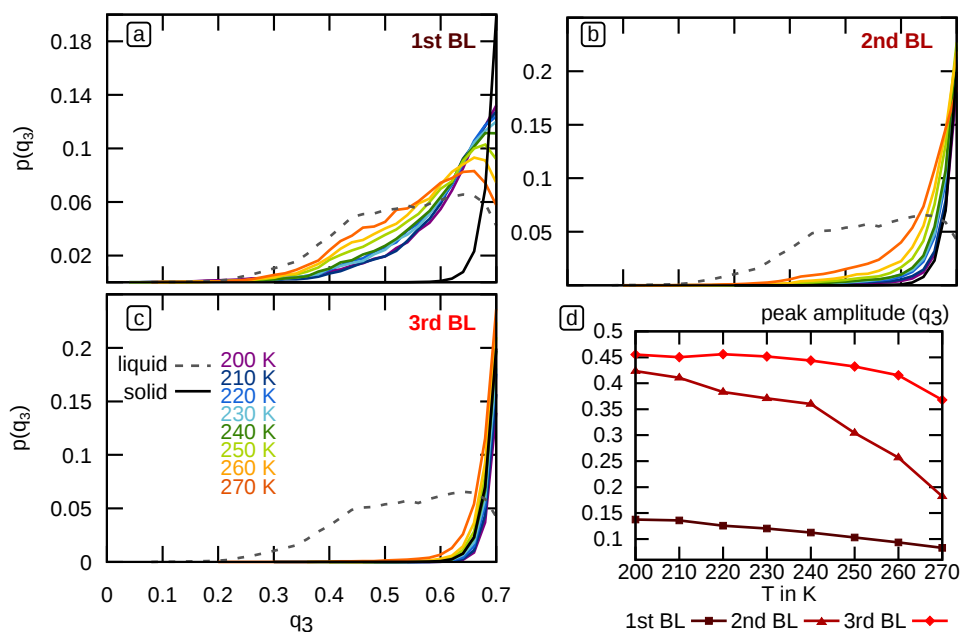


Fig. 8.52: Temperature-dependent behaviour of the distributions for q_3 for the upper three bilayers of the primary prismatic plane.

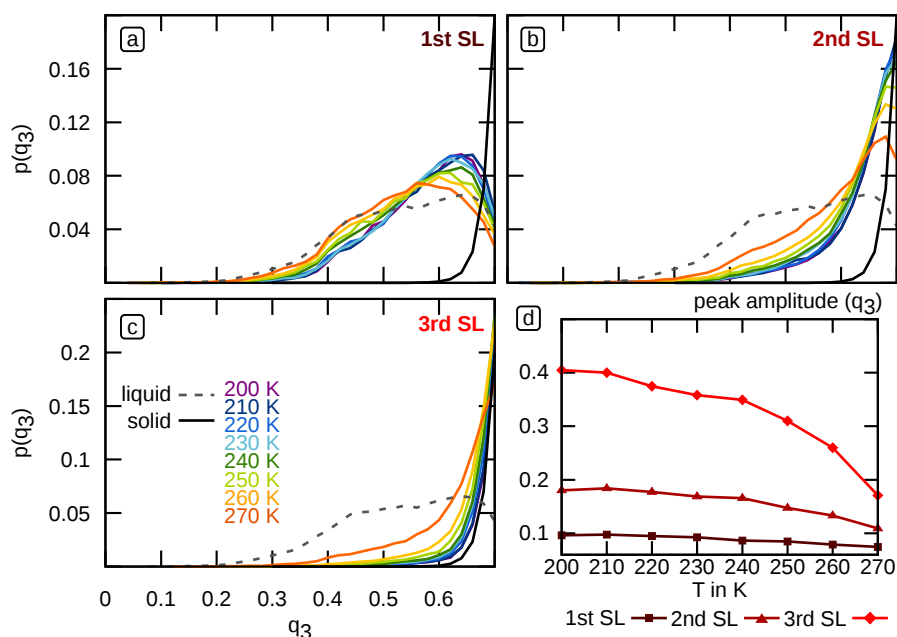


Fig. 8.53: Temperature-dependent behaviour of the distributions for q_3 for the upper three single-layers of the secondary prismatic plane.

q_5

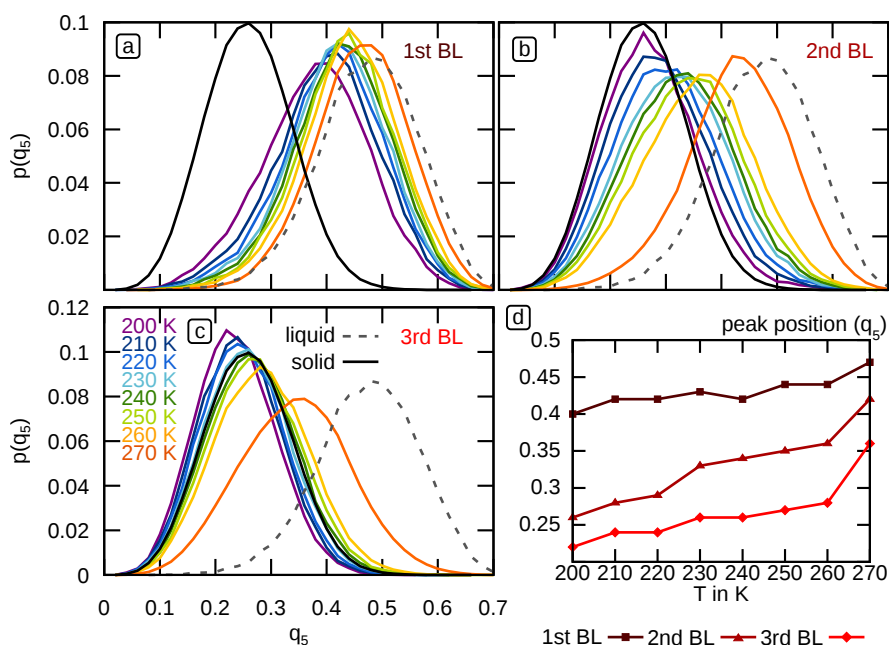


Fig. 8.54: Temperature-dependent behaviour of the distributions for q_5 for the upper three bilayers of the basal plane.

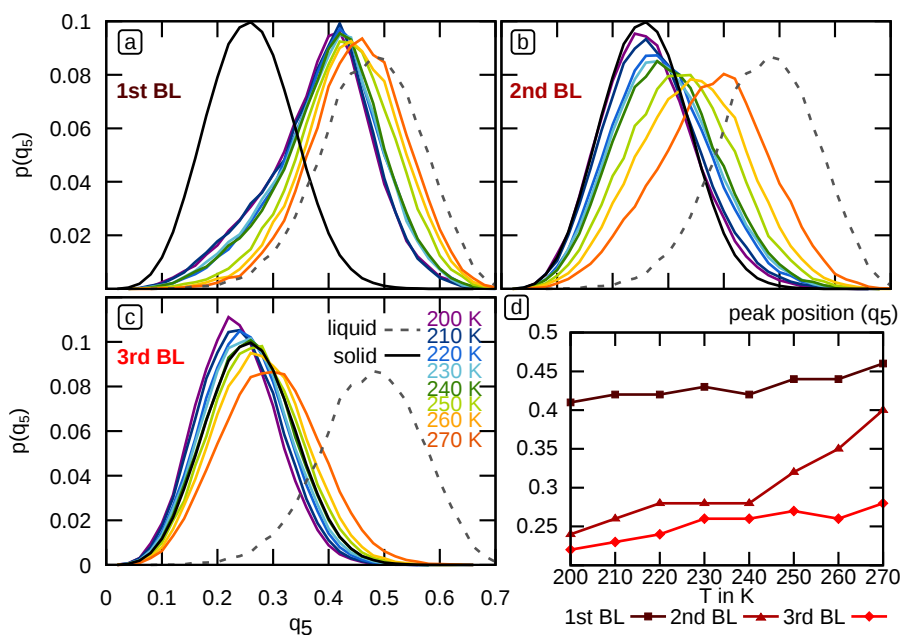


Fig. 8.55: Temperature-dependent behaviour of the distributions for q_5 for the upper three bilayers of the primary prismatic plane.

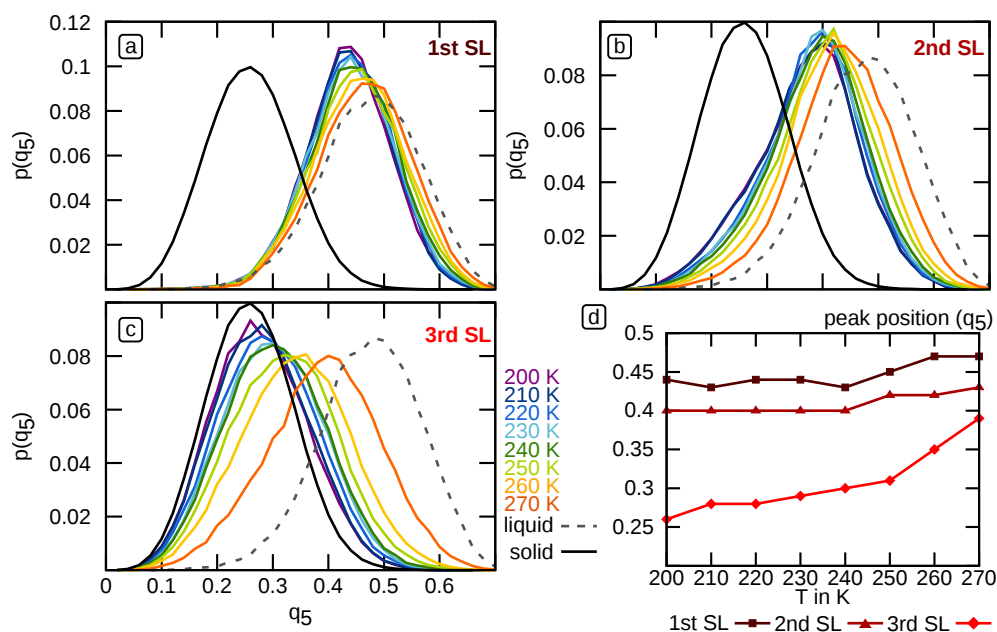


Fig. 8.56: Temperature-dependent behaviour of the distributions for q_5 for the upper three single-layers of the secondary prismatic plane.

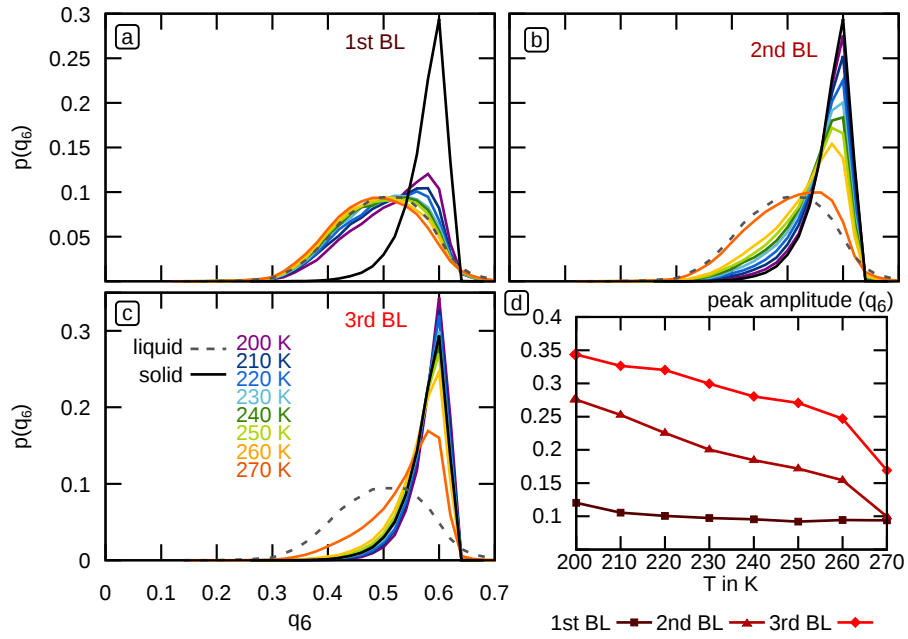


Fig. 8.57: Temperature-dependent behaviour of the distributions for q_6 for the upper three bilayers of the basal plane.

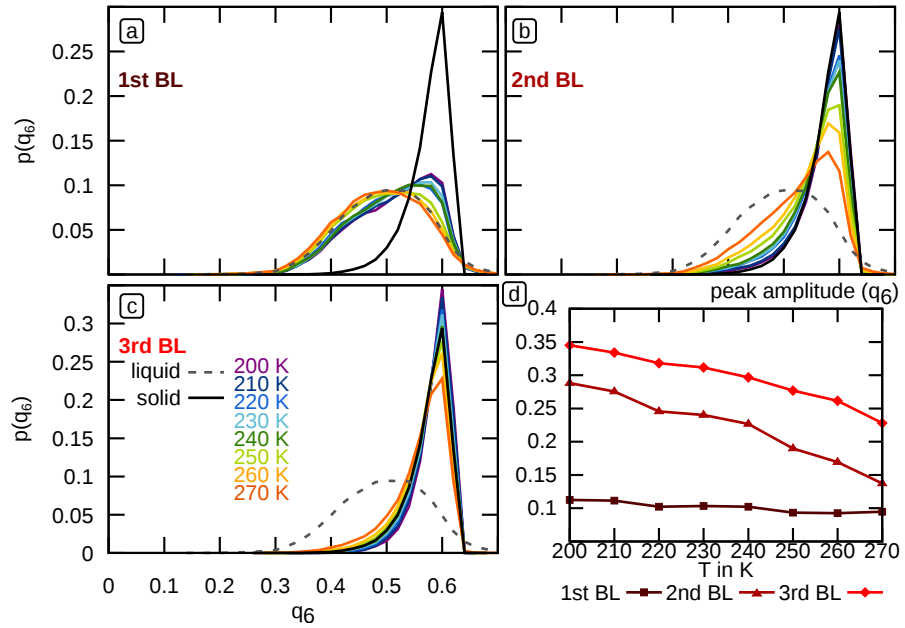


Fig. 8.58: Temperature-dependent behaviour of the distributions for q_6 for the upper three bilayers of the primary prismatic plane.

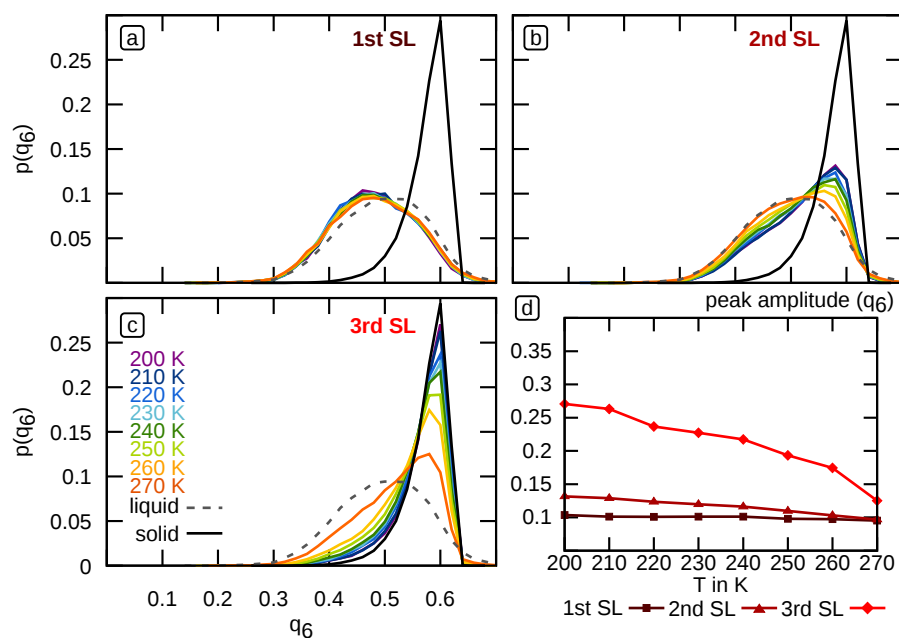


Fig. 8.59: Temperature-dependent behaviour of the distributions for q_6 for the upper three single-layers of the secondary prismatic plane.

8.4.4 Temperature-dependent layer-resolved LSOP distributions of the upper six layers of the low-index surfaces of hexagonal ice

q_2

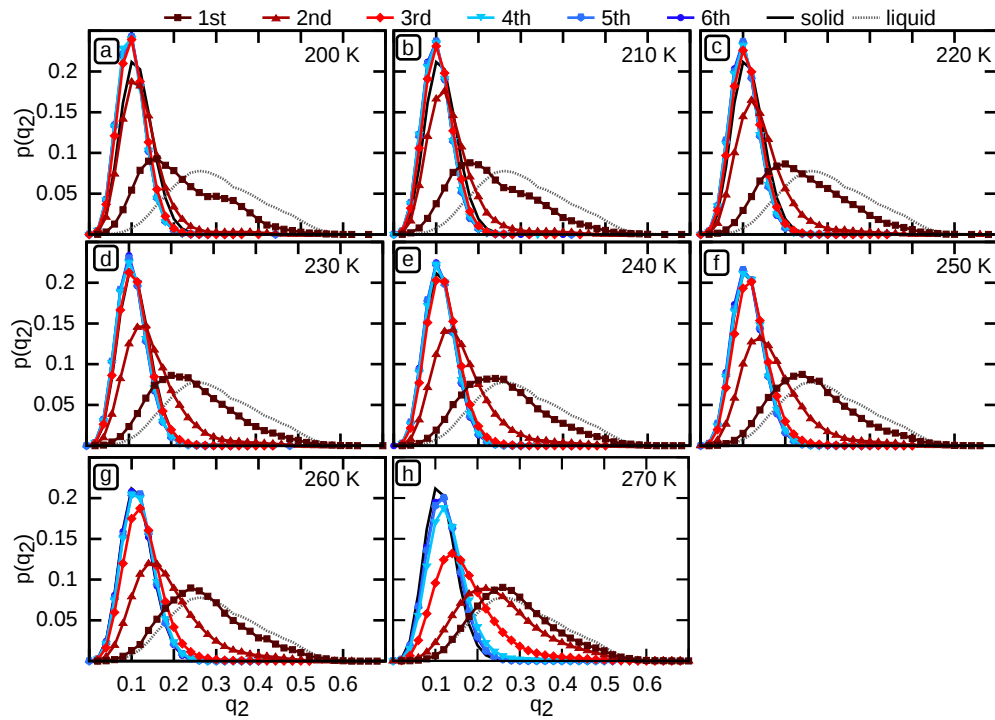


Fig. 8.60: Temperature-dependent layer-resolved distributions for q_2 of the upper six bilayers of ice slabs of the basal plane.

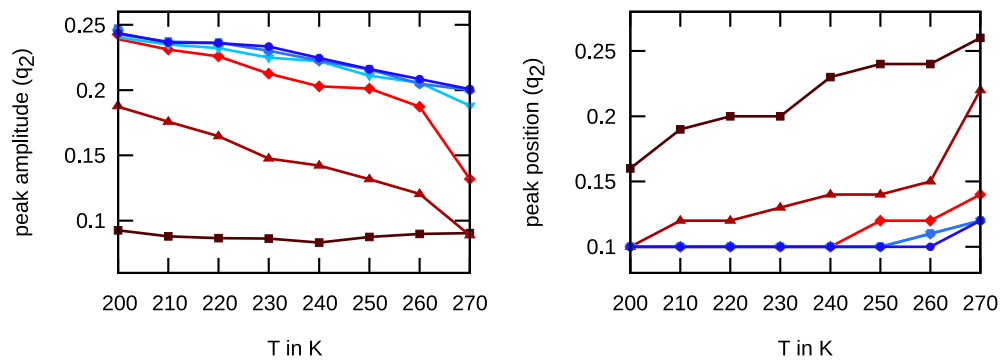


Fig. 8.61: Temperature-dependent trends of the upper six bilayers from Figure 8.60.

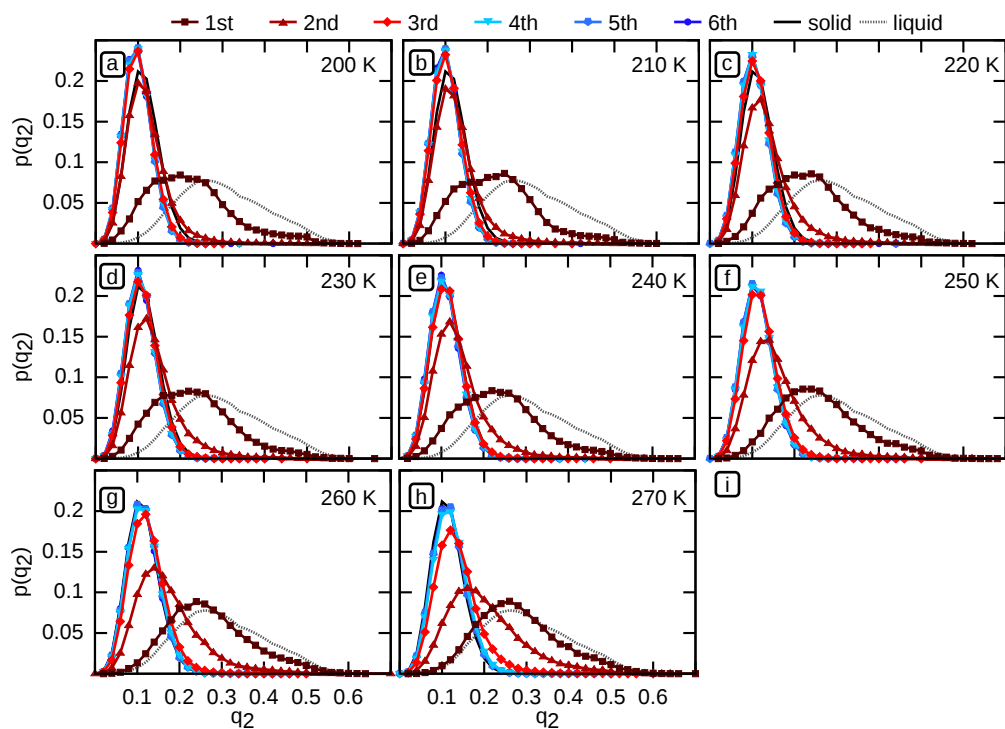


Fig. 8.62: Temperature-dependent layer-resolved distributions for q_2 of the upper six bilayers of ice slabs of the primary prismatic plane.

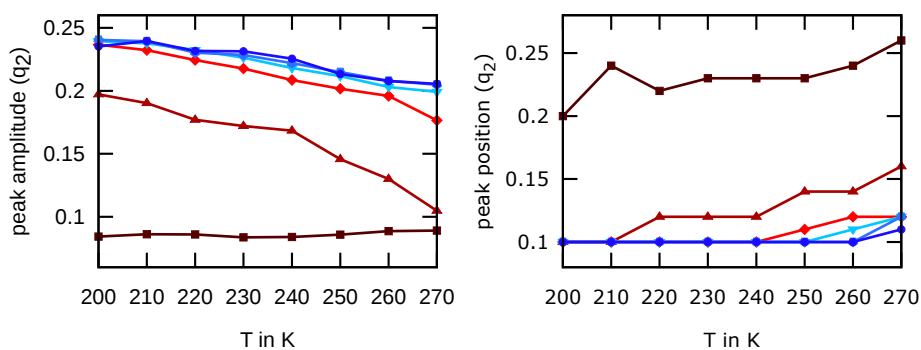


Fig. 8.63: Temperature-dependent trends of the upper six bilayers from Figure 8.62.

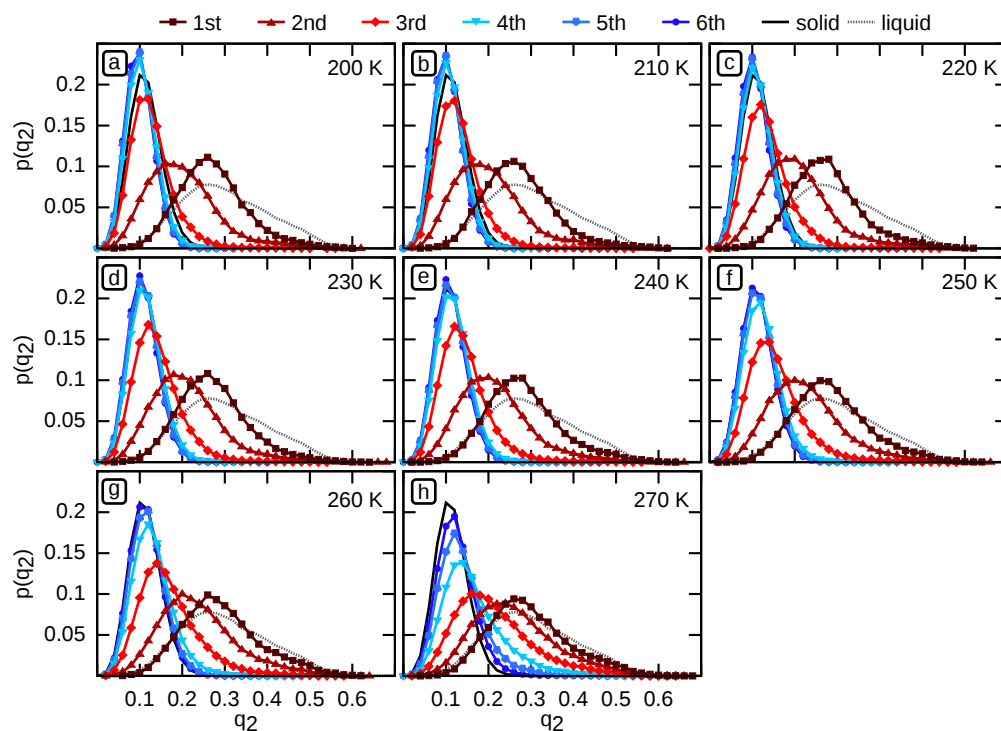


Fig. 8.64: Temperature-dependent layer-resolved distributions for q_2 of the upper six single-layers of ice slabs of the secondary prismatic plane.

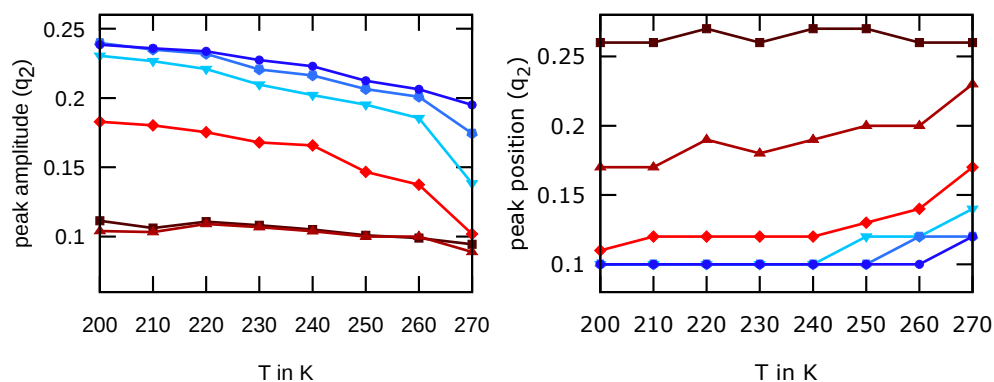


Fig. 8.65: Temperature-dependent trends of the upper six single-layers from Figure 8.64.

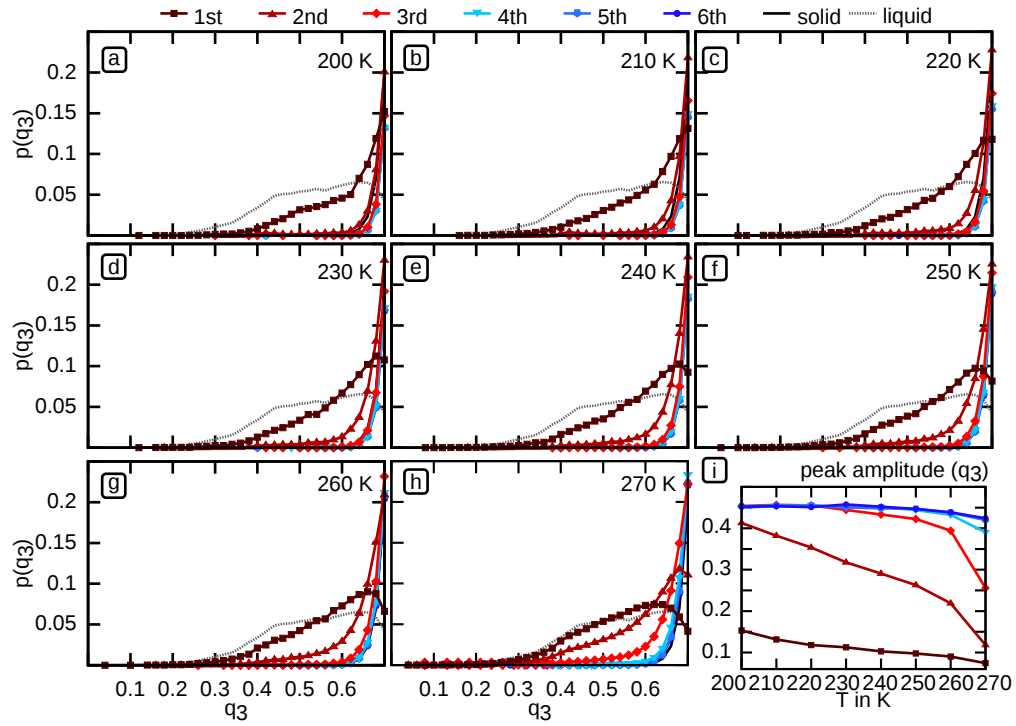


Fig. 8.66: Temperature-dependent layer-resolved distributions for q_3 of the upper six bilayers of ice slabs of the basal plane.

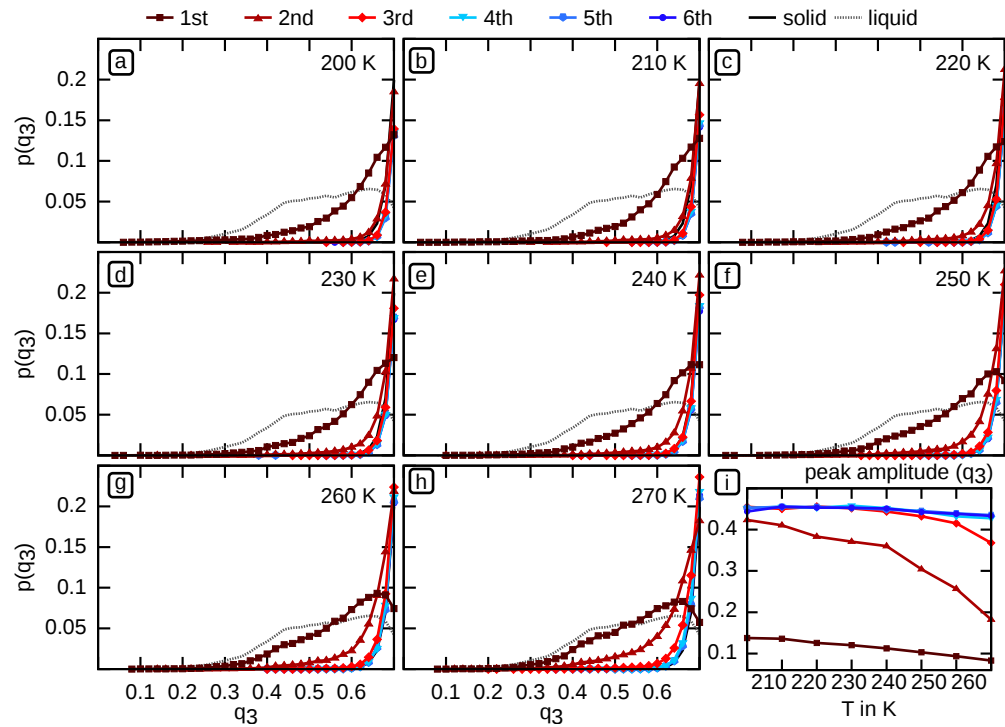


Fig. 8.67: Temperature-dependent layer-resolved distributions for q_3 of the upper six bilayers of ice slabs of the primary prismatic plane.

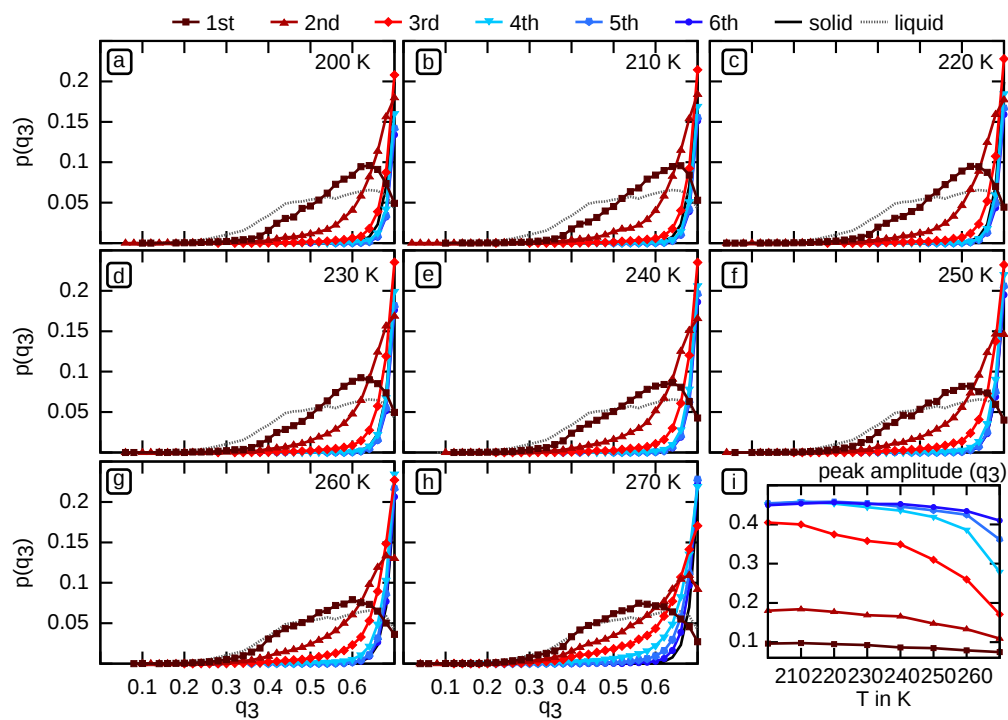


Fig. 8.68: Temperature-dependent layer-resolved distributions for q_3 of the upper six single-layers of ice slabs of the secondary prismatic plane.

q₆

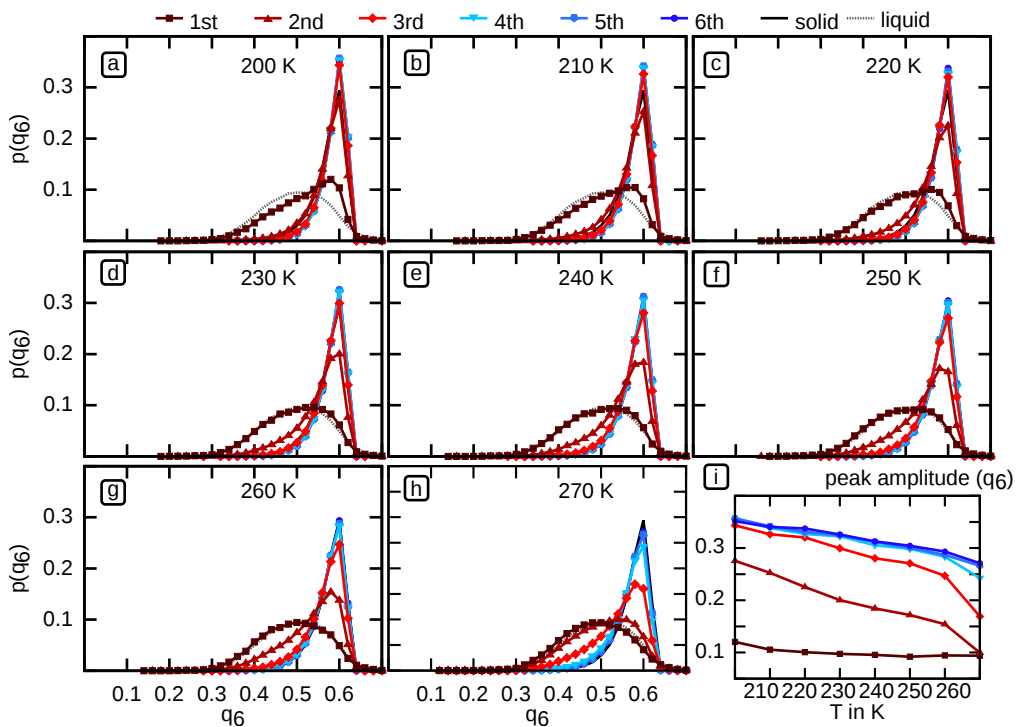


Fig. 8.69: Temperature-dependent layer-resolved distributions for q_6 of the upper six bilayers of ice slabs of the basal plane.

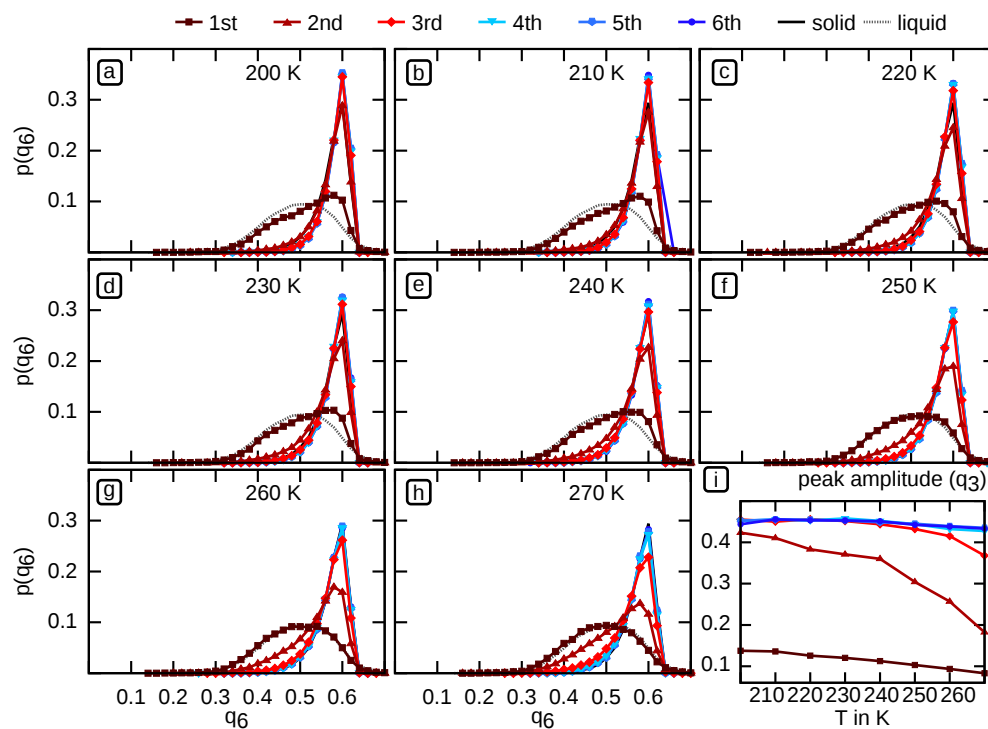


Fig. 8.70: Temperature-dependent layer-resolved distributions for q_6 of the upper six bilayers of ice slabs of the primary prismatic plane.

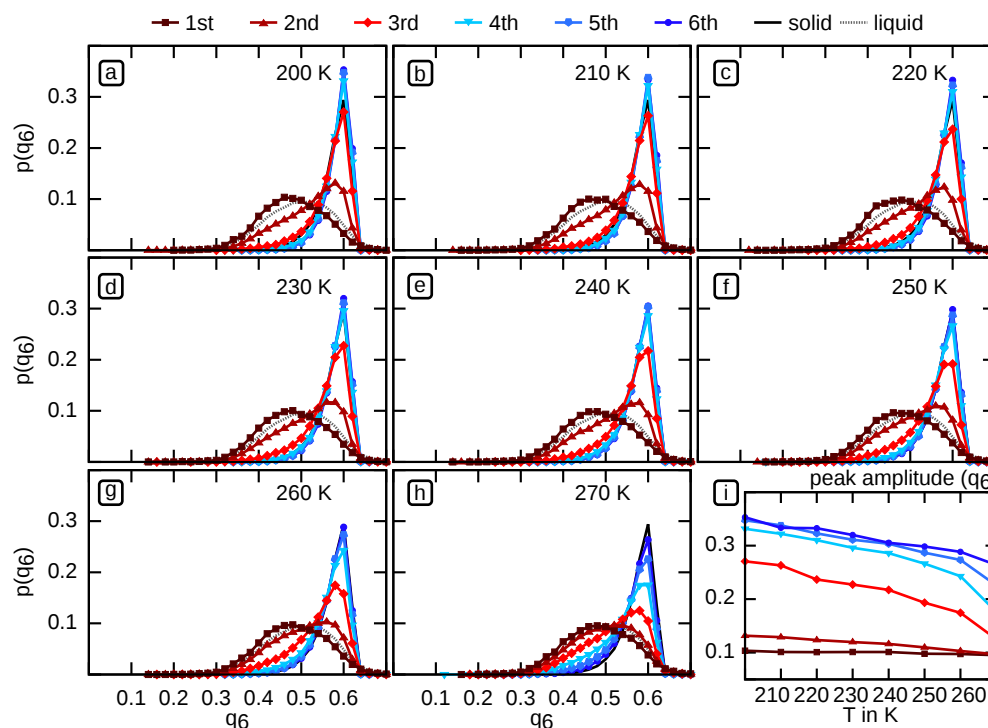


Fig. 8.71: Temperature-dependent layer-resolved distributions for q_6 of the upper six single-layers of ice slabs of the secondary prismatic plane.

8.4.5 Comparison between the criterion used in this work and an alternate criterion to select neighbours based on H-bonds

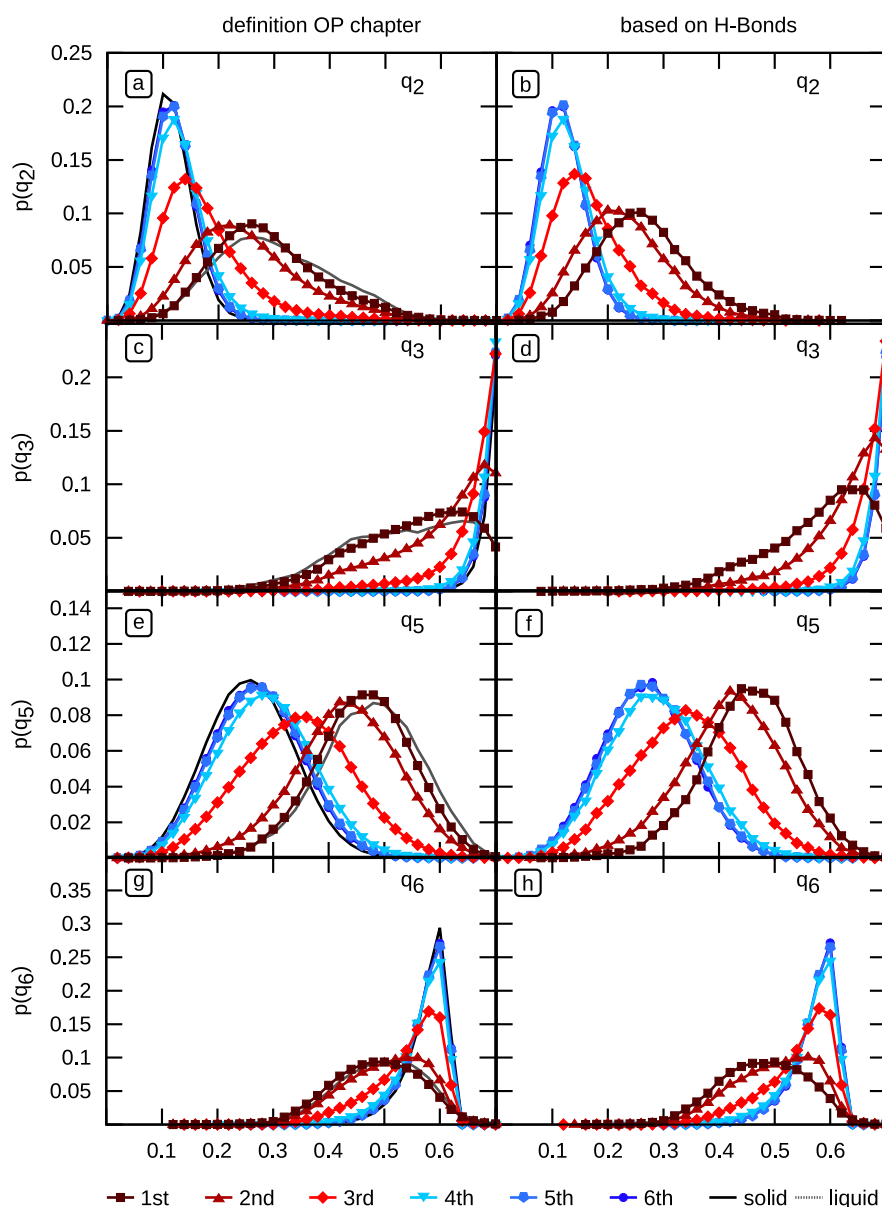


Fig. 8.72: Temperature-dependent bilayer-resolved distribution for q_i , $i = 2, 3, 5, 6$ for the basal plane at 270 K for two definitions of the next neighbours. For the plots in the left columns the definition using the four nearest neighbours within a cut-off distance as applied in Chapter 5 is used, while for the right column the definition utilising the H-bond criteria described in Chapter 4 is applied. No major difference is observed and both approaches seem to be valid.

8.5 Chapter 6: Self-diffusivity of the three most prominent ice surfaces

8.5.1 Out-of-plane diffusion

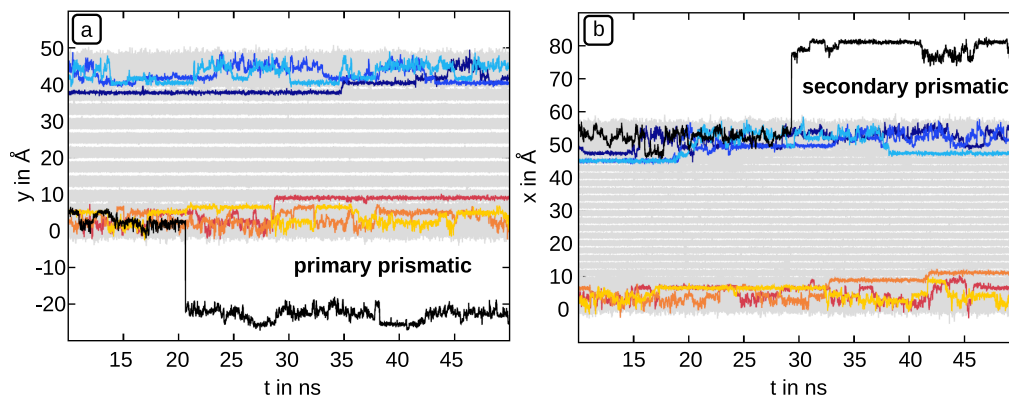


Fig. 8.73: Z-components of all oxygen atom trajectories for the last forty nanoseconds of the simulation of (a) the primary prismatic plane, and (b) the secondary prismatic plane at 270 K. Six selected trajectories are highlighted.

8.5.2 In-plane diffusion

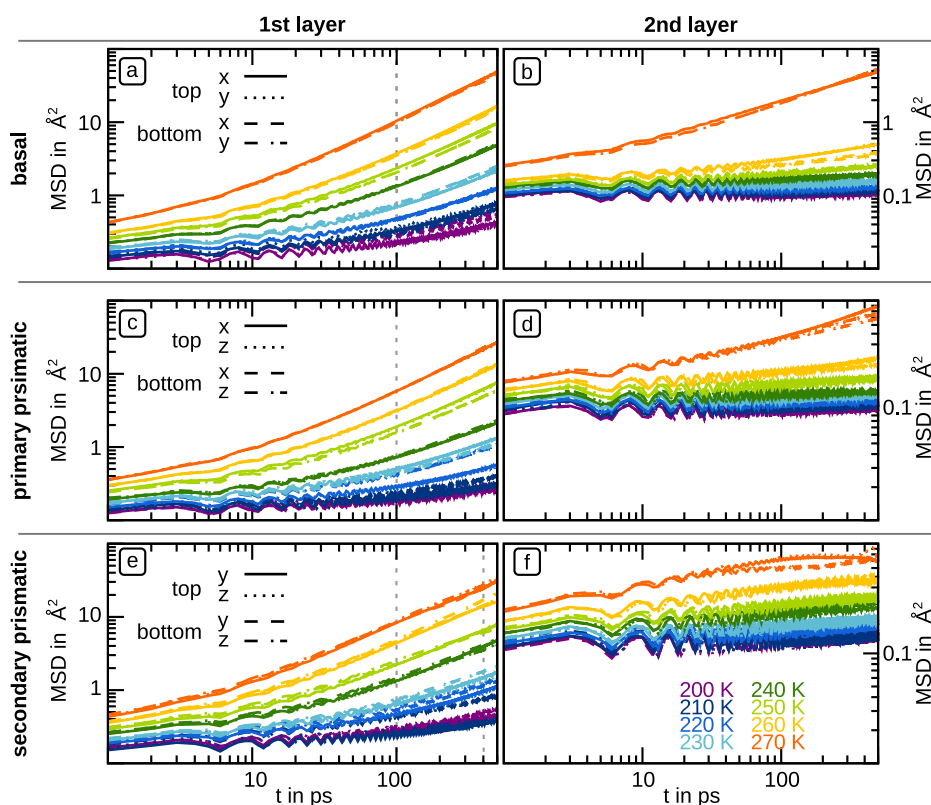


Fig. 8.74: Temperature-dependent mean square displacements for the first two bilayers of the basal plane, the primary prismatic plane, and the secondary prismatic plane. The time interval between 100 ps and 500 ps (400 ps for 270 K of the secondary prismatic plane) is indicated by grey dotted lines, because both linearity and statistics are considered sufficient within that range for a self-diffusion analysis. The corresponding contributions for the top and bottom surfaces and respectively the in-plane directions are displayed separately.

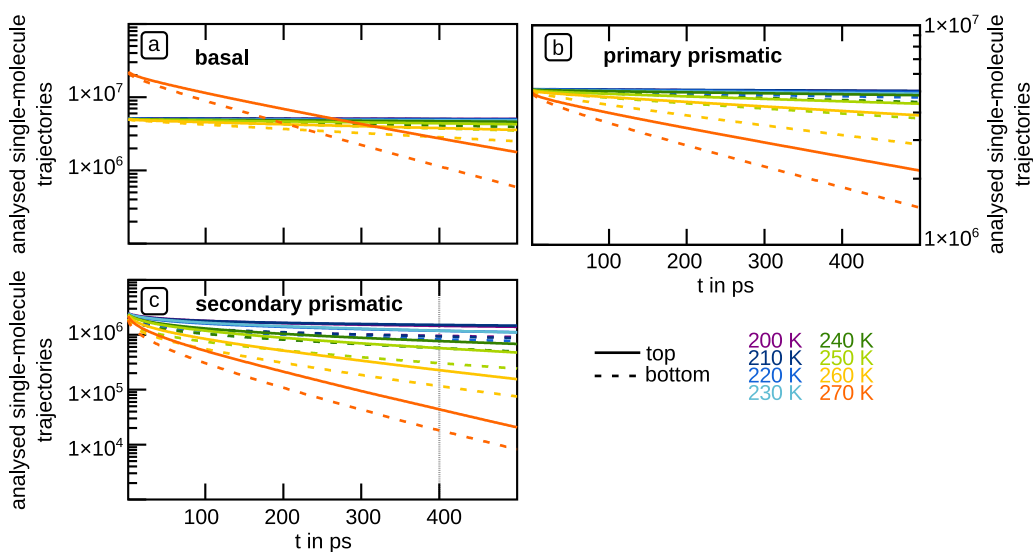


Fig. 8.75: Temperature-dependent amount of single-molecule trajectories contributing to the MSD of a length t for the first layers of the (a) basal plane, the (b) primary prismatic plane, and (c) the secondary prismatic plane. The grey dotted line indicates the amount of traces, which is above 10^4 for the highest temperature of the secondary prismatic plane.

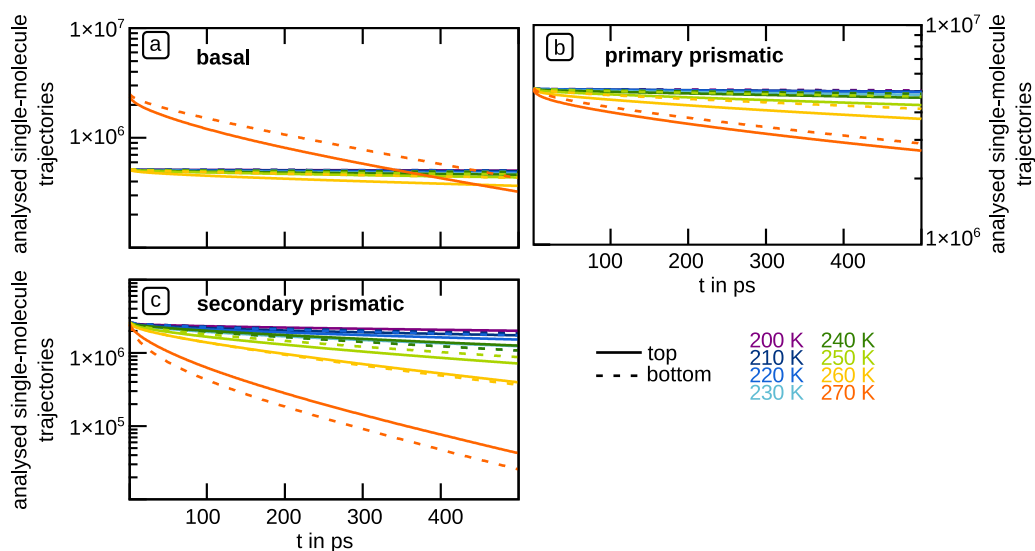


Fig. 8.76: Temperature-dependent number of analysed traces for the second layers of the hexagonal ice surfaces for the simulated top and bottom surfaces separately.

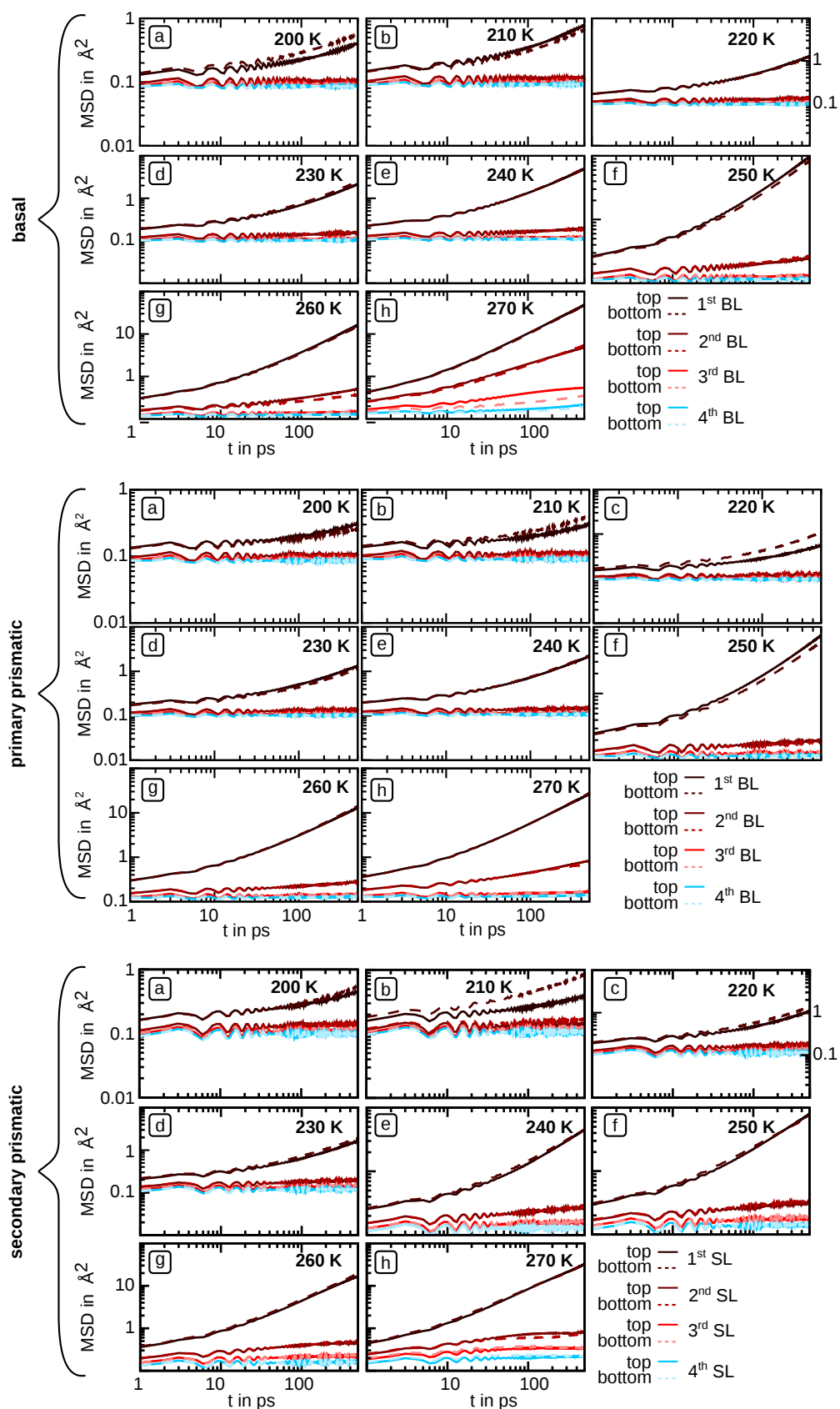


Fig. 8.77: MSDs of the first four layers for all temperatures and surfaces. The wiggling below 100 ps is caused by oscillations of the molecules around their equilibrium positions.

Tab. 8.3: Fitted exponents for the first layers of the three most prominent ice surfaces. For all exponents a time interval of 100 ps–500 ps was chosen, but for 270 K for the secondary prismatic plane, where an interval of 100 ps–400 ps was selected.

Basal	top x	bottom x	top y	bottom y	average
200	0.41	0.40	0.36	0.44	0.40 ± 0.02
210	0.54	0.48	0.50	0.51	0.51 ± 0.01
220	0.61	0.61	0.64	0.60	0.62 ± 0.01
230	0.73	0.76	0.71	0.71	0.73 ± 0.01
240	0.82	0.84	0.83	0.81	0.83 ± 0.01
250	0.89	0.89	0.90	0.87	0.89 ± 0.01
260	0.93	0.93	0.92	0.92	0.92 ± 0.00
270	0.96	0.94	0.95	1.00	0.96 ± 0.01
Primary prismatic	top x	bottom x	top z	bottom z	average
200	0.30	0.24	0.28	0.20	0.26 ± 0.02
210	0.27	0.33	0.26	0.35	0.31 ± 0.02
220	0.44	0.59	0.42	0.61	0.51 ± 0.05
230	0.62	0.60	0.61	0.58	0.60 ± 0.01
240	0.68	0.71	0.71	0.69	0.70 ± 0.01
250	0.87	0.83	0.88	0.85	0.86 ± 0.01
260	0.91	0.93	0.91	0.93	0.92 ± 0.01
270	0.96	0.98	0.94	0.96	0.96 ± 0.01
Secondary prismatic	top y	bottom y	top z	bottom z	average
200	0.30	0.40	0.31	0.37	0.35 ± 0.03
210	0.26	0.39	0.26	0.42	0.33 ± 0.04
220	0.56	0.57	0.52	0.56	0.55 ± 0.01
230	0.63	0.54	0.58	0.65	0.60 ± 0.02
240	0.80	0.65	0.74	0.75	0.74 ± 0.03
250	0.78	0.70	0.80	0.65	0.73 ± 0.03
260	0.82	0.80	0.83	0.90	0.84 ± 0.02
270	0.77	0.80	0.85	0.78	0.80 ± 0.02

Tab. 8.4: Fitted exponents for the second layers of the three most prominent ice surfaces. A time interval of 100 ps–500 ps was selected for fitting.

Basal	top x	bottom x	top y	bottom y	average
200	0.02	0.01	0.01	0.01	0.01 ± 0.00
210	0.03	0.03	0.03	0.03	0.03 ± 0.00
220	0.04	0.04	0.04	0.04	0.04 ± 0.00
230	0.06	0.08	0.06	0.08	0.07 ± 0.00
240	0.10	0.10	0.10	0.09	0.10 ± 0.00
250	0.15	0.16	0.13	0.15	0.15 ± 0.01
260	0.30	0.21	0.31	0.24	0.26 ± 0.03
270	0.57	0.67	0.56	0.67	0.62 ± 0.03
Primary prismatic	top x	bottom x	top z	bottom z	average
200	0.02	0.01	0.02	0.01	0.02 ± 0.00
210	0.02	0.03	0.01	0.02	0.02 ± 0.00
220	0.03	0.05	0.02	0.04	0.03 ± 0.01
230	0.03	0.04	0.03	0.03	0.03 ± 0.00
240	0.03	0.05	0.03	0.04	0.04 ± 0.00
250	0.09	0.08	0.06	0.06	0.07 ± 0.01
260	0.18	0.16	0.10	0.10	0.13 ± 0.02
270	0.41	0.31	0.35	0.28	0.34 ± 0.03
Secondary prismatic	top y	bottom y	top z	bottom z	average
200	0.06	0.07	0.04	0.05	0.05 ± 0.01
210	0.03	0.08	0.03	0.06	0.05 ± 0.01
220	0.09	0.09	0.06	0.05	0.07 ± 0.01
230	0.07	0.10	0.07	0.06	0.07 ± 0.01
240	0.12	0.14	0.11	0.09	0.12 ± 0.01
250	0.11	0.10	0.05	0.09	0.09 ± 0.01
260	0.09	0.14	0.07	0.06	0.09 ± 0.02
270	0.01	0.10	0.04	0.17	0.08 ± 0.03

Tab. 8.5: Separate temperature-dependent self-diffusion coefficients (in $\text{cm}^2 \text{s}^{-1}$) obtained by fitting the MSDs using the Einstein relation with GNUPLLOT. The errors correspond to the standard errors.

Basal	top x	bottom x	top y	bottom y	average
240 K	4.41E-07	4.73E-07	4.60E-07	4.40E-07	$4.54\text{E-}07 \pm 7.88\text{E-}09$
250 K	9.15E-07	7.97E-07	9.27E-07	7.80E-07	$8.55\text{E-}07 \pm 3.85\text{E-}08$
260 K	1.59E-06	1.48E-06	1.54E-06	1.46E-06	$1.52\text{E-}06 \pm 3.07\text{E-}08$
270 K	4.77E-06	4.33E-06	4.60E-06	4.90E-06	$4.65\text{E-}06 \pm 1.24\text{E-}07$
Primary prismatic	top x	bottom x	top z	bottom z	average
250 K	7.11E-07	5.44E-07	6.86E-07	5.47E-07	$6.22\text{E-}07 \pm 4.43\text{E-}08$
260 K	1.27E-06	1.38E-06	1.24E-06	1.33E-06	$1.30\text{E-}06 \pm 3.10\text{E-}08$
270 K	2.64E-06	2.79E-06	2.53E-06	2.63E-06	$2.65\text{E-}06 \pm 5.47\text{E-}08$
Secondary prismatic	top y	bottom y	top z	bottom z	average
260 K	1.49E-06	1.53E-06	1.56E-06	2.01E-06	$1.65\text{E-}06 \pm 1.21\text{E-}07$
270 K	2.62E-06	2.85E-06	3.22E-06	2.92E-06	$2.90\text{E-}06 \pm 1.24\text{E-}07$

Tab. 8.6: Fit parameters of the Arrhenius plots of Figure 6.6 by utilising $\ln(D) = \ln(D_0) - \frac{E_{A,\text{mol}}}{R \cdot T} = \ln(D_0) - \frac{E_A}{k_B \cdot T}$. The errors correspond to the standard errors of the separate values.

$E_{A,\text{mol}}$ in kJ mol^{-1}	t x	b x	t y	b y	average
basal	41.27	39.77	38.85	42.01	40.47 ± 0.71
primary prismatic	36.78	36.55	45.96	44.07	40.84 ± 2.44
secondary prismatic	33.06	42.27	36.36	21.98	33.42 ± 4.26
E_A in eV	t x	b x	t y	b y	average
basal	0.43	0.41	0.40	0.44	0.42 ± 0.01
primary prismatic	0.38	0.38	0.48	0.46	0.42 ± 0.03
secondary prismatic	0.34	0.44	0.38	0.23	0.35 ± 0.04
D_0 in $\text{cm}^2 \text{s}^{-1}$	t x	b x	t y	b y	average
basal	0.039	0.019	0.012	0.052	0.031 ± 0.009
primary prismatic	0.003	0.003	0.224	0.090	0.080 ± 0.052
secondary prismatic	0.001	0.048	0.003	0.000	0.013 ± 0.012

8.5.3 Liquid water references

Tab. 8.7: Fitted exponents of the ln-ln-fits of the MSDs for supercooled water for a time interval of 100 ps–3000 ps.

T in K	x	y	z	average
200	0.53	0.52	0.52	0.52 ± 0.00
210	0.73	0.69	0.72	0.71 ± 0.01
220	0.75	0.77	0.77	0.76 ± 0.01
230	0.94	0.91	0.99	0.94 ± 0.02
240	0.95	0.97	0.97	0.96 ± 0.01
250	1.00	0.98	0.99	0.99 ± 0.01
260	0.99	0.98	0.99	0.99 ± 0.00
270	0.97	1.02	1.00	1.00 ± 0.01
272	1.01	1.02	0.99	1.01 ± 0.01
275	0.98	0.99	1.00	0.99 ± 0.01
300	0.99	0.99	1.01	1.00 ± 0.01

Tab. 8.8: Separate temperature-dependent self-diffusion coefficients (in $\text{cm}^2 \text{s}^{-1}$) for (super-cooled) water obtained by fitting the MSDs ($t = 100 \text{ ps} - 3000 \text{ ps}$) using the Einstein relation with GNUPLLOT. The error corresponds to the standard error

T in K	D_x	D_y	D_z	D_{av}
230	6.11E-08	5.47E-08	7.19E-08	$6.26\text{E-}08 \pm 5.00\text{E-}09$
240	1.03E-07	1.07E-07	1.14E-07	$1.08\text{E-}07 \pm 3.06\text{E-}09$
250	4.52E-07	4.18E-07	4.40E-07	$4.36\text{E-}07 \pm 1.00\text{E-}08$
260	1.55E-06	1.50E-06	1.61E-06	$1.55\text{E-}06 \pm 3.22\text{E-}08$
270	2.15E-06	2.43E-06	2.39E-06	$2.32\text{E-}06 \pm 8.72\text{E-}08$
272	3.07E-06	3.06E-06	2.86E-06	$3.00\text{E-}06 \pm 6.90\text{E-}08$
275	2.96E-06	2.84E-06	3.05E-06	$2.95\text{E-}06 \pm 5.83\text{E-}08$
300	9.50E-06	9.03E-06	9.81E-06	$9.45\text{E-}06 \pm 2.26\text{E-}07$

Tab. 8.9: Parameters of the Arrhenius fit for the (supercooled) water reference. Errors correspond to standard errors.

	x	y	z	average
D₀ in cm ² s ⁻¹	854.56	1021.42	571.25	815.74 ± 131.40
	x	y	z	average
E_{A,mol} in kJ mol ⁻¹	44.60	45.03	43.63	44.42 ± 0.41
	x	y	z	average
E_A in eV	0.46	0.47	0.45	0.46 ± 0.00

8.5.4 Self-diffusion anisotropy

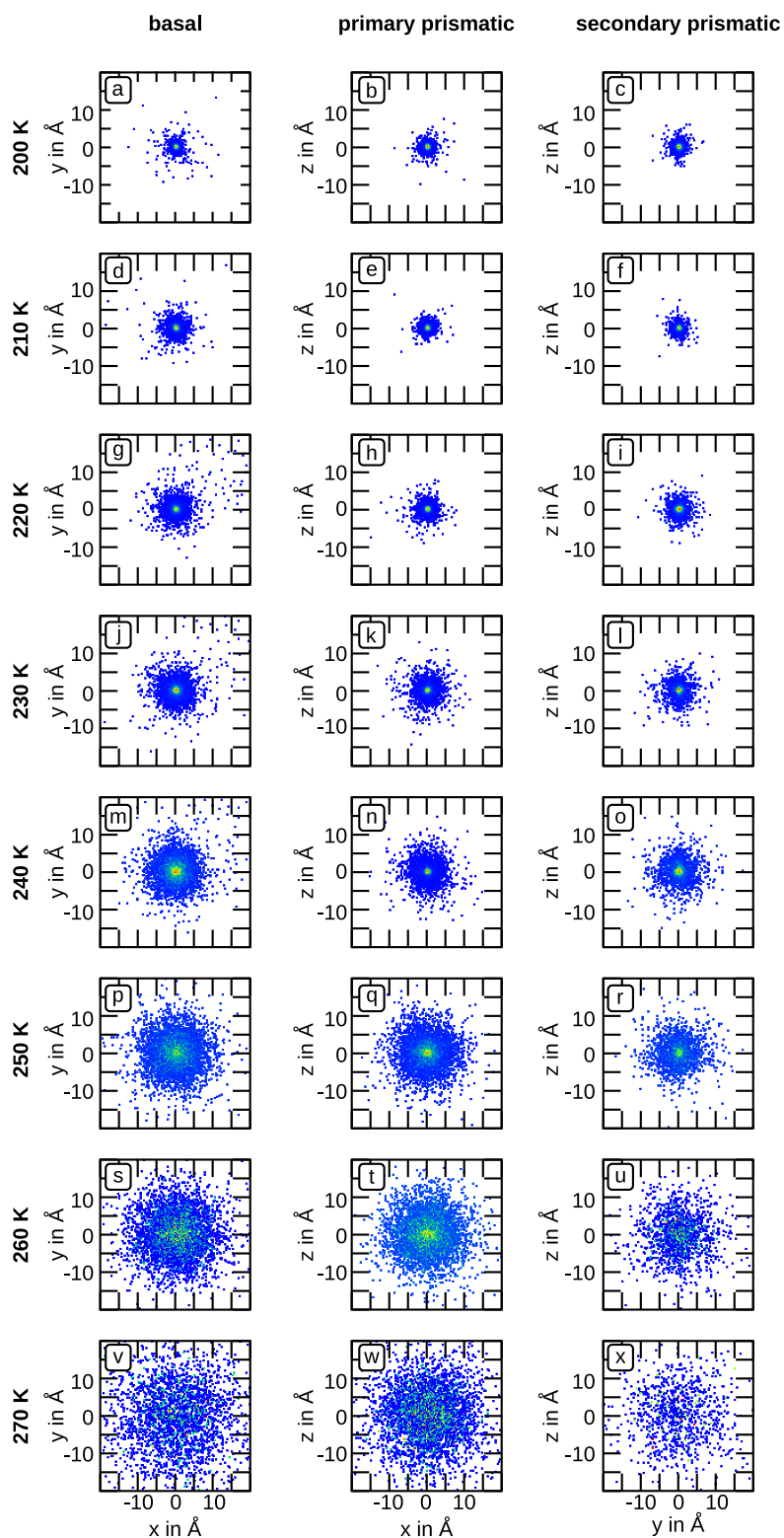


Fig. 8.78: Distribution of self-diffusion directions at the top layers of the three surfaces at all temperatures. No regular pattern is observed. Forty snapshots in an interval of 1 ns were analysed each.

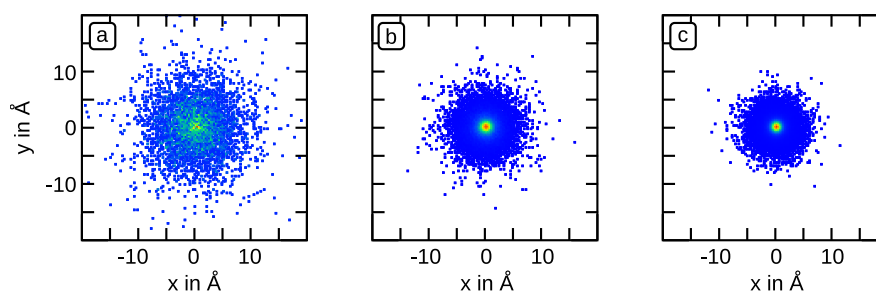


Fig. 8.79: Distribution of self-diffusion directions at the top layer of the basal plane at 250 K obtained by analysing three different time intervals: **(a)** 1 ns, **(b)** 0.1 ns, and **(c)** 0.02 ns.

8.6 Software list

Excerpt of software and scripts used in this thesis:

- *DLPOLY*:^[122] All simulations have been conducted with the DL POLY software.
- A script to determine hydrogen-bonded rings written by Sabrina Gaito, Davide Ceresoli, and Davide Donadio.
- A script to calculate order parameters by Felix Kling.
- An H-bond analysis script by Felix Kling.
- Script for removing centre-of-mass-motion from a trajectory written by Rengin Pekoez.
- *Gnuplot*^[174]
- Several small scripts by Felix Kling.
- *Gromacs*:^a Software used for the calculation of some RDFs employing the tool *g_rdf*.
- *VMD 1.9*^[117]
- *Gwyddion*^[128]: Open source software used for the production of the FFT images of the two-dimensional density maps (Chapter 3).

^a.

Bibliography

- [1] M. A. Sánchez, T. Kling, T. Ishiyama, et al., “Experimental and theoretical evidence for bilayer-by-bilayer surface melting of crystalline ice”, *Proceedings of the National Academy of Sciences* **2017**, *114*, 227–232.
- [2] P. Bridgman, “High pressures and five kinds of ice”, *Journal of the Franklin Institute* **1914**, *177*, 315–332.
- [3] A. N. Dunaeva, D. V. Antsyshkin, O. L. Kuskov, “Phase diagram of H₂O: thermodynamic functions of the phase transitions of high-pressure ices”, *Solar System Research* **2010**, *44*, 202–222.
- [4] T. Bartels-Rausch, V. Bergeron, J. H. E. Cartwright, et al., “Ice structures, patterns, and processes: a view across the icefields”, *Reviews of Modern Physics* **2012**, *84*, 885–944.
- [5] C. P. Herrero, R. Ramírez, “Configurational entropy of ice from thermodynamic integration”, *Chemical Physics Letters* **2013**, *568–569*, 70–74.
- [6] C. Lobban, J. L. Finney, W. F. Kuhs, “The structure of a new phase of ice”, *Nature* **1998**, *391*, 268–270.
- [7] O. Mishima, L. D. Calvert, E. Whalley, “An apparently first-order transition between two amorphous phases of ice induced by pressure”, *Nature* **1985**, *314*, 76–78.
- [8] O. Mishima, H. E. Stanley, “The relationship between liquid, supercooled and glassy water”, *Nature* **1998**, *396*, 329–335.
- [9] N. Giovambattista, F. Sciortino, F. W. Starr, et al., “Potential energy landscape of the apparent first-order phase transition between low-density and high-density amorphous ice”, *The Journal of Chemical Physics* **2016**, *145*, 224501.
- [10] J. D. Bernal, R. H. Fowler, “A theory of water and ionic solution, with particular reference to hydrogen and hydroxyl ions”, *The Journal of Chemical Physics* **1933**, *1*, 515–548.
- [11] Z. Raza, D. Alfè, C. Salzmann, et al., “Proton ordering in cubic ice and hexagonal ice; a potential new ice phase—XI_c”, *Physical Chemistry Chemical Physics* **2011**, *13*, 19788–19795.
- [12] M. Faraday, “On regelation, and on the conservation of force”, *Philosophical Magazine Series 4* **1859**, *17*, 162–169.
- [13] J. G. Dash, “Surface melting”, *Contemporary Physics* **1989**, *30*, 89–100.
- [14] G. J. Kroes, “Surface melting of the (0001) face of TIP4P ice”, *Surface Science* **1992**, *275*, 365–382.

- [15] K. Bolton, J. B. C. Pettersson, "Trapping—desorption and surface penetration of argon on ice", *Chemical Physics Letters* **1999**, 312, 71–76.
- [16] K. Bolton, J. B. C. Pettersson, "A molecular dynamics study of the long-time ice I_h Surface Dynamics", *The Journal of Physical Chemistry B* **2000**, 104, 1590–1595.
- [17] J. G. Dash, "History of the search for continuous melting", *Reviews of Modern Physics* **1999**, 71, 1737–1743.
- [18] J. G. Dash, A. W. Rempel, J. S. Wettlaufer, "The physics of premelted ice and its geophysical consequences", *Reviews of Modern Physics* **2006**, 78, 695–741.
- [19] R. Rosenberg, "Why is ice slippery?", *Physics Today* **2005**, 58, 50–54.
- [20] J. S. Wettlaufer, J. G. Dash, "Melting below zero", *Scientific American* **2000**, 282, 50–53.
- [21] J. G. Dash, H. Fu, J. S. Wettlaufer, "The premelting of ice and its environmental consequences", *Reports on Progress in Physics* **1995**, 58, 115–167.
- [22] C. Schoof, "Ice-sheet acceleration driven by melt supply variability", *Nature* **2010**, 468, 803–806.
- [23] M. T. Kalichevsky, D. Knorr, P. J. Lillford, "Potential food applications of high-pressure effects on ice-water transitions", *Trends in Food Science and Technology* **1995**, 6, 253–259.
- [24] B. Li, D.-W. Sun, "Novel methods for rapid freezing and thawing of foods—a review", *Journal of Food Engineering* **2002**, 54, 175–182.
- [25] K. Cook, R. Hartel, "Mechanisms of ice crystallization in ice cream production", *Comprehensive Reviews in Food Science and Food Safety* **2010**, 9, 213–222.
- [26] T. Bartels-Rausch, H.-W. Jacobi, T. F. Kahan, et al., "A review of air–ice chemical and physical interactions (AICI): liquids, quasi-liquids, and solids in snow", *Atmospheric Chemistry and Physics* **2014**, 14, 1587–1633.
- [27] Y. Furukawa, M. Yamamoto, T. Kuroda, "Ellipsometric study of the transition layer on the surface of an ice crystal", *Journal of Crystal Growth* **1987**, 82, 665–677.
- [28] H. Dosch, A. Lied, J. H. Bilgram, "Glancing-angle X-ray scattering studies of the premelting of ice surfaces", *Surface Science* **1995**, 327, 145–164.
- [29] B. Bullemer, N. Riehl, "Bulk and surface conductivity of ice", *Solid State Communications* **1966**, 4, 447–448.
- [30] I. Golecki, C. Jaccard, "Intrinsic surface disorder in ice near the melting point", *Journal of Physics C: Solid state physics* **1978**, 11, 4229–4237.
- [31] I. Golecki, C. Jaccard, "The surface of ice near 0 °C studied by 100 keV proton channeling", *Physics Letters A* **1977**, 63, 374–376.
- [32] M. T. Suter, P. U. Andersson, J. B. C. Pettersson, "Surface properties of water ice at 150 K to 191 K studied by elastic helium scattering", *Journal of Chemical Physics* **2006**, 125, 174704.
- [33] X. Wei, P. B. Miranda, C. Zhang, et al., "Sum-frequency spectroscopic studies of ice interfaces", *Physical Review B* **2002**, 66, 085401.
- [34] Y. Mizuno, N. Hanafusa, "Studies of surface properties of ice using nuclear magnetic resonance", *Le Journal de Physique Colloques* **1987**, 48, C1–511.

- [35] D. Nason, N. H. Fletcher, "Photoemission from ice and water surfaces: quasiliquid layer effect", *The Journal of Chemical Physics* **1975**, 62, 4444–4449.
- [36] Y. Furukawa, H. Nada, "Anisotropic surface melting of an ice crystal and its relationship to growth forms", *Journal of Physical Chemistry B* **1997**, 101, 6167–6170.
- [37] A. Döppenschmidt, H. J. Butt, "Measuring the thickness of the liquid-like layer on ice surfaces with atomic force microscopy", *Langmuir* **2000**, 16, 6709–6714.
- [38] B. Pittenger, S. C. Fain, M. J. Cochran, et al., "Premelting at ice-solid interfaces studied via velocity-dependent indentation with force microscope tips", *Physical Review B* **2001**, 63, 134102.
- [39] M. P. Goertz, X.-Y. Zhu, J. E. Houston, "Exploring the liquid-like layer on the ice surface", *Langmuir* **2009**, 25, 6905–6908.
- [40] H. Bluhm, D. F. Ogletree, C. S. Fadley, et al., "The premelting of ice studied with photoelectron spectroscopy", *Journal of Physics: Condensed Matter* **2002**, 14, L227–L233.
- [41] M. Elbaum, S. G. Lipson, J. G. Dash, "Optical study of surface melting on ice", *Journal of Crystal Growth* **1993**, 129, 491–505.
- [42] M. M. Conde, C. Vega, A. Patrykiewicz, "The thickness of a liquid layer on the free surface of ice as obtained from computer simulation", *The Journal of Chemical Physics* **2008**, 129, 014702.
- [43] Creative Commons, CC-BY license 3.0, **2007**, <https://creativecommons.org/licenses/by/3.0/legalcode>.
- [44] A. Kouchi, Y. Furukawa, T. Kuroda, "X-ray diffraction pattern of quasi-liquid layer on ice crystal surface", *Journal de Physique Colloques* **1987**, 48, C1–675.
- [45] H. Dosch, A. Lied, J. H. Bilgram, "Disruption of the hydrogen-bonding network at the surface of I_h ice near surface premelting", *Surface Science* **1996**, 366, 43–50.
- [46] V. Buch, H. Groenzin, I. Li, et al., "Proton order in the ice crystal surface", *Proceedings of the National Academy of Sciences* **2008**, 105, 5969–5974.
- [47] A. Döppenschmidt, M. Kappl, H.-J. Butt, "Surface properties of ice studied by atomic force microscopy", *The Journal of Physical Chemistry B* **1998**, 102, 7813–7819.
- [48] J. S. Wettlaufer, "Impurity effects in the premelting of ice", *Physical Review Letters* **1999**, 82, 2516–2519.
- [49] V. F. McNeill, T. Loerting, F. M. Geiger, et al., "Hydrogen chloride-induced surface disordering on ice", *Proceedings of the National Academy of Sciences* **2006**, 103, 9422–9427.
- [50] V. F. McNeill, F. M. Geiger, T. Loerting, et al., "Interaction of hydrogen chloride with ice surfaces: the effects of grain size, surface roughness, and surface disorder", *The Journal of Physical Chemistry A* **2007**, 111, 6274–6284.
- [51] G. Sazaki, S. Zepeda, S. Nakatsubo, et al., "Elementary steps at the surface of ice crystals visualized by advanced optical microscopy.", *Proceedings of the National Academy of Sciences* **2010**, 107, 19702–19707.
- [52] G. Sazaki, S. Zepeda, S. Nakatsubo, et al., "Quasi-liquid layers on ice crystal surfaces are made up of two different phases", *Proceedings of the National Academy of Sciences* **2011**, 109, 1052–1055.

- [53] G. Sazaki, H. Asakawa, K. Nagashima, et al., “Double spiral steps on I_h ice crystal surfaces grown from water vapor just below the melting point”, *Crystal Growth and Design* **2014**, *14*, 2133–2137.
- [54] H. Asakawa, G. Sazaki, E. Yokoyama, et al., “Roles of surface/volume diffusion in the growth kinetics of elementary spiral steps on ice basal faces grown from water vapor”, *Crystal Growth and Design* **2014**, *14*, 3210–3220.
- [55] H. Asakawa, G. Sazaki, K. Nagashima, et al., “Prism and other high-index faces of ice crystals exhibit two types of quasi-liquid layers”, *Crystal Growth and Design* **2015**, *15*, 3339–3344.
- [56] K. I. Murata, H. Asakawa, K. Nagashima, et al., “In situ determination of surface tension-to-shear viscosity ratio for quasiliquid layers on ice crystal surfaces”, *Physical Review Letters* **2015**, *115*, 256103.
- [57] H. Asakawa, G. Sazaki, K. Nagashima, et al., “Two types of quasi-liquid layers on ice crystals are formed kinetically”, *Proceedings of the National Academy of Sciences* **2016**, *113*, 1749–1753.
- [58] K. Nagashima, G. Sazaki, T. Hama, et al., “Direct visualization of quasi-liquid layers on ice crystal surfaces induced by hydrogen chloride gas”, *Crystal Growth and Design* **2016**, *16*, 2225–2230.
- [59] K. I. Murata, H. Asakawa, K. Nagashima, et al., “Thermodynamic origin of surface melting on ice crystals”, *Proceedings of the National Academy of Sciences* **2016**, *113*, E6741.
- [60] M. J. Shultz, P. J. Bisson, A. Brumberg, “Best face forward: crystal-face competition at the ice-water interface”, *Journal of Physical Chemistry B* **2014**, *118*, 7972–7980.
- [61] P. Conrad, G. E. Ewing, R. L. Karlinsey, et al., “Ice nucleation on $BaF_2(111)$ ”, *The Journal of Chemical Physics* **2005**, *122*, 064709.
- [62] V. Sadtchenko, P. Conrad, G. E. Ewing, “ H_2O adsorption on $BaF_2(111)$ at ambient temperatures”, *The Journal of Chemical Physics* **2002**, *116*, 4293–4301.
- [63] M. Maruyama, T. Ashida, C. A. Knight, “Disk crystals of ice grown in air-free water: no effect of dissolved air on the morphology”, *Journal of Crystal Growth* **1999**, *205*, 391–394.
- [64] W. C. Pfalzgraff, R. M. Hulscher, S. P. Neshyba, “Scanning electron microscopy and molecular dynamics of surfaces of growing and ablating hexagonal ice crystals”, *Atmospheric Chemistry and Physics Discussions* **2009**, *9*, 20739–20763.
- [65] M. J. Shultz, A. Brumberg, P. J. Bisson, et al., “Producing desired ice faces”, *Proceedings of the National Academy of Sciences* **2015**, *112*, E6096–E6100.
- [66] S. Engemann, H. Reichert, H. Dosch, et al., “Interfacial melting of ice in contact with SiO_2 ”, *Physical Review Letters* **2004**, *92*, 205701.
- [67] B. F. Henson, L. F. Voss, K. R. Wilson, et al., “Thermodynamic model of quasiliquid formation on H_2O ice: comparison with experiment”, *The Journal of Chemical Physics* **2005**, *123*, 144707.
- [68] X. Wei, P. Miranda, C. Zhang, et al., “Sum-frequency spectroscopic studies of ice interfaces”, *Physical Review B* **2002**, *66*, 085401.
- [69] T. Ishiyama, H. Takahashi, A. Morita, “Origin of vibrational spectroscopic response at ice surface”, *Journal of Physical Chemistry Letters* **2012**, *3*, 3001–3006.

- [70] X. Wei, P. B. Miranda, Y. R. Shen, "Surface vibrational spectroscopic study of surface melting of ice", *Physical Review Letters* **2001**, 86, 1554–1557.
- [71] A. Lied, H. Dosch, J. H. Bilgram, "Surface melting of ice I_h single crystals revealed by glancing angle X-ray scattering", *Physical Review Letters* **1994**, 72, 3554–3557.
- [72] D. Marx, J. Hutter, *Ab initio molecular dynamics: basic theory and advanced methods*, Cambridge University Press, **2009**.
- [73] M. P. Allen, D. J. Tildesley, *Computer simulation of liquids*, Oxford university press, **1989**.
- [74] C. Peter, K. Kremer, "Multiscale simulation of soft matter systems—from the atomistic to the coarse-grained level and back", *Soft Matter* **2009**, 5, 4357–4366.
- [75] E. B. Moore, E. De La Llave, K. Welke, et al., "Freezing, melting and structure of ice in a hydrophilic nanopore", *Physical Chemistry Chemical Physics* **2010**, 12, 4124–4134.
- [76] T. D. Shepherd, M. A. Koc, V. Molinero, "The quasi-liquid layer of ice under conditions of methane clathrate formation", *Journal of Physical Chemistry C* **2012**, 116, 12172–12180.
- [77] O. A. Karim, A. Haymet, "The ice/water interface", *Chemical Physics Letters* **1987**, 138, 531–534.
- [78] F. Paesani, G. A. Voth, "Quantum effects strongly influence the surface premelting of ice", *Journal of Physical Chemistry C* **2008**, 112, 324–327.
- [79] C. Vega, J. L. F. Abascal, E. Sanz, et al., "Can simple models describe the phase diagram of water?", *Journal of Physics: Condensed Matter* **2005**, 17, S3283.
- [80] C. Vega, J. L. F. Abascal, "Simulating water with rigid non-polarizable models: a general perspective", *Physical Chemistry Chemical Physics* **2011**, 13, 19663–19688.
- [81] C. Vega, J. L. F. Abascal, M. M. Conde, et al., "What ice can teach us about water interactions: a critical comparison of the performance of different water models", *Faraday Discussions* **2009**, 141, 251–276.
- [82] D. T. Limmer, D. Chandler, "Premelting, fluctuations, and coarse-graining of water-ice interfaces", *The Journal of Chemical Physics* **2014**, 141, 18C505.
- [83] S.-C. Park, E.-S. Moon, H. Kang, "Some fundamental properties and reactions of ice surfaces at low temperatures", *Physical Chemistry Chemical Physics* **2010**, 12, 12000–12011.
- [84] N. Materer, U. Starke, A. Barbieri, et al., "Molecular-surface structure of a low-temperature ice I_h (0001) crystal", *Journal of Physical Chemistry* **1995**, 99, 6267–6269.
- [85] C. Vega, M. Martin-Conde, A. Patrykiewicz, "Absence of superheating for ice I_h with a free surface: a new method of determining the melting point of different water models", *Molecular Physics* **2006**, 104, 3583–3592.
- [86] C. L. Bishop, D. Pan, L. M. Liu, et al., "On thin ice: surface order and disorder during pre-melting", *Faraday Discussions* **2009**, 141, 277–292.
- [87] S. Neshyba, E. Nugent, M. Roeselova, et al., "Molecular dynamics study of ice–vapor interactions via the quasi-liquid layer", *The Journal of Physical Chemistry C* **2009**, 113, 4597–4604.

- [88] W. Pfalzgraff, S. Neshyba, M. Roeselova, “Comparative molecular dynamics study of vapor-exposed basal, prismatic, and pyramidal surfaces of ice”, *Journal of Physical Chemistry A* **2011**, *115*, 6184–6193.
- [89] E. Mazzega, U. Del Pennino, A. Loria, et al., “Volta effect and liquidlike layer at the ice surface”, *The Journal of Chemical Physics* **1976**, *64*, 1028–1031.
- [90] W. Lechner, C. Dellago, “Accurate determination of crystal structures based on averaged local bond order parameters”, *The Journal of Chemical Physics* **2008**, *129*, 114707.
- [91] S. W. Rick, “A reoptimization of the five-site water potential (TIP5P) for use with Ewald sums”, *The Journal of Chemical Physics* **2004**, *120*, 6085–6093.
- [92] R. G. Pereyra, M. A. Carignano, “Ice nanocolumns: a molecular dynamics study”, *The Journal of Physical Chemistry C* **2009**, *113*, 12699–12705.
- [93] J. Benet, P. Llombart, E. Sanz, et al., “Premelting-induced smoothening of the ice-vapor interface”, *Physical Review Letters* **2016**, *117*, 096101.
- [94] L. B. Skinner, C. Huang, D. Schlesinger, et al., “Benchmark oxygen-oxygen pair-distribution function of ambient water from X-ray diffraction measurements with a wide Q-range”, *The Journal of Chemical Physics* **2013**, *138*, 074506.
- [95] A. K. Soper, C. J. Benmore, “Quantum differences between heavy and light water”, *Physical Review Letters* **2008**, *101*, 065502.
- [96] C. Zhang, D. Donadio, G. Galli, “First-principle analysis of the IR stretching band of liquid water”, *The Journal of Physical Chemistry Letters* **2010**, *1*, 1398–1402.
- [97] M. Sulpizi, M. Salanne, M. Sprik, et al., “Vibrational sum frequency generation spectroscopy of the water liquid–vapor interface from density functional theory-based molecular dynamics simulations”, *The Journal of Physical Chemistry Letters* **2013**, *4*, 83–87.
- [98] J. Schaefer, E. H. G. Backus, Y. Nagata, et al., “Both inter- and intramolecular coupling of O–H groups determine the vibrational response of the water/air interface”, *The Journal of Physical Chemistry Letters* **2016**, *7*, 4591–4595.
- [99] M. Tuckerman, *Statistical mechanics: theory and molecular simulation*, Oxford University Press, **2010**.
- [100] M. P. Allen et al., “Introduction to molecular dynamics simulation”, *Computational soft matter: from synthetic polymers to proteins* **2004**, *23*, 1–28.
- [101] L. Verlet, “Computer ‘experiments’ on classical fluids: thermodynamical properties of Lennard-Jones molecules”, *Physical Review* **1967**, *159*, 98–103.
- [102] L. Verlet, “Computer ‘experiments’ on classical fluids. II. Equilibrium correlation functions”, *Physical Review* **1968**, *165*, 201–214.
- [103] H. C. Andersen, “Rattle: a ‘velocity’ version of the shake algorithm for molecular dynamics calculations”, *Journal of Computational Physics* **1983**, *52*, 24–34.
- [104] W. C. Swope, H. C. Andersen, P. H. Berens, et al., “A computer simulation method for the calculation of equilibrium constants for the formation of physical clusters of molecules: application to small water clusters”, *The Journal of Chemical Physics* **1982**, *76*, 637–649.
- [105] G. Bussi, D. Donadio, M. Parrinello, “Canonical sampling through velocity rescaling”, *The Journal of Chemical Physics* **2007**, *126*, 014101.

- [106] P. P. Ewald, "Die Berechnung optischer und elektrostatischer Gitterpotentiale", *Annalen der Physik* **1921**, 369, 253–287.
- [107] T. Darden, D. York, L. Pedersen, "Particle mesh Ewald: an $N \cdot \log(N)$ method for Ewald sums in large systems", *The Journal of Chemical Physics* **1993**, 98, 10089–10092.
- [108] M. Deserno, C. Holm, "How to mesh up Ewald sums. I. A theoretical and numerical comparison of various particle mesh routines", *The Journal of Chemical Physics* **1998**, 109, 7678–7693.
- [109] J.-P. Ryckaert, G. Ciccotti, H. J. Berendsen, "Numerical integration of the cartesian equations of motion of a system with constraints: molecular dynamics of n-alkanes", *Journal of Computational Physics* **1977**, 23, 327–341.
- [110] A. Heinecke, W. Eckhardt, M. Horsch, et al., *Supercomputing for molecular dynamics simulations: handling multi-trillion particles in nanofluidics*, Springer, **2015**.
- [111] B. Guillot, "A reappraisal of what we have learnt during three decades of computer simulations on water", *Journal of Molecular Liquids* **2002**, 101, Molecular Liquids. Water at the New Millenium, 219–260.
- [112] J. L. Aragones, E. G. Noya, J. L. F. Abascal, et al., "Properties of ices at 0 K: a test of water models", *The Journal of Chemical Physics* **2007**, 127, 154518.
- [113] J. L. F. Abascal, E. Sanz, R. G. Fernández, et al., "A potential model for the study of ices and amorphous water: TIP4P/Ice", *Journal of Chemical Physics* **2005**, 122, 234511–234519.
- [114] J. L. F. Abascal, C. Vega, "Dipole-quadrupole force ratios determine the ability of potential models to describe the phase diagram of water", *Physical Review Letters* **2007**, 98, 237801.
- [115] J. L. F. Abascal, C. Vega, "The melting point of hexagonal ice (I_h) is strongly dependent on the quadrupole of the water models", *Physical Chemistry Chemical Physics* **2007**, 9, 2775–2778.
- [116] J. L. F. Abascal, C. Vega, "A general purpose model for the condensed phases of water: TIP4P/2005", *The Journal of Chemical Physics* **2005**, 123, 234505.
- [117] W. Humphrey, A. Dalke, K. Schulten, "VMD: visual molecular dynamics", *Journal of Molecular Graphics* **1996**, 14, 33–38.
- [118] V. F. Petrenko, R. W. Whitworth, *Physics of ice*, Oxford University Press Oxford, **1999**.
- [119] V. Buch, P. Sandler, J. Sadlej, "Simulations of H_2O solid, liquid, and clusters, with an Emphasis on ferroelectric ordering transition in hexagonal ice", *The Journal of Physical Chemistry B* **1998**, 102, 8641–8653.
- [120] J. Alejandre, F. Bresme, M. González-Melchor, et al., "Effect of softness of the potential on the stress anisotropy in liquids", *The Journal of Chemical Physics* **2007**, 126, 224511.
- [121] C. Vega, E. De Miguel, "Surface tension of the most popular models of water by using the test-area simulation method", *The Journal of Chemical Physics* **2007**, 126, 154707.
- [122] I. T. Todorov, W. Smith, K. Trachenko, et al., "DL_POLY_3: new dimensions in molecular dynamics simulations via massive parallelism", *Journal of Materials Chemistry* **2006**, 16, 1911–1918.
- [123] M. J. Shultz, "Ice surfaces", *Annual Review of Physical Chemistry* **2017**, 68, 285–305.

- [124] A. Brumberg, K. Hammonds, I. Baker, et al., “Single-crystal I_h ice surfaces unveil connection between macroscopic and molecular structure”, *Proceedings of the National Academy of Sciences* **2017**, *114*, 5349–5354.
- [125] K. G. Libbrecht, “The physics of snow crystals”, *Reports on Progress in Physics* **2005**, *68*, 855–895.
- [126] K. G. Libbrecht, An experimental apparatus for observing deterministic structure formation in plate-on-pedestal ice crystal growth, **2015**.
- [127] Y. Kajima, S. Ogata, R. Kobayashi, et al., “Fluctuating local recrystallization of quasi-liquid layer of sub-micrometer-scale ice: a molecular dynamics study”, *Journal of the Physical Society of Japan* **2014**, *83*, 083601.
- [128] D. Nečas, P. Klapetek, “Gwyddion: an open-source software for SPM data analysis”, *Central European Journal of Physics* **2012**, *10*, 181–188.
- [129] A. K. Soper, “The radial distribution functions of water and ice from 220 to 673 K and at pressures up to 400 MPa”, *Chemical Physics* **2000**, *258*, 121–137.
- [130] M. Jochum, D. Andrienko, K. Kremer, et al., “Structure-based coarse-graining in liquid slabs”, *The Journal of Chemical Physics* **2012**, *137*, 064102.
- [131] R. M. Lynden-Bell, S. C. Morris, J. D. Barrow, et al., *Water and life: the unique properties of H_2O* , CRC Press, **2010**.
- [132] M. F. Chaplin, “Water’s hydrogen bond strength”, *Water and life: the unique properties of H_2O* **2010**, 69–86.
- [133] J. Sun, B. K. Clark, S. Torquato, et al., “The phase diagram of high-pressure superionic ice”, *Nature Communications* **2015**, *6*, 8156.
- [134] E. Arunan, G. R. Desiraju, R. A. Klein, et al., “Definition of the hydrogen bond (IUPAC Recommendations 2011)”, *Pure and Applied Chemistry* **2011**, *83*, 1637–1641.
- [135] M. W. Feyereisen, D. Feller, D. A. Dixon, “Hydrogen bond energy of the water dimer”, *The Journal of Physical Chemistry* **1996**, *100*, 2993–2997.
- [136] K. Stokely, M. G. Mazza, H. E. Stanley, et al., “Effect of hydrogen bond cooperativity on the behavior of water”, *Proceedings of the National Academy of Sciences* **2010**, *107*, 1301–1306.
- [137] M. Matsumoto, “Relevance of hydrogen bond definitions in liquid water”, *The Journal of Chemical Physics* **2007**, *126*, 054503.
- [138] P. Gasparotto, M. Ceriotti, “Recognizing molecular patterns by machine learning: an agnostic structural definition of the hydrogen bond”, *The Journal of Chemical Physics* **2014**, *141*, 174110.
- [139] Y. A. Mantz, F. M. Geiger, L. T. Molina, et al., “First-principles molecular-dynamics study of surface disordering of the (0001) face of hexagonal ice”, *Journal of Chemical Physics* **2000**, *113*, 10733–10743.
- [140] D. S. Franzblau, “Computation of ring statistics for network models of solids”, *Physical Review B* **1991**, *44*, 4925–4930.
- [141] R. Martoňák, D. Donadio, M. Parrinello, “Polyamorphism of ice at low temperatures from constant-pressure simulations”, *Physical Review Letters* **2004**, *92*, 225702.

- [142] J.-M. Leyssale, J. Delhommelle, C. Millot, “Atomistic simulation of the homogeneous nucleation and of the growth of N₂ crystallites”, *The Journal of Chemical Physics* **2005**, *122*, 104510.
- [143] G. E. Walrafen, “Raman spectral studies of water structure”, *The Journal of Chemical Physics* **1964**, *40*, 3249–3256.
- [144] J. R. Errington, P. G. Debenedetti, “Relationship between structural order and the anomalies of liquid water”, *Nature* **2001**, *409*, 318–321.
- [145] P. J. Steinhardt, D. R. Nelson, M. Ronchetti, “Bond-orientational order in liquids and glasses”, *Physical Review B* **1983**, *28*, 784–805.
- [146] J. S. van Duijneveldt, D. Frenkel, “Computer simulation study of free energy barriers in crystal nucleation”, *The Journal of Chemical Physics* **1992**, *96*, 4655–4668.
- [147] M. A. Blanco, M. Flórez, M. Bermejo, “Evaluation of the rotation matrices in the basis of real spherical harmonics”, *Journal of Molecular Structure: THEOCHEM* **1997**, *419*, 19–27.
- [148] J. R. Espinosa, E. Sanz, C. Valeriani, et al., “Homogeneous ice nucleation evaluated for several water models”, *The Journal of Chemical Physics* **2014**, *141*, 18C529.
- [149] E. Sanz, C. Vega, J. R. Espinosa, et al., “Homogeneous ice nucleation at moderate supercooling from molecular simulation”, *Journal of the American Chemical Society* **2013**, *135*, 15008–15017.
- [150] A. Reinhardt, J. P. K. Doye, E. G. Noya, et al., “Local order parameters for use in driving homogeneous ice nucleation with all-atom models of water”, *The Journal of Chemical Physics* **2012**, *137*, 194504.
- [151] T. Li, D. Donadio, G. Russo, et al., “Homogeneous ice nucleation from supercooled water”, *Physical Chemistry Chemical Physics* **2011**, *13*, 19807–19813.
- [152] P. R. ten Wolde, M. J. Ruiz-Montero, D. Frenkel, “Numerical calculation of the rate of crystal nucleation in a Lennard-Jones system at moderate undercooling”, *The Journal of Chemical Physics* **1996**, *104*, 9932–9947.
- [153] I. Volkov, M. Cieplak, J. Koplik, et al., “Molecular dynamics simulations of crystallization of hard spheres”, *Physical Review E* **2002**, *66*, 061401.
- [154] P. R. ten Wolde, D. Frenkel, “Homogeneous nucleation and the Ostwald step rule”, *Physical Chemistry Chemical Physics* **1999**, *1*, 2191–2196.
- [155] I. Gladich, W. Pfalzgraff, O. Maršálek, et al., “Arrhenius analysis of anisotropic surface self-diffusion on the prismatic facet of ice”, *Physical Chemistry Chemical Physics* **2011**, *13*, 19960–19969.
- [156] A. Barros de Oliveira, P. A. Netz, T. Colla, et al., “Structural anomalies for a three dimensional isotropic core-softened potential”, *The Journal of Chemical Physics* **2006**, *125*, 124503.
- [157] Z. Yan, S. V. Buldyrev, P. Kumar, et al., “Structure of the first-and second-neighbor shells of simulated water: quantitative relation to translational and orientational order”, *Physical Review E* **2007**, *76*, 051201.
- [158] R. Brown, “A brief account of microscopical observations made in the months of June, July and August 1827, on the particles contained in the pollen of plants; and on the general existence of active molecules in organic and inorganic bodies”, *Philosophical Magazine Series 2* **1828**, *4*, 161–173.

- [159] T. Lucretius Carus, H. A. J. Munro, G. Long, *On the nature of things*, Encyclopaedia Britannica, **1952**.
- [160] W. Sutherland, "A dynamical theory of diffusion for non-electrolytes and the molecular mass of albumin", *Philosophical Magazine* **1905**, 9, 781–785.
- [161] A. Einstein, "Über die von der molekularkinetischen Theorie der Wärme geforderte Bewegung von in ruhenden Flüssigkeiten suspendierten Teilchen", *Annalen der Physik* **1905**, 322, 549–560.
- [162] A. Einstein, A. Beck, P. Havas, *The collected papers of Albert Einstein*, Vol. 2, Princeton University Press, **1989**.
- [163] M. von Smoluchowski, "Zur kinetischen Theorie der Brownschen Molekularbewegung und der Suspensionen", *Annalen der Physik* **1906**, 326, 756–780.
- [164] P. Langevin, "Sur la théorie du mouvement brownien", *Comptes rendus de l'Académie des sciences* **1908**, 146, 530–533.
- [165] D. S. Lemons, A. Gythiel, "Paul Langevin's 1908 paper 'on the theory of Brownian motion' ['Sur la théorie du mouvement brownien,' CR Acad. Sci.(Paris) 146, 530–533 (1908)]", *American Journal of Physics* **1997**, 65, 1079–1081.
- [166] M. S. Green, "Markoff random processes and the statistical mechanics of time-dependent phenomena. II. Irreversible processes in fluids", *The Journal of Chemical Physics* **1954**, 22, 398–413.
- [167] R. Kubo, "Statistical-mechanical theory of irreversible processes. I. General theory and simple applications to magnetic and conduction problems", *Journal of the Physical Society of Japan* **1957**, 12, 570–586.
- [168] I. M. Sokolov, "Models of anomalous diffusion in crowded environments", *Soft Matter* **2012**, 8, 9043–9052.
- [169] R. Metzler, J.-H. Jeon, A. G. Cherstvy, et al., "Anomalous diffusion models and their properties: non-stationarity, non-ergodicity, and ageing at the centenary of single particle tracking", *Physical Chemistry Chemical Physics* **2014**, 16, 24128–24164.
- [170] R. Huang, I. Chavez, K. M. Taute, et al., "Direct observation of the full transition from ballistic to diffusive Brownian motion in a liquid", *Nature Physics* **2011**, 7, 576–580.
- [171] P. Chaudhuri, L. Berthier, S. Sastry, et al., "Diffusion in glassy systems" in *Diffusion Fundamentals III*, (Eds.: C. Chmelik, N. Kanellopoulos, J. Kärger, et al.), Leipziger Universitätsverlag, Leipzig, **2009**, pp. 334–352.
- [172] M. Kizilyalli, J. Corish, R. Metselaar, "Definitions of terms for diffusion in the solid state", *Pure and Applied Chemistry* **1999**, 71, 1307–1325.
- [173] P. Chaudhuri, L. Berthier, S. Sastry, et al., *Diffusion fundamentals III*, (Eds.: C. Chmelik, N. Kanellopoulos, J. Kärger, et al.), Leipziger Universitätsverlag, **2009**.
- [174] T. Williams, C. Kelley, many others., Gnuplot 5: an interactive plotting program, <http://gnuplot.sourceforge.net/>, **2015**.
- [175] D. Rozmanov, P. G. Kusalik, "Transport coefficients of the TIP4P-2005 water model", *The Journal of Chemical Physics* **2012**, 136, 044507.
- [176] W. S. Price, H. Ide, Y. Arata, "Self-diffusion of supercooled water to 238 K using PGSE NMR diffusion measurements", *The Journal of Physical Chemistry A* **1999**, 103, 448–450.

- [177] J. R. Espinosa, C. Navarro, E. Sanz, et al., "On the time required to freeze water", *The Journal of Chemical Physics* **2016**, 145, 211922.
- [178] V. Babin, C. Leforestier, F. Paesani, "Development of a "first principles" water potential with flexible monomers: dimer potential energy surface, VRT spectrum, and second virial coefficient", *Journal of Chemical Theory and Computation* **2013**, 9, 5395–5403.
- [179] V. Babin, G. R. Medders, F. Paesani, "Development of a "first principles" water potential with flexible monomers. II: trimer potential energy surface, third virial coefficient, and small clusters", *Journal of Chemical Theory and Computation* **2014**, 10, 1599–1607.
- [180] G. R. Medders, V. Babin, F. Paesani, "Development of a 'first-principles' water potential with flexible monomers. III. Liquid phase properties", *Journal of Chemical Theory and Computation* **2014**, 10, 2906–2910.
- [181] G. R. Medders, F. Paesani, "Infrared and Raman spectroscopy of liquid water through 'first-principles' many-body molecular dynamics", *Journal of Chemical Theory and Computation* **2015**, 11, 1145–1154.
- [182] S. K. Reddy, S. C. Straight, P. Bajaj, et al., "On the accuracy of the MB-pol many-body potential for water: interaction energies, vibrational frequencies, and classical thermodynamic and dynamical properties from clusters to liquid water and ice", *The Journal of Chemical Physics* **2016**, 145, 194504.
- [183] D. Beaglehole, D. Nason, "Transition layer on the surface on ice", *Surface Science* **1980**, 96, 357–363.
- [184] Y. Furukawa, I. Ishikawa, "Direct evidence for melting transition at interface between ice crystal and glass substrate", *Journal of Crystal Growth* **1993**, 128, 1137–1142.
- [185] V. I. Kvlivdze, V. F. Kiselev, A. B. Kurzaev, et al., "The mobile water phase on ice surfaces", *Surface Science* **1974**, 44, 60–68.
- [186] M. Ohtomo, G. Wakahama, "Growth rate of recrystallization in ice", *The Journal of Physical Chemistry* **1983**, 87, 4139–4142.
- [187] T. Ishizaki, M. Maruyama, Y. Furukawa, et al., "Premelting of ice in porous silica glass", *Journal of Crystal Growth* **1996**, 163, 455–460.
- [188] H. Bluhm, T. Inoue, M. Salmeron, "Friction of ice measured using lateral force microscopy", *Physical Review B* **2000**, 61, 7760–7765.
- [189] C. R. Slaughterbeck, "Electric field effects on force curves for oxidized silicon tips and ice surfaces in a controlled environment", *Journal of Vacuum Science & Technology A: Vacuum Surfaces and Films* **1996**, 14, 1213–1218.
- [190] V. F. Petrenko, "Study of the surface of ice, ice/solid and ice/liquid interfaces with scanning force microscopy", *The Journal of Physical Chemistry B* **1997**, 101, 6276–6281.
- [191] H. Groenzin, I. Li, V. Buch, et al., "The single-crystal, basal face of ice I_h investigated with sum frequency generation", *The Journal of Chemical Physics* **2007**, 127, 214502.
- [192] H. Groenzin, I. Li, M. J. Shultz, "Sum-frequency generation: polarization surface spectroscopy analysis of the vibrational surface modes on the basal face of ice I_h ", *The Journal of Chemical Physics* **2008**, 128, 214510.
- [193] I. L. Barnett, H. Groenzin, M. J. Shultz, "Hydrogen bonding in the hexagonal ice surface", *Journal of Physical Chemistry A* **2011**, 115, 6039–6045.

- [194] M. Maruyama, M. Bienfait, J. G. Dash, et al., “Interfacial melting of ice in graphite and talc powders”, *Journal of Crystal Growth* **1992**, 118, 33–40.
- [195] C. Toubin, S. Picaud, P. N. M. Hoang, et al., “Dynamics of ice layers deposited on MgO(001): quasielastic neutron scattering experiments and molecular dynamics simulations”, *Journal of Chemical Physics* **2001**, 114, 6371–6381.
- [196] J. Braun, A. Glebov, A. Graham, et al., “Structure and phonons of the ice surface”, *Physical Review Letters* **1998**, 80, 2638–2641.
- [197] A. Goto, K. Akiya, T. Hondoh, et al., “Characterization of the (0001) surface of ice I_h crystal by crystal truncation rod scattering with the use of a synchrotron radiation source”, *Journal of Crystal Growth* **1992**, 121, 360–364.
- [198] U. K. Krieger, T. Huthwelker, C. Daniel, et al., “Rutherford backscattering to study the near-surface region of volatile liquids and solids”, *Science* **2002**, 295, 1048–1050.
- [199] F. E. Livingston, J. A. Smith, S. M. George, “Depth-profiling and diffusion measurements in ice films using infrared laser resonant desorption”, *Analytical Chemistry* **2000**, 72, 5590–5599.
- [200] F. E. Livingston, J. A. Smith, S. M. George, “General trends for bulk diffusion in ice and surface diffusion on ice”, *The Journal of Physical Chemistry A* **2002**, 106, 6309–6318.
- [201] V. Sadtchenko, G. E. Ewing, “A new approach to the study of interfacial melting of ice: infrared spectroscopy”, *Canadian Journal of Physics* **2003**, 81, 333–341.
- [202] V. Sadtchenko, G. E. Ewing, “Interfacial melting of thin ice films: an infrared study”, *Journal of Chemical Physics* **2002**, 116, 4686–4697.
- [203] A. Kaverin, V. Tsionsky, D. Zagidulin, et al., “A novel approach for direct measurement of the thickness of the liquid-like layer at the ice/solid interface”, *The Journal of Physical Chemistry B* **2004**, 108, 8759–8762.
- [204] S. Valeri, S. Mantovani, “The liquidlike layer at the ice surface: a direct experimental evidence”, *The Journal of Chemical Physics* **1978**, 69, 5207–5208.
- [205] R. S. Bradley, “The electrical conductivity of ice”, *Transactions of the Faraday Society* **1957**, 53, 687–691.
- [206] F. Heinmets, R. Blum, “Conductivity measurements on pure ice”, *Transactions of the Faraday Society* **1963**, 59, 1141–1146.
- [207] M. A. Maidique, “Transfer of protons through ‘pure’ ice I_h single crystals. III. Extrinsic versus intrinsic polarization; surface versus volume conduction”, *The Journal of Chemical Physics* **1971**, 54, 150–160.
- [208] P. Wilson, J. Arthur, A. Haymet, “Ice premelting during differential scanning calorimetry”, *Biophysical Journal* **1999**, 77, 2850–2855.
- [209] W. D. Kingery, “Regelation, surface diffusion, and ice sintering”, *Journal of Applied Physics* **1960**, 31, 833–838.
- [210] R. Gilpin, “Wire regelation at low temperatures”, *Journal of Colloid and Interface Science* **1980**, 77, 435–448.
- [211] J. Ocampo, J. Klinger, “Modification of the surface structure of ice during ageing”, *The Journal of Physical Chemistry* **1983**, 87, 4167–4170.

- [212] T. F. Kahan, J. P. Reid, D. J. Donaldson, "Spectroscopic probes of the quasi-liquid layer on ice", *Journal of Physical Chemistry A* **2007**, *111*, 11006–11012.
- [213] T. F. Kahan, S. N. Wren, D. J. Donaldson, "A pinch of salt is all it takes: chemistry at the frozen water surface", *Accounts of Chemical Research* **2014**, *47*, 1587–1594.
- [214] T. Gonda, T. Arai, T. Sei, "Experimental study on the melting process of ice crystals just below the melting point", *Polar meteorology and glaciology* **1999**, *13*, 38–42.
- [215] D. R. Haynes, N. J. Tro, S. M. George, "Condensation and evaporation of water on ice surfaces", *The Journal of Physical Chemistry* **1992**, *96*, 8502–8509.

List of Figures

1.1	(a) Snowflake displaying six-fold symmetry. (b) Molecular picture of hexagonal ice.	1
1.2	(a) Schematic drawing of the I_h unit cell. (b) The unit cell with a proton-disordered hydrogen arrangement. (c) The three most prominent planes. .	2
1.3	Bulk crystal after cleaving: Surface rearrangement versus pre-melting. . . .	3
1.4	Comparison of different methods to derive the thickness of the disordered interface (DI) at the ice/vapour interface versus the degree of supercooling $\Delta T = T_m - T$	6
1.5	Experimental technique to grow single-crystalline ice.	8
1.6	Experimental determination of the orientation of the grown ice crystal. . .	8
1.7	Time and spatial resolution of the main molecular dynamics (MD) simulation methods.	10
1.8	Periodic boundary conditions in lateral directions.	11
1.9	Parking lot mechanism of in-plane diffusion.	13
2.1	Flowchart of a classical MD simulation.	15
2.2	The phase diagrams and the melting points of prominent water models in comparison to the experimental values.	21
2.3	Geometry of the TIP4P and TIP4P/Ice models.	22
2.4	Side view of the simulation cell for the primary prismatic plane.	23
3.1	Top view of the basal plane.	27
3.2	Schematic drawing of the three low-index surfaces of hexagonal ice relative to the hexagonal unit cell.	28
3.3	Top view of the (a) basal, (0001) (b) primary prismatic ($10\bar{1}0$), and (c) secondary prismatic ($\bar{1}2\bar{1}0$) surfaces of hexagonal ice.	28
3.4	Hexagonal arrangement of oxygen atoms for the (a) basal {0001} and (b) primary prismatic surfaces $\{10\bar{1}0\}$ of hexagonal ice.	29
3.5	Density profiles obtained with the TIP4P/ice model for the (a) basal, (b) primary prismatic plane and (c) secondary prismatic plane of hexagonal ice.	29
3.6	Z-intervals for the two-dimensional density maps.	30
3.7	Two-dimensional density maps of the oxygen atoms belonging to the first layer of the three most prominent ice surfaces.	31
3.8	Assignment of special features of the two-dimensional density maps to molecular arrangements.	31
3.9	Snapshots of the oxygen atoms of the first layers of the three most prominent ice surfaces at three selected temperatures (200 K, 250 K, and 270 K).	32

3.10	Two-dimensional density map of the basal surface (a) and the corresponding 2D-FFT (α).	33
3.11	Illustration of the calculation of a radial distribution function (RDF).	34
3.12	Temperature-dependent RDFs of solid ice and liquid water and the first three layers of the basal plane.	35
3.13	Temperature-dependent RDFs of reference ice and supercooled water and the first three layers of the primary prismatic plane.	36
3.14	Temperature-dependent RDFs of the outer four layers of the secondary prismatic plane.	36
4.1	Floating ice in the Weddell Sea (Antarctic).	39
4.2	Visualisation of the selected H-bond criteria used in this work.	40
4.3	Temperature-dependent percentage of free OH at the surface, percentage of strong H-bonds, average $\angle O_D H O_A$ -angles, and the average $r_{O_D O_A}$ of the pre-melting slabs of hexagonal ice with the three low-index surfaces exposed to vacuum for the upper three to six layers.	42
4.4	Spherical orientation of the OH-vectors for (a) the bulk ice reference at 250 K and (b) the liquid reference at 300 K.	44
4.5	Spherical orientation of the OH-vectors for the upper three layers of the three most prominent ice surfaces at the three selected temperatures.	45
4.6	Spherical orientation of the OH-vectors for the upper three bilayers of the basal plane for 270 K.	46
4.7	Dynamical properties of the H-Bonding at the three most prominent surfaces of hexagonal ice.	47
4.8	Stacked bar diagram of the amount of rings per molecule of the first three bilayers of the basal plane.	49
4.9	Stacked bar diagram of the amount of rings per molecule of the first three bilayers of the primary prismatic plane.	51
4.10	Stacked bar diagram of the amount of rings per molecule of the first three single-layers of the secondary prismatic plane.	51
5.1	Tetrahedral bonding arrangement of the neighbouring oxygen atoms of a central oxygen atom in the hexagonal ice lattice.	53
5.2	Contributions to q_1 for a linear arrangement.	55
5.3	Contributions to q_1 for a tetrahedral arrangement.	55
5.4	$q_{\text{tetrahedral}}$ and the LSOPs for $l = 1, 8$ for a pseudo-random distribution (grey line), a square (blue dash-dotted line), and a tetrahedron (magenta dashed line).	57
5.5	Selected LSOPs for $l = 2, 3, 5, 6$ for a bulk solid reference at $T = 250$ K, a bulk liquid reference at $T = 300$ K, and an ice slab with the basal plane exposed to vacuum at $T = 250$ K.	58
5.6	Bilayer-resolved LSOPs, for $l = 2, 3, 5, 6$, for an ice slab at 250 K with the basal plane exposed to the vacuum.	61
5.7	Verification of the bilayer approach.	61
5.8	Distributions of q_5 for the upper six bilayers for an ice slab with the basal plane exposed to the vacuum.	62

5.9	Distributions of q_5 for the upper six bilayers for an ice slab with the primary prismatic plane exposed to the vacuum.	63
5.10	Distributions of q_5 for the upper six single-layers for ice slabs with the secondary prismatic plane exposed to the vacuum.	64
6.1	Z-components of all oxygen atom trajectories for the last forty nanoseconds of the simulation of the basal plane at 270 K.	69
6.2	Arrhenius plot of the exchange rates between the layers for all systems. . .	69
6.3	Temperature-dependent mean square displacements for the first two layers of the basal plane, the primary prismatic plane, and the secondary prismatic plane.	70
6.4	Selected single-molecule trajectories of (a) the first bilayer and (b) the second bilayer of the basal plane at 270 K.	71
6.5	Fitted exponents for the first two layers of the three ice surfaces.	71
6.6	Arrhenius fits of the top and bottom surfaces and their respective in-plane directions.	72
6.7	(a) Mean square displacement (x-y-z-average). (b) Number of evaluated single-molecule trajectories. (c) Fitted exponents. (d) Fitted self-diffusion coefficients and their respective Arrhenius fits.	73
6.8	Fitted self-diffusion coefficients for the reference liquid water, the basal, the primary prismatic, and the secondary prismatic ice surfaces and their respective Arrhenius fits.	74
6.9	Comparison of the Arrhenius plot of our simulations to the literature. . . .	74
6.10	Two-dimensional histograms of the oxygen atom motion vectors in the top layer of all three surfaces at 200 K, 250 K, and 270 K.	75
8.1	Miller-Bravais indices and its vectors.	82
8.2	Determination of the secondary prismatic plane ($\bar{1}2\bar{1}0$). based on the Miller-Bravais indices.	82
8.3	Examples of the symmetry-equivalent planes for the three low-index surfaces of hexagonal ice.	83
8.4	Full set of symmetry equivalent planes for the basal plane	83
8.5	Full set of symmetry equivalent planes for the primary prismatic plane. . .	83
8.6	Full set of symmetry equivalent planes for the secondary prismatic plane. .	83
8.7	Two-dimensional density maps of the oxygen atoms belonging to the first layer of the basal, primary prismatic plane, and secondary prismatic plane for all simulated temperatures.	84
8.8	Details about the 2D-FFT of the secondary prismatic plane	84
8.9	Illustrations for the rescaling of the RDF for a slab with two sharp interfaces.	85
8.10	Percentage of free OH present on a non-rearranged basal plane.	86
8.11	Percentage of free OH present on a non-rearranged primary prismatic plane.	87
8.12	Percentage of free OH present on a non-rearranged secondary prismatic plane.	87
8.13	Overview of the statical H-bond analysis of all surfaces in one plot.	88
8.14	Spherical orientation of the <i>OH</i> -vectors for the upper three bilayers of the basal plane at all temperatures.	89

8.15	Spherical orientation of the <i>OH</i> -vectors for the upper three bilayers of the primary prismatic plane at all temperatures.	90
8.16	Spherical orientation of the <i>OH</i> -vectors for the upper three layers of the secondary prismatic plane at all temperatures.	91
8.17	Z-resolved two-dimensional histograms of the distributions of the <i>OH</i> -vector perpendicular to the basal plane.	92
8.18	Z-resolved two-dimensional histograms of the distributions of the <i>OH</i> -vector perpendicular to the primary prismatic plane.	93
8.19	Z-resolved two-dimensional histograms of the distributions of the <i>OH</i> -vector perpendicular to the secondary prismatic plane.	94
8.20	Dynamical H-bond analysis for all surfaces in one plot.	95
8.21	Trends of the ring analysis for the first three layers of the basal plane	95
8.22	Trends of the ring analysis for the first three layers of the primary prismatic plane	96
8.23	Trends of the ring analysis for the first three layers of the secondary prismatic plane	96
8.24	Trends of the ring analysis for the first three layers of all surfaces in one plot.	97
8.25	Temperature-dependent total amount of <i>n</i> -membered rings for <i>n</i> = 3–10 for systems with the basal plane exposed to the vacuum.	97
8.26	Temperature-dependent total amount of <i>n</i> -membered rings for <i>n</i> = 3–10 for systems with the primary prismatic plane exposed to the vacuum.	98
8.27	Temperature-dependent total amount of <i>n</i> -membered rings for <i>n</i> = 3–10 for systems with the secondary prismatic plane exposed to the vacuum.	98
8.28	Z-position of the centre-of-mass of the rings for three selected temperatures (200 K, 250 K, and 270 K) for slabs with the basal plane exposed to the vacuum.	99
8.29	Explanation for the formation of the ten-membered rings and its connection to the position of the original six-membered rings.	99
8.30	Z-position of the centre-of-mass of the rings for three selected temperatures (200 K, 250 K, and 270 K) for slabs with the primary prismatic plane exposed to the vacuum.	100
8.31	Z-position of the centre-of-mass of the rings for three selected temperatures of 200 K, 250 K, and 270 K for slabs with the secondary prismatic plane exposed to the vacuum.	101
8.32	Percentage of molecules analysed per layer for the low-index surfaces of ice.	102
8.33	Distributions of <i>q</i> ₂ for the basal plane.	103
8.34	Distributions of <i>q</i> ₂ for the primary prismatic plane.	104
8.35	Distributions of <i>q</i> ₂ for the secondary prismatic plane.	105
8.36	Distributions of <i>q</i> ₃ for the basal plane	106
8.37	Distributions of <i>q</i> ₃ for the primary prismatic plane.	107
8.38	Distributions of <i>q</i> ₃ for the secondary prismatic plane.	108
8.39	Distributions of <i>q</i> ₅ for the basal plane.	109
8.40	Distributions of <i>q</i> ₅ for the primary prismatic plane.	110
8.41	Distributions of <i>q</i> ₅ for the secondary prismatic plane.	111
8.42	Distributions of <i>q</i> ₆ for the basal plane.	112
8.43	Distributions of <i>q</i> ₆ for the primary prismatic plane.	113

8.44	Distributions of q_6 for the secondary prismatic plane.	114
8.45	Temperature-dependent behaviour of the distributions for q_2 for the upper three bilayers of the basal plane.	115
8.46	Trends of the distributions from Figure 8.45.	115
8.47	Temperature-dependent behaviour of the distributions for q_2 for the upper three bilayers of the primary prismatic plane.	116
8.48	Trends of the distributions from Figure 8.47.	116
8.49	Temperature-dependent behaviour of the distributions for q_2 for the upper three single-layers of the secondary prismatic plane.	117
8.50	Trends of the distributions from Figure 8.49.	117
8.51	Temperature-dependent behaviour of the distributions for q_3 for the upper three bilayers of the basal plane.	118
8.52	Temperature-dependent behaviour of the distributions for q_3 for the upper three bilayers of the primary prismatic plane.	118
8.53	Temperature-dependent behaviour of the distributions for q_3 for the upper three single-layers of the secondary prismatic plane.	119
8.54	Temperature-dependent behaviour of the distributions for q_5 for the upper three bilayers of the basal plane.	119
8.55	Temperature-dependent behaviour of the distributions for q_5 for the upper three bilayers of the primary prismatic plane.	120
8.56	Temperature-dependent behaviour of the distributions for q_5 for the upper three single-layers of the secondary prismatic plane.	120
8.57	Temperature-dependent behaviour of the distributions for q_6 for the upper three bilayers of the basal plane.	121
8.58	Temperature-dependent behaviour of the distributions for q_6 for the upper three bilayers of the primary prismatic plane.	121
8.59	Temperature-dependent behaviour of the distributions for q_6 for the upper three single-layers of the secondary prismatic plane.	122
8.60	Temperature-dependent layer-resolved distributions for q_2 of the upper six bilayers of ice slabs of the basal plane.	123
8.61	Temperature-dependent trends of the upper six bilayers from Figure 8.60. .	123
8.62	Temperature-dependent layer-resolved distributions for q_2 of the upper six bilayers of ice slabs of the primary prismatic plane.	124
8.63	Temperature-dependent trends of the upper six bilayers from Figure 8.62. .	124
8.64	Temperature-dependent layer-resolved distributions for q_2 of the upper six single-layers of ice slabs of the secondary prismatic plane.	125
8.65	Temperature-dependent trends of the upper six single-layers from Figure 8.64.	125
8.66	Temperature-dependent layer-resolved distributions for q_3 of the upper six bilayers of ice slabs of the basal plane.	126
8.67	Temperature-dependent layer-resolved distributions for q_3 of the upper six bilayers of ice slabs of the primary prismatic plane.	126
8.68	Temperature-dependent layer-resolved distributions for q_3 of the upper six single-layers of ice slabs of the secondary prismatic plane.	127
8.69	Temperature-dependent layer-resolved distributions for q_6 of the upper six bilayers of ice slabs of the basal plane.	127

8.70	Temperature-dependent layer-resolved distributions for q_6 of the upper six bilayers of ice slabs of the primary prismatic plane.	128
8.71	Temperature-dependent layer-resolved distributions for q_6 of the upper six single-layers of ice slabs of the secondary prismatic plane.	128
8.72	Temperature-dependent layer-resolved distribution for q_i , $i = 2, 3, 5, 6$ for the basal plane at 270 K for two definitions of the next neighbours.	129
8.73	Z-components of all oxygen atom trajectories for the last forty nanoseconds of the simulation of (a) the primary prismatic plane, and (b) the secondary prismatic plane at 270 K.	130
8.74	Temperature-dependent mean square displacements for the first two bilayers of the basal plane, the primary prismatic plane, and the secondary prismatic plane.	131
8.75	Temperature-dependent amount of single-molecule trajectories contributing to the MSD of a length t for the first layers of the (a) basal plane, the (b) primary prismatic plane, and (c) the secondary prismatic plane.	131
8.76	Temperature-dependent number of analysed traces for the second layers of the hexagonal ice surfaces for the simulated top and bottom surfaces separately.	132
8.77	MSDs of the first four layers for all temperatures and surfaces.	133
8.78	Distribution of self-diffusion directions at the top layers of the three surfaces at all temperatures.	138
8.79	Self-diffusion directions for different time intervals.	139

List of Tables

2.1	Comparison of parameters for the TIP4P, the TIP4P/2005 and the TIP4P/Ice model. ^[113,114]	22
2.2	Sizes of the simulation cells for the basal, primary prismatic, and secondary prismatic slabs obtained after the NpT simulation, its respective surface areas and its (estimated) densities without the applied vacuum.	24
2.3	Dimensions of the simulation cells of the solid and liquid reference samples and their respective densities obtained after the NpT simulation.	25
4.1	H-bonding analysis for the solid ice reference at 250 K and the liquid water reference at 300 K.	41
4.2	Amount of n -membered rings ($n = 3-10$) per molecule for a solid ice reference system at 250 K and a liquid water reference system at 300 K.	49
5.1	Local Steinhardt order parameters as calculated for a tetrahedral arrangement of neighbours while reducing the number of neighbours sequentially.	60
6.1	Fit parameters of the Arrhenius plots of Figure 6.6.	72
8.1	Measurement techniques probing the hexagonal ice surface.	81
8.2	Amount of analysed molecules in %	102
8.3	Fitted exponents for the first layers of the three most prominent ice surfaces.	134
8.4	Fitted exponents for the second layers of the three most prominent ice surfaces.	135
8.5	Separate temperature-dependent self-diffusion coefficients.	135
8.6	Fit parameters of the Arrhenius plots of Figure 6.6.	136
8.7	Fitted exponents of the ln-ln-fits of the MSDs for supercooled water.	136
8.8	Separate temperature-dependent self-diffusion coefficients for (supercooled) water.	136
8.9	Parameters of the Arrhenius fit for the (supercooled) water reference.	137

Acknowledgement

Curriculum vitae

[REDACTED]

Higher education

[REDACTED]

Education

[REDACTED]

